



AALBORG UNIVERSITY
DENMARK

Aalborg Universitet

Design and Control of the PowerTake-Off System for a Wave Energy Converter with Multiple Absorbers

Hansen, Rico Hjerm

Publication date:
2013

Document Version
Publisher's PDF, also known as Version of record

[Link to publication from Aalborg University](#)

Citation for published version (APA):
Hansen, R. H. (2013). *Design and Control of the PowerTake-Off System for a Wave Energy Converter with Multiple Absorbers*. Department of Energy Technology, Aalborg University.

General rights

Copyright and moral rights for the publications made accessible in the public portal are retained by the authors and/or other copyright owners and it is a condition of accessing publications that users recognise and abide by the legal requirements associated with these rights.

- Users may download and print one copy of any publication from the public portal for the purpose of private study or research.
- You may not further distribute the material or use it for any profit-making activity or commercial gain
- You may freely distribute the URL identifying the publication in the public portal -

Take down policy

If you believe that this document breaches copyright please contact us at vbn@aub.aau.dk providing details, and we will remove access to the work immediately and investigate your claim.

Design and Control of the Power Take-Off System for a Wave Energy Converter with Multiple Absorbers

by
Rico Hjerm Hansen

Dissertation submitted to the Faculty of Engineering & Science at Aalborg University
in partial fulfilment of the requirements for the degree of Doctor of Philosophy in
Energy Technology

2013



Department of
ENERGY TECHNOLOGY 

WAVESTAR

Design and Control of the Power Take-Off System for a Wave Energy Converter with Multiple Absorbers

By

Rico Hjerm Hansen

Department of Energy Technology



AALBORG UNIVERSITY
DENMARK

A Dissertation Submitted to
The Faculty of Engineering, Science and Medicine, Aalborg University
in Partial Fulfilment for the Degree of Doctor of Philosophy

October 2013
Aalborg, Denmark

Design and Control of the Power Take-Off System
for a Wave Energy Converter with Multiple Absorbers

Copyright © Rico Hjerem Hansen, 2013
All rights reserved

Aalborg University
Department of Energy Technology
Pontoppidanstraede 101
9220 Aalborg East
Denmark

Printed in Denmark by Uniprint, 2014

ISBN 978-87-92846-34-1

Preface

This dissertation has been submitted to the Faculty of Engineering and Science at Aalborg University in partial fulfilment of the requirements for the Ph.D. degree in Energy Technology. The work has been carried out at Wave Star A/S and at the Institute of Energy Technology at Aalborg University. The work has been partially funded by the Danish Ministry of Science Technology and Innovation under the Industrial Ph.D. initiative.

The work had not been possible without the settings provided by Wavestar, who has continuously balanced between providing free reins to the project and tightening them when the project needed to push forward. In this regard I would like to direct a big thanks to the company and colleagues for their support and making this work possible. Specially, I would like to thank Morten Kramer, whom I have bothered both day and night whenever I needed to discuss wave theory or required new hydro-dynamic calculations asap.

I would like to thank my offices mates, Søren Stubkier, Anders Hansen, Lasse Schmidt, Daniel Rømer and Per Johansen for the many enjoyable and fun hours, inspirational discussions and being able to follow their interesting projects as well.

Supporting this work, a group of master students, Nick Berg, Rasmus Holm and Morten Walkusch, did an outstanding job in their master thesis on implementing a prototype magnetic gear, which I highly acknowledge. I would also like to direct a big thanks to Peter Omand Rasmussen for his relentless interest in the project and many ideas on non-hydraulic solutions.

Special thanks go to my supervisor, Prof. Torben O. Andersen, for many pleasant and enlightening conversations and hours, both on and off-topic, and for his great moral support throughout this work. Likewise, I would like to thank Asc. Prof. Henrik C. Pedersen, always being ready for providing insights and feedback on my work.

I would also like to thank my university colleagues for many memorable conference trips. I still smile when I think back on moments like climbing the Great Wall of China, which almost got the best of us (or at-least, some of us).

My undoubtedly greatest gratitude goes to my special lady, Thea, to stand by and support me during this long period, and for whom I in the endgame ended up giving a puppy, Gwenda, for making sure she still got some of the attention and love she so greatly deserves. And at this moment of writing, I cannot wait for getting started on the caching up.

Looking in the mirror after having performed such a long intensive study, I still bless ignorance; otherwise I would never have gotten the great idea of buying and restoring a house half way into the Ph.D. period.

Aalborg, 28th October, 2013

Rico Hjerm Hansen

Contents

Abstract	I
Resumé	III
List of Publications	V
Nomenclature and Abbreviations	VII
1 Introduction	1
1.1 Wave Energy Concepts and Active Projects	1
1.2 Current Trend and Potential of the Wave Energy Sector	4
1.3 Short Historical Perspective	5
1.4 Wave Energy Technology Challenges	6
1.5 Power Take-Off Design Aspects	7
1.6 Basic Power Extraction	8
1.7 Case System: Wavestar C5 WEC	11
1.8 Outline of Dissertation	16
1.9 Reading Instructions	19
2 Modelling of the Wavestar WEC	21
2.1 Mechanical Overview of C5	21
2.2 Wave Model	25
2.3 Single Absorber Model	30
2.4 Multi Absorber Model	38
2.5 Model Verification by 1:20 Scale Tank Tests	40
2.6 Summary	44
3 Implementation of Reactive Control	47
3.1 Introduction to Wave Power Extraction	47
3.2 Optimal Control of Absorbers	49
3.3 Causal Reactive Control in Irregular Waves	54
3.4 Including PTO Efficiency in Reactive Control Design	56
3.5 Tank Test Verification of Control Strategies	62
3.6 Summary	64
4 Wave Power Extraction Algorithms	67
4.1 Method for Optimising and Comparing WPEAs	67
4.2 Causal Reactive Control	73
4.3 Linear Damping Control	77
4.4 Coulomb Damping Control	77
4.5 Latching Control	82
4.6 De-Clutching Control	88
4.7 Ratchet based PTO	92
4.8 OCIR Control	97
4.9 Comparison of WPEA Algorithms	100
4.10 Summary	113

5	Evaluation of State-of-the-Art in PTO Systems	115
5.1	PTO Assessment Chart	115
5.2	Energy Storage Technologies	116
5.3	Power Converters	119
5.4	Direct Drive	120
5.5	Magnetic Transmission	126
5.6	Mechanical Transmission	134
5.7	Hydraulic Transmissions	138
5.8	Overall Discussion and Summary of PTO Systems	164
6	Three Potential PTO Systems	171
6.1	DDPM based PTO	171
6.2	Discrete Displacement Cylinder PTO	174
6.3	Magnetic Lead Screw based PTO	188
6.4	Choice of PTO for Further Investigation	196
7	Design and Validation of DDC PTO System	199
7.1	PTO Layout	199
7.2	Modelling Overview	202
7.3	Control of a 20 Absorber PTO	203
7.4	Simulation Results	205
7.5	Summary	209
8	Full Scale Test-bench and PTO Prototype	211
8.1	The Prototype DDC	211
8.2	Full Scale PTO Test-Bench	212
8.3	Test-bench Simulation Model	213
8.4	Test-Bench Control Design	213
8.5	Test-Bench Control Test	223
8.6	PTO Model	225
8.7	Initial DDC-Module Tests	227
8.8	DDC-Module Test with Moving Cylinder	229
8.9	Improved Control of DDC-Module	233
8.10	Test of DDC in Irregular Wave	233
8.11	Summary	236
9	Conclusion, Summary and Future Work	241
	Summary	241
	Future Work	246
	Conclusion	247
	Bibliography	266

Abstract

Most active Wave Energy Converter (WEC) concepts are based on harvesting energy from ocean waves by placing buoyant bodies in the sea. As the bodies are forced to oscillate by the waves, power is produced by converting the oscillations into electricity, which is performed by the Power Take-Off (PTO).

Despite 40 years of research activities within wave energy, the PTO is still a hindrance. No matured designs exist and no installed prototypes have demonstrated average electrical production above 250kW. Looking beyond 1MW, limited research exists, making the lack of advances in PTO research a contributing factor to wave energy remaining in a pre-commercialisation phase - a phase where electrical power production has been demonstrated, but needs to find a road to larger power scales and effective production.

The purpose of the research documented in this dissertation is to find a PTO capable of meeting current and future needs of WECs, i.e. meeting requirements of efficiency, controllability and durability while having the important feature of scalability. The case study for the research is the Wavestar 600kW 20 float multiple absorber, but the research has general applicability to WECs based on converting bi-directional motions into electricity.

All PTO technologies are kept open and based on a thorough analysis and evaluation of state-of-the-art, the PTO technologies with greatest potential are identified. The state-of-the-art covers both PTOs for wave energy, but also general advances in high power transmissions, which have applicability to wave energy.

One of the difficulties in PTO design is performing the trade-off between contradicting PTO characteristics, e.g. controllability, efficiency and peak power capacity. A PTO system for wave energy is a classic example of a mechatronic design problem, where all aspects of the design couples. To this end a framework is presented where all classic wave power extraction methods (reactive control, linear damping, latching control, de-clutching, etc.) are analysed according to a generic PTO formulation and optimised using numerical simulations in irregular waves. This enables a comparison of the performance of the wave power extraction methods according to PTO requirements. The framework also allows comparing performance of fundamentally different PTOs.

The idea of reactive control for increasing power absorption dates back to the 1970's, and today its feasibility for real PTO systems still causes dispute. In this dissertation an analytical result is provided, proving that reactive control is highly beneficial at even "low" PTO efficiencies.

The formulated reactive control is tested in a wave tank with 1:20 scale absorbers, validating the expected performance. The wave tank tests also verify the derived wave and absorber models, which are based on linear wave theory. This increases the confidence in the heavy use of models through-out the work.

A new high performing control method is developed for wave power extraction characterised in that the Oscillation Control is Implemented Resistively (OCIR). The OCIR

control implements a causal non-linear control, which achieve similar manipulation of the absorber's behaviour as reactive control, but through non-linear damping techniques. The control is shown to be superior to other resistive control techniques.

The research leads to three potential PTO systems, where one is a magnetic gear based PTO. The gear is based on implementing the function of a screw and nut magnetically by placing permanent magnets in a helical pattern. A PTO layout with the magnetic lead screw is found and analysed using simulations. The feasibility leads to having a group of master students designing a working prototype at a scale of 17kN with a half meter stroke. The magnetic lead screw is able to directly convert a linear motion of 0.5m/s to a rotational motion above 1000rpm, driving a conventional generator.

Two other hydraulic PTO solutions are also found highly feasible. One of them is based on discrete control of a hydraulic cylinder, and is assessed to be the most promising solution. It is therefore analysed in depth. The solution is named a Discrete Displacement Cylinder (DDC). The developed DDC allows discrete force control of a multi-chambered cylinder driven by the absorber, while efficiently transferring the generated power directly into a battery of high pressure accumulators. The concept allows DDCs of multiple absorbers to supply the same accumulator battery, where a hydraulic motor may use the stored energy to drive a generator at near constant load.

A complete PTO with the DDC is designed and simulated for a 20 absorber Wavestar 600kW WEC. The simulation comprises a 20 absorber hydrodynamic model, all PTO component models, and all main system control. The plus 600 state simulation model proves the expected PTO performance.

A working full scale 420kN prototype of the DDC for one absorber is designed and tested. The DDC consists of a multi-chambered cylinder with 2m stroke and a prototype valve manifold. The manifold is implemented using high performance proportional valves instead of on/off valves. This allows emulating an arbitrary on/off valve. The prototype DDC has a peak power capacity of 210kW. To test the DDC prototype, commissioning of a full-scale test-bench was necessary. The test-bench uses a second hydraulic cylinder to emulate the movement of an absorber in waves. A control solution based on state-space control is developed, which tracks a real-time implemented simulation model of the absorber. This enables the test-bench to emulate the absorber dynamics while suppressing its natural modes. The test-bench is shown to emulate the absorber dynamics, including being able to respond correctly to PTO loads.

Systematic tests are performed on the prototype DDC, validating the calculated requirements of valves etc. Anticipated problems with line dynamics are experienced, where the impact pressure during shifting gives a 30% extra pressure peak. The measured responses could be simulated exactly, and by using the models, an improved shifting technique is developed solving the problem.

Finally, an initial test of the prototype DDC in irregular waves is successfully performed on the test-bench, verifying the applied models and approaches.

Resumé

De fleste aktive bølgeenergikoncepter er baseret på at høste energi ved at placere diverse former for pontoner/flydere ude i havet. Disse flydere bringes i bevægelse af bølger, og bevægelserne omdannes til elektricitet. Omdannelsen af den oscillerende bevægelse til elektricitet foretages af et system kaldet et Power Take-Off (PTO).

Til trods for at der er forsket i bølgeenergi de sidste 40 år, så er PTO-designet stadig ikke løst. Ingen gennemtestede designs eksisterer, og ingen installerede prototyper har demonstreret en gennemsnitlig elproduktion på over 250kW. Ser man på anlæg over 1MW findes der næsten ingen forskning, hvilket gør manglende PTO-udvikling en medvirkende faktor til, at bølgeenergi hænger i en præ-kommercialiseringsfase - en fase, hvor el-produktion er mulig, men hvor der skal findes en vej til større og mere effektive anlæg.

Formålet med forskningen i denne afhandling er at finde frem til et PTO-system, som er i stand til at opfylde nuværende og fremtidige behov indenfor bølgeenergi, dvs. høj effektivitet, kontrollerbarhed og holdbarhed. Samtidig skal systemet være skalerbar. Forskningen i denne afhandling tager udgangspunkt i Wavestar's 600kW konverter med 20 flydere, men de udviklede metoder og resultater har generel anvendelighed for bølgeenergikoncepter baseret på omdannelse af oscillerende bevægelser.

Alle PTO-teknologier bliver til at starte med holdt åbne, hvorefter der gennemføres en grundig afdækning og evaluering af løsninger. På baggrund af dette udvælges de teknologier, som har tilstrækkelig potentiale. I den henseende har det været nødvendigt også at afdække relevante fremskridt indenfor andre områder omhandlende transmissioner i store maskiner.

En af udfordringer i bølgeenergi er afvejningen mellem modstridende PTO-egenskaber, f.eks. kontrollerbarhed, effektivitet og spidseffektkapacitet. PTO-udvikling til bølgeenergi er et klassisk eksempel på et mekatronisk designproblem, hvor alle aspekter af designet er koblet. I afhandlingen præsenteres en metode til sammenligning af alle klassiske bølgeenergi-udvindingsmetoder (reaktiv kontrol, lineær dæmpning, latching kontrol, Coulomb dæmpning, etc.). De klassiske metoder bliver analyseret vha. en general formulering af et PTO-system, hvor formuleringen optimeres vha. numeriske simuleringer i uregelmæssige bølger. Dette tillader en sammenligning af udvindingsmetodernes performance som funktion af PTO-egenskaber. Metoden tillader også at sammenligne performance af grundlæggende forskellige PTO-systemer.

Ideen om reaktiv kontrol for at øge energiabsorption daterer sig tilbage til 1970'erne, og der hersker stadig den dag i dag uenighed om dens anvendelighed i "virkelige" PTO-systemer med tab. I denne afhandling opnås et analytisk resultat, der beviser at reaktiv kontrol er anvendelig, endda for PTO-systemer med lave virkningsgrader.

Den reaktive styring blev testet i et bølgebassin på en flyder i skala 1:20. Testen efterviste den beregnede performance. Tests blev desuden udført for at eftervise de opstillede modeller for bølge/flyder-interaktionen. Disse modeller er baseret på lineær bølge teori.

En ny kontrolmetode kaldet OCIR (Oscillation Control Implmented Resistively) blev

ligeledes præsenteret til udvinding af bølgeenergi. OCIR implementerer en kausal ikke-lineær styring, som opnår lignende manipulation af flyderens bevægelse som reaktiv kontrol, men alene ved anvendelse af ikke-lineære dæmpningsteknikker. Kontrollen har vist sig at være overlegen i forhold til andre resistive kontrolmetoder.

Den udførte forskning leder frem til tre potentielle PTO-systemer, hvor det ene er baseret på et magnetisk gear. Gearet er baseret på magnetisk at efterligne funktionen af en skrue og møtrik ved at placere permanentmagneter i et gevindmønster. Et PTO-layout med denne magnetiske ledeskrue er etableret og analyseret ved hjælp af simuleringer. Dette førte til, at en gruppe kandidatstuderende designede en fungerende prototype på 17kN med en halv meter slaglængde. Den magnetiske ledeskrue er i stand til direkte at konvertere en lineær bevægelse med en hastighed på 0.5m/s til en roterende bevægelse på over 1000rpm, som kan drive en konventionel generator.

To hydrauliske PTO-løsninger vurderes ligeledes egnede. Den ene, der er baseret på diskret kontrol af en hydraulisk cylinder, anses for at være den bedst egnede og analyseres derfor dybdegående. Løsningen kaldes for en Diskret Displacement Cylinder (DDC). Den udviklede DDC tillader diskret kraftstyring af en multi-kamret cylinder, som drives direkte af flyderen, mens cylinderens producerede effekt overføres direkte til et batteri af højtryksakkumulatorer. Konceptet giver mulighed for at DDC'erne fra flere flydere kan tilsluttes samme akkumulatorbatteri, hvor en hydraulisk motor kan bruge den lagrede energi til at drive en generator ved nær konstant belastning.

Et komplet PTO med DDC bliver designet og simuleret for et 20-flyder Wavestar 600kW anlæg. Simuleringsmodellen anvender en hydrodynamisk model for 20 flydere. Alle PTO-komponenter er modelleret, og alle de vigtigste systemstyringer er udviklet og implementeret. Modellen har over 600 tilstande og viser den forventede PTO-performance.

En 420kN DDC-prototype for en flyder bliver udviklet og testet. DDC'en består af en multi-kamret cylinder med 2m slaglængde og en prototype ventilmanifold. Manifoldden er implementeret ved hjælp af hurtige proportionalventiler i stedet for on/off ventiler. Dette gør det muligt at efterligne en vilkårlig on/off ventil. DDC-prototypen har en spidseffekt på 210kW. For at teste DDC-prototypen udvikles en fuld-skala testbænk, som benytter den anden hydraulisk cylinder til at emulere bevægelsen af en flyder i bølger. En styring baseret på tilstandsregulering bliver udviklet og er i stand til at få cylinderen til at følge bevægelsen beregnet af en reeltids-simulering af flyderen. Testbænken er derved i stand til at efterligne flyderens dynamik og reagere korrekt på PTO-belastninger.

Systematiske tests blev udført på DDC'en og validerede de beregnede krav til ventiler m.m. Forventede udfordringer med slangedynamik blev oplevet, hvor der under ventilsift viste sig trykstød, som gav 30% forhøjet tryk i forhold til normalt niveau. De målte trykstød kunne simuleres, og vha. anvendelse af modellerne blev en forbedret skifteteknik, der kunne løse problemet, udviklet.

Til sidst blev en indledende test af DDC'en succesfuldt foretaget i uregelmæssige bølger på testbænken. Udover at verificere DDC-designet, verificerede den også de anvendte modeller og metoder.

List of Publications

Scientific Papers

- [A] Rico H. Hansen, Morten M. Kramer & Enrique Vidal, 2013, “Discrete Displacement Hydraulic Power Take-Off System for the Wavestar Wave Energy Converter”, *Energies*, vol 6, no. 8, pp. 4001-4044.
- [B] Rico H. Hansen, Torben O. Andersen & Henrik C. Pedersen, 2013, “Comparison of Reactive and Non-Reactive Control Strategies for Wave Energy Converters with Non-Ideal Power Take-Off Systems”, Accepted for publication, *Renewable Energy*, 2013.
- [C] Rasmus K. Holm, Nick I. Berg, M. Walkusch, Peter O. Rasmussen & Rico H. Hansen, “Design of a Magnetic Lead Screw for Wave Energy Conversion”, *IEEE Transactions on Industry Applications*, vol.PP, no.99, pp.1,1.
- [D] Henrik C. Pedersen, Anders H. Hansen, Rico H. Hansen, Torben O. Andersen & Michael M. Bech, 2012, “Design and Control of Full Scale Wave Energy Simulator System”, in *Proceedings of the ASME Symposium on Fluid Power and Motion Control (FPMC 2012)*. American Society of Mechanical Engineers, pp. 551-564.
- [E] Rico H. Hansen, Torben O. Andersen & Henrik C. Pedersen, 2012, “Determining required valve performance for discrete control of PTO cylinders for wave energy”, in N. Johnston & A.R. Plummer (eds), *Proceedings of ASME Symposium on Fluid Power and Motion Control, FPMC 2012*. American Society of Mechanical Engineers, Great Britain, pp. 565-578.
- [F] Rasmus K. Holm, Nick I. Berg, Peter O. Rasmussen, Rico H. Hansen & M. Walkusch, 2012, “Design of a magnetic lead screw for wave energy conversion”, in *Proceedings of the 2012 International Conference on Electrical Machines (ICEM)*. IEEE Press, Marseille, pp. 618 - 626.
- [G] Rico H. Hansen, Anders H. Hansen & Torben O. Andersen, 2012, “Influence and Utilisation of Pressure Propagation in Pipelines for Secondary Controlled Discrete Displacement Cylinders”, *Applied Mechanics and Materials*, vol 233, pp. 72-75.
- [H] Anders H. Hansen, Rico H. Hansen & Henrik C. Pedersen, 2012, “Optimisation of Working Areas in Discrete Hydraulic Power Take off-system for Wave Energy Converters”, in *Proceedings of the 5th Workshop on Digital Fluid Power*. Tampere University of Technology, pp. 43-56.
- [I] Rico H. Hansen, Anders H. Hansen & Torben O. Andersen, 2012, “Simulation of Utilisation of Pressure Propagation for Increased Efficiency of Secondary Controlled Discrete Displacement Cylinders”, *Applied Mechanics and Materials*, vol 233, pp. 3-6.
- [J] Morten M. Kramer, Andrew Zurkinden, Enrique Vidal & Rico H. Hansen , 2012, “Comparison between linear numerical models and experimental results on a Wavestar point absorber”, poster session at the 4th International Conference on Ocean Energy, 17 October, Dublin.
- [K] Enrique S. Vidal, Rico H. Hansen & Morten M. Kramer, 2012, “Early Performance Assessment of the Electrical Output of Wavestar’s prototype”, in *Proceedings of the 4th International Conference on Ocean Energy*, 17 October, Dublin.
- [L] Enrique Vidal, Rico H. Hansen & Morten M. Kramer, 2012, “Control Performance Assessment and Design of Optimal Control to Harvest Ocean Energy”, Submitted for publication, *IEEE Journal of Oceanic Engineering*.
- [M] Rico H. Hansen, Torben O. Andersen & Henrik C. Pedersen, 2011, “Analysis of discrete pressure level systems for wave energy converters”, in *Proceedings of the 2011 International Conference on Fluid Power and Mechatronics*. IEEE Press, pp. 552-558.

- [N] Rico H. Hansen & Morten M. Kramer, 2011, “Modelling and Control of the Wavestar Prototype”, in AS Bahaj (ed.), Proceedings of the 9th European Wave and Tidal Energy Conference, EWTEC 2011. University of Southampton.
- [O] Rico H. Hansen, Torben O. Andersen & Henrik C. Pedersen, 2011, “Model based design of efficient power take-off systems for wave energy converters”, in Proceedings of the 12th Scandinavian International Conference on Fluid Power, SICFP 2011. Tampere University Press, pp. 35-49.
- [P] Rico H. Hansen, Torben O. Andersen & Henrik C. Pedersen, 2010, “Development and Implementation of an Advanced Power Management Algorithm for Electronic Load Sensing on a Telehandler”, in Proc. ASME Symposium on Fluid Power and Motion Control, FPMC 2010. American Society of Mechanical Engineers.
- [Q] Henrik C. Pedersen, Torben O. Andersen, Rico H. Hansen & Soeren Stubkier, 2010, “Investigation of Separate Meter-In Separate Meter-Out Control Strategies for Systems with Over Centre Valves”, in Proc. of the ASME Symposium on Fluid Power and Motion Control, FPMC 2010. American Society of Mechanical Engineers.
- [R] Rico H. Hansen, Asger M. Iversen, Mads S. Jensen, Torben O. Andersen & Henrik C. Pedersen, 2010, “Modeling and Control of a teletruck using electronic load sensing”, in Proc. of the 10th Biennial Conference on Engineering Systems Design and Analysis, ESDA 2010. American Society of Mechanical Engineers, pp. 769-778.
- [S] Rico H. Hansen, 2009, “Advanced Power Management of a Telehandler using Electronic Load Sensing”, in Proceedings of the 10th International Workshop on Research and Education in Mechatronics, REM2009. University of Strathclyde.

Patent Applications

1. Rico H. Hansen, Enrique Vidal & Morten M. Kramer, “Discrete Displacement Hydraulic Power Take-Off System”, PA15295DK01.
2. Rico H. Hansen & Peter O. Rasmussen, “Power take-off with integrated resonator for energy extraction from linear motions”, PA15369DK01.
3. Enrique Vidal, Rico H. Hansen & Morten M. Kramer, “Autonomous control of point absorber to harvest ocean energy”, PA15511DK01.

Scientific Awards

1. Best Paper Award, 2010, at Bath/ASME Symposium on Fluid Power and Motion Control for the paper, “Development and Implementation of an Advanced Power Management Algorithm for Electronic Load Sensing on a Telehandler”.
2. Best Paper Award, 2012, at Bath/ASME Symposium on Fluid Power and Motion Control for the paper, “Design and Control of Full Scale Wave Energy Simulator System”.
3. Yoshio Masuda Memorial Price EWTEC 2011 (best young researcher), at the 9th European Wave and Tidal Energy Conference, UK, 2011, for the paper “Modelling and Control of the Wavestar Prototype”.

Abbreviations

DDC	Discrete Displacement Cylinder
PSD	Power Density Spectrum
DDT	Discrete Displacement Technology
DDP	Digital Displacement Pump
DDPM	Digital Displacement Pump/Motor
DDM	Digital Displacement Motor
DoF	Degree of Freedom
MLS	Magnetic Lead Screw
MWL	Mean Water Level
OCIR	Oscillation Control Implemented Resistively
PM	Permanent Magnet
PM-spectrum	Pierson-Moskowitz spectrum
VRPM generator	Variable Reluctance Permanent Magnet generator
WAMIT	Software tool analysing wave interactions
WEC	Wave Energy Converter
WPEA	Wave Power Extraction Algorithm

Nomenclature Chapter 1-5

α_C	Coulomb damping build up gradient (ω_{arm} input)	[Nm]
α_D	Normalised Coulomb damping build up gradient (ω_{arm} input)	[-]
α_J	Control parameter for cancelling an absorber's inertia term	[-]
β_{eff}	Effective bulk modulus of the fluid	[Pa]
Φ	Parameter set for a WPEA control law in a given sea state	N/A
Φ_{opt}	Optimal parameter set for a WPEA in a given sea state	N/A
$\varphi_{rand,i}$	Random phase component for a wave component	[rad]
Δp	Differential pressure across a hydraulic component	[Pa]
γ_J	Peak enchantment factor, JONSWAP spectrum	[-]
$\eta_{PTO,1}$	Conversion efficiency of the "reactive" part of the PTO	[-]
$\eta_{PTO,2}$	Conversion efficiency of the "non-reactive" part of the PTO	[-]
η_{PTO}	Power conversion efficiency of a PTO	[-]
$\eta_{PTO,base}$	Efficiency of PTO when operating at rated power	[-]
η_w	Wave height	[m]
κ_{FA}	Force density or air gap stress of electrical machines	[kN/m ²]
λ	Scaling parameter for WEC scaling	[-]
θ_{arm}	Angular position of arm	[rad]
θ_d	Angular deflection of input and output shaft of a ratchet	[rad]
θ_w	Wave angle	[rad]
ρ_{water}	Density of sea water	[kg/m ³]
$\tau_{Coulomb}$	Magnitude of Coulomb force in Coulomb damping WPEA	[Nm]
τ_{ext}	Exciting wave torque in linear wave theory	[Nm]
τ_{latch}	Torque being applied by a latching mechanism	[Nm]

$\tau_{\text{latch,req}}$	Requested of estimated required latching torque	[Nm]
$\tau_{\text{latch,max}}$	Magnitude of allowable latching torque	[Nm]
τ_{PTO}	Applied PTO torque	[Nm]
$\tau_{\text{PTO,ref}}$	PTO torque reference given to the PTO system	[Nm]
ω_{arm}	Angular velocity of Wavestar arm	[rad/s]
ω_{C5}	Natural frequency of C5 absorber ballasted and in water	[rad/s]
$\omega_{\text{n,PTO}}$	Natural frequency of PTO torque tracking dynamics	[rad/s]
ω_{P}	Peak wave frequency	[rad/s]
$\omega_{\text{peak,90}}$	The absorber velocity is below this limit 90% of the time	[rad/s]
ω_{s}	Speed of the main shaft in ratchet based PTOs	[rad/s]
ω_{w}	Wave frequency in radians per second.	[rad/s]
$\Psi(\cdot)$	WPEA feedback law based on absorber and wave states	[Nm]
Ψ_{B}	Linear damping WPEA	[Nm]
Ψ_{k}	Spring based reactive WPEA	[Nm]
Ψ_{inv}	Inverse control WPEA	[Nm]
Ψ_{conj}	Complex-conjugated WPEA	[Nm]
Ψ_{α}	A reactive control partial cancelling absorber dynamics	[Nm]
Ψ_{OCIR}	OCIR WPEA	[Nm]
ζ	Damping factor of a second order system	[-]
ζ_{PTO}	Damping factor of PTO torque tracking dynamics	[-]
$\{A\}$	Float arm fixed reference frame at arm pivot	$ $
A_{c}	Effective piston area of a cylinder	$[m^2]$
A_{ext}	Gain from wave amplitude to exciting wave torque	[N]
A_{f}	Cross-sectional area of the float at the draft line	$[m^2]$
A_{o}	Valve opening area	$[m^2]$
$A_{\text{o,i}}$	On/off valve's opening area for the cylinders' i'th chamber	$[m^2]$
A_{w}	Amplitude of a regular wave	[m]
$\{B\}$	Main tune fixed reference frame at arm pivot	$ $
B_{d}	Damping coefficient of ratchet mechanism	[Nms]
B_{hyd}	Hydro-dynamic damping coefficient	$[\frac{kgm^2}{s}]$
B_{PTO}	Damping coefficient in PTO control law	$[\frac{kgm^2}{s}]$
C_{d}	Valve discharge coefficient	[-]
D	Matrix of time-wise distribution of sea states	[-]
d_{A}	Moment arm of PTO cylinder	[m]
E_{year}	Annual produced energy to grid	[J]
f_{absorber}	Vector field of absorber model	
f_{WPEA}	A WPEA law	[Nm]
g	Gravitational acceleration	$[m/s^2]$
$H_{\text{A}}(s)$	Transfer function for absorber from applied torque to ω_{arm}	$[\frac{1}{Nms}]$
$H_{\text{ext}}(s)$	Transfer function from wave elevation η_{w} to τ_{ext}	[N]
$h_{\text{B}}(t)$	Inverse Fourier of the hydro-dynamic damping $B_{\text{hyd}}(j\omega)$	$[\frac{kgm^2}{s^2}]$
$h_{\text{c}}(t)$	Impulse function of a linear the control law	
$h_{\text{ext}}(t)$	Impulse filer for wave excitation torque	$ $
$h_{\text{i}}(t)$	Impulse function of the intrinsic impedance	[Nm]
$h_{\text{PM}}(t)$	Impulse response of PM-spectrum	

H_{m0}	Significant wave height	[m]
$J_{\text{add},\infty}$	Added inertia at infinite frequency	[kgm ²]
J_{mech}	Inertia of Wavestar float and arm with ballast water	[kgm ²]
$J_{\text{mech},0}$	Inertia of Wavestar float and arm, no ballast water	[kgm ²]
J_{PTO}	Inertia coefficient in PTO control law	[kgm ²]
k_d	Stiffens of ratchet mechanism	[Nm/rad]
k_{PTO}	Spring coefficient in PTO control law	[Nm/rad]
k_{res}	Spring coefficient of hydrostatic restoring force	[Nm/rad]
$k_r(t)$	Impulse function describing radiation torque (ω_{arm} input)	[Nms]
$K_r(s)$	Transfer function describing radiation torque (ω_{arm} input)	[Nms]
p_A	Pressure in B-side of cylinder	[Pa]
p_B	Pressure in A-side of cylinder	[Pa]
P_{mat}	Average power output power-matrix	[kW]
\bar{P}_{eff}	Average extracted power	[W]
P_{eff}	Instantaneous extracted/absorbed power	[W]
p_M	Pressure at hydraulic motor inlet	[Pa]
\bar{P}_{out}	Average power output of PTO	[W]
$P_{\text{PTO,rated}}$	Rated power of PTO system	[W]
p_T	Tank pressure in hydraulic circuit	[Pa]
P_v	Instantaneous loss across a valve from flow throttling	[W]
R_c	Real part or resistance of the control law $Z_c(s)$	[Nms]
R_i	Real part or resistance of the intrinsic impedance	[Nms]
Q_i	Cylinder displacement flow from i'th chamber	[m ³ /s]
$S_\eta(f)$	Wave power spectrum	[m ² /Hz]
$S_{\text{PM}}(f)$	Pierson-Moskowitz (PM) spectrum	[m ² /Hz]
$\text{sgn}()$	Sign function	[-]
$T_{0,2}$	Mean wave period	[s]
t_{clutch}	Clutch duration in de-clutching control	[s]
t_{latch}	Latching duration in latching control	[s]
T_p	Peak wave period	[s]
T_s	Sample time	[s]
T_w	Period of a regular wave	[s]
u_{latch}	Boolean control signal send to latching mechanism	[-]
V_A	Current volume of A-side in cylinder	[m ³]
V_B	Current volume of B-side in cylinder	[m ³]
v_c	Cylinder velocity	[m/s]
V_{disp}	The volume of displaced water of an absorber	[m ³]
V_β	Volume of oil required to increase pressure with Δp	[Pa]
$\{W\}$	Wave reference frame	[]
$\mathbf{x}_{\text{absorber}}$	State vector of absorber model	
X_c	Imaginary part or reactance of the control law $Z_c(s)$	[Nms]
$x_{c,0}$	Cylinder stroke at which $\theta_{\text{arm}}=0$	[m]
X_i	Imaginary part or reactance of the intrinsic impedance	[Nms]
$Z_c(s)$	Transfer function of the control law $h_c(t)$	
$Z_i(s)$	Intrinsic impedance of absorber $(J_{\text{mech}}+J_{\text{add},\infty})s+K_r(s)+\frac{k_{\text{res}}}{s}$	[Nms]
z_{float}	Vertical displacement of the Wavestar float	[m]
Z_{rad}	Impedance describing wave radiation torque (ω_{arm} input)	[Nms]

Nomenclature Chapter 6-8

β_{eff}	Effective bulk-modulus	[Pa]
Δp	Valve or orifice difference pressure	[Pa]
Δx	Length of line element	[m]
γ	Control parameter to reduce power absorption	[-]
γ_{A_o}	Loss ratio of a shift	[-]
γ_g	Gear ratio $\omega_{\text{MLS}}/\omega_{\text{arm}}$	[-]
φ	Control parameter to manifold control	[J]
η_{tot}	Total PTO conversion efficiency	[-]
η_{DDC}	Efficiency of DDC	[-]
$\eta_{\text{to-Gn}}$	Efficiency from absorber to generators	[-]
ν	Kinematic viscosity of fluid	[Pa s]
ρ_{fluid}	Hydraulic fluid density	[kg/m ³]
$\omega_{n,s}$	Natural frequency coefficient of valve spool ctrl.	[-]
ω_{HP}	Break frequency of high pass filter	[rad/s]
ω_{MLS}	Angular velocity of MLS rotor	[rad/s]
ω_{GN}	Speed of generators	[-]
$\dot{\omega}_{\text{arm,peak}}$	Peak angular acceleration of absorber arm	[rad/s ²]
τ_{Gn}	Generator torque	[Nm]
τ_{MLS}	Total torque transmitted by MLS rotor	[Nm]
$\tau_{\text{MLS,J}}$	Torque load on MLS due to inertia	[Nm]
ψ	Control parameter for scheduling generators' speed	[-]
ζ_s	Damping coefficient of valve spool ctrl.	[-]
A_1	Area of PTO chamber 1	[m ²]
A_2	Area of PTO chamber 2	[m ²]
A_3	Area of PTO chamber 3	[m ²]
\mathbf{A}	System matrix, wave cylinder system	
$A_{c,ws}$	Piston area of symmetric wave cylinder	[m ²]
A_{H}	Hose cross-section area	[m ²]
A_o	Opening area of valve	[m ²]
$A_{o,r}$	Total opening area reference to wave cyl.	[m ²]
$A_{o,M,\text{max}}$	Max opening area of MOOG valve	[m ²]
$A_{o,P,\text{max}}$	Max opening area of Parker valve	[m ²]
$A_{o,M}$	Current opening area of MOOG valve	[m ²]
$A_{o,P}$	Current opening area of Parker valve	[m ²]
\mathbf{B}	Input matrix, wave cylinder system	
B_{MLS}	Internal damping of MLS	[kg/s]
B_{ws}	Total viscous friction coefficient, wave system	[kg/s]
\mathbf{C}	Output matrix, wave cylinder system	
C_d	Discharge coefficient	[-]
d_i	Diameter of i'th line element	[m]
d_{lead}	Lead of MLS	[m]
D_M	Total active motor displacement	[m ³ /rad]
$D_{\omega,\text{MLS}}$	Relation of linear and angular velocity	[m/rad]

$E_{\beta\text{-loss}}$	Compression loss	[J]
$E_{\beta\text{-loss,tot}}$	Total compression losses	[J]
E_{ext}	Total energy extraction	[J]
E_{shift}	Energy cost of discrete force shift	[J]
$E_{\text{shift},\infty}$	Minimum shift loss at infinite fast valve	[-]
$E_{\text{tot},v}$	Valve throttling losses	[J]
\mathbf{F}	State-feedback gain matrix	[]
F_b	Allowed force tracking error of DDC	[N]
$F_{\text{fric,ws}}$	Friction wave cylinder	[N]
F_c	Force of PTO cylinder	[N]
F_{MLS}	Linear force of MLS	[N]
$F_{\text{PTO,ref}}$	PTO cylinder reference	[N]
F_{ref}	PTO force reference	[N]
F_{pA}	PTO cylinder force based on pressure meas.	[N]
F_{stall}	Stall force of MLS	[N]
J_{Gn}	Inertia of generator	[kgm ²]
J_{MLS}	Inertia of MLS rotor	[kgm ²]
k_-	Optimum force number less than current	[-]
k_+	Optimum force number greater than current	[-]
k_+	Current force number	[-]
k_{GN}	Number of generators	[-]
k_{MLS}	Force of MLS as relative displacement of thread	[N/m]
l_{HA1}	Length of hoses to chamber A1	[m]
l_{HA2}	Length of hoses to pipes to A2	[m]
l_{PA2}	Length of pipes to chamber A2	[m]
l_{HA3}	Length of hoses to pipes to A3	[m]
l_{PA3}	Length of pipes to chamber A3	[m]
m_{tot}	Total moving mass in testbench	[kg]
p_0	Initial pressure in a chamber	[Pa]
p_1	End pressure in a chamber	[Pa]
$p_{\text{avg,expected}}$	Expected total average power	[-]
p_{A1}	Pressure at manifold, PTO chamber A1	[Pa]
$p_{\text{A1,old}}$	Current pressure of chamber A1	[Pa]
$p_{\text{A1,new}}$	Pressure of chamber A1 after shift	[Pa]
p_{A2}	Pressure at manifold, PTO chamber A2	[Pa]
$p_{\text{A2,old}}$	Current pressure of chamber A2	[Pa]
$p_{\text{A2,new}}$	Pressure of chamber A2 after shift	[Pa]
p_{A3}	Pressure at manifold, PTO chamber A3	[Pa]
$p_{\text{A3,old}}$	Current pressure of chamber A3	[Pa]
$p_{\text{A3,new}}$	Pressure of chamber A3 after shift	[Pa]
p_{A}	A-side pressure in wave cylinder	[Pa]
p_{B}	B-side pressure in wave cylinder	[Pa]
p_{λ}	Pressure drop in strait line	[Pa]
p_c	Pressure in a PTO cylinder chamber	[Pa]
p_{C1}	Pressure in PTO cylinder chamber A1	[Pa]
p_{C2}	Pressure in PTO cylinder chamber A2	[Pa]
p_{c3}	Pressure in PTO cylinder chamber A3	[Pa]

$P_{\Delta\text{init}}$	Equivalent average power due to stored energy	[W]
$p_{H_i,\text{fric}}$	Pressure drop of i'th line element	[Pa]
p_H	Pressure of high pressure line	[Pa]
$P_{\text{in,avg}}$	Average power input to a subsystem	[W]
p_i	Pressure of i'th line element	[Pa]
p_{ξ}	Pressure drop of a fitting	[Pa]
p_L	Load pressure of wave cylinder	[Pa]
p_L	Pressure of low pressure line	[Pa]
$p_{L,H}$	High pass filtered load pressure	[Pa]
p_M	Pressure of intermediate pressure line	[Pa]
$p_{M,\text{ref}}$	Intermediate pressure reference	[Pa]
p_{os}	Pressure overshoot	[Pa]
$P_{\text{out,avg}}$	Average power output to a subsystem	[W]
p_P	Pump or supply pressure	[Pa]
p_T	Tank pressure	[Pa]
p_{us}	Pressure undershoot	[Pa]
p_V	Pressure in a chamber	[Pa]
Q_i	Flow out of i'th line element	[Pa]
Q_L	Load flow of wave cylinder	[m ³ /s]
Q_{ref}	Flow reference	[m ³ /s]
Re	Reynolds number	[-]
t_d	Valve timing control parameter	[s]
t_v	On/off opening and closing time	[-]
T_{min}	Minimum time between shift	[s]
$x_{c,\text{ref}}$	PTO cylinder position reference	[m]
$x_{c,\text{ws}}$	Wave cylinder position/stroke	[m]
$x_{s,\text{ref}}$	Spool reference	[-]
$x_{sP,\text{db}}$	Dead-band compensation of Parker valve	[m]
\mathbf{x}_{tb}	State-vector of wave cylinder sys.	
\mathbf{u}_c	Vector of input signal to on/off valves	[-]
u_{ws}	Input, wave cylinder system	
V	Volume of a chamber	[m ³]
V_{0A}	Minimum volume of A-side wave cyl.	[m ³]
V_{0B}	Minimum volume of B-side wave cyl.	[m ³]
V_{A1}	Current volume of chamber A1	[m ³]
V_{A2}	Current volume of chamber A2	[m ³]
V_{A3}	Current volume of chamber A3	[m ³]
V_{β}	Fluid compression	[m ³]
$v_{c,\text{ref}}$	PTO cylinder velocity reference	[m]
v_{MLS}	Relative linear velocity of MLS rotor and stator	[m/s]
$v_{\text{ws,ref}}$	Velocity reference for wave cylinder	[m/s]
v_s	Spool velocity	[1/s]

Chapter 1

Introduction

Everyday 2TW power of concentrated solar energy roams the globe in form of ocean surface waves [1, 2, 3] - a resource of the same size as the world's average electrical power consumption (2.4TW) [4]. Accordingly, since the oil crisis in 1973, research has been ongoing to make an economical exploitation of wave energy, leading to many radically different designs to surface in this period.

Today, 40 years later, designers still struggle to commercialise wave energy solutions, and as the first designs of the 1970's, the principle of most designs today remain the same - *waves exerting buoyant bodies into oscillation*. The captured motion is converted into electricity by a system referred to as the *Power Take-Off* (PTO), which likewise, 40 years later, is an area requiring great attention.

This attention to design and control of the PTO is attempted bestowed in this dissertation, while trying to do the best at incorporating lessons of the past.

1.1 Wave Energy Concepts and Active Projects

Today, more than 90 different wave energy technologies are reported active, witnessing that wave energy is still in a converging phase, trying to identify the best designs - analogue to wind turbines before converging on the three bladed design. Of the 90 projects, 10% have reached full scale sea tests [5]. The variety of these devices spans the categorisation of Fig. 1.1.

Most active Wave Energy Converter (WEC) technologies base on letting waves induce mechanical oscillation in buoyant bodies. The produced mechanical oscillation is converted into useful work by the PTO, most often electricity. These WEC systems may overall be categorised as in Fig. 1.1a based on shape and orientation in regard to the wave field [1]. A point absorber extracts energy using a buoyant body of a smaller extension than the average wave length. The attenuator consists of an elongated buoyant structure, often articulated and aligned with the wave direction. Its counterpart is the terminator device, acting perpendicular to the wave direction.

WEC technologies, often having their own classes, are the over-topping devices and the oscillating water columns shown in Fig. 1.1b. The over-topping devices channel incoming waves into an elevated reservoir, producing energy by draining the elevated water back to the sea through turbines. The oscillating water column utilises the wave surface to produce a bi-directional airflow directed through a special turbine, rotating in the same direction independent of flow direction using a Welch turbine.

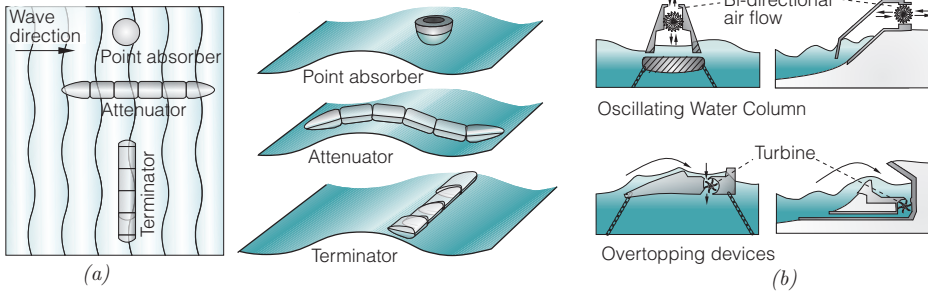


Figure 1.1: In (a) description of classes suited for WECs based on oscillating bodies [1]. In (b) illustration of over-topping devices and oscillating water columns.

To give a brief insight in the current state of the industry, a selection of active WEC developers with operational prototypes at sea is given in Fig. 1.2. All the systems are based on extracting power from the motion of oscillating floating bodies.

Wavestar Operating a 500kW test section at Hanstholm, Denmark. The concept is a multiple absorber system, resting on the sea bed. Power is extracted by the relative motion of absorbers and structure. The concept's aim is a combined wind and wave farm, lowering overall installation and operation cost. The system has a hydraulic based PTO, converting the motion into electricity. [6]

Pelamis Have previously installed and tested four first version P1-machines, and are now operating two P2 prototypes of 750kW at Orkney, Scotland. The concept is a moored articulated structure, consisting of linked sections, moving with the wave curvature. Power is extracted at the joints from the relative motion of the sections. A hydraulic based PTO is employed. [7]

Aquamarine Power Have previously installed a 315kW prototype, and are now focusing on their Oyster 800 prototype at Orkney, Scotland. The concept is a buoyant hinged flap attached to the seabed, where oscillating motion is used for pumping high pressure water onshore to a conventional hydro-electric turbine. [8]

AW-Energy Focusing on three 100kW section for Portugal. Their Wave Roller concept consists of buoyant panels hinged at the sea bed. The system has a hydraulic based PTO, converting the motion into electricity. [9, 10]

Ocean Power Technology Have tested multiple version of their PowerBuoy at sea. Their largest prototype Mark 3 was installed in Scotland, 2011. The concept consists of two bodies, a floating buoy and a submerged part, where power is extracted by their relative motion. [11]

Seabased AB Have installed multiple prototypes in Sweden. The concept consists of a floating body, actuating a seabed installed PTO system through a wire. The PTO is a direct driven linear generator. [12]

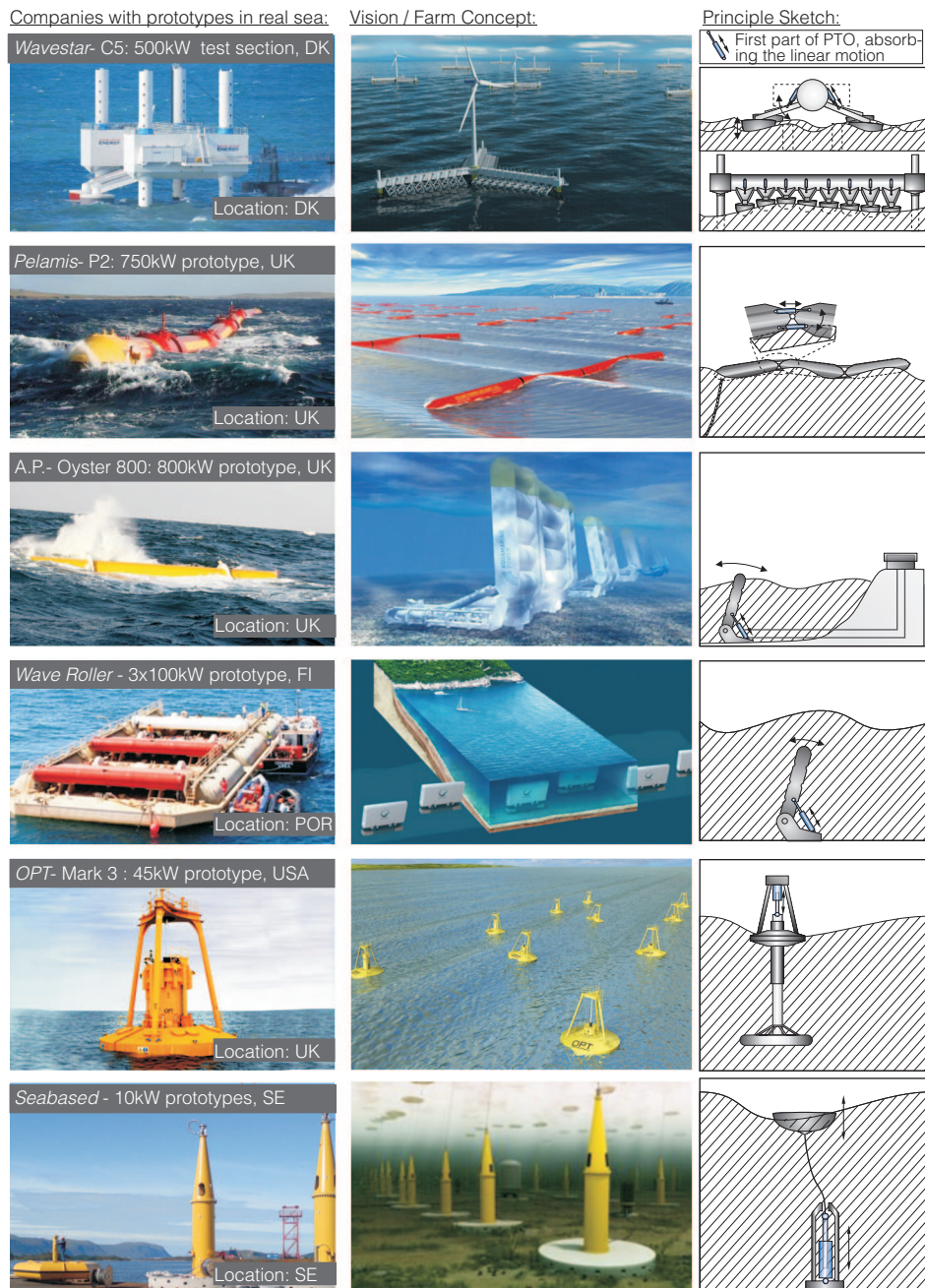


Figure 1.2: Selection of active WEC developers with prototypes at sea.

1.2 Current Trend and Potential of the Wave Energy Sector

Displayed by the active WEC companies, wave energy is in a pre-commercialisation phase, demonstrating electrical power production with various 300-800kW prototypes.

The incentives to take the next step and mature wave energy to a competitive source of energy are present. Currently, 67% of the world's electricity production bases on fossil fuel [13], and by 2035 an increase of 45% in the total energy consumption is expected [13]. To meet the challenge, Europe has set a target that by 2020, 20% of Europe's total energy consumption will be from renewable sources [14], with an expected contribution of ocean energy of 0.15%. Ocean energy covers both wave and tidal energy, where tidal energy is the technology of using tidal generated currents to produce energy, e.g. using underwater turbines. In 2009, 19.9% of Europe's electricity consumption was from renewables [14]. Aiding to meet the targets, projects as the "THV Mermaid" has been launched for constructing a 450MW offshore energy park in the North Sea, 50km North of Belgium, wherein wave energy is scheduled to provide 20MW [15]. The European Union has also launched the FP7-OCEAN-2011.1 on "Multi-use offshore platforms" for development of energy facilities, herein offshore wind and wave energy [16].

An overview of the planned installation of ocean energy in Europe by 2020 is given in Fig. 1.3a, showing that the main markets are France, Ireland, Portugal, Spain, and the United Kingdom [14]. The European wave energy resource is estimated to be 120-190TWh/year offshore and 34-46TWh/year near-shore by the European Ocean Energy Association [5]. The distribution of wave energy for Europe is given in Fig. 1.3b. The wave power is measured as power per width of wave front [kW/m], thus for Europe the largest resources are at the west coasts of Britain, France, Spain, Portugal, Iceland and Norway. Denmark is in the lee side of Britain - still for Denmark, with about 15kW/m, wave energy is estimated to have a potential of 11TWh/year [17]. This corresponds to one third of the current Danish electric power consumption. For the United Kingdom, the economical feasible resource is estimated to be 50TWh per year [18], corresponding to about 14% of UK's current electricity consumption.

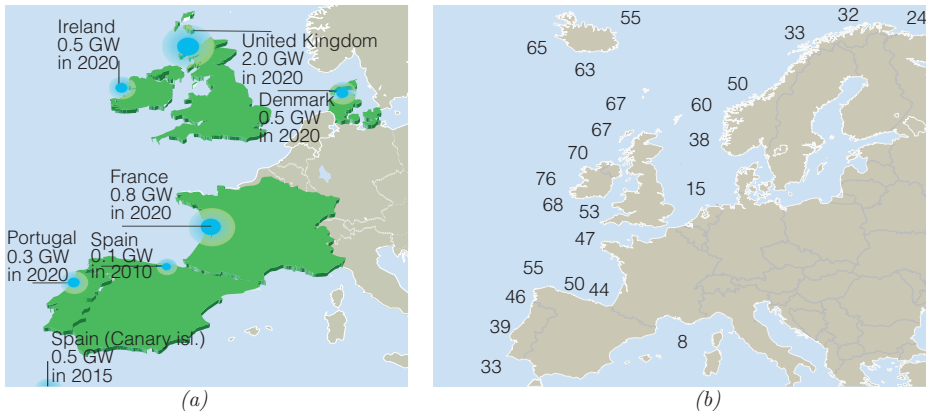


Figure 1.3: In (a) the targets for ocean energy in Europe [13] and in (b) the average annual wave power distribution in Europe in kW/m [17].

Globally, the wave power distribution is given in Fig. 1.4, showing that the wave power is concentrated into two belts in the northern and southern hemisphere, with highest intensity near west oriented coasts. The resources are greatest in the southern belt, having a lower seasonal variation [1]. Different estimates have been given of the exploitable amount of wave energy. A report in 2004 by the World Energy Council estimated the economically feasible resources to be 140-750 TWh/year with matured designs, and a potential of 2000 TWh/year with improved designs [19]. This corresponds to 10% of the yearly electricity consumption of the world, being 21000 TWh [4]. In [20] the economically feasible resource for locations above 20 kW/m is estimated to be 100-500 TWh, and in [3] the resource was in 2012 estimated to be 850 TWh per year based on the performance of current wave energy technologies.

To introduce the challenges of wave energy, a brief flash back to the roots of wave energy is given.

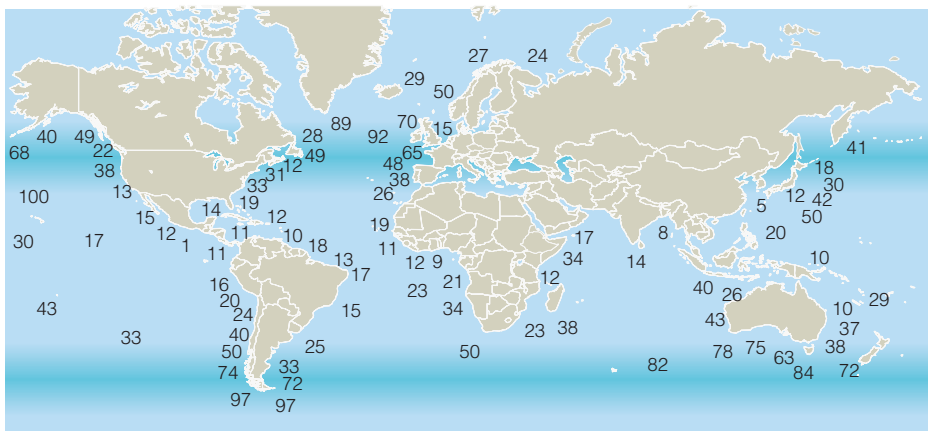


Figure 1.4: Distribution of wave energy as power per width of wave front [kW/m].

1.3 Short Historical Perspective

Focused research on understanding and utilising wave energy starting back in the 1970's at Edinburgh University in Scotland. Many of the fundamental properties and complex challenges of wave energy were identified, and with the achieved understanding, the famous “duck” design by Prof. Stephen Salter emerged, capable of absorbing above 80% of the incoming wave power in (regular) wave conditions [21].

The duck consisted of asymmetric shape, performing a nodding motion as seen in Fig. 1.5a, absorbing the incoming wave and leaving near calm water in its wake. Energy would be produced by using the nodding motion to power a generator. A picture of laboratory tank test of the duck is seen in Fig. 1.5b.

One of the key discoveries, leading to the somewhat unintuitive “duck” design, was

realising that the horizontal motion of the wave is energy-wise just as important as the vertical. Thus, despite a heaving/vertical moving device, as in the top illustration of Fig. 1.5c, being perhaps the most intuitive, it may only absorb 15% of the available energy in the wave. By sloping the movement of the same absorber, as in the bottom illustration of Fig. 1.5c, the absorption would increase to 50% [1]. This is achieved as the absorber reacts to the horizontal displacement of the wave as well.

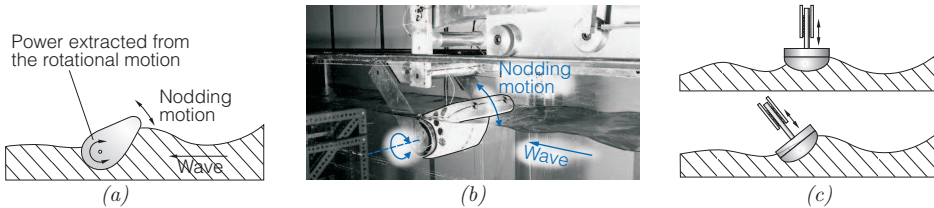


Figure 1.5: In (a) and (b) illustration and photo of the duck. In (c) a point absorber in heave and sloped mode.

Despite the achieved understanding of wave power, projects as the duck did not go beyond tank tests. The challenges of Power Take-off, materials and survival would require and still requires much development and maturing. As expressed in 2000 by Jamie Taylor, part of the Edinburgh team, “*The duck is often referred to as a third generation device, it is dependent on new technologies, such as digital hydraulics and materials that are particular tolerant to the marine environment.*” [22].

1.4 Wave Energy Technology Challenges

As realised in the 1970’s, four main technological challenges are required solved for creating a viable Wave Energy Converter (WEC). These challenges are shown in Fig. 1.6.

For a given wave energy site, a WEC converter is designed for efficient producing energy in the wave conditions where most of the annual energy is concentrated. However, the WEC must still be able to survive the wave condition beyond the normal production scope, and even survive the 10 or 50 years occurring freak waves. Thus, the challenge of *survivability* is to have a survivability strategy, which avoids a costly and inefficient over-dimensioning of the entire WEC and Power Take-Off “just” to survive the rare extreme waves.

Next challenge is the *power capture performance*. As discussed previously, a simple vertical oscillating body may only extract 15% of the available wave power, whereas a sloped version may extract 50%. Hence, a viable WEC concept possesses the potential of achieving a high ratio of extracted power versus cost.

A sound WEC concept also incorporates an efficient and power smoothing *Power Take-Off system*. The PTO realises the WECs potential of high power extraction, and converts the fluctuating wave power into a steady electricity production.

Finally, strategies for *the construction, installation and maintenance* of the WEC tech-

nology are required, allowing the concept to become economical feasible.

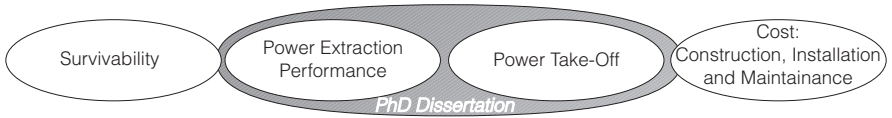


Figure 1.6: The four main properties required for a successful WEC concept.

As indicated in Fig. 1.6 the focus of this Ph.D. dissertation lies in the challenges of PTO and realising the potential power extraction for a given WEC concept.

When referring to PTO-systems for wave energy, it will in this dissertation be for WECs using oscillating bodies, where the reciprocating linear or angular motion is to be converted into electricity. WEC systems for performing other tasks than electricity production exist, e.g. desalination of sea water [23, 24, 25, 26, 1], but these are not the scope of this work. The definition of the PTO is illustrated in Fig. 1.7a. The float or absorber of the device generating the linear motion is not regarded as a part of the PTO. The used PTO technology mainly fall into the groups of Fig. 1.7b, either using a mechanical or hydraulic transmission to power a conventional high speed generator, or applying special designed high force/torque generators for direct drive.

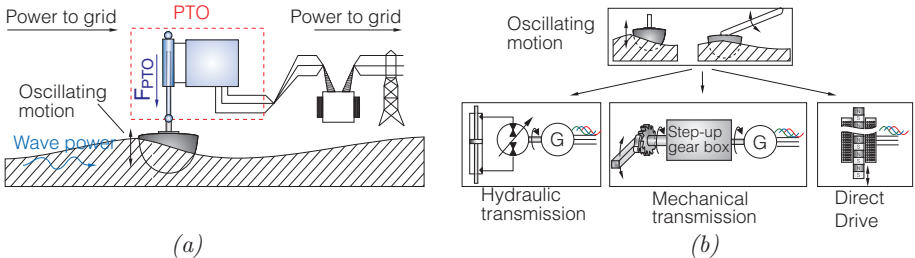


Figure 1.7: In (a) the definition of PTO system and in (b) the main PTO groups.

1.5 Power Take-Off Design Aspects

As realised by the Edinburgh team, the success of wave energy was largely dependent on advancement in PTO-technology, and now 30 years later, commercial available technologies still have hard time reaching satisfactory performance. Reliable PTO systems are rarely seen with a power conversion efficiency above 60% from absorber motion to grid [A] .

The problem faced is that the movement or oscillations of bodies caused by sea waves are very slow, bidirectional and irregular. An example is given in Fig. 1.8 from paper [A], showing the resulting velocities of a $\varnothing 5\text{m}$ point absorber in the Wavestar concept. The torque τ_{PTO} is the load torque applied by the PTO system about the arm pivot in order to extract adequate power from the absorber motion. The graphs in Fig. 1.8b show the very slow oscillation, resulting in a requirement of a 1 MNm bi-directional load torque for

extracting an average of 28kW. In comparison, a wind turbine would produce 1.4MW when loaded with an uni-directional load torque of 1 MNm, if rated output is obtained at a rotor speed of approximately 13RPM. Hence, the torque density requirement for wave power is immense. Furthermore, wave power extraction is characterised by requiring high peak power capacity, i.e. a factor of 10 between mean and peak power is normal for performing decent power extraction, confer Fig. 1.8c and [27]. Note that in Fig. 1.8b the right axis shows the corresponding linear velocity and PTO load force viewed from the vertical displacement of the absorber. The peak linear velocity is about 2m/s.

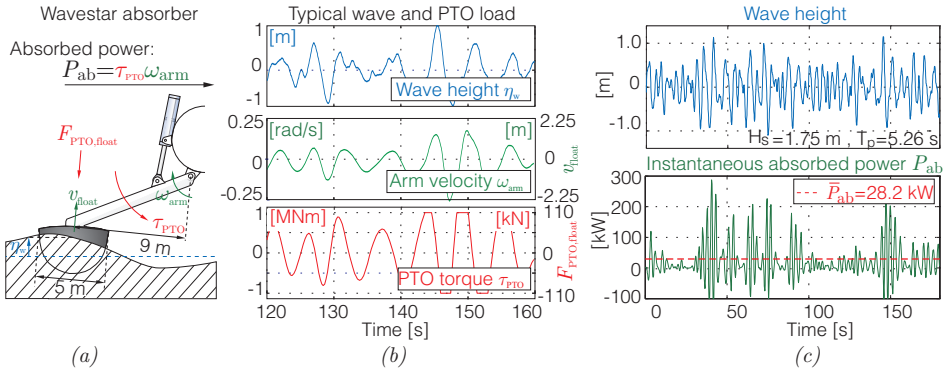


Figure 1.8: In (a) a Wavestar absorber and in (b) velocities and PTO load forces in typical production waves. In (c) instantaneous power during production for a single absorber [A].

Due to the above described inherent properties of waves, a PTO having a complex transmission with a very high gearing ratio is required to make an oscillating body power a generator. Moreover, to extract adequate amount of energy from waves, the PTO applied load force F_{PTO} or torque τ_{PTO} should be controlled as a function of wave and body movement. This is the reason for the varying torque load in Fig. 1.8b. For a wind turbine this corresponds to always be varying the torque on the rotor independent of rotor speed. Finally, to fully maximise energy extraction, the PTO should often be able to operate in four-quadrant mode.

1.6 Basic Power Extraction

The requirement of controllability and four-quadrant behaviour is to compensate for the inherent off-resonance behaviour of absorbers, especially for point absorbers. Frequency-wise, point absorbers are characterised by being narrow-banded with an under-damped resonance. An example is given in the bottom graph of Fig. 1.9a, showing the response from wave excitation to absorber velocity for the Wavestar absorber in Fig. 1.8a. The narrow banded behaviour of a point absorber is a poor match for the broad-banded frequency content of ocean waves. Typical power spectra for different wave conditions typical for the absorber are shown in top of Fig. 1.9a. Thus, for a sea state with a peak period T_P of e.g. 4.5s, the absorber will respond poorly, resulting in a poor power

extraction. The *peak period* is the wave period where most energy is concentrated for a given sea state.

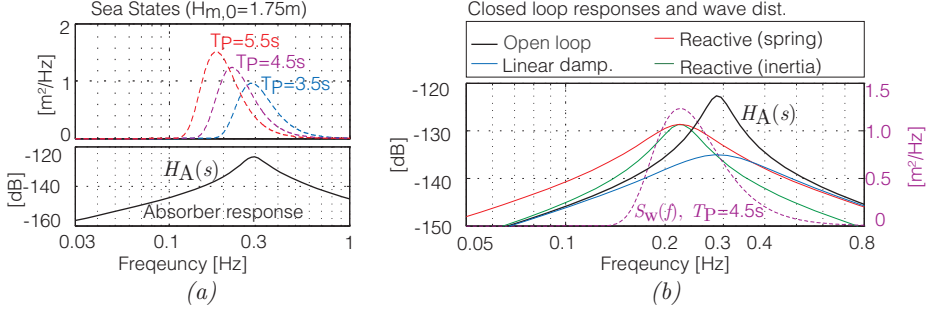


Figure 1.9: In the bottom graph of (a) the absorber’s frequency response from excitation to velocity. In the top graph of (a) typical wave distributions for different sea states. In (b) the response of the absorber is shown for different control strategies together with a wave distribution.

To compensate for the absorber’s inadequate frequency-response, the PTO force or torque τ_{PTO} applied to the absorber is controlled as a feedback of the absorber’s motion. This allows the PTO to adjust the absorber’s external frequency response to match the frequency content of the incident wave [28, 29, 27]. Popular said, optimal energy transfer from wave to an absorber occurs when the incident wave frequency matches the resonance frequency of the absorber.

In Fig. 1.9b different feedback strategies are applied for a sea state of $T_p = 4.5\text{s}$. The plot shows the incident wave spectrum and the frequency responses of the different feed-back strategies. Linear damping feedback strategy, Eq. (1.1), only allows the response to be attenuated without moving the resonance frequency, leaving the absorber to operate off-resonance. To move the resonance, the PTO may for example emulate extra inertia, Eq. (1.2), or implement a negative spring, Eq. (1.3). However, both methods require the PTO to provide and process reactive power, i.e. the PTO is operating in four-quadrant mode. These reactive strategies yield improved responses. With the PTO implementing a negative spring term, it may even widen the absorber response, better matching the broad-banded frequency content of a wave.

$$\text{Linear damping:} \quad \tau_{\text{PTO}} = B_{\text{PTO}}\omega_{\text{arm}} + B_{\text{PTO}}\dot{\omega}_{\text{arm}} \quad [\text{Nm}] \quad (1.1)$$

$$\text{Reactive (inertia):} \quad \tau_{\text{PTO}} = B_{\text{PTO}}\omega_{\text{arm}} + J_{\text{PTO}}\dot{\omega}_{\text{arm}} \quad [\text{Nm}] \quad (1.2)$$

$$\text{Reactive (spring):} \quad \tau_{\text{PTO}} = B_{\text{PTO}}\omega_{\text{arm}} + k_{\text{PTO}}\theta_{\text{arm}} \quad [\text{Nm}] \quad (1.3)$$

The PTO damping coefficient is denoted B_{PTO} [kgm^2/s], the emulated extra inertia is named J_{PTO} [kgm^2] and the emulated spring term is k_{PTO} [kgm^2/s^2], which is often negative.

The result of applying these control methods in sea waves is shown in Fig. 1.9, where the different approaches have been optimised with respect to wave and a PTO system with an efficiency of 80%. The results are from paper [B].

The first column shows the result for the simplest PTO control, applying a constant force in either direction, thereby acting as a Coulomb damping. In the second column, the result of the linear damping approach is shown and finally reactive control is applied. As seen, the average power extraction is doubled with reactive scheme compared to linear damping. The constant force approach has the poorest performance.

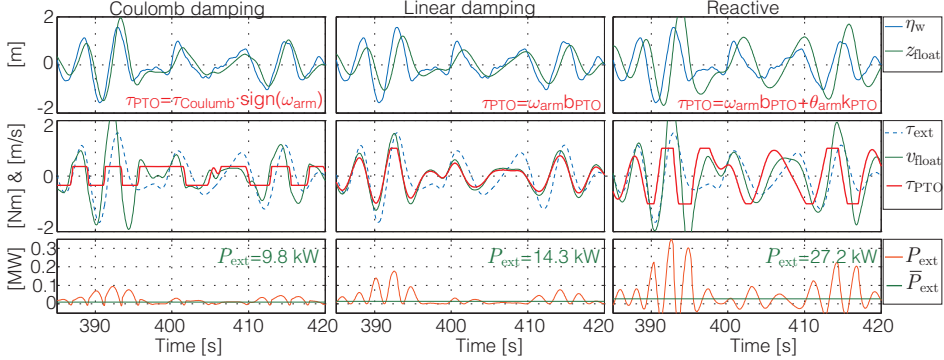


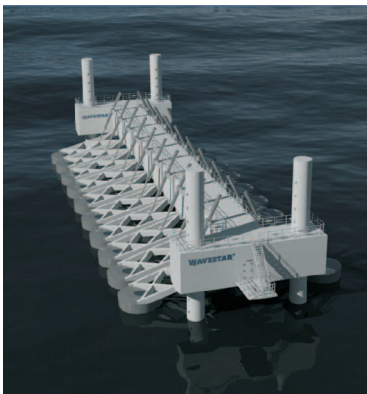
Figure 1.10: Different PTO load force control schemes applied on the absorber in Fig. 1.8a. The same wave is used in all three examples. The wave characteristics are a PM-wave with $H_{m,0} = 1.75$ m and $T_{0,2} = 4.5$ s

To summarise, a PTO system must be able to:

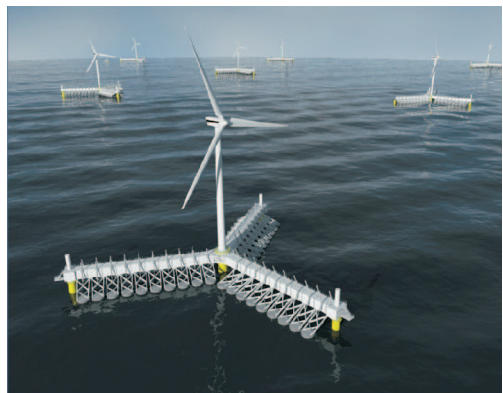
- Exhibit a high force/torque density to cope with the slow motion of wave energy devices.
- Handle a bi-directional motion input.
- Implement controllability of load force to ensure sufficient power absorption.
- Maintain efficiency with a ratio of approximately 10 between peak and mean power load.
- Maintain efficiency at both low and high energetic sea states.
- Be able to reduce power absorption when full load capacity is reached during high energetic sea states - similar to wind turbines pitching out of the wind.
- Smooth the highly fluctuating wave power to an output acceptable for the grid.
- Show high reliability.
- Be able to survive extreme wave conditions.

1.7 Case System: Wavestar C5 WEC

The case WEC system of this Ph.D. dissertation on PTO design is the Wavestar's C-concept - a multi-absorber WEC, which is visualised in Fig. 1.11. The C-concept consists of semi-submerged hemisphere-shaped floats mounted on separate arms. Each arm is mounted and rotationally supported by a common platform, which is resting on the sea bed through a number of piles. The system is designed for water depths up to 40m using e.g. monopile foundations. The advantage of a multiple point absorber WEC is the increased power smoothing achieved when the waves pass through the system, as the system spans multiple wave lengths. To maximise this effect, the machine is placed parallel to the dominating wave direction. The system may also achieve high absorption by exploiting coordinated control of multiple absorbers to focus the radiated wave field by exploiting the interference pattern.



Wavestar C-Concept



Wavestar SC-Concept

Figure 1.11: The Wavestar C-concept with 20 absorbers and the Wavestar SC-concept with 57 floats. The SC concept is a star-configuration of the C-machine with integration of a wind turbine.

For storm protection and extreme seas, the Wavestar concept incorporates a jacking-system, allowing the floats and platform to be lifted out of the water. This is illustrated in Fig. 1.12. Resultantly, the PTO system and absorbers only have to be designed for “production” waves (which for the C5 is 3m significant wave height). The jacking-system is also used to compensate for tides and surges. Except for the cylinders, all PTO components are housed within the main tube in a controlled and conditioned environment.

The C-concept is a part of the strategy for integration of wave power into wind farms as shown in Fig. 1.11 with the SC-concept (star concept). This reduces establishment, installation and maintenance cost, while having an energy park with a higher power density and a more stable energy output - the latter achieved as waves and wind often are phase-shifted in time.

Wavestar was established in 2003 and has in the 10 years been through various scaled



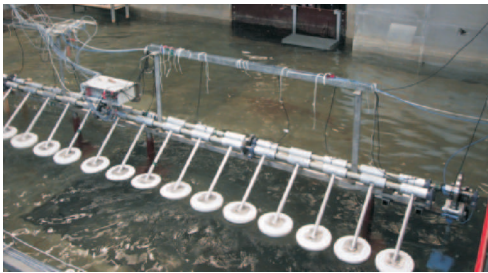
Figure 1.12: Wavestar in storm protection. The right photo is the Wavestar prototype in storm protection, 2009

prototypes, maturing the concept as shown in Fig. 1.13. In 2004 a 1:20 scale system was tested in a wavetank at Aalborg University. The scale is given relative to the C5, which has $\text{\O}5\text{m}$ floats. Following the validation of the concept and identification of float design, a 1:5 scale system was installed in the Danish fjord, Limfjorden. The system had 40 $\text{\O}1\text{m}$ floats and was in service for four years. The PTO of the 1:5 scale system comprised a simple hydraulic circuit, where each float operated a cylinder, pumping high pressure fluid to a common hydraulic motor. The motor drove a small grid-connected generator.

In 2009 Wavestar installed a two-float test-section of the 600kW C5 at Hanstholm, which is at the West coast of Denmark. The WEC has been in operation until fall 2013 [30], where it was shipped into harbour for installing a new PTO and installing additional floats. The prototype was located at the end of Roshage pier as shown in Fig. 1.14 with the depth varying between 5-8m, which is somewhat shallow. Besides only being equipped with two floats and having a shortened main tube, the WEC is identical to the C5. The prototype was equipped with hydraulic PTO, where each float drives separate 55kW generators using a conventional hydro-static transmission. The transmission allowed operating the generator at fixed speed while controlling the load force on the float.

The prototype was in operation for more than three years, surviving the many storms encountered during this period. During the period the concept's structural strength has been proven and its power extraction capabilities validated. Measured power absorption is shown in Fig. 1.15, which is measured as the pressure times flow leaving the cylinder. Thus, the values are the absorbed power minus the power loss due to cylinder friction. The system agrees with the simulated expected results up to 2m significant wave height, whereafter the rate of power increase reduces.

When the wave height passes 2m at the site, the waves begin to break as shown in the photo of Fig. 1.15 due to the shallow water. This causes the waves to slam the sides of the floats instead of producing useful work, explaining the disagreement with expectation. At a "real" production site, the depth will be higher, preventing the waves from breaking.



Tank test at Aalborg University Denmark

Period: 2004
 Number of floats: 20
 Float diameter: 0.25 m
 Wavestar C5-scale: 1:20

PTO: Common shafts with mechanical brake for dissipating extracted energy. Float arms are connected to shafts using a ratchet mechanism. Energy is only extracted during float up-stroke



Test at Nissum Bredning, Limfjorden, Denmark

Period: 2006-2010
 Number of floats: 40
 Float diameter: 1.0 m
 Wavestar C5-scale: 1:5

PTO: Simple hydraulic transmission driving one common generator. Energy is only extracted during float up-stroke where a constant load force is applied. System was grid connected.



C5 prototype located at the Westcoast of Denmark

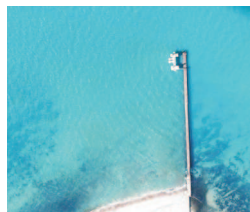
Period: 2009-present
 Number of floats: 2
 Float diameter: 5.0 m
 Wavestar C5-scale: 1:1 (2-float testsection)
 Arm-length: 10 m
 Generators: 2 x 55kW
 Total machine weight: 1000 ton

PTO: Hydrostatic transmission where floats drive separate generators. Control of applied load force on both up and down strokes..

Figure 1.13: Wavestar prototypes.



300m long pier with gangway



Located at Roshage pier

Figure 1.14: Location of the Wavestar prototype at Roshage pier, Denmark.

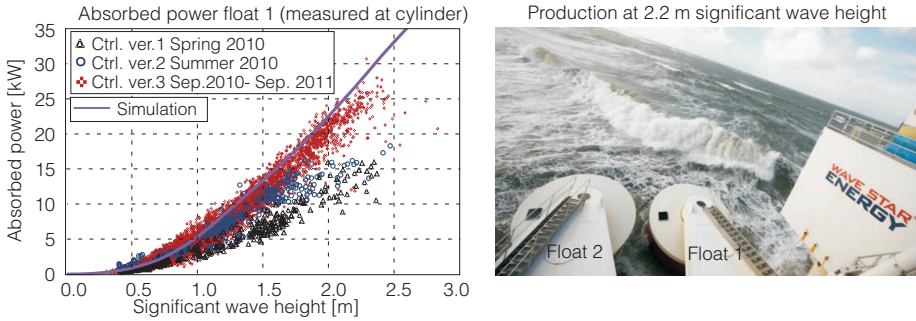


Figure 1.15: Measured average power absorption of one float for different control strategies. Each point represents a 10 minutes average.

An insight into the experience gathered from the prototype is given in Tab. 1.1, showing a segment of operational data. The mentioned phases are a part of the test-programme agreed between Wavestar and Energinet.dk established in July 2010 with the project title “Energy production on Roshage test systems (WSE-02)”, project no. 2009-1-10305. The project documents that the prototype was able to deliver the expected power according to wave climate and expectations for a full commercial converter.

As seen, the system has in the selected 11 months been operational for an average 78% of the time, where 62% was spent in production, i.e. 3100 hours. The system was not in production when the waves were outside the range of significant wave heights from 0.5m-2.5m. The non-operational hours encompass system and control updates, tests, visits, maintenance and system checks.

		2011							2012				Avg.	
		May	Jun	Jul	Aug	Sep	Oct	Nov	Dec	Jan	Feb	Mar		Apr
Operational	[%]	91	92	90	93	79	69	46	17	End of phase 1 - phase 2 start Feb.	98	96	93	78
Production	[%]	56	45	72	61	63	71	36	73		66	79	62	62
Storm	[%]	2	3	1	6	11	4	12	13		9	1	0	6
Calm sea	[%]	39	50	25	31	24	24	50	0		22	19	35	29
Transition	[%]	3	2	3	1	2	2	2	14		2	1	2	3
Extracted energy	[kWh]	4859	4420	5278	4721	4941	6790	1256	1272		5915	8465	5131	4823
Electricity	[kWh]	827	1111	992	1128	1127	3524	666	715	3210	4920	2901	1920	
PTO eff.	[%]	17.0	25.1	18.8	23.9	22.8	51.9	53.0	56.2	54.3	58.1	56.5	39.8	
Max average electrical pwr	[kW]	25.8	23.2	21.5	28.1	25.3	29.0	15.9	16.3	32.8	35.7	30.0	25.8	

Table 1.1: Operational data from the Wavestar prototype.

The prototype system has demonstrated the expected power extraction, but the PTO efficiency is rather low, yielding an average 58.1% for the best month. The PTO of the prototype is illustrated in Fig. 1.16. The measured efficiency is measured from the hydraulic power produced by the cylinder to the electrical output of the generator, not

including inverters and power for some of the auxiliary systems. Thus when included, the actual PTO efficiency will be lower. The main objective of the prototype has been to demonstrate the expected power absorption and durability, which has been fulfilled.

The hydraulic PTO is capable of controlling the load force on the absorbers to maximise power absorption while operating the generator at a fixed speed. Thus, the hydraulic circuit implements a completely variable gearing ratio between float movement and generator. The pump/motor is in closed circuit configuration with a symmetric cylinder. The pump/motor is capable of operating over-centre, meaning that the flow direction may reverse while maintaining uni-directional shaft rotation. To cool and filter the fluid in the closed circuit, and apply a boost pressure to avoid cavitation in the cylinder, a booster/flushing circuit is required. The drawback of the above PTO is that all components (motor, generator, inverter) have to be rated for the peak-power level as no intermediate storage for power smoothing is possible. Especially the large $250\text{cm}^3/\text{rev}$ motor (may operate continuously at 200kW at 350bar and 1500rpm) has a poor efficiency when operating at an average of $10\text{-}40\text{kW}$. Also, having generators for each float gives a larger nominal generator capacity compared to the rating of the entire system.

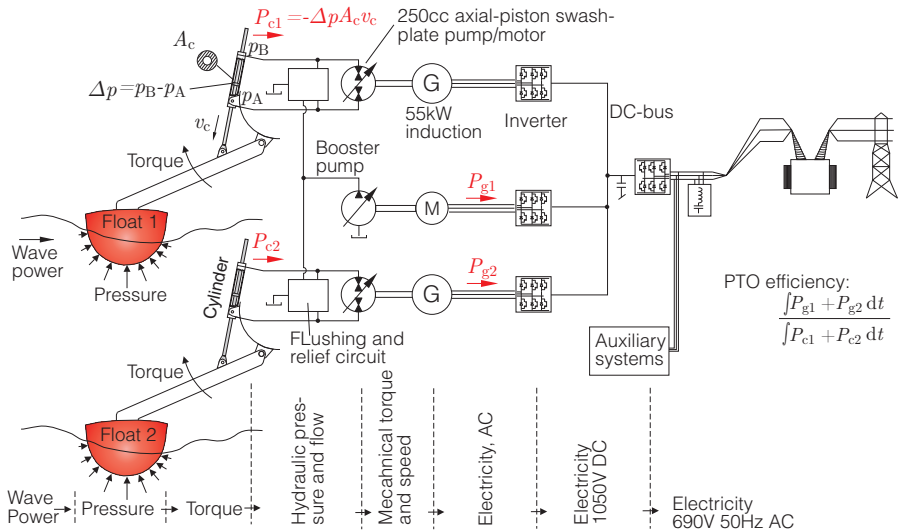


Figure 1.16: Power Take-Off layout of prototype.

The focus of the research disclosed in this dissertation is to propose, investigate and design a PTO for the Wavestar C-concept, which may meet future demands and be suitable for commercialisation. The system used as case design is the commercial C5 system, which is described in Tab. 1.2.

The C5 is allowed to produce power at up to 3m significant wave height, corresponding to maximum wave height of 6m. Going beyond this limit gives a risk of reaching cylinder endstop.

Table 1.2: Technical data for commercial Wavestar C5-converter and prototype at Hanstholm. MWL is mean water level [30] .

Parameter	Commercial Wavestar C5	Prototype at Hanstholm
Number of floats	20	2
Float diameter	Ø 5 m	Ø 5 m
Max. depth	20 m	8 m
Max. wave height	6 m	6 m
Water depth	10 to 20 m	5 to 8 m
Arm length	10 m	10 m
Main dimensions	70 m × 17 m × 6.5 m (L × W × H)	32 m × 17 m × 6.5 m
Length of legs	≈ 15-25 m above MWL	≈ 18 m above MWL
Operation height	5.5 m above MWL	5.5 m above MWL
Storm secure height	Site depended, 6-15 m above MWL	8 m above MWL
Weight	1600 Tons	1000 Tons
Materials	Main structure: Steel. Floats: Fibreglass	Main structure: Steel Floats: Fibreglass
Foundation	Four skirted spud cans, or two monopiles or gravity based foundations	Four gravity based foundations
Design service life	Minimum 20 years	Minimum 20 years
Nominal power	600 kW	110 kW

The C5 system is just an introductory scale WEC, thus an important aspect of the PTO design is to ensure scalability for increased system sizes. The PTO should also optimise power production, which requires understanding the complex coupling between PTO characteristics and the energy extraction performance.

1.8 Outline of Dissertation

To properly investigate and set forth a viable PTO solution for a multi-absorber system, the following work is disclosed:

- Establishment of a single and multi-absorber dynamic model of the Wavestar C5 WEC. The single absorber is verified through tank tests.
- Development of a framework for optimising and evaluating all available Power Extraction Algorithms (WPEAs) for point absorbers based on PTO characteristics. Reactive control, latching, de-clutching, linear damping, Coulomb-damping and ratchet-mechanisms are all optimised and evaluated with regard to PTO constraints.
- Suggestion of a new causal WPEA algorithm where Oscillation Control is Implemented Resistively (OCIR). Through non-linear damping the OCIR algorithm achieves same power production as a causal reactive strategy.
- A thorough review and evaluation is performed of State-of-the-Art within PTOs using the developed framework for estimating power production based on PTO characteristics.

- Evolvement of three potential PTO-concepts for the Wavestar C5 - two hydraulic PTOs and one magnetic gear based. All three PTOs are further investigated, exploring expected performance and identifying challenges with the designs.
- A discrete-displacement hydraulic PTO is chosen for full design. A full design is made for a 20 absorber C5, which is verified through a complete wave-to-wire model of the PTO, which is simulated in different irregular wave conditions.
- Design of a optimised hydraulic PTO design for the C5, where a complete model is developed. The model is coupled with the 20 float simulation model, and performance results is presented for operation in different sea states.
- A full-scale prototype of the hydraulic PTO is designed and implemented for a single absorber. The prototype PTO has a peak power capability of 210kW, a stroke of 2m and may produce load force of 420kN.
- To test the prototype, a 16m long full-size test-bench is design and constructed, comprising a 350kW hydraulic pump station for driving a 840kN hydraulic cylinder for simulating the wave force. The necessary control for emulating the absorber dynamics is developed and implemented.
- Verification of dynamics models of the PTO through testing of the prototype.
- Test results validating the expected performance of the PTO prototype.

The dissertation is organised as follows:

Chapter 2: Modelling of the Wavestar WEC

The required geometry and sizes of the C5 WEC are defined. Afterwards the used wave-model for numerical simulation is presented, which is based on filtering white noise. Next, a hydro-dynamic model of a single Wavestar absorber is developed based on linear wave theory. The hydro-dynamic model parameters are obtained fby employing the commercial software WAMIT. The absorber model are verified to be very accurate through scaled wave-tank tests. A simplified 20 absorber model is finally presented, which includes the effect of the complex diffraction pattern of having 20 closely spaced absorbers.

Chapter 3: Implementation of Reactive Control

The question of feasibility of using reactive control for real PTOs is an ongoing discussion. In reactive control the PTO attempts to periodically transfer energy into the absorber to increase the average output. However, is this feasible when the PTO has a realistic efficiency? To this end, an analytical solution is derived, showing the reactive control's dependency on PTO efficiency and how it may be designed accordingly. The results show that reactive control is feasible.

Optimal reactive control is inherently non-causal. The chapter also shows how different causal implementations relate and suggest a new method with robust and high performance by partially cancelling the absorber dynamics to widen the frequency response.

The chapter gives the required knowledge to perform optimisation of reactive control in irregular wave in chapter 4.

Chapter 4: Wave Power Extraction Algorithms

The chapter is dedicated to investigate Wave Power Extraction Algorithms (WPEAs), which is the algorithm for how the PTO load force should be controlled to maximise energy extraction. State-of-the-art has not provided a sufficient study, comparing the performance of the many different WPEAs, especially when taking PTO characteristics into account. This makes choosing the optimal PTO nearly impossible, as the many different WPEAs possess fundamental different requirements to the PTO. Resultantly, chapter 3 presents a developed framework, where all strategies are optimised for their given PTO type for different PTO efficiencies, part load performance and force limits. The treated WPEAs are reactive control, latching, de-clutching, linear damping, Coulomb-damping and ratchet-mechanisms. These are all mapped to curves of expected yearly production as a function of PTO force limit and efficiency. The chapter also presents a new causal non-linear WPEA (OCIR), which has a performance very similar to causal reactive control. The chapter results serve both for choosing best suited WPEA when having a given PTO, but also give the required base for comparing different PTO systems.

Chapter 5: Evaluation of State-of-the-Art in PTO Systems

To understand the accumulated knowledge of 40 years research in PTOs, a very thorough State-of-the-art analysis is presented, which also includes looking at some potential technologies from other industries. To assess and keep track of the many different PTOs, a small table is made for each concept where expected size, annual production and other characteristics are summarised and given a score. The annual production is estimated by identifying available WPEA algorithms for the PTO, whereafter the production estimate from the previous chapter may be used. The chapter is concluded by comparing all the found PTOs, identifying the most potential concepts.

Chapter 6: Three Potential PTO Systems

Based on obtained knowledge of the State-of-the-Art evaluation, three potential PTOs are developed and investigated. The first is based on a hydraulic digital displacement pump/motors, where a configuration is presented for the Wavestar. Based on earlier performed wave-to-wire simulations of a similar PTO design with a conventional pump/motor, the concept is evaluated. The next PTO being treated is also hydraulic, which is based on a discrete displacement cylinder. To identify the correct PTO structure and evaluate feasibility, a framework is developed for quickly testing different system configurations. The framework gives the optimum PTO layout, and gives a specification of required component performance for the PTO to be feasible. As the final PTO, a magnetic lead screw is evaluated. The mechanical and magnetic design was verified by a scaled prototype, which was performed by a three students as a part of their Master thesis. A complete simulation model is made on how the magnetic screw PTO interacts with an absorber and affects its performance. Based on the evaluation, the magnetic lead screw is seen as a very good PTO solution.

Chapter 7: Design and Validation of DDC PTO System

The hydraulic Discrete Displacement Cylinder (DDC) PTO is found to be the best road for the Wavestar. This chapter presents a complete design for the 20 absorber C5. The PTO is rigorously modelled from wave-to-grid, including all components. Strategies for controlling the large PTO systems are given, which is afterwards simulated in irregular wave. The performance of the PTO is validated to maintain efficiency in both small and large waves, and incorporate the ability to “pitch” out of the waves.

Chapter 8: PTO Prototype and Full scale Test-bench

The chapter presents a full-scale prototype of the PTO, having a peak power capability of 210kW, a stroke of 2m and may produce a load force of 420kN. To test the PTO, a laboratory test-bench has been constructed, consisting of a large cylinder emulating the absorber loads on the PTO cylinder. To make realistic efficiency tests, the test-bench is required to emulate the absorber dynamics, i.e. react on the PTO cylinder load force. As the DDC PTO load force is of discrete nature, this is very challenging. The developed wave simulator controller for solving this is presented. PTO prototype tests are afterwards conducted, showing interesting aspects of the design, including the foreseen complex transmission line phenomena. These problems are treated and the PTO prototype is operated in simulated irregular waves.

Chapter 9: Conclusion and Future Work

This chapter summarises the work and gives the conclusions of the dissertation. Finally, some of the relevant future work is outlined.

1.9 Reading Instructions

A list of acronyms and symbols is placed in the Nomenclature just before chapter 1. Note that the Nomenclature is in two parts, one for Ch.1-5 and one for Ch.6-8. The bibliography is placed in the back of the dissertation where references are made in the text with a number in square brackets, e.g. according to [5]. References to papers prepared as part of the Ph.D. study are made with capital letter in square brackets, e.g. paper [C]. The list of these papers is found just before the Nomenclature.

Many of the published papers are based on the work in this monograph; however some of the monograph is also based on the published papers, where further knowledge may be found.

Some notation information: Matrices and vectors are made with bold symbols, e.g. vector \mathbf{x} and matrix \mathbf{A} . The operator “*” denotes convolution, $\mathcal{L}\{\}$ is the Laplace transform and $\mathcal{F}\{\}$ is the Fourier transform. The variable “s” is the complex variable of the Laplace domain.

Chapter 2, regarding modelling of waves and absorber hydro-dynamics, is relative low on novelty, and lends itself more to appliance of known theory. Thus, for readers familiar with linear-wave theory and numeric generation of waves, this may be skipped. However,

the chapter contains some comparison of wave-tank measurements and simulations that may be of interest to see the performance of the models.

Chapter 3 starts with presenting optimal control of absorbers, i.e. complex-conjugated. The novel part of the chapter is relating the different causal implementations in the frequency domain and introducing new implementations. The chapter is continued by introducing PTO efficiency into the reactive control design, which is a novel approach. Thus, for readers interested in reactive control, and how it may be practically implemented with success for a PTO with losses, the chapter is of interest. However, it is possible to read the next chapter on comparison of different control algorithms without diving into this chapter.

Chapter 4 deals with control of absorbers with respect to the produced power output of the PTO. This chapter contains novelty with regard to new control strategies, applied methods and developed frameworks. Thus, for a comparison of the performance of all classic control strategies (latching, reactive, linear damping, etc.) as function of PTO constraint as load force limits and efficiency, the chapter should be of interests. The chapter is also the foundation for performing evaluation of PTO concepts.

Chapter 5 is on evaluation of the state-of-the-art in PTO concepts. The performed evaluation and discussion of suitability for the Wavestar WEC is dependent on the previous chapters. However, if the reader is only interested in an overview of PTO technologies and their current state, the chapter may be read independent of chapters 2, 3 and 4 as the performed evaluations are placed in intermediate boxes in the text, which may be easily skipped.

Chapter 6 and 7 present and investigate novel PTO designs, and base on using the developed models and control strategies of chapter 2, 3 and 4. Chapter 8 is both on design and control of PTO test-bench, and tests and control of the prototype PTO. For readers interesting in control of hydraulic servo systems, hydraulic transmission line modelling and verification, or discrete displacement cylinders, the chapter may also be of interest independent of the previous chapters.

Chapter 2

Modelling of the Wavestar WEC

This chapter introduces the required models of waves and absorbers for PTO design and control, as both numerical simulations and analytical approaches are going to be applied throughout the work. The models are an important part, as the PTO design problem is a mechatronic problem, characterised in that for example PTO hardware and PTO control cannot be designed separately. Accordingly, a model based design approach is required to optimally solve the PTO design. Moreover, implementation and testing of PTO designs is extremely expensive, especially at full size, hence model based design approaches are also required for being cost-efficient.

The chapter first presents a mechanical overview of the C5 WEC. Next the white-noise method for wave generation is presented. This is followed by introducing a single absorber model based on linear wave theory. This is afterwards extended to an array of 20 absorbers according to the C5 layout. To verify the models, simulated behaviour is compared with wave tank tests.

The chapter's content may also partially be found in papers [N] , [B] and [A] !.

2.1 Mechanical Overview of C5

Basic geometry and sizes of the Wavestar C5 is given in Fig.2.1, showing both side views and top views. The sizes are based on extending the C5 prototype at Hanstholm to a 20 float design.

The C5 consists of two jacking sections with a main tube in between, carrying the 20 float arms. The one-DoF float arms may rotate independently. The main tube also provides a stationary and conditioned environment for housing the PTO and other components.

The floats of the C5 may geometrically be described as a combination of a sphere with a truncated cone upper part. The diameter of the sphere (referred to as the diameter of the float) is 5.0m. The float is mainly made of glass-fibre, and contains a ballast chamber, which may be filled through a bottom hole in the float. The ballast chamber may contain approximately 15 m^3 water and is always full during power production. The ballast is used for lowering the natural frequency of the absorber and yield the correct draft of the float. Before lifting the floats into storm protection the ballast chambers are emptied using an air pressure system. The PTO cylinders are also used as the mechanism for lifting the floats into storm protection.

The operating range of the float arm is shown with a PTO cylinder of 3m stroke. The wave height (trough to crest) may at maximum be 6m, otherwise the lower limit is reached. This corresponds to a sea state with significant wave height of 3m. Above this limit, the floats are lifted into storm protection. In severe storm conditions the entire platform is jacked up. Accordingly, the PTO and floats only have to be designed for power production conditions. The jacking system is also utilised to adjust the machine level according to tide level.

During power production only 2m stroke of the cylinder is used. Retraction of the last 1m only occurs during storm protection.

The floats on each row are spaced with one meter apart. The machine is installed with the “forward” facing the dominating wave direction.

To model the system, some basic reference-frames and quantities are required, which are defined in Fig. 2.2. The arm position is described by the angle θ_{arm} , which is defined to be zero, when the float is horizontal. The arm angle may be seen as the angle between the x -axes of the machine fixed reference frame $\{B\}$ and the arm fixed reference frame $\{A\}$. Positive rotation is defined as the float moving upwards. The angular velocity of the arm is denoted ω_{arm} . The PTO cylinder force is denoted F_c and the cylinder stroke x_c .

When describing the wave height at different locations, this is performed using the wave reference-frame $\{W\}$ positioned in the centre between the first two floats. The wave reference-frame is also shown in Fig. 2.4a. The wave direction θ_w is also defined in Fig. 2.4a. Zero wave angle corresponds to the waves only moving in the x_w -direction, i.e. parallel to the machine.

Quantities used for describing cylinder and arm kinematics are shown in Fig. 2.4b. The length $x_{c,0}$ is the cylinder stroke at which the arm angle θ_{arm} is zero. The distance d_A is the cylinder’s moment arm for applying torque to the float arm and is dependent on the angle θ_{arm} . The relation of cylinder stroke and arm angle may be expressed as,

$$x_c = -c_c + \sqrt{-2a_c b_c \cos(\theta_a - \varphi_c|_{\theta_{\text{arm}}=0}) + a_c^2 + b_c^2} \quad [\text{m}] \quad (2.1)$$

where

$$\varphi_c|_{\theta_{\text{arm}}=0} = \cos^{-1} \left(\frac{a_c^2 + b_c^2 - (c_c + x_{c,0})^2}{2a_c b_c} \right) \quad [\text{rad}] \quad (2.2)$$

The cylinder’s moment arm d_A may be expressed as:

$$d_A = \frac{a_2 b_2 \sin(\theta_a - \theta_{a,0})}{(x_c + c_2)} \quad [\text{m}] \quad (2.3)$$

Using the C5 dimensions given in Tab. 2.1, the equations 2.1 and 2.3 give the result shown in Fig. 2.3. At neutral position the moment arm is $d_A = 2.36\text{m}$.

Masses and mass moment of inertia of the float and arm, both un-ballasted and ballasted, are listed in Tab. 2.1.

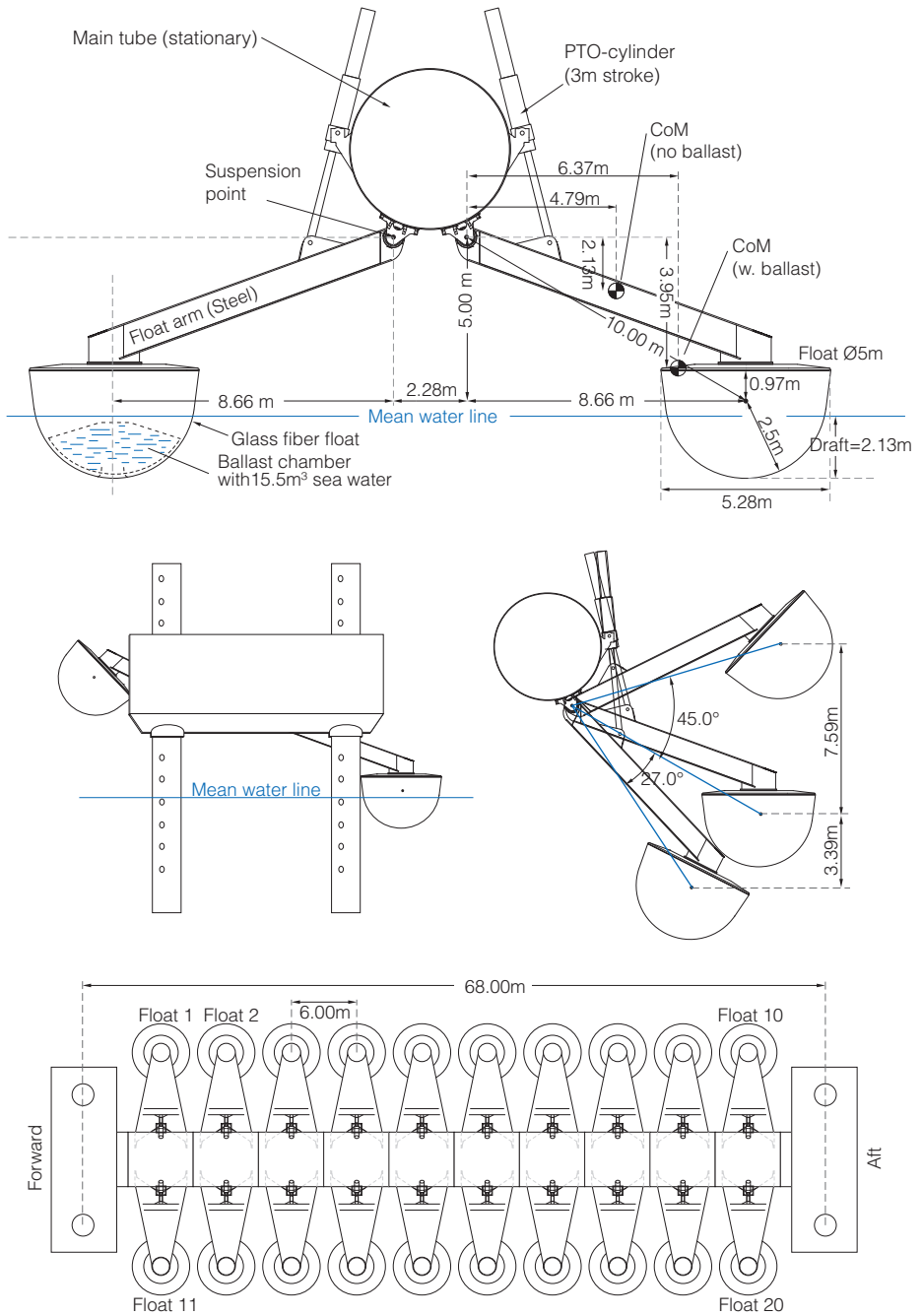


Figure 2.1: Overview of the Wavestar C5 WEC.

Defintion of reference frames and arm angle

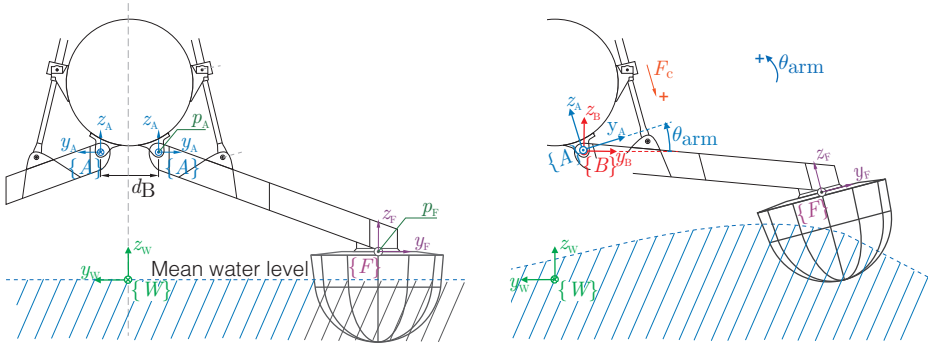


Figure 2.2: Reference frames and arm angle.

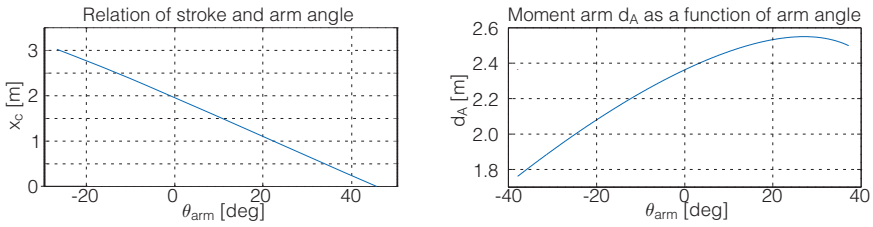
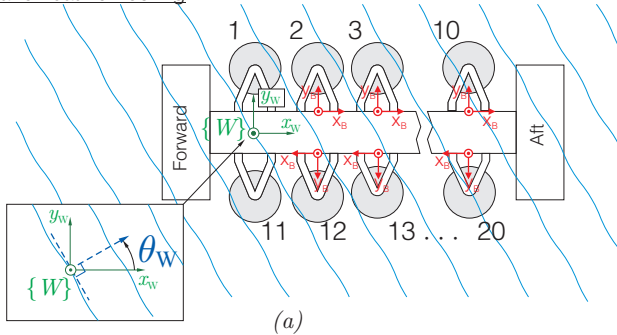


Figure 2.3: C5 cylinder and arm kinematics.

Defintion of wave angle and float numbering



Cylinder kinematics

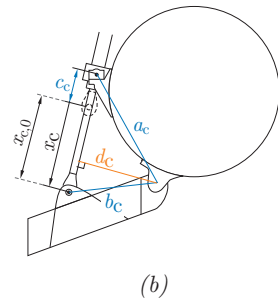


Figure 2.4: Wave reference frame, wave direction and cylinder kinematics

Table 2.1: Sized and dimensions for the Wavestar C5.

Symbol	Description	Value
$J_{\text{mech},0}$ [kgm ²]	Mass inertia moment of arm and float	784e3
J_{mech} [kgm ²]	Mass inertia moment of arm and float w. ballast water	2460e3
$m_{\text{mech},0}$ [kg]	Mass of arm and float	20.4e3
m_{mech} [kg]	Mass of arm and float w. ballast water	34.5e3
a_c [m]	Cylinder kinematics	3.68
b_c [m]	Cylinder kinematics	2.54
c_c [m]	Cylinder kinematics	1.60
$x_{c,0}$ [m]	Cylinder stroke for $\theta_{\text{arm}}=0$	1.94

2.2 Wave Model

Irregular waves have varying frequency and wave height. For a measured wave, the period may be defined as two successive zero-down crossings of the mean water level and the wave height is the distance from wave trough to wave crest [31]. This is illustrated in Fig. 2.5.

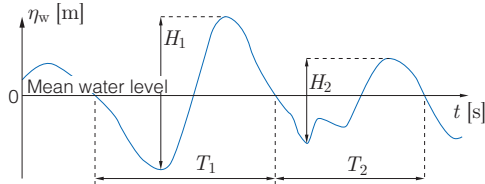


Figure 2.5: An irregular waves and how wave period and wave height may be measured.

To characterise an irregular wave, a spectrum is often used where two quantities are essential to the spectrum - the *peak wave period* T_p and the *significant wave height* H_{m0} . For a measured irregular wave, the peak wave period T_p may be viewed as the wave period where most energy is concentrated and the significant wave height H_{m0} interpreted as the average wave height of the one-third highest waves. These two parameters along with an underlying assumption of the shape of the Power Density Spectrum (PSD) may qualitative define an irregular wave through a frequency representation. The shape of the spectrum is highly site dependent, and may also shows changes at the same site.

As spectrum or PSD function $S_\eta(f)$ for describing the frequency content of an irregular wave, the Pierson-Moskowitz (PM) spectrum $S_{\text{PM}}(f)$ is often utilised [32]. The spectrum describes a fully developed sea, which means that a wind has blown long enough over a large distance for waves being fully developed under the given wind conditions. The spectrum is given in its single sided version below [32] as a function of frequency f [Hz]:

$$S_{\text{PM}}(f) = \frac{A}{f^5} e^{-\frac{B}{f^4}} \text{ [m}^2\text{/Hz]}, \quad B = \frac{5}{4} \frac{1}{T_p^4}, \quad A = \frac{1}{4} B H_{m0}^2 \quad (2.4)$$

The PM-spectrum is seen in Fig. 2.6, along with spectral definition of peak frequency

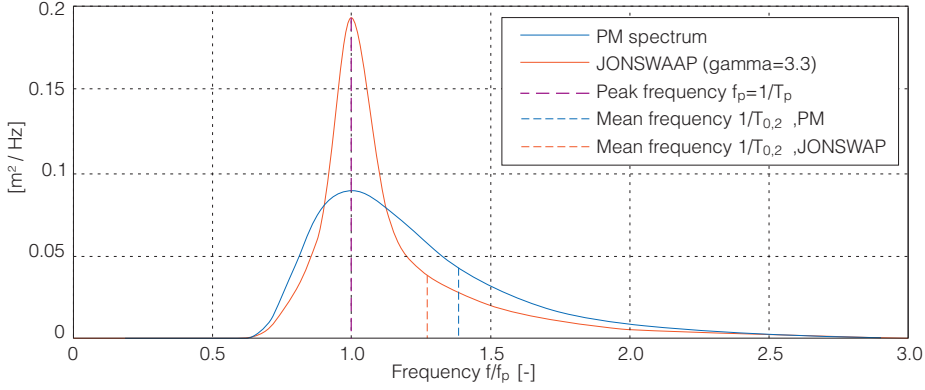


Figure 2.6: PM and JONSWAP spectra.

$f_p = 1/T_p$, [33]

$$f_p = f \Big|_{S_\eta(f)=\max(S_\eta(f))} \quad [\text{Hz}] \quad (2.5)$$

and mean period $T_{0,2}$, which is defined as,

$$T_{0,2} = \sqrt{\frac{m_0}{m_2}} \quad [\text{s}] \quad (2.6)$$

where the n 'th order moment m_n is defined as:

$$m_n = \int_0^\infty f^n S_\eta(f) df \quad (2.7)$$

The significant wave height H_{m0} is defined as:

$$H_{m0} = 4\sqrt{(m_0)} \quad [\text{m}] \quad (2.8)$$

Another commonly used spectrum for describing sea states is the JONSWAP spectrum [34], which was developed by the offshore industry (Joint North Sea Wave Project) to characterise the waves in the North Sea. Here the waves have a shorter distance to develop, whereby the wind-wave equilibrium condition described by the PM-spectrum ceases to hold. The JONSWAP spectrum adds a “peak-enhancement” factor to the PM-spectrum, concentrating the energy in a narrower frequency band [35]:

$$S_J(f) = A_\gamma S_{\text{PM}}(f) \gamma^e \quad \left[\frac{\text{m}^2}{\text{Hz}} \right] \quad (2.9)$$

$$\sigma = \begin{cases} \sigma_a & ; f \leq f_p \\ \sigma_b & ; f > f_p \end{cases}$$

$$A_\gamma = 1 - 0.287 \ln(\gamma) \quad (2.10)$$

where γ_J is a non-dimensional peak enhancement factor, and σ_a and σ_b are the spectral width parameters.

Based on experiments, [35] gives average values of $\gamma_J = 3.3$, $\sigma_a = 0.07$, $\sigma_b = 0.09$. Comparison of PM and JONSWAP spectrum is seen in Fig. 2.6, showing that the JONSWAP spectrum is more narrow-banded. The relation of mean and peak period is spectrum-dependent, but is for PM and JONSWAP given as [35]:

$$\text{PM-spectrum: } T_p = 1.41T_{0,2}$$

$$\text{JONSWAP-spectrum } (\gamma_J = 3.3): T_p = 1.29T_{0,2}$$

Considering estimating power extraction performance of a WEC, the PM-spectrum is often the more conservative choice, as the power is spread across a wider band of frequencies compared to e.g. the JONSWAP. This makes efficient power extraction more difficult, as the absorber frequency response tends to be narrow banded. Resultantly, to evaluate the performance of the control, the PM-spectrum is applied in this work to avoid overestimating power extraction performance.

To perform time simulation in different sea state conditions, realisation of a wave complying with the spectrum is required. An often used method is to generate a wave by converting the spectrum into a finite number of *regular wave* components, which are added with a random phase for each component. The amplitudes of the individual regular wave components are created using the spectrum [36],

$$\eta_{w,i}(t) = \sqrt{2S_\eta(f_i)\Delta f} \sin(2\pi f_i t) \quad [\text{m}] \quad (2.11)$$

and a irregular wave time series generated as,

$$\eta_w(t) = \sum_{i=1}^n \sqrt{2S_\eta(f_i)\Delta f} \sin(2\pi f_i t + \varphi_{\text{rand},i}) \quad [\text{m}] \quad (2.12)$$

where $\varphi_{\text{rand},i}$ is a random phase for each component. This is illustrated in Fig. 2.7.

This simple method has been experienced to be adequate for estimating average power absorption [37]. However, the method does not reproduce for example wave grouping correctly [38]. Studies indicate that using the method, the mean length of wave groups is too short [38]. Thus, the random phase generated waves may not accurately test the PTO's capability of power smoothing and average production, as this is dependent on the degree of wave grouping. Instead, [38] suggests that by filtering Gaussian white noise, better representation of ocean waves may be achieved, and arbitrarily long series may be generated. The white noise method is also treated in [39]. The spectrum of the waves produced with the white noise method also shows fluctuation around the target PM-spectrum, which is more consistent with real sea wave observations, also showing a non-smooth spectrum. How this method has been implemented is described in the following.

2.2.1 White Noise Wave Generation Method

Giving a stochastic process $x(t)$ with power spectrum density (PSD) function $S_{xx}(f)$, applying this input to a linear filter $H(f)$ produces the stochastic process $y(t)$, whose PSD $S_{yy}(f)$ is given as:

$$S_{yy}(f) = S_{xx}(f)|H(f)|^2 \quad \left[\frac{\text{m}^2}{\text{Hz}} \right] \quad (2.13)$$

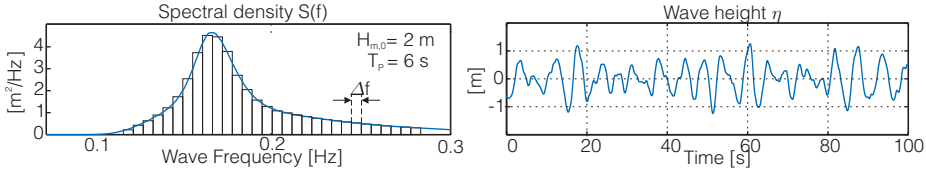


Figure 2.7: Random phase method for realising waves.

If the input process to the filter $x(t)$ is white noise, which is defined by having a flat spectrum $S_{xx}(f) = \sigma_{xx}^2$, and the filter $H(f)$ is designed according to the PM-spectrum (double-sided), $H(f) = \sqrt{S_{PM}(f)}$, then,

$$S_{yy}(f) = \sigma_{xx}^2 \cdot |\sqrt{S_{PM}(f)}|^2 = S_{PM}(f) \quad \left[\frac{\text{m}^2}{\text{Hz}} \right] \quad (2.14)$$

where a white noise with variance $\sigma_{xx}^2 = 1$ has been used as input. Thus, by filtering white noise $x(t)$ with the filter $H(f) = \sqrt{S_{PM}(f)}$ yields an output $y(t)$, having a spectrum agreeing with the target PM spectrum.

The double-sided PM-spectrum is given as,

$$S_{PM}(f) = \frac{1}{2} \frac{A}{|f^5|} e^{\frac{-B}{f^4}}, \quad \left[\frac{\text{m}^2}{\text{Hz}} \right] \quad (2.15)$$

for $f \in]-\infty; +\infty[$ and A and B given as in Eq. (2.4).

To implement the filter, the impulse response function $h_{PM}(t)$ of the filter $H_{PM}(f) = \sqrt{S_{PM}(f)}$ may be obtained by the inverse Fourier transform:

$$h_{PM}(t) = \int_{-\infty}^{+\infty} \sqrt{S_{PM}(f)} e^{j2\pi ft} df \quad (2.16)$$

The impulse response is shown for three spectra in Fig. 2.8. As the phase of $H_{PM}(f)$ is zero ($H_{PM}(f)$ is real) the resulting impulse response becomes symmetric and non-causal (non-zero for negative time). A discrete white noise signal $x_{wn}(nT_s)$ is used as input to the filter with variance $\sigma_{wn}^2 = 1$ and sample time T_s . A part of the white noise signal is seen Fig. 2.9, along with its calculated spectrum, showing a flat PSD fluctuating around 1 as desired.

To produce η_w the white noise signal $x_{wn}(nT_s)$ is convoluted with the impulse response in Eq. (2.16):

$$\eta_w(n \cdot T_s) = T_s \sum_{k=-\infty}^{k=\infty} x_{wn}(kT_s) h_{PM}((n-k)T_s) \quad [\text{m}] \quad (2.17)$$

An example of a generated wave is shown in Fig. 2.10 for $H_{m0} = 1.75$ m and $T_p = 5.5$ s. Analysing the spectrum of the generated wave η_w gives the PSD in Fig. 2.10, which agrees with the target PM-spectrum, with fluctuations around the target spectrum.

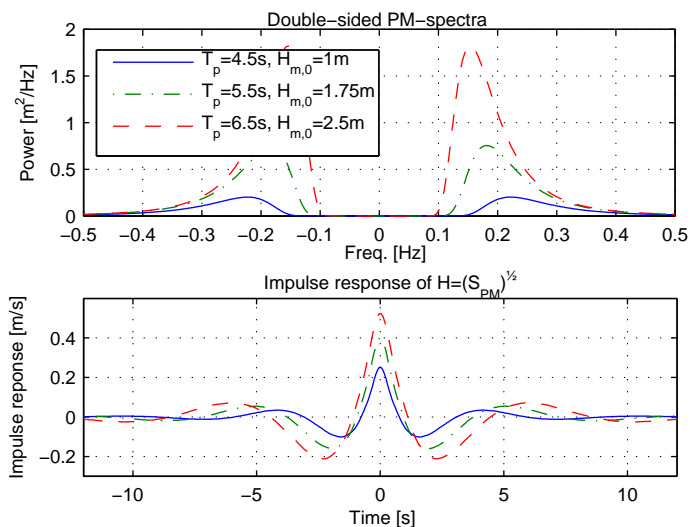


Figure 2.8: Double-sided PM-spectra and impulse response of corresponding filters, see [B].

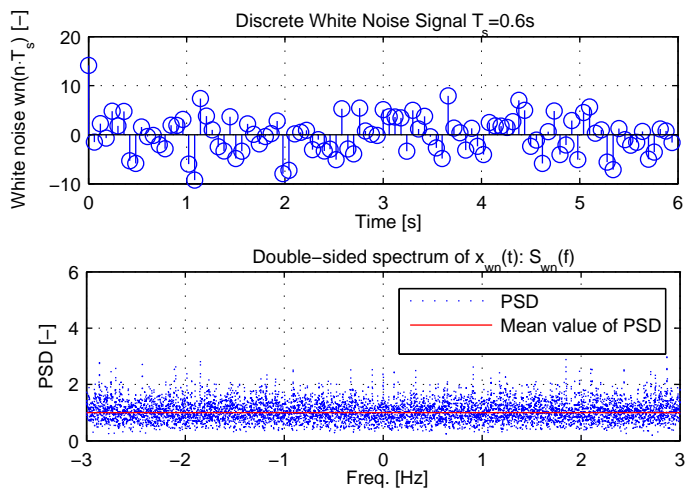


Figure 2.9: Discrete white noise signal $x_{wn}(n \cdot T_s)$ and calculated spectrum [B].

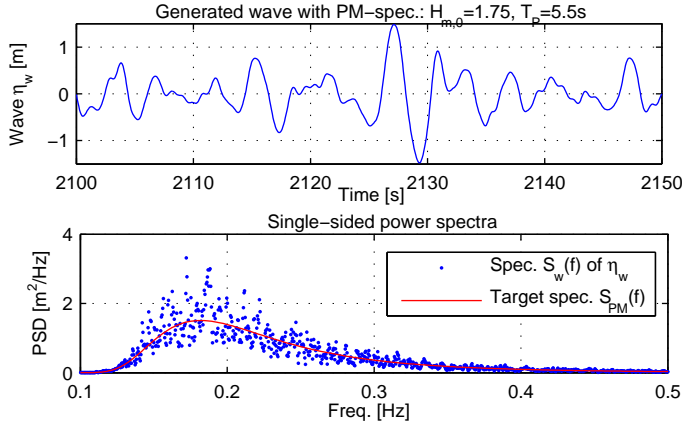


Figure 2.10: Generated wave and calculated spectrum, which is compared to the target PM-spectrum.

2.3 Single Absorber Model

The aim of this section is to describe how the resulting movement of a Wavestar absorber is described as a function of wave and PTO loads. Each absorber represents a single degree of freedom system described by its angular motion θ_{arm} , Fig. 2.11a. When describing the motion of a single absorber, the incoming waves is described in a wave reference frame WS in the centre of the float as illustrated in Fig. 2.11a.

The following derivation of the model for single absorber may also be found in papers [N] and [A].

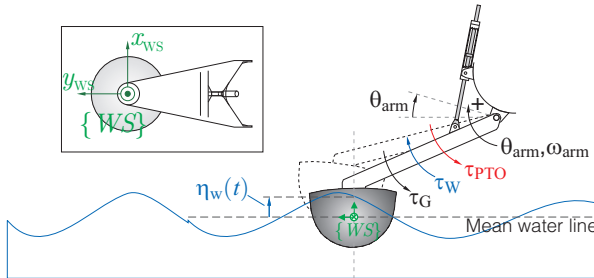


Figure 2.11: Definition of torques, sizes and reference frame for single float model.

The equation of motion for the float is given as,

$$J_{\text{mech}} \ddot{\theta}_{\text{arm}} = \tau_W - \tau_G - \tau_{\text{PTO}} \quad [\text{Nm}] \quad (2.18)$$

where J_{mech} is the total moment of inertia of arm, float and ballast water, τ_W is applied

torque due to the wave-float interaction, τ_{PTO} is TPO applied torque and τ_{G} is the torque due to gravity.

To describe the wave-float interaction τ_{W} *linear wave theory* is standard used for WECs as it yields an adequate description in the wave conditions where a WEC produces energy [32].

This theory describes waves under the assumption that the viscous forces in the fluid are negligible, and that no whirling occurs. As a result, the forces in the fluid becomes conservative and linear potential theory may be applied, which is solved for a number of boundary conditions, e.g. the particles cannot cross the seabed, submerged bodies, and the water-surface. In order to linearise and solve the boundary conditions, the wave is also assumed to have small amplitude relative to the size of the body.

The small amplitude assumptions make the model improper for estimating wave loads in extreme sea conditions. However, for a WEC in production the waves and absorber motion are more moderate, making the model adequate for estimating power extraction and PTO design. However, at the largest production waves, measurements are required to ensure that power production is not over-estimated due to violation of the small amplitude assumption.

To solve the above discussed linear potential problem, Numerical tools are applied, determining the parameters for describing the wave-float interaction. Different commercial software packages exist to solve the potential problem, e.g. WAMIT [40], which is used for estimating wave loads on sea structures and is used by Wavestar. The hydrodynamics parameters presented in this PhD dissertation has found and supplied by Wavestar.

Using linear wave theory, the wave-float interaction τ_{W} is described by superimposing the three following effects:

- The force exerted by an incoming wave on the float. This is called the exciting wave torque $\tau_{\text{ext}}(t)$. The effect of the diffracted wave due to the body is also included.
- Moving the float in the water causes wave radiation, which gives a reaction to the float itself. This effect is denoted radiated wave torque $\tau_{\text{rad}}(t)$.
- The effect of the Archimedes force $\tau_{\text{Arch}}(t)$, i.e. buoyancy.

The effects may be described individually and superimposed. Hence, the exciting wave torque $\tau_{\text{ext}}(t)$ is found for a fixed float, the radiation torque $\tau_{\text{rad}}(t)$ for a mass-less float moved in otherwise calm water, and the Archimedes force for an absorber displaced in calm water.

2.3.1 Exciting Wave Torque

The torque an incoming wave applies to a float held fixed is referred to as the exciting wave torque τ_{ext} and is illustrated in Fig. 2.12a. Using e.g. WAMIT the fluid equations are solved for a regular wave passing a fixed submerged float, yielding the pressures

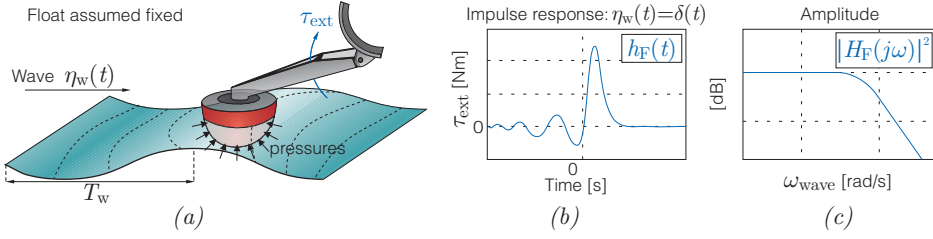


Figure 2.12: Illustration of the exciting wave torque τ_{ext} .

along all submerged surfaces as a function of time. These pressures are then integrated into resulting forces and torques on the absorber.

By solving the equations for each wave frequency, a filter relating the wave $\eta_w(t)$ to the exciting wave torque $\tau_{ext}(t)$ is established. The filter may be formulated as an impulse response function $h_{ext}(t)$. The exciting wave torque may then be found by convolution:

$$\tau_{ext} = \int_{-\infty}^{\infty} h_{ext}(t - \tau) \eta_w(\tau) d\tau = h_{ext}(t) * \eta_w(t) \quad [\text{Nm}] \quad (2.19)$$

An example of an impulse response for the Wavestar absorber is given in Fig. 2.12b. Note that the impulse response is non-zero for $t < 0$, rendering the filter non-causal. This means that the current excitation force depends on the future incident waves. This is partly due to the fact, that the waves hit the float before the reaching the reference point in the centre of the float, where η_w is defined. Also, the defined wave height is not the direct cause to the wave excitation torque, but is a quantity defined model wise [41]. Thus, both are caused by some unknown process, resultantly their relation are not forced to causal. In Fig. 2.12c the magnitude response is shown, resembling a typical low-pass filter.

As the produced wave fore is dependent on the wave direction of the sea state, a force filter is used for a each incoming wave direction θ_w .

2.3.2 Hydrostatic Restoring Torque

The Archimedes force illustrated in Fig. 2.13a is equal to the weight of the displaced water,

$$\tau_{Arch} = V_{disp}(\theta_{arm}) \rho_{water} g d_A(\theta_{arm}) \quad [\text{Nm}] \quad (2.20)$$

where V_{disp} is the volume of the submerged part of the float, ρ_{water} is the density of sea water, d_A is the floats moment arm, and g is the gravitational acceleration.

If the torque due to the gravitational force on the float and arm is denoted τ_G , then the hydrostatic restoring torque τ_{RES} is the combination of τ_{Arch} and τ_G ,

$$\tau_{RES}(t) = \tau_{Arch}(t) - \tau_G(t) \quad [\text{Nm}] \quad (2.21)$$

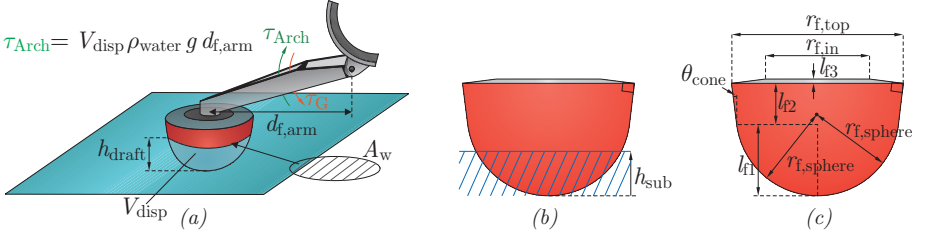


Figure 2.13: Illustration of the hydrostatic restoring force.

Often the torque τ_{RES} is linearised around the draft of the float, defined as the position where $\tau_{\text{Arch}} = \tau_{\text{G}}$. Hence, the linearised hydrostatic restoring torque τ_{res} may be described as:

$$\tau_{\text{res}}(t) = \left. \frac{\partial \tau_{\text{RES}}}{\partial \theta_{\text{arm}}} \right|_{\theta_{\text{arm}}=0} = -k_{\text{res}} \theta_{\text{arm}}(t) \quad [\text{Nm}] \quad (2.22)$$

The spring constant or hydrostatic restoring coefficient k_{res} may due to the float's large moment arm $d_{\text{f,arm}}$ be approximated as $k_{\text{res}} \approx \rho_{\text{water}} g A_{\text{f}} d_{\text{f,arm}}$, where A_{f} is the cross-sectional area of the float at the draft line.

2.3.3 Radiated Wave Torque

When moving the float in calm water it will radiate waves as illustrated in Fig. 2.14a. If a massless float is forced to oscillate with a frequency ω_{w} in otherwise calm water, the torque applied to the float due to wave radiation τ_{rad} may be described as:

$$\tau_{\text{rad}}(t) = -J_{\text{add}}(\omega_{\text{w}}) \dot{\omega}_{\text{arm}}(t) - B_{\text{hyd}}(\omega_{\text{w}}) \omega_{\text{arm}}(t) \quad [\text{Nm}] \quad (2.23)$$

The parameter $J_{\text{add}}(\omega_{\text{w}})$ is referred to as the added mass or inertia and $B_{\text{hyd}}(\omega_{\text{w}})$ is the hydrodynamic damping coefficient. The damping term is due to the power being dissipated by the float to radiate waves. The added mass (inertia) term is due to the effect that when oscillating a float, it will appear to have a greater mass due to the nearby water being displaced along with it.

The above mixed time and frequency notation only make sense for regular waves. To perform time domain simulation, Eq. (2.23) may be written as,

$$\tau_{\text{rad}} = -J_{\text{add},\infty} \ddot{\theta}_{\text{arm}} - k_{\text{r}} * \omega_{\text{arm}} \quad [\text{Nm}] \quad (2.24)$$

where the function k_{r} is the radiation-force impulse-response function and $J_{\text{add},\infty}$ is the added mass at infinite high frequencies.

The convolution expression in Eq. (2.24) may be obtained by taking the Fourier transform of Eq. (2.23), yielding the expression:

$$\begin{aligned} \tau_{\text{rad}}(\omega) &= -J_{\text{add}}(\omega) j\omega \omega_{\text{arm}}(\omega) - B_{\text{hyd}}(\omega) \omega_{\text{arm}}(\omega) \\ &= \underbrace{(J_{\text{add}}(\omega) j\omega - B_{\text{hyd}}(\omega))}_{Z_{\text{rad}}(\omega)} \omega_{\text{arm}}(\omega) \end{aligned} \quad (2.25)$$

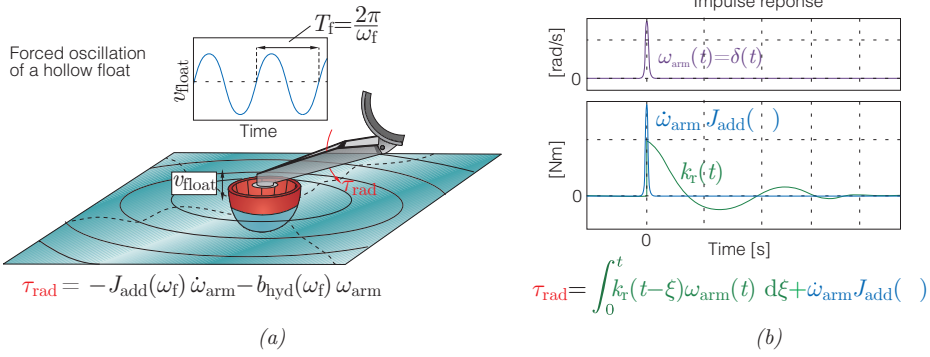


Figure 2.14: Illustration of the radiated wave torque τ_{rad} .

The frequency response $Z_{\text{rad}}(\omega)$ thus relates τ_{rad} and ω_{arm} . The idea is now to take the inverse Fourier transform \mathcal{F}^{-1} of $Z_{\text{rad}}(\omega)$ to obtain an impulse response function for time domain convolution. It is known that $B_{\text{hyd}}(\omega)$ vanishes for $\omega \rightarrow \infty$, however, this is not the cases for the added inertia as $J_{\text{add}} \rightarrow J_{\text{add},\infty} \neq 0$ for $\omega \rightarrow \infty$ (this will be seen later one). This will lead to an infinite valued impulse response when solving the inverse Fourier of $Z_{\text{rad}}(\omega)$. To avoid this, the added mass at infinite frequency $J_{\text{add},\infty}$ may be subtracted by rearranging the expression

$$\tau_{\text{rad}}(\omega) = -((J_{\text{add}}(\omega) - J_{\text{add},\infty})j\omega - B_{\text{hyd}}(\omega)) \omega_{\text{arm}} - J_{\text{add},\infty} \omega_{\text{arm}} \quad (2.26)$$

By noting $\mathcal{F}^{-1}(J_{\text{add},\infty} \omega_{\text{arm}}) = J_{\text{add},\infty} \dot{\omega}_{\text{arm}}$, the expression in Eq. (2.24) may now be obtained by inverse Fourier of Eq. (2.26), where:

$$\begin{aligned} k_r(t) &= \mathcal{F}^{-1}(- (J_{\text{add}}(\omega) - J_{\text{add},\infty})j\omega - B_{\text{hyd}}(\omega)) \\ &= - \int_{-\infty}^{\infty} ((J_{\text{add}}(\omega) - J_{\text{add},\infty})j\omega + B_{\text{hyd}}(\omega)) e^{j\omega t} d\omega \quad [\text{Nm}] \quad (2.27) \end{aligned}$$

$$\Rightarrow \tau_{\text{rad}} = -k_r * \omega_{\text{arm}} - J_{\text{add},\infty} \ddot{\theta}_{\text{arm}} \quad [\text{Nm}] \quad (2.28)$$

2.3.4 Single Absorber Equation of Motion

By inserting the found wave load terms Eq. (2.22) and Eq. (2.24) into the equation of motion of the absorber Eq. (2.18), the following equation is obtained,

$$\ddot{\theta}_{\text{arm}} = \frac{1}{J_{\text{mech}} + J_{\text{add},\infty}} (-k_{\text{res}} \theta_{\text{arm}} - k_r * \omega_{\text{arm}} - \tau_{\text{PTO}} + \tau_{\text{ext}}) \quad \left[\frac{\text{rad}}{\text{s}^2} \right] \quad (2.29)$$

which expresses a linear model of the float, with the exciting wave torque τ_{ext} as input and the float angle θ_{arm} as output. The transfer function version is given as,

$$\frac{\omega_{\text{arm}}(s)}{\tau_{\text{ext}}(s) - \tau_{\text{PTO}}(s)} = \frac{1}{(J_{\text{mech}} + J_{\text{add},\infty})s^2 + K_r(s)s + k_{\text{res}}} \quad (2.30)$$

where $K_r(s) = \mathcal{L}(k_r(t))$.

If the input to the model is a regular wave, the mixed time and frequency expression for the radiated wave in Eq. (2.23) may be used, yielding that for a given input wave frequency ω_w :

$$\frac{\theta_{\text{arm}}(s)}{\tau_{\text{ext}}(s) - \tau_{\text{PTO}}(s)} = \frac{1}{(J_{\text{mech}} + J_{\text{add}}(\omega_w))s^2 + B_{\text{hyd}}(\omega_w)s + k_{\text{res}}} \quad (2.31)$$

2.3.5 Single Absorber Model Parameters for C5

By applying WAMIT to the C5 float, the force excitation filter shown in Fig. 2.15 has been obtained. The filter is for a wave direction of $\eta_w = 0^\circ$. As seen the filter is dependent on approximately future five seconds (non-zero from -5s to 0s), when using the wave height at the absorber centre as input.

From the impulse response the wave excitation torque may be found by discrete convolution:

$$\tau_{\text{ext}}(n \cdot T_s) = T_s \sum_{k=-\infty}^{k=\infty} \eta_w(kT_s) h_{\text{ext}}((n-k)T_s) \text{ Nm} \quad (2.32)$$

Corresponding magnitude plots $|H_{\text{ext}}|$ of h_{ext} for different wave direction is also shown in Fig. 2.15. Waves with a positive wave angle give a slight increase in gain from wave to exciting wave torque. At positive wave angles the waves approach the float arm from behind, causing the horizontal force exertion on the float to generate useful torque τ_{ext} . However, at negative wave angles, the horizontal force components counteract the desired movement of the float.

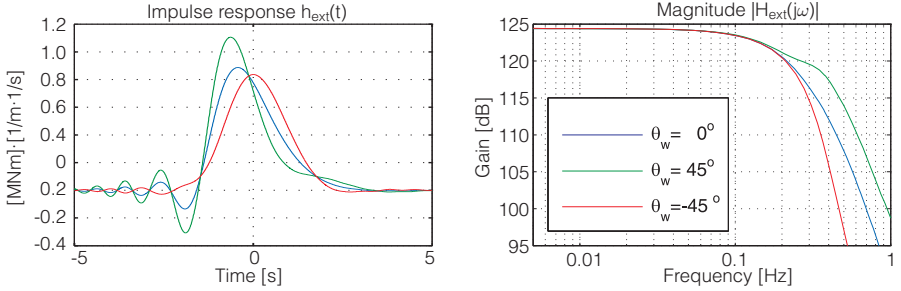


Figure 2.15: Force filter for a single absorber for different wave directions.

The convolution may be implemented as a discrete Finite Impulse Response (FIR) filter as illustrated in Fig. 2.16a. Simulation wise, the signal τ_{ext} will be delayed $T_s n_-$ relative to η_w , where n_- is the number of negative time samples of the impulse function. To obtain time coherent signals, η_w may be delayed afterwards with $T_s n_-$. As illustrated in Fig. 2.16b, coherent input of the wave height and exciting wave torque is now obtained. The FIR filter coefficients are sampled values of the impulse response function:

$$b_0 = h_{\text{ext}}(-n_- T_s), b_1 = h_{\text{ext}}((-n_- + 1)T_s), \dots, b_m = h_{\text{ext}}((n_+)T_s) \quad (2.33)$$

Another method is to pre-compute the excitation torque (e.g. by the FIR-filtering method). This is allowed as the excitation torque is independent of the float motion, cf. the superposition of the wave-float interaction. This is also the used method in the majority of the simulations performed in this dissertation.

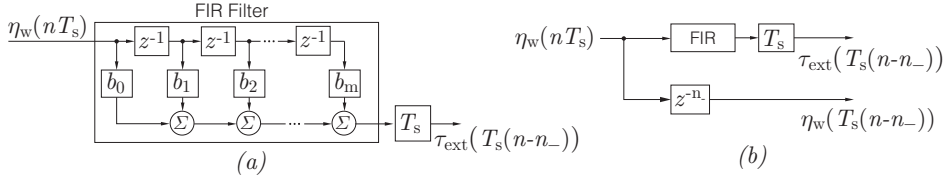


Figure 2.16: FIR filter implementation of the force filter to obtain τ_{ext} from η_w .

The hydrodynamic damping B_{hyd} and added mass J_{add} are shown in Fig. 2.17. The corresponding radiation-force impulse-response function $k_r(t)$ is shown in Fig. 2.18. To avoid performing the convolution $\tau_{rad,kr} = k_r(t) * \omega_{arm}(t)$ in each simulation, the convolution is instead approximated as a system of Ordinary Differential Equations (ODE). This is performed using Prony's method [42], but may also be fitted in frequency domain using e.g. (invfreqs()) in MATLAB. In frequency domain, the required order of the fit may be easier assessed compared to impulse response fitting. The resulting fifth order approximation is shown in Fig. 2.18, which is given as,

$$K_r(s) = \frac{b_0 s^5 + \dots + b_4 s + b_5}{a_0 s^5 + \dots + a_4 s + a_5} \omega_{arm}(s) \quad (2.34)$$

, with the parameters listed in Tab. 2.2.

By Laplace transforming Eq. (2.29) and inserting the radiated wave approximation, the following transfer function is obtained:

$$\frac{\theta_{arm}(s)}{\tau_{ext}(s) - \tau_{PTO}(s)} = \frac{1}{(J_{mech} + J_{add,\infty})s^2 + K_r(s) \cdot s + k_{res}} \quad (2.35)$$

A Bode-diagram of Eq. (2.35) is given in Fig. 2.19 with the parameters in Tab. 2.2. The Bode-diagram shows that the system has a resonance peak at $f_r = 0.285$ Hz, corresponding to a natural period of 3.51 s. The 3.50 s corresponds to the shortest wave periods

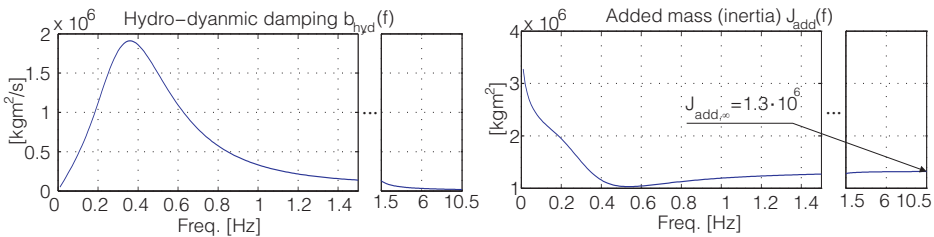


Figure 2.17: Hydrodynamic damping and added mass for the C5 absorber.

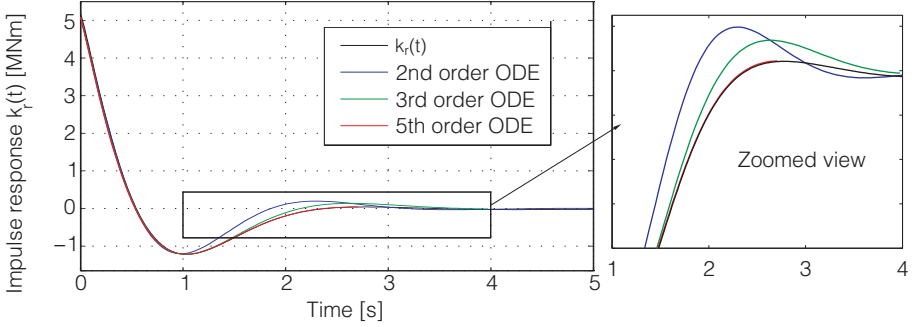


Figure 2.18: Approximation of the impulse response function $k_r(t)$.

($T_{0,2}=3.5$), where the absorber will be extracting energy. At shorter periods, the energy content becomes to low at the absorber's sites.

The system may also be expressed in state-space form as,

$$\dot{\mathbf{x}}_{\text{absorber}} = \mathbf{f}_{\text{absorber}}(\mathbf{x}_{\text{absorber}}, \tau_{\text{PTO}}, \tau_{\text{ext}}) \quad (2.36)$$

where the state vector $\mathbf{x}_{\text{absorber}}$ and vector field $\mathbf{f}_{\text{absorber}}$ are given as:

$$\begin{pmatrix} \dot{\theta}_{\text{arm}} \\ \dot{\omega}_{\text{arm}} \\ \dot{\tau}_{\text{kr}} \\ \dot{x}_{\text{kr},1} \\ \dot{x}_{\text{kr},2} \\ \dot{x}_{\text{kr},3} \\ \dot{x}_{\text{kr},4} \end{pmatrix} = \begin{pmatrix} \omega_{\text{arm}} \\ \frac{1}{J_{\text{mech}} + J_{\text{add},\infty}} (-k_{\text{res}}\theta_{\text{arm}} - \tau_{\text{kr}} - \tau_{\text{PTO}} + \tau_{\text{ext}}) \\ -a_1\tau_{\text{kr}} + x_{\text{kr},1} + (b_1 - a_1b_0)\omega_{\text{arm}} \\ -a_2\tau_{\text{kr}} + x_{\text{kr},2} + (b_2 - a_2b_0)\omega_{\text{arm}} \\ -a_3\tau_{\text{kr}} + x_{\text{kr},3} + (b_3 - a_3b_0)\omega_{\text{arm}} \\ -a_4\tau_{\text{kr}} + x_{\text{kr},4} + (b_4 - a_4b_0)\omega_{\text{arm}} \\ -a_5\tau_{\text{kr}} + (b_5 - a_5b_0)\omega_{\text{arm}} \end{pmatrix} \quad (2.37)$$

Note that the system Eq. (2.37) is linear and may be written in standard matrix form.

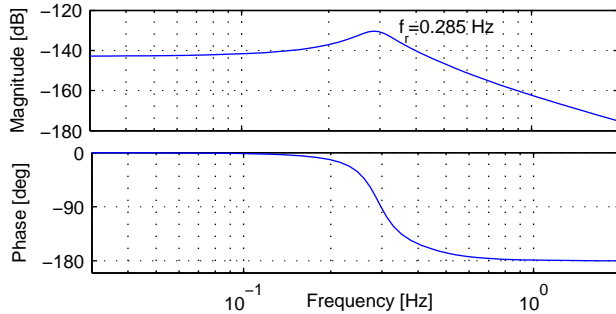


Figure 2.19: Bode diagram of Eq. (2.35), $\theta_{\text{arm}}(s)/\tau_{\text{ext}}(s)$.

Table 2.2: Parameter values for the Wavestar Prototype.

Hydrodynamic model parameters:			
Inertia of arm and float (w. ballast water)	J_{mech}	$2.45 \cdot 10^6$	[kgm ²]
Hydrostatic restoring torque coefficient	k_{res}	$14.0 \cdot 10^6$	[Nm/rad]
Added-inertia $J_{\text{add}}(\omega)$ for $\omega \rightarrow \infty$	$J_{\text{add},\infty}$	$1.32 \cdot 10^6$	[kgm ²]
Transfer-function coefficients for $K_r(s)$:			
$(b_0, b_1, \dots, b_5) = (0.0001, 0.0144, 0.624, 8.16, 13.1, 1.44) \cdot 10^6$			
$(a_0, a_1, \dots, a_5) = (0.0010, 0.0906, 1.67, 6.31, 13.3, 9.18)$			

2.4 Multi Absorber Model

For performing complete PTO simulation for a C5 with 20 absorbers a multi-absorber model is required, capturing the “shadowing” effect of having many absorber on a row, and how the individual absorbers moves due to their distributed locations.

In an array of absorbers as the Wavestar, the absorbers interact through both wave radiation and diffraction. The diffraction part may be obtained by placing 20 floats in a given array, and then determine a force filter h_{ext} for each float:

$$\boldsymbol{\tau}_{\text{ext}} = \int_{-\infty}^{\infty} \mathbf{h}_{\text{ext}}(t - \tau) \boldsymbol{\eta}_w(\tau) d\tau \quad (2.38)$$

$$\boldsymbol{\tau}_{\text{ext}} = [\tau_{\text{ext},1} \cdots \tau_{\text{ext},20}]^T, \quad \mathbf{h}_{\text{ext}}(t) = [h_{\text{ext},1}(t) \cdots h_{\text{ext},20}(t)]^T \quad (2.39)$$

Considering the radiation effect, the equation of motion for each float, before given as Eq. (2.29), now becomes coupled,

$$\dot{\boldsymbol{\theta}}_{\text{arm}} = \boldsymbol{\omega}_{\text{arm}} \quad (2.40)$$

$$\dot{\boldsymbol{\omega}}_{\text{arm}} = \frac{1}{J_{\text{mech}} + J_{\text{add},\infty}} \left(-\mathbf{K}_{\text{res}} \boldsymbol{\theta}_{\text{arm}} - \int_0^t \mathbf{K}_r(t - \tau) \boldsymbol{\omega}_{\text{arm}}(\tau) d\tau - \boldsymbol{\tau}_{\text{PTO}} + \boldsymbol{\tau}_{\text{ext}} \right) \quad (2.41)$$

as the matrix $\mathbf{K}_r(t)$ containing the radiation impulse responses is non-diagonal:

$$\boldsymbol{\omega}_{\text{arm}} = \begin{bmatrix} \omega_{\text{arm},1} \\ \omega_{\text{arm},2} \\ \vdots \\ \omega_{\text{arm},20} \end{bmatrix}, \quad \mathbf{K}_{\text{res}} = \begin{bmatrix} k_{\text{res}} & & & 0 \\ & k_{\text{res}} & & \\ & & \ddots & \\ 0 & & & k_{\text{res}} \end{bmatrix}, \quad \boldsymbol{\tau}_{\text{PTO}} = \begin{bmatrix} \tau_{\text{PTO},1} \\ \tau_{\text{PTO},2} \\ \vdots \\ \tau_{\text{PTO},20} \end{bmatrix} \quad (2.42)$$

$$\mathbf{K}_r(t) = \begin{bmatrix} k_{r,1,1}(t) & k_{r,1,2}(t) & \cdots & k_{r,1,20}(t) \\ k_{r,2,1}(t) & k_{r,2,2}(t) & \cdots & k_{r,2,20}(t) \\ \vdots & & \ddots & \vdots \\ k_{r,20,1}(t) & k_{r,20,2}(t) & \cdots & k_{r,20,20}(t) \end{bmatrix} \quad (2.43)$$

E.g. the impulse response $k_{r,2,20}(t)$ describes the cross-coupling from the velocity of float number 20 to float number 2.

With the focus of this dissertation on designing the PTO, the radiation cross terms are neglected in the 20-float model, i.e. $k_{r\ x,y} = 0$ for $(x \neq y)$. Inclusion of the cross terms mostly affects how the absorbers should be coordinated controlled to further increase power absorption, i.e. controlling and utilising the resulting radiation field from 20 absorbers. How the floats loads the PTO is sufficiently obtained using the single absorber dynamics. However, it is still required to have the effect of the wave propagation, such that the floats operate out of phase due to their distributed locations. This is obtained by still applying the separate force filters.

2.4.1 Multi Absorber Model Parameters for C5

The force filters obtained by applying WAMIT are shown in Fig. 2.20. The filters show that for $\theta_w = 0^\circ$ the wave reaches the floats farthest back (number 10 and 20) approximately 7s later after exciting float number 1. The shadowing effect may be seen from the decreasing magnitude of the wave excitation filters from front to rear absorbers. For the $\theta_w = 0^\circ$ the input for the float are pair-wise equal, whereas this is not true for the wave angle $\theta_w = -45^\circ$.

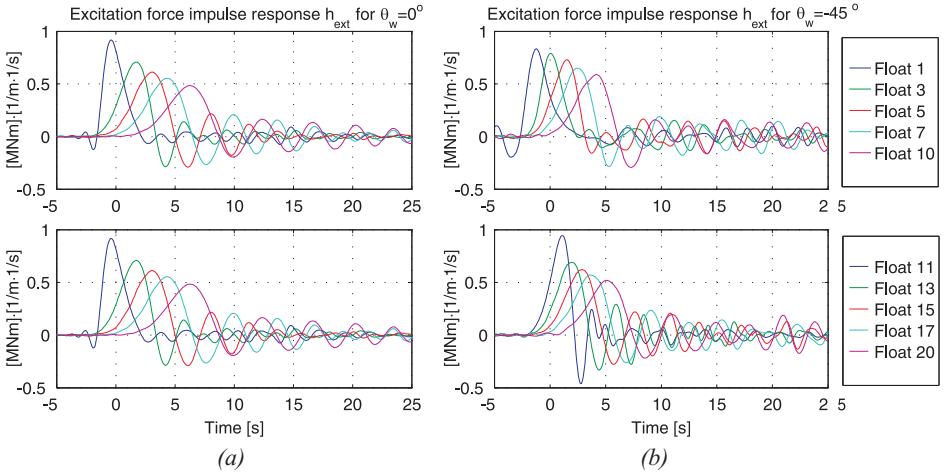


Figure 2.20: In (a) the wave excitation force filter impulse responses h_{ext} for different floats. The first column is for wave directions $\eta_w = 0^\circ$ and the second column is for wave directions $\eta_w = -45^\circ$. In (b) the wave “measurement” point, float numbering definition and definition of wave angle θ_w .

From WAMIT all the impulse-response functions $k_{r\ x,y}(t)$ describing the radiation-force are also obtained, including the cross terms $(x \neq y)$. However, these are neglected, and the single absorber radiation impulse response is used instead.

2.4.2 Multi Absorber Model Validation

The 20 absorber model has been implemented and simulated in irregular waves. To show the shadowing effect, a reactive control law $\tau_{PTO} = k_{PTO}\theta_{arm} + \omega_{arm}B_{PTO}$ optimised for

80% PTO efficiency (Sec. 4.2.1) is applied to each absorber with a torque saturation $\tau_{\text{PTO,max}} = 1 \text{ MNm}$. The results for three wave directions θ_w are shown in Fig. 2.22, where Fig. 2.4a may be conferred for float numbering. Both at $\theta_w = 0$ and $\theta_w = -45^\circ$ the absorbers operate out of phase, smoothing the total power. Taken to the extreme of -90° , the two rows of absorbers operate pair wise with a low amount of smoothing. However, this is an extreme case, and real waves would always have a directional spread, reducing the shown effect. Note that float 11-20 performs better due to the wave approaching the absorber from behind, c.f. Fig. 2.15.

The average produced power of the absorbers for the shown cases is seen in Fig. 2.21. For $\theta_w = 0^\circ$, approximately a 3% less power production is experienced for each subsequent absorber, except for the last absorber, where a 20% greater reduction is experienced. The other directions are also shown. Note that the results are for individual control of absorbers, and not for coordinated array control.

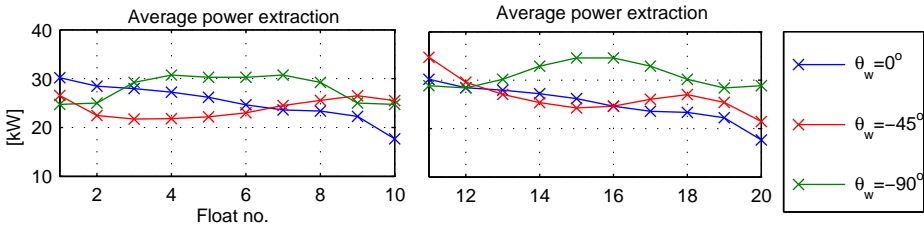


Figure 2.21: Average power extraction of absorbers \bar{P}_{ext} 1-20 for $H_{m0} = 1.75$, $T_{0,2} = 4.5 \text{ s}$. Confer Fig. 2.4a for float numbering.

2.5 Model Verification by 1:20 Scale Tank Tests

To verify the absorber model scaled tests were carried out in a wave-tank. The tests were carried out in the period 26th-28th November as a part of PhD-course participation, “Advanced Control Theory for Wave Energy Utilization” held at the Department of Civil Engineering, Aalborg University. Some of the verification is also documented in paper [J].

The test system corresponds to a 1:20 scale C5 Wavestar absorber as seen in Fig. 2.23. The test system includes a PTO capable of force control, a PTO force sensor and a position sensor.

An overview of the wave-tank is given in Fig. 2.23, which is based on [43]. To relate the model scale to the C5, model laws exist, which are briefly introduced in the following section.

2.5.1 WEC Scaling Law

Scaling laws for model tests are used to describe how forces and movement of a model relate to a full-scaled system. When scaling a system for model testing, the three

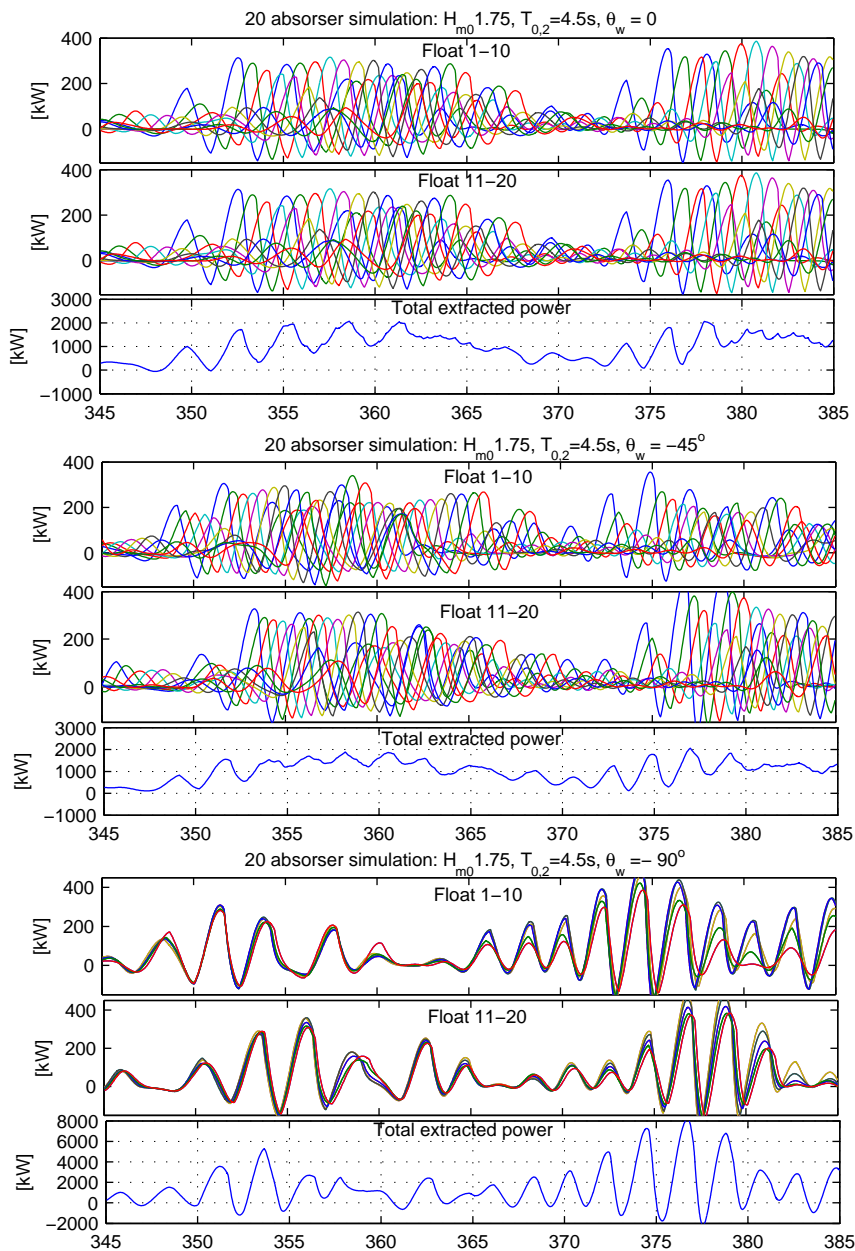


Figure 2.22: Simulation of 20 absorber model for three different wave directions.

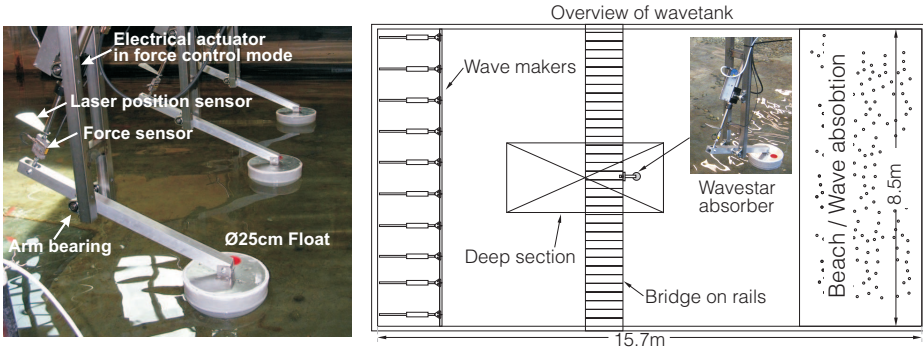


Figure 2.23: A 1:20 scale absorber and the used wave-tank at the Department of Civil Engineering, Aalborg University.

following properties should be met between original and scaled system [44]:

Geometric similarity: All lengths scale with the same factor.

Kinematic similarity: All velocity vectors maintain direction and scale with same factor.

Dynamic similarity: All forces maintain direction and scale with the same factor.

However, with the above requirement, one cannot ensure that the ratio of all forces types (gravity, inertia, viscous, pressure forces, etc.) remain the same for the scaled system. As ocean surface waves are gravity driven, having a fixed ratio between gravity and inertia forces is used for WECs. This type of similarity is the Froude model law. How to scale a WEC system with λ according to Froude's model law is summarised in Tab. 2.3. For determining basic hydrodynamic behaviour the law is adequate [1].

The model scale in the wave tank test is $\lambda = 1/20$ (relative to the C5).

Parameter	Scale	Unit	Parameter	Scale	Unit
Length	$1 : \lambda$	[m]	Force	$1 : \lambda^3$	[N]
Time	$1 : \sqrt{\lambda}$	[s]	Torque	$1 : \lambda^4$	[Nm]
Mass	$1 : \lambda^3$	[kg]	Power	$1 : \lambda^{3.5}$	[W]

Table 2.3: Scaling of parameters using Froudes Model Law. [44]

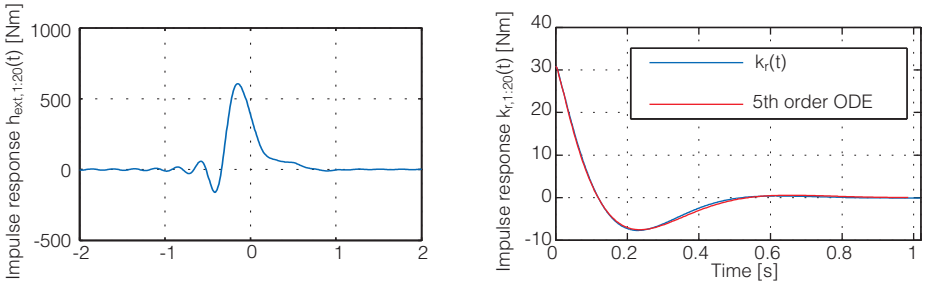
2.5.2 Scale Model

The hydrodynamics parameters have been obtained by applying WAMIT to the scaled float. The parameters of the scaled float are summarised in Tab. 2.4.

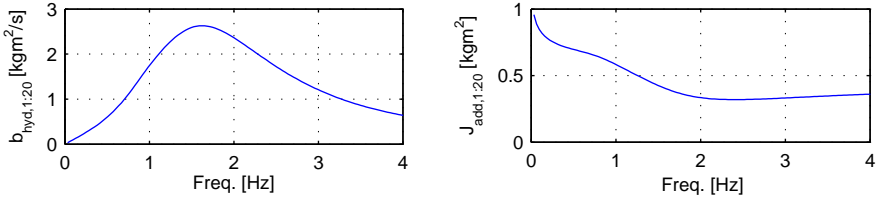
The force filter is seen to the left in Fig. 2.24 and the radiation impulse $k_{r,1:20}$ is seen in the right. Again a 5th order model has been fitted to approximate the convolution. The coefficients are given in Tab. 2.4.

Table 2.4: Parameter values for the Wavestar Prototype.

Hydrodynamic model parameters of 1:20 absorber			
Inertia of arm and float (w. ballast water)	$J_{\text{mech},1:20}$	0.95	[kgm ²]
Hydrostatic restoring torque coefficient	$k_{\text{res},1:20}$	87	[Nm/rad]
Added-inertia $J_{\text{add},1:20}(\omega)$ for $\omega \rightarrow \infty$	$J_{\text{add},1:20,\infty}$	0.41	[kgm ²]
Transfer-function coefficients for $K_{r,1:20}(s)$:			
$(b_0, b_1, \dots, b_5) = (0.03087 \ 37.6 \ 9457 \ 3e6 \ 3.006e8 \ 6.058e7)$			
$(a_0, a_1, \dots, a_5) = (1218.2 \ 8.907e4 \ 1.004e7 \ 1.201e8 \ 8.486e8)$			

**Figure 2.24:** Exciting torque filter and radiate impulse response for a 1:20 scale float.

The added mass and hydrodynamic damping is shown in Fig. 2.25.

**Figure 2.25:** Hydrodynamic damping and added mass for a 1:20 absorber.

The implemented model is shown in Fig. 2.26. The input to the model is the wave elevation at the float centre. The moment arm map is to relate the force of the linear actuator to the applied PTO torque.

2.5.3 Test Results

To verify the model the wave tank is configured to repeat a 20.48s second long irregular wave sequence. First the wave is measured at the float's position with the float lifted out of the water. This is performed to measure the incident wave, which is the input to the model. The incident wave is the undisturbed wave.

The used irregular wave is based on the PM-spectrum and has a significant wave height

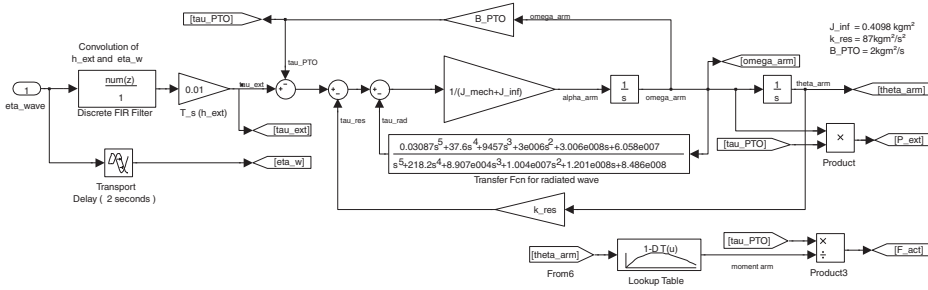


Figure 2.26: Scaled model in SIMULINK .

of $H_{m0} = 0.07$ m and $T_p = 1.5$ s. Using the scaling law, this would correspond to a sea state of:

$$H_{m0} = H_{m0,1:20} \lambda = 1.4 \text{ m} , \quad T_p = T_{p,1:20} \sqrt{\lambda} = 6.7 \text{ s} \quad (2.44)$$

The measured incident wave is shown in top of Fig. 2.27, and is used as input to the simulation model.

For the test, the PTO of the scale model is controlled to apply a damping torque $\tau_{PTO} = B_{PTO}\omega_{arm}$ where $B_{PTO} = 4\text{kgm}^2/\text{s}$. Comparison of tested and simulated behaviour is seen Fig. 2.27, where both simulation and model have been operated for some time to remove possible initial transients. The agreement between model and measurement is very good for all signals. This validates the modelling approach of the Wavestar absorber.

Considering the excitation torque alone, experiments have performed with the same set-up with the float arm fixed in [45]. The results from [45] are shown for two sea states in [45]. As seen even for larger waves $H_{m0,1:20} = 0.242$ m, which corresponds to a $H_{m0} = 4.84$ m for the C5, good agreement is found between measurements and model.

2.6 Summary

The Wavestar C5 comprise 20 identical absorbers, which are modelled as a single-DoF systems described by the rotation about the arm pivot, θ_{arm} . Based on linear wave theory, the dynamics of a single isolated absorber is first described, ending up with a 7th order system as shown in Fig. 2.29. The model basically consists of a second-order spring-damper system with a 5th order damping term $K_r(s)$. For regular waves, the damping term may be represented by a 0-order system, i.e. $K_r(s)$ is replaced with the damping coefficient B_{hyd} .

The excitation torque τ_{ext} caused by the incident wave is found by convoluting η_w with the non-causal impulse function h_{ext} of the excitation force filter, which is implemented as a discrete FIR filter. As the excitation torque is independent of the absorber motion,

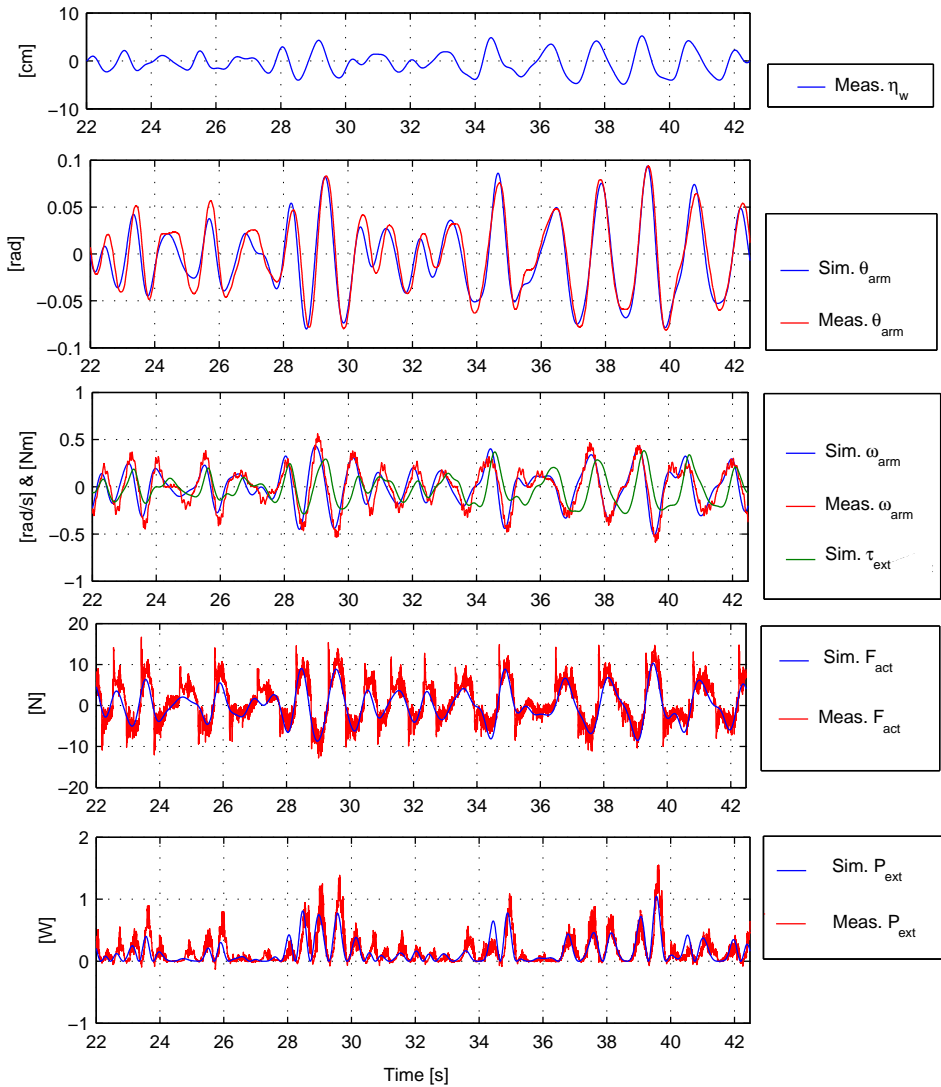


Figure 2.27: Comparison of measured and simulated trajectories. The measured wave (incident wave) is used as input to the model.

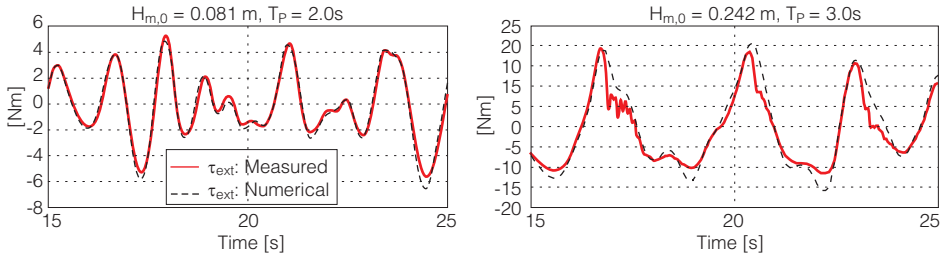


Figure 2.28: Comparison of measured and simulated excitation torque for a absorber held fixed. [45]

this may be pre-computed which solves the non-causality problem. Different force filters are used for different wave directions. The force filters and model parameters are obtained through WAMIT, and the model in Fig. 2.29 was verified through wave tank tests.

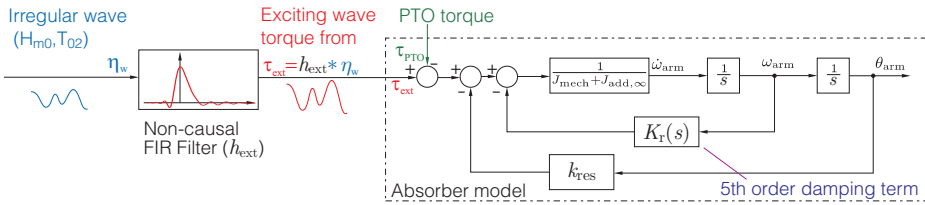


Figure 2.29: Single absorber model.

The model in Fig. 2.29 was expanded to a pseudo-multi-absorber model, where the single absorber model is used, but the computed force filters for 20 absorbers in an array are used instead, which takes into account the complex diffraction pattern. The cross-radiation terms are neglected, but the model is assessed to be sufficient for PTO simulations, as the shadowing and diffraction effect is present and the important effect of the wave propagation is still present, which describes how the floats operate out of phase due to their distributed locations.

To model the waves, the Pierson-Moskowitz spectrum is used, where a time-series realisations complying with the spectrum is obtained based on filtering white-noise with an impulse function obtained from the spectrum. This white noise method is used to reproduce the groupiness of waves which is required for adequate testing of the PTO performance.

Implementation of Reactive Control

To extract energy from waves using an absorber a PTO system applies a torque τ_{PTO} , causing the absorber to produce work on the PTO, which is converted in to electricity. However, the amount of energy produced is very dependent on correct control of the applied PTO torque.

Different strategies exist for implementing the control, where it can be shown that in the optimal case (complex-conjugated control), both a four-quadrant PTO is required and future wave information should be available. The four-quadrant behaviour is required, as the PTO in the ideal case periodically assists the absorber motion to provoke resonant behaviour. Popular said, the PTO invests energy to get energy back with interest. Control where energy is occasionally supplied to the absorber from the PTO is referred to as reactive control. Due to the requirement of future wave, the optimal is non-causal and therefore not practical implementable in its raw form.

The available theory on reactive control does not sufficiently cover how the reactive control should be optimised if the PTO has losses. Resultantly, it has not been possible to find whether reactive control is practical useful for real PTOs, or at which PTO efficiencies the control becomes useful. This is the main focus of this chapter, along with finding a practical implementation of reactive control.

Accordingly, first the well-established optimal control is introduced. Afterwards, different implementations are discussed on how the control could be made causal. This includes discussing the robustness of the strategies. Finally, an analytical result is given on how the PTO efficiency affects the reactive control and to design it accordingly. The result shows that even for an 80% efficient PTO, the reactive control may produce more than two-fold in a regular wave compared to linear damping.

To verify the reactive control, the chapter is concluded with tank tests, comparing simulated and measured behaviour.

The used idea of efficiency inclusion in the reactive control is first disclosed in paper [O], and further treated in papers [L] and [B].

3.1 Introduction to Wave Power Extraction

The amount of energy absorbed by a point absorber is highly dependent on the load force or torque applied by the PTO. Frequency-wise, point absorbers are characterised by being narrow-banded with an under-damped resonance frequency. This gives a poor

basis for energy absorption, as the energy in sea wave is broad-banded, having both a varying and wide frequency band.

In Fig. 3.1 the absorber's velocity response and the energy distribution of a typical sea state are plotted together, exposing how the absorber's velocity response is poorly matched to the energy distribution. As the extracted instantaneous power P_{ext} is the PTO torque τ_{PTO} times the arm velocity ω_{arm} ,

$$P_{\text{ext}}(t) = \tau_{\text{PTO}}(t)\omega_{\text{arm}}(t) \quad [\text{W}] \quad (3.1)$$

poor velocity response equals poor power extraction. Hence, due to the narrow frequency response, point absorbers are prone to operate non-optimal.

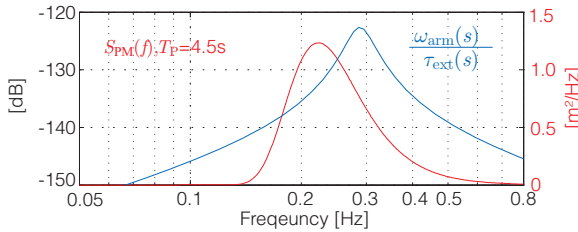


Figure 3.1: Comparison of typical wave spectrum and the frequency response of the Wavestar absorber ($\tau_{\text{PTO}}=0$).

To compensate for the inherit off-resonance behaviour, the resonance frequency could be made adjustable. This is often not feasible by mechanical means. Looking at the C5 absorber, the natural frequency ω_{C5} is approximately given as,

$$\omega_{\text{C5}} \approx \sqrt{\frac{k_{\text{res}}}{J_{\text{add},\infty} + J_{\text{mech}}}} = 1.78 \frac{\text{rad}}{\text{s}} \quad (3.2)$$

corresponding to a natural period of 3.5s. If variation of the natural period was to be implemented by mechanical variation of mass moment of inertia, increasing the natural period from 3.5s to 4.5s would require adding $2.4\text{e}6 \text{kgm}^2$ of inertia to the system. This corresponds to same amount provided by the current arm and float, including ballast water (a total of 35000kg). Thus, the required adjustable mass size is enormous, and moreover, the inertia should ideally be varied without changing the draft of the absorber.

Another method to compensate for the inherit off-resonance behaviour is to use the PTO to modify the external experienced response of the absorber. For example, the PTO may be controlled to emulate the effect of inertia or spring. These different approaches for controlling the PTO to improve the frequency response are in this work referred to as Wave Power Extraction Algorithms (WPEA), and may generally be formulated as a feedback law Ψ of the form,

$$\tau_{\text{PTO,ref}}(t) = \Psi\left(\ddot{\theta}_{\text{arm}}(t), \dot{\theta}_{\text{arm}}(t), \theta_{\text{arm}}(t), \eta_w(t + t_{\text{future}})\right) \quad [\text{Nm}] \quad (3.3)$$

where t_{future} indicates that future knowledge of the wave η_w may be required, i.e. non-causal control laws.

The feedback law is illustrated in Fig. 3.2. The feedback enables the PTO to adjust the absorber's frequency response to maximise the average extracted power \bar{P}_{ext} :

$$\bar{P}_{\text{ext}} = \frac{1}{t} \int_0^t P_{\text{ext}}(t) dt \quad [\text{W}] \quad (3.4)$$

Optimal power extraction is achieved when the WPEA ensures that the velocity of the absorber is in phase with the excitation force and the PTO damping matches the absorber's hydrodynamic damping [28]. For a regular wave, this may be viewed as the PTO adjusting the absorber's natural frequency to match the wave frequency. In electrical circuit analogy it corresponds to maximal power transfer by matching the load impedance to the internal impedance of a voltage source. In the simple case, the load resistance should equal to the source resistance.

However, performing the optimal control in irregular waves, which is a stochastic input, requires accurate knowledge or prediction of the incident wave η_w for some time t_{future} , where the horizon is similar to the time for the transients to die out for an impulse response of the absorber. Thus, the optimal control is non-causal [28].

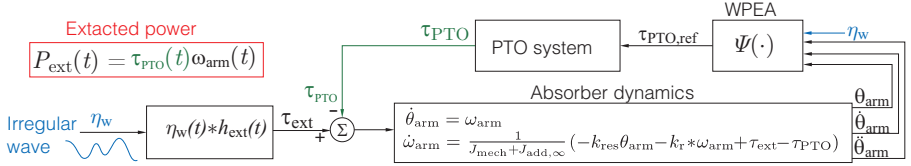


Figure 3.2: Definition of WPEA.

Using the PTO to emulate inertia or a spring element results in the PTO transferring energy to the absorber in parts of an oscillation cycle. WPEAs requiring supplying energy to the absorber are referred to as *reactive strategies*. Reactive strategies require a PTO capable of four-quadrant behaviour and a PTO scaled to process the additional reactive power as well. The WPEAs not requiring bi-directional power transfer is referred to as *resistive strategies*.

3.2 Optimal Control of Absorbers

Optimum control of absorbers with linear methods has been well treated in literature, most notably by Falnes in [32, 28, 46]. Some of the theory is presented in this work to provide the background for discussing practical implementations of reactive control.

Generally, linear WPEAs may be written as a linear feedback-law $\Psi(\cdot)$ of the absorber motion,

$$\tau_{\text{PTO,ref}}(t) = \Psi(\cdot) = h_c(t) * \omega_{\text{arm}}(t) \Leftrightarrow \tau_{\text{PTO,ref}}(s) = Z_c(s)\omega_{\text{arm}}(s) \quad (3.5)$$

where $h_c(t)$ is an impulse function describing the control law $\Psi(\cdot)$, and $Z_c(s)$ is the transfer function corresponding to the impulse function $h_c(t)$. In the following the PTO

dynamics is omitted, corresponding to assuming sufficient tracking performance of the PTO such that $\tau_{\text{PTO}} = \tau_{\text{PTO,ref}}$.

The transfer function for the absorber motion given in Eq. (2.35) may be re-formulated with angular velocity ω_{arm} as input:

$$\frac{\omega_{\text{arm}}(s)}{\tau_{\text{ext}}(s) - \tau_{\text{PTO}}(s)} = \frac{1}{(J_{\text{mech}} + J_{\text{add},\infty})s + K_{\text{r}}(s) + \frac{1}{s}k_{\text{res}}} \quad (3.6)$$

By defining the absorber impedance $Z_{\text{i}} = (J_{\text{mech}} + J_{\text{add},\infty})s + K_{\text{r}}(s) + \frac{1}{s}k_{\text{res}}$, and inserting the control law Eq. (3.5), the following transfer function is obtained for the absorber:

$$H_{\Lambda}(s) = \frac{\omega_{\text{arm}}(s)}{\tau_{\text{ext}}(s)} = \frac{1}{Z_{\text{i}}(s) + Z_{\text{c}}(s)} \quad (3.7)$$

The transfer function H_{Λ} describes the closed-loop behaviour of absorber velocity with the exciting wave torque as input. The impedance Z_{i} is also referred to as the intrinsic impedance by Falnes. The intrinsic impedance Z_{i} may according to Eq. (2.25) be written as,

$$\begin{aligned} Z_{\text{i}}(j\omega) &= j\omega J_{\text{mech}} + Z_{\text{rad}}(j\omega) - j \frac{k_{\text{res}}}{\omega} \\ &= B_{\text{hyd}}(\omega) + j\omega(J_{\text{mech}} + J_{\text{add}}(\omega)) - j \frac{k_{\text{res}}}{\omega} = R_{\text{i}}(\omega) + jX_{\text{i}}(\omega) \end{aligned} \quad (3.8)$$

where resistance $R_{\text{i}} = B_{\text{hyd}}(\omega)$ and reactance $X_{\text{i}} = (J_{\text{mech}} + J_{\text{add}}(\omega))\omega - \frac{k_{\text{res}}}{\omega}$.

3.2.1 Optimal Power Extraction for Regular Waves

For a regular wave input $\eta_{\text{w}} = A_{\text{w}} \sin(\omega_{\text{w}}t)$, the excitation torque is given as $\tau_{\text{ext}} = |H_{\text{ext}}(j\omega_{\text{w}})|A_{\text{w}} \sin(\omega_{\text{w}}t + \angle H_{\text{ext}}(j\omega_{\text{w}}))$. Defining $A_{\text{ext}} = A_{\text{w}}|H_{\text{ext}}(j\omega_{\text{w}})|$, the average extracted power \bar{P}_{ext} power is according to Tab. 3.1 given as,

$$\bar{P}_{\text{ext}} = \frac{A_{\text{ext}}^2}{2} \frac{\text{Re}\{Z_{\text{c}}(j\omega_{\text{w}})\}}{|Z_{\text{c}}(j\omega_{\text{w}}) + Z_{\text{i}}(j\omega_{\text{w}})|^2} = \frac{A_{\text{ext}}^2}{2} \frac{R_{\text{c}}}{(X_{\text{i}} + X_{\text{c}})^2 + (R_{\text{i}} + R_{\text{c}})^2} \quad [\text{W}] \quad (3.9)$$

where reactance $X_{\text{c}} = \text{Im}\{Z_{\text{c}}(j\omega_{\text{w}})\}$ and resistance $R_{\text{c}} = \text{Re}\{Z_{\text{c}}(j\omega_{\text{w}})\}$.

The expression is equivalent to the optimal power transfer from source to load in an electrical circuit, if Z_{i} is viewed as the internal impedance of a voltage source and Z_{c} the load impedance. This is illustrated in Fig. 3.3 and is the approach practised in e.g. [32]. To maximise \bar{P}_{ext} , the load reactance X_{c} should cancel the source reactance, i.e. $X_{\text{c}} = -X_{\text{i}}$, yielding

$$\bar{P}_{\text{ext}} = \frac{A_{\text{ext}}^2}{2} \frac{R_{\text{c}}}{(R_{\text{i}} + R_{\text{c}})^2} \quad [\text{W}] \quad (3.14)$$

and the load resistance should match the source resistance to maximise Eq. (3.14). Thus, optimal power transfer is obtained from wave to PTO if $Z_{\text{c}} = Z_{\text{i}}^*$, implying that the control cancels the source dynamics. Inserting into Eq. (3.6) yields that,

$$\frac{\omega_{\text{arm}}(\omega)}{\tau_{\text{ext}}(\omega)} = \frac{1}{2B_{\text{hyd}}} \quad (3.15)$$

Table 3.1: Optimal power extraction in regular waves

Assume the PTO torque is a linear feedback of the absorber velocity:

$$\tau_{\text{PTO}}(s) = Z_c(s)\omega_{\text{arm}}(s) \quad (3.10)$$

For a regular wave input $\eta_w = A_w \sin(\omega_w t)$, the excitation torque is given as $\tau_{\text{ext}} = |H_{\text{ext}}(j\omega_w)|A_w \sin(\omega_w t + \angle H_{\text{ext}}(j\omega_w))$. As the system is linear, the velocity of the absorber output will also be a harmonic oscillation with the same frequency as the input amplified with $|H_A(j\omega)|$ and phase-shifted with $\angle H_A(j\omega)$:

$$\begin{aligned} \omega_{\text{arm}}(t) &= A_{\text{ext}}|H_A(j\omega)| \sin(\omega t + \angle H_A(j\omega) + \angle H_{\text{ext}}(j\omega)) \\ \tau_{\text{PTO}}(t) &= A_{\text{ext}}|H_A(j\omega)||Z_c(j\omega)(j\omega)| \sin(\omega t + \angle H_A(j\omega) + \angle H_{\text{ext}}(j\omega_w) + \angle Z_c(j\omega)) \end{aligned}$$

where $A_{\text{ext}} = A_w |H_{\text{ext}}(j\omega_w)|$. The instantaneous power $P_{\text{ext}}(t)$ is given as:

$$\begin{aligned} P_{\text{ext}}(t) &= \omega_{\text{arm}}(t)\tau_{\text{PTO}}(t) = A_{\text{ext}}^2 |H_A(j\omega)|^2 |Z_c(j\omega)(j\omega)| \cdot \\ &\quad \sin(\omega t + \angle H_A(j\omega)) \sin(\omega t + \angle H_A(j\omega) + \angle H_{\text{ext}}(j\omega_w) + \angle Z_c(j\omega)) \end{aligned}$$

To calculate the average power only the relative phase shift of the two sine waves is required, thus $\angle H_A(j\omega)$ and $\angle H_{\text{ext}}(j\omega_w)$ may be omitted,

$$\begin{aligned} P_{\text{ext}}(t) &= A_{\text{ext}}^2 |H_A(j\omega)|^2 |Z_c(j\omega)(j\omega)| \sin(\omega t) \sin(\omega t + \angle Z_c(j\omega)(j\omega)) \\ &= A_{\text{ext}}^2 |H_A(j\omega)|^2 |Z_c(j\omega)(j\omega)| \frac{\cos \phi - \cos(2\omega t + \phi)}{2} \end{aligned} \quad (3.11)$$

where $\phi = \angle C(j\omega)$ and the following trigonometric relation have been used:

$$\sin(\omega t) \sin(\omega t + \phi) = \frac{\cos \phi - \cos(2\omega t + \phi)}{2} \quad (3.12)$$

The period of the instantaneous power is given as π/ω_w (half the period of the wave), thus the average power \bar{P}_{ext} is given as:

$$\begin{aligned} \bar{P}_{\text{ext}} &= \frac{\omega}{\pi} \int_{t=0}^{t=\frac{\pi}{\omega}} P_{\text{ext}}(t) dt \\ &= \frac{1}{2} A_{\text{ext}}^2 |H_A(j\omega)|^2 |Z_c(j\omega)| \frac{\omega}{\pi} \underbrace{\int_{t=0}^{t=\frac{\pi}{\omega}} \cos \phi - \cos(2\omega t + \phi) dt}_{= \frac{\pi}{\omega} \cos \phi = \frac{1}{|Z_c(j\omega)|} \text{Re}\{Z_c(j\omega)\}} \\ &= \frac{1}{2} A_{\text{ext}}^2 \frac{\text{Re}\{Z_c(j\omega)\}}{|Z_i(j\omega) + Z_c(j\omega)|^2} = \frac{A_{\text{ext}}^2}{2} \frac{R_c}{(X_i + X_c)^2 + (R_i + R_c)^2} \end{aligned} \quad (3.13)$$

For a four-quadrant PTO, the reactance X_c may be different from zero. To optimise \bar{P}_{ext} with respect to X_c is to minimise the denominator $(X_i + X_c)^2 + (R_i + R_c)^2$, which is obtained for $X_c = -X_i$, corresponding to forcing ω_{arm} and τ_{ext} into phase. Maximising the remainder $R_i/(R_i + R_c)^2$ gives $R_c = R_i$, i.e. matching the resistance or damping coefficient of the source.

If the PTO is resistive, then $X_c = 0$ and the optimal value of R_c is $R_c = \sqrt{R_i^2 + X_i^2}$ which follows from:

$$\frac{\partial \bar{P}_{\text{ext}}}{\partial R_i} \Big|_{X_c=0} = \frac{A_{\text{ext}}}{2} \frac{X_i^2 + (R_i + R_c)^2 - 2R_c(R_c + R_i)}{(X_i^2 + (R_i + R_c)^2)^2} = 0 \Rightarrow R_c^2 = X_i^2 + R_i^2 = |Z_i|^2$$

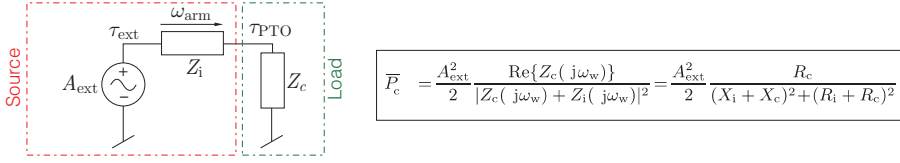


Figure 3.3: Electrical equivalent of linear control of absorber for maximising power transfer.

showing that for the optimum condition, the exciting wave torque is in phase with the absorber velocity, c.f. $\tau_{\text{ext}}(t) = 2B_{\text{hyd}}\omega_{\text{arm}}(t)$.

To implement the control in regular waves the PTO control may be formulated as a linear combination of absorber position, velocity and acceleration,

$$\tau_{\text{PTO}}(t) = k_{\text{PTO}}\theta_{\text{arm}}(t) + B_{\text{PTO}}\dot{\theta}_{\text{arm}}(t) + J_{\text{PTO}}\ddot{\theta}_{\text{arm}}(t) \quad [\text{Nm}] \quad (3.16)$$

⇓

$$Z_c(j\omega) = B_{\text{PTO}} + j \left(-\frac{k_{\text{PTO}}}{\omega} + \omega J_{\text{PTO}} \right) \quad (3.17)$$

The optimal control may be implemented both using position and velocity feedback Eq. (3.19) or acceleration and velocity feedback Eq. (3.18):

$$J_{\text{PTO}} = -(J_{\text{arm}} + J_{\text{add}}) + \frac{k_{\text{res}}}{\omega^2}, \quad k_{\text{PTO}} = 0, \quad B_{\text{PTO}} = B_{\text{hyd}} \quad (3.18)$$

$$k_{\text{PTO}} = (J_{\text{arm}} + J_{\text{add}})\omega^2 - k_{\text{res}}, \quad J_{\text{PTO}} = 0, \quad B_{\text{PTO}} = B_{\text{hyd}} \quad (3.19)$$

The natural frequency of the absorber in regular waves is given as,

$$\omega_N = \sqrt{\frac{k_{\text{res}} + k_{\text{PTO}}}{J_{\text{arm}} + J_{\text{add}} + J_{\text{PTO}}}} \quad \left[\frac{\text{rad}}{\text{s}} \right] \quad (3.20)$$

thus by inserting Eq. (3.18) or Eq. (3.19) it is evident that both implementations move the system's resonance frequency to the wave frequency ω_w .

If the PTO is not allowed to supply power to the absorber, this imposes the constraint that $k_{\text{PTO}} = J_{\text{PTO}} = 0$. As a result, linear damping control remains and the damping coefficient B_{PTO} , maximising Eq. (3.14), is equal to the length of the intrinsic impedance (c.f. Tab. 3.1):

$$B_{\text{PTO}} = |Z_i|, \quad k_{\text{PTO}} = J_{\text{PTO}} = 0 \quad (3.21)$$

In Fig. 3.4 the velocity responses are shown for optimal implementation of Eq. (3.18), Eq. (3.19) and Eq. (3.21) for a regular wave with period $T_w = 4.5\text{s}$. The reactive control laws Eq. (3.18) and Eq. (3.19) move the resonance as desired, and has an amplitude equal to $\frac{1}{2B_{\text{hyd}}(\omega)}$ at the wave frequency. The linear damping control is not able to reach resonance, but instead resort to over-damping to maximise energy extraction.

An important observation is that the spring based reactive control gives a flatter response than the inertia based control, see Fig. 3.4. Hence, for irregular waves, the spring based control will be superior, as it is more responsive off-resonance as well.

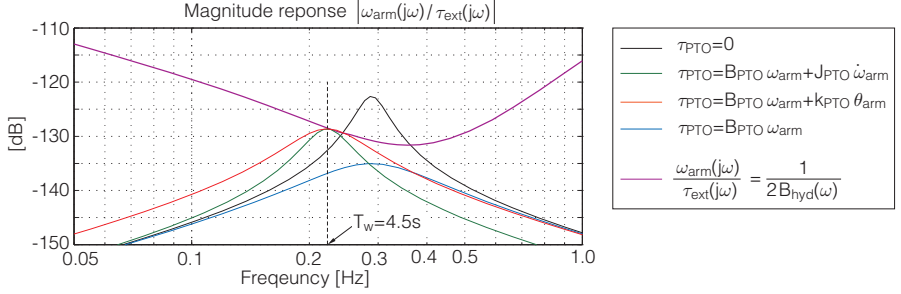


Figure 3.4: Comparison of different implementations of linear control in regular waves.

3.2.2 Optimal Control in Irregular Wave

When moving to irregular waves, the optimal control should still enforce that the exciting wave torque is always in phase with the absorber velocity (the wave always transfers energy to the absorber), and that the PTO damping matches the hydro-dynamic damping. This is achieved if the control law is given by $Z_c(j\omega) = Z_1^*(j\omega)$ as in the regular cases, except that this should be valid for all frequencies instead of just a single frequency. Thus, for irregular waves the optimal control enforces [32],

$$\frac{\omega_{\text{arm}}(\omega)}{\tau_{\text{ext}}(\omega)} = \frac{1}{2B_{\text{hyd}}(\omega)}, \quad \omega \in]-\infty; \infty[\quad (3.22)$$

which infers that the closed-loop response of the absorber has zero-phase, c.f. $\frac{1}{2B_{\text{hyd}}(\omega)}$ is real. Seen externally, this corresponds to that the absorber's dynamics are cancelled and the absorber behave as a pure damper. Performing inverse Fourier transform on Eq. (3.22) yields,

$$\tau_{\text{ext}}(t) = 2h_{\text{B}}(t) * \omega_{\text{arm}}(t) \quad [\text{Nm}] \quad (3.23)$$

where the impulse response $h_{\text{B}}(t)$ corresponding to $B_{\text{hyd}}(\omega)$ is given as:

$$h_{\text{B}}(t) = \mathcal{F}^{-1}\{B_{\text{hyd}}(\omega)\} \quad (3.24)$$

Thus, the optimal control law reduces the dynamics of the system to Eq. (3.23). By inspecting the equation of motion for the absorber below,

$$(J_{\text{arm}} + J_{\text{add},\infty})\ddot{\theta}_{\text{arm}} = \tau_{\text{ext}} - k_{\text{res}}\theta_{\text{arm}} - k_{\text{r}} * \omega_{\text{arm}} - \tau_{\text{PTO}} \quad (3.25)$$

Eq. (3.23) infers that the optimal law, also referred to as complex-conjugate control, is given as,

$$\Psi_{\text{conj}} = -\ddot{\theta}_{\text{arm}}(J_{\text{arm}} + J_{\text{add},\infty})k_{\text{res}}\theta_{\text{arm}} - k_{\text{r}} * \omega_{\text{arm}} + 2h_{\text{B}}(t) * \omega_{\text{arm}} \quad [\text{Nm}] \quad (3.26)$$

as it cancels the dynamics and reduces Eq. (3.25) to Eq. (3.23). However, the last term $2 * h_B(t) \omega_{\text{arm}}$ is non-causal. As $B_{\text{hyd}}(\omega)$ is real, i.e. zero-phase, the corresponding impulse response $h_B(t)$ must be symmetric, and thereby non-zero for positive time, rendering the impulse non-causal. Actually, by using the fact that the impedance of the control Ψ_{conj} should be the complex conjugate of the absorber's intrinsic impedance, the following is obtained,

$$\Psi_{\text{conj}}(\omega) = Z_i^*(j\omega) \omega_{\text{arm}}(\omega) \Rightarrow \Psi_{\text{conj}}(t) = h_i(-t) \omega_{\text{arm}}(t) \quad [\text{Nm}] \quad (3.27)$$

where h_i is the impulse function given as $\mathcal{F}^{-1}\{Z_i(j\omega)\}$.

As the impulse of the intrinsic impedance is causal ($h_i(t) = 0, t < 0$), the above shows that the control is actual anti-causal, and the required future knowledge required is the duration of the absorber response. The anti-causal behaviour could also have been seen from Eq. (3.26) by that the sum $-k_r * \omega_{\text{arm}} + 2h_B(t) * \omega_{\text{arm}}(t)$ may carefully be re-formulated as $k_r(-t) * \omega_{\text{arm}}(t)$

The resulting non-causal property may also be directly seen from Eq. (3.22), as the resulting system has varying gain, but zero phase, which is impossible to implement causally.

Thus, the control law is dependent on future values of ω_{arm} . According to Eq. (3.23), if the control law was indeed implemented, the velocity would be given as:

$$\omega_{\text{arm}}(\omega) = \tau_{\text{ext}}(\omega) \frac{1}{2B_{\text{hyd}}(\omega)} \Rightarrow \omega_{\text{arm}}(t) = \frac{1}{2} \tau_{\text{ext}}(t) * h_{B-1} \quad [\text{rad/s}] \quad (3.28)$$

where the impulse response $h_{B-1} = \mathcal{F}^{-1}\{\frac{1}{B_{\text{hyd}}(\omega)}\}$. Thus, the non-causal Eq. (3.28) may be used to compute the optimum absorber velocity if future values of the wave excitation torque may be predicted. If possible, the optimum control may then be implemented by using the PTO torque to make the absorber track the estimated optimum absorber velocity. This is the suggestion by Faldes in [32].

3.3 Causal Reactive Control in Irregular Waves

To make the control in Eq. (3.26) causal, the non-causal part $2h_B(t) * \omega_{\text{arm}}(t)$ may be replaced with a causal term, e.g. a damping term with fixed coefficient $2B_{\text{PTO}} \omega_{\text{arm}}(t)$, whereby the following control law Ψ_{inv} is obtained:

$$\Psi_{\text{inv}} = -\ddot{\theta}_{\text{arm}}(J_{\text{arm}} + J_{\text{add},\infty}) - k_{\text{res}} \theta_{\text{arm}} - k_r * \omega_{\text{arm}} + 2B_{\text{PTO}} \omega_{\text{arm}}(t) \quad [\text{Nm}] \quad (3.29)$$

The same control is to some degree suggested in [47], but is obtained through the idea of feed-back linearisation. Inserting Eq. (3.29) into the absorber equation of motion Eq. (3.25) yields,

$$2B_{\text{PTO}} \omega_{\text{arm}}(t) = \tau_{\text{ext}} \quad [\text{Nm}] \quad (3.30)$$

showing that the velocity is in phase with the exciting wave torque. This is a sub-optimal control as though the phase is correct, the PTO damping now only matches

the hydro-dynamic damping B_{hyd} at a single frequency instead for the whole frequency range.

Though the control Eq. (3.29) is causal, this “inverse” control is practically unstable, as it cancels all the absorber dynamics by assigning zeros to all system poles. E.g. as the “spring” feedback is cancelled, just a small error in cancelling the hydrostatic torque may make the absorber position unstable. The acceleration feedback to cancel the inertia may also be sensitive. There will be small parameter errors as the system is under modelled, i.e. linear wave theory is used to approximate a non-linear system. Hence, the inverse control will be infeasible in its raw form for practical implementations.

To make the control stable, an approach could be not to cancel the spring and inertia term totally. This may be performed by introducing a factor on either the spring or inertia, determining to what degree the terms are cancelled. Shown for the inertia, the factor is introduced as $\alpha_J \in [0; 1]$, defining a new sub-optimal control given as,

$$\Psi_\alpha = -\ddot{\theta}_{\text{arm}}\alpha_J(J_{\text{arm}} + J_{\text{add},\infty}) + k_{\text{PTO}}\theta_{\text{arm}} - k_r * \omega_{\text{arm}} + 2 * B_{\text{PTO}}\omega_{\text{arm}}(t) \quad (3.31)$$

As the system dynamics is no longer completely cancelled, the PTO spring term k_{PTO} is chosen to yield a desired resonance frequency,

$$\omega_N^2 = \frac{k_{\text{res}} + k_{\text{PTO}}}{J_{\text{arm}} + J_{\text{add}} + J_{\text{PTO}}} \Rightarrow k_{\text{PTO}} = (1 - \alpha_J)(J_{\text{arm}} + J_{\text{add},\infty})\omega_N^2 - k_{\text{res}} \quad (3.32)$$

to move the remaining peak of the flatten frequency response to the main energy content of the wave.

A root-locus of the system as α_J is varied from 0 to 1 is given in Fig. 3.5. The left plot shows the poles of the radiation dynamics K_r , and how they are always cancelled by zeros of the control law. The right figure shows the locus of the two remaining system poles. The natural frequency is constant for all complex pole pairs, however, as $\alpha_J \rightarrow 1$, the resonance peak is reduced and the response will become more flat as the poles approach the real axis. Finally, one pole vanishes in the zero at the origin and the other goes to infinity. This corresponds to the inverse control in Eq. (3.29), where the system reduces to operating as a pure damper, and seen from the position θ_{arm} , a pure integrator, which means it is marginally stable. Note that a small error in the parameters will make e.g. the pole approaching the origin cross into the right half plane, rendering the system unstable. Thus, the root-locus shows the increased robustness gained by choosing $\alpha_J < 1$ at the cost of a less flat frequency response.

If acceleration feedback is unavailable, $\alpha_J = 0$, the control reduces to,

$$\Psi_\alpha \Big|_{\alpha_J=0} = k_{\text{PTO}}\theta_{\text{arm}} - k_r * \omega_{\text{arm}} + 2B_{\text{PTO}}\omega_{\text{arm}} \quad [\text{Nm}] \quad (3.33)$$

where the radiation term is still cancelled. Finally, the simplest spring based reactive control may be obtained, which is given as,

$$\Psi_k = k_{\text{PTO}}\theta_{\text{arm}} + B_{\text{PTO}}\omega_{\text{arm}} \quad [\text{Nm}] \quad (3.34)$$

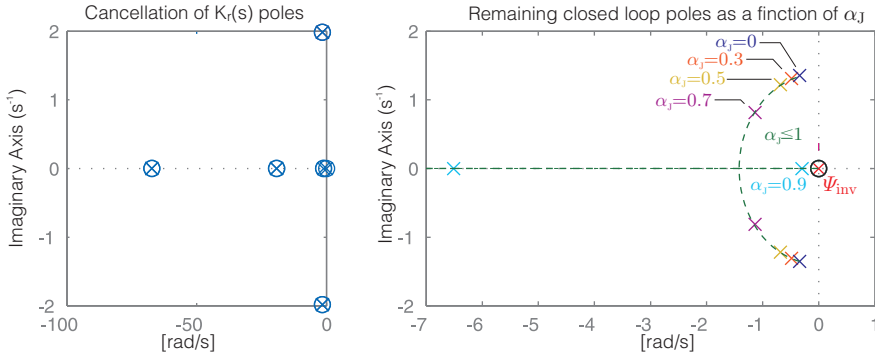


Figure 3.5: Root locus for WPEAs Ψ_α and Ψ_{inv} .

where, the radiation term is not cancelled, but a fixed PTO damping is applied. If the PTO is unable to supply reactive power, the control reduces to the familiar liner damping:

$$\Psi_B = B_{PTO}\omega_{arm} \quad [\text{Nm}] \quad (3.35)$$

Comparison of the presented linear WPEAs is given in Fig. 3.6, showing the resulting magnitude and phase plot of the absorber. All the WEPA algorithms are tuned for a sea state of $T_p = 4.5$ s. The shown responses are from excitation torque to absorber velocity. The non-causal complex conjugated control Ψ_{conj} results in zero-phase and a magnitude response varying according to $\frac{1}{2B_{hyd}(\omega)}$. Resultantly, the exciting wave torque is in phase with the velocity for all frequencies and the PTO damping is equal to the hydrodynamic damping for all frequencies.

The causal implementation (inverse control) Ψ_{inv} gives the desired zero-phase response, but only yields a constant gain, which is only optimal at a single frequency. The stable implementations of the inverse control, Ψ_α has a resonance peak, which gets more pronounced as $\alpha_J \rightarrow 0$. However, looking at a stable implementation with e.g. $\alpha_J = 0.7$, the response is still reasonable flat around the energy content of the wave spectrum. Neglecting PTO constraints, $\alpha_J = 0.7$ will properly be the best implementation of a causal linear reactive control in practice if a low noise acceleration feed-back is available. Formulating a non-linear version of the hydro-static restoring torque may also improve the performance.

3.4 Including PTO Efficiency in Reactive Control Design

Tuning of the reactive control is very dependent on the PTO's power conversion efficiency η_{PTO} . To treat this aspect, the reactive control is first treated for regular waves. The analytical result may be then used for an initial guess of control parameters when optimising in irregular waves in the next chapter.

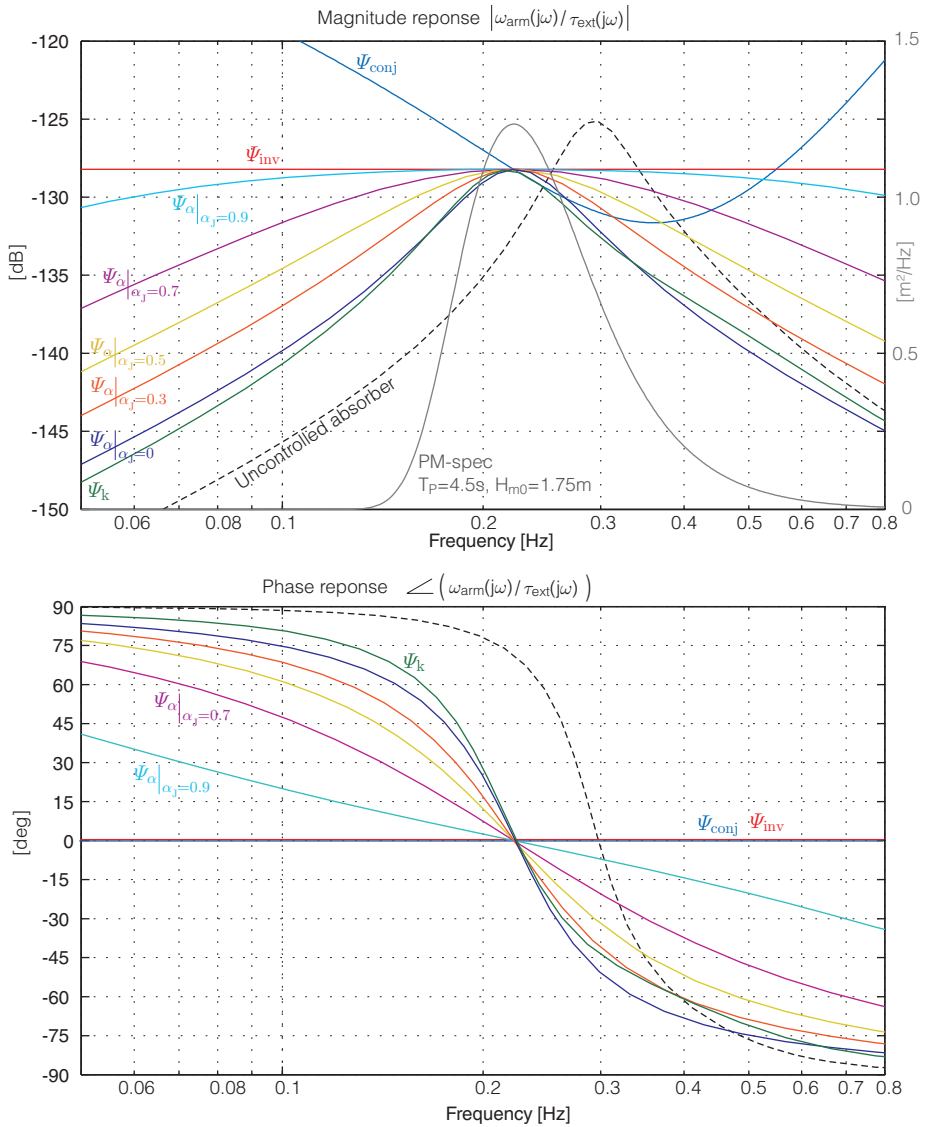


Figure 3.6: Bode-plots of Ψ_{inv} , Ψ_{α} and Ψ_k .

To include the PTO efficiency in the control, the essential idea found in this work is to define the following non-linear map, connecting the instantaneous power $P_{\text{ext}}(t)$ to the instantaneous power output $P_{\text{out}}(t)$ of the PTO,

$$P_{\text{out}}(t) = \begin{cases} P_{\text{ext}}(t) \eta_{\text{PTO}} & ; P_{\text{ext}}(t) > 0 \\ P_{\text{ext}}(t) \frac{1}{\eta_{\text{PTO}}} & ; P_{\text{ext}}(t) \leq 0 \end{cases} \quad [\text{W}] \quad (3.36)$$

where η_{PTO} is the power conversion efficiency of the PTO. The idea is first disclosed in [O]. This nice property of the map is that it does not affect the formulation of the control or dynamic equations, but only re-defines the cost function, which they should be optimised according to. The map up-scales negative power flow and reduces positive power flow according to efficiency as illustrated in Fig. 3.7a.

For regular waves with frequency ω_w , the absorber velocity may according to Eq. (3.7) be described as

$$H_A(s) = \frac{\omega_{\text{arm}}(s)}{\tau_{\text{ext}}(s)} = \frac{1}{Z_i(s) + Z_c(s)} \quad (3.37)$$

where it has been used that $\tau_{\text{PTO}}(s) = Z_c(s)\omega_{\text{arm}}(s)$. The excitation torque is described as:

$$\tau_{\text{ext}} = A_{\text{ext}} \sin(\omega t) \quad (3.38)$$

As the system is linear and the input is a harmonic oscillation, the velocity of the absorber output will also be a harmonic oscillation with the same frequency as the input, amplified with $|H_A(j\omega)|$ and phase-shifted with $\angle H_A(j\omega)$:

$$\omega_{\text{arm}}(t) = A_{\text{ext}} |H_A(j\omega)| \sin(\omega t + \angle H_A(j\omega)) \quad (3.39)$$

$$\tau_{\text{PTO}}(t) = A_{\text{ext}} |H_A(j\omega)| |Z_c(j\omega)| \sin(\omega t + \angle H_A(j\omega) + \angle Z_c(j\omega)) \quad (3.40)$$

The instantaneous power $P_{\text{ext}}(t)$ between PTO and absorber is then given as:

$$P_{\text{ext}}(t) = \omega_{\text{arm}}(t) \tau_{\text{PTO}}(t) = A_{\text{ext}}^2 |H_A(j\omega)|^2 |Z_c(j\omega)| \cdot \sin(\omega t + \angle H_A(j\omega)) \sin(\omega t + \angle H_A(j\omega) + \angle Z_c(j\omega)) \quad (3.41)$$

To calculate the average power of Eq. (3.41) only the relative phase shift of the two sine waves is required, thus $\angle H_A(j\omega)$ may be omitted given the power expression $\tilde{P}(t)$,

$$\begin{aligned} \tilde{P}(t) &= A_{\text{ext}}^2 |H_A(j\omega)|^2 |Z_c(j\omega)| \sin(\omega t) \sin(\omega t + \angle Z_c(j\omega)) \\ &= A_{\text{ext}}^2 |H_A(j\omega)|^2 |Z_c(j\omega)| \frac{\cos \phi - \cos(2\omega t + \phi)}{2} \end{aligned} \quad (3.42)$$

where $\phi = \angle Z_c(j\omega)$ and the following trigonometric relation have been used:

$$\sin(\omega t) \sin(\omega t + \phi) = \frac{1}{2} (\cos \phi - \cos(2\omega t + \phi)) \quad (3.43)$$

To include the efficiency as in Eq. (3.36) to calculate the instantaneous power output, the direction of the power transfer is required known to perform the correct scaling of the signal, see Fig. 3.7a.

Thus, for one “power” period $T_{\text{pwr}} = \frac{\pi}{\omega}$ of $\tilde{P}(t)$ it is required to identify when the power is transferred to the PTO, ($\tilde{P}(t) > 0$) and when power is transferred to the absorber ($\tilde{P}(t) \leq 0$). This is obtained by noting that the sign of $\tilde{P}(t)$ changes when $\cos \phi - \cos(2\omega t + \phi) = 0$, which is for:

$$t = \frac{-\phi + \pi k}{\omega} \quad \vee \quad t = \frac{\pi k}{\omega}, \quad k = 0, 1, 2, \dots \quad (3.44)$$

This gives the following two cases dependent on the phase ϕ ,

$$\text{for } \phi \in [0; \pi] \quad \begin{cases} \tilde{P}(t) > 0 & \text{for } 0 \leq t \leq \frac{\pi - \phi}{\omega} \\ \tilde{P} \leq 0 & \text{for } \frac{\pi - \phi}{\omega} < t \leq \frac{\pi}{\omega} \end{cases} \quad (3.45)$$

$$\text{for } \phi \in [-\pi; 0] \quad \begin{cases} \tilde{P} < 0 & \text{for } 0 \leq t \leq \frac{-\phi}{\omega} \\ \tilde{P} \geq 0 & \text{for } \frac{-\phi}{\omega} < t \leq \frac{\pi}{\omega} \end{cases} \quad (3.46)$$

where case 1 and 2 is illustrated in Fig. 3.7a and Fig. 3.7b respectively. The result of average produced power will be the same for case 1 and 2, thus only case 1 is treated.

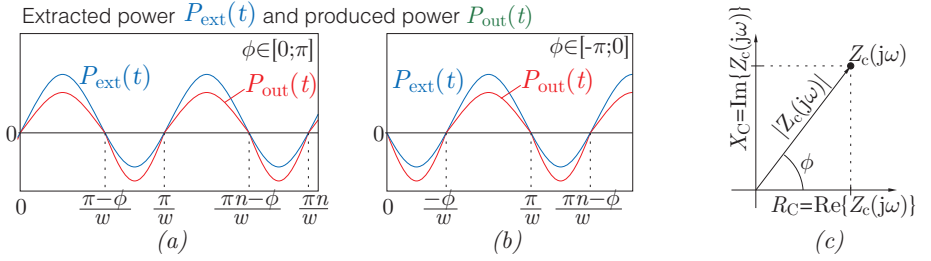


Figure 3.7: In (a) and (b) an illustration of how P is scaled due to the PTO efficiency η_{PTO} . In (c) illustration of the complex value $|Z_c(j\omega)|$

As the PTO has a power conversion efficiency of η (shortened from η_{PTO} for short notation in this section), the power produced when $\tilde{P} > 0$ is $\tilde{P}_{\text{out}} = \tilde{P}\eta$, and the power delivered from the PTO when $\tilde{P} < 0$ is $\tilde{P}_{\text{out}} = \frac{1}{\eta}\tilde{P}$. Hence, the average produced output \bar{P}_{out} may be found as:

$$\bar{P}_{\text{out}} = \frac{1}{T_{\text{pwr}}} \left(\int_{t=0}^{t=\frac{\pi - \phi}{\omega}} \eta \tilde{P}(t) dt + \int_{t=\frac{\pi - \phi}{\omega}}^{t=\frac{\pi}{\omega}} \frac{1}{\eta} \tilde{P}(t) dt \right) \quad (3.47)$$

$$= \frac{1}{2} A_{\text{ext}}^2 |H_A(j\omega)|^2 |Z_c(j\omega)| \frac{\omega}{\pi} g(t) \quad (3.48)$$

where Eq. (3.42) and Eq. (3.43) have been inserted into Eq. (3.47), and $g(t)$ is given as:

$$\begin{aligned} g(t) &= \eta \int_{t=0}^{t=\frac{\pi - \phi}{\omega}} \cos \phi - \cos(2\omega t + \phi) dt + \frac{1}{\eta} \int_{t=\frac{\pi - \phi}{\omega}}^{t=\frac{\pi}{\omega}} \cos \phi - \cos(2\omega t + \phi) dt \\ &= \left(\eta\pi - \phi \left(\eta - \frac{1}{\eta} \right) \right) \frac{1}{\omega} \cos \phi + \left(\eta - \frac{1}{\eta} \right) \frac{1}{\omega} \sin(\phi) \end{aligned} \quad (3.49)$$

Table 3.2: Solving the integral $g(t)$:

$$\begin{aligned}
g(t) &= \eta \int_{t=0}^{t=\frac{\pi-\phi}{\omega}} \cos \phi - \cos(2\omega t + \phi) dt + \frac{1}{\eta} \int_{t=\frac{\pi-\phi}{\omega}}^{t=\frac{\pi}{\omega}} \cos \phi - \cos(2\omega t + \phi) dt \\
&= \eta \left[t \cos \phi - \frac{\sin(2\omega t + \phi)}{2\omega} \right]_{t=0}^{t=\frac{\pi-\phi}{\omega}} + \frac{1}{\eta} \left[t \cos \phi - \frac{\sin(2\omega t + \phi)}{2\omega} \right]_{t=\frac{\pi-\phi}{\omega}}^{t=\frac{\pi}{\omega}} \\
&= \eta \frac{\pi - \phi}{\omega} \cos \phi - \eta \frac{1}{2\omega} \sin(2\pi - \phi) + \eta \frac{1}{2\omega} \sin(\phi) + \\
&\quad \frac{1}{\eta} \frac{\pi}{\omega} \cos \phi - \frac{1}{\eta} \frac{1}{2\omega} \sin(2\pi + \phi) - \frac{1}{\eta} \frac{\pi - \phi}{\omega} \cos \phi + \frac{1}{\eta} \frac{1}{2\omega} \sin(2\pi - \phi) \\
&= \eta \frac{\pi - \phi}{\omega} \cos \phi + \eta \frac{1}{2\omega} \sin \phi + \eta \frac{1}{2\omega} \sin \phi + \\
&\quad \frac{1}{\eta} \frac{\pi}{\omega} \cos \phi - \frac{1}{\eta} \frac{1}{2\omega} \sin \phi - \frac{1}{\eta} \frac{\pi - \phi}{\omega} \cos \phi - \frac{1}{\eta} \frac{1}{2\omega} \sin \phi \\
&= \left(\eta(\pi - \phi) + \frac{1}{\eta} \pi - \frac{1}{\eta}(\pi - \phi) \right) \frac{1}{\omega} \cos \phi + \left(\eta + \eta - \frac{1}{\eta} - \frac{1}{\eta} \right) \frac{1}{2\omega} \sin \phi \\
&= \left(\eta\pi - \phi \left(\eta - \frac{1}{\eta} \right) \right) \frac{1}{\omega} \cos \phi + \left(\eta - \frac{1}{\eta} \right) \frac{1}{\omega} \sin \phi \tag{3.50}
\end{aligned}$$

The rewriting of expression $g(t)$ to Eq. (3.49) is given in Tab. 3.2.

According to Fig. 3.7c the angle ϕ from Eq. (3.42) and dependent expression may be expressed as,

$$|Z_c(j\omega)| = \sqrt{R_c^2 + X_c^2}, \quad |H_A(j\omega)| = \frac{1}{(R_c + R_i)^2 + (X_c + X_i)^2} \tag{3.51}$$

$$\cos \phi = \frac{R_c}{\sqrt{R_c^2 + X_c^2}}, \quad \sin \phi = \frac{X_c}{\sqrt{R_c^2 + X_c^2}}, \quad \tan \phi = \frac{X_c}{R_c} \tag{3.52}$$

Inserting $g(t)$ into Eq. (3.48) yields,

$$\begin{aligned}
\bar{P}_{\text{out}} &= \frac{A_{\text{ext}}^2}{2} |H_A(j\omega)|^2 |Z_c(j\omega)| \frac{1}{\pi} \left(\left(\eta\pi - \phi \left(\eta - \frac{1}{\eta} \right) \right) \cos \phi + \left(\eta - \frac{1}{\eta} \right) \sin \phi \right) \\
&= \frac{\frac{1}{2} A_{\text{ext}}^2}{(X_i + X_c)^2 + (R_i + R_c)^2} \left(\left(\eta - \frac{1}{\pi} \left(\eta - \frac{1}{\eta} \right) \arctan\left(\frac{X_c}{R_c}\right) \right) R_c + \frac{1}{\pi} \left(\eta - \frac{1}{\eta} \right) X_c \right) \tag{3.53}
\end{aligned}$$

where:

$$\begin{aligned}
R_i &= \text{Re}\{Z_i(j\omega)\} = B_{\text{hyd}}(\omega), & X_i &= \text{Im}\{Z_i(j\omega)\} = \omega(J_{\text{mech}} + J_{\text{add}}(\omega)) - k_{\text{res}} \frac{1}{\omega} \\
R_c &= \text{Re}\{Z_c(j\omega)\} = B_{\text{PTO}}, & X_c &= \text{Im}\{Z_c(j\omega)\} = \omega J_{\text{PTO}} - k_{\text{PTO}} \frac{1}{\omega}
\end{aligned}$$

The PTO control example is for $\tau_{\text{PTO}} = k_{\text{PTO}} \theta_{\text{arm}} + B_{\text{PTO}} \omega_{\text{arm}} + J_{\text{PTO}} \dot{\omega}_{\text{arm}}$.

Thus, for a reactive control law the power output of the PTO with power conversion efficiency η may be calculated from Eq. (3.53). Note that for an ideal PTO, $\eta = 1$, Eq. (3.53) reduces to the well known result for the power output,

$$\bar{P}_{\text{out}} \Big|_{\eta=1} = \frac{1}{2} A_{\text{ext}}^2 \frac{R_c}{(X_i + X_c)^2 + (R_i + R_c)^2} \quad (3.54)$$

where the optimum control law, maximising \bar{P}_{out} , is $R_c = R_i$ and $X_c = -X_i$.

In Falnes [32], the PTO loss is suggested cleverly formulated as an equivalent damping coefficient B_{loss} , such that $R_i = B_{\text{hyd}} + B_{\text{loss}}$. However, this does actual not affect the optimum value of X_c in Eq. (3.54), meaning that the PTO is still using the necessary reactive power to bring ω_{arm} and τ_{ext} into phase. Hence, the $R_i = B_{\text{hyd}} + B_{\text{loss}}$ is often not a sufficient penalty compared to using the suggested efficiency formulation in Eq. (3.36).

3.4.1 Example of Optimal Reactive Control using Eq. (3.53)

To compute an example, assume that the wave period of a regular wave is T_w is 5.5s, which is slower compared to the Wavestar absorber, having a natural period of 3.5s. If the PTO efficiency is assumed to be $\eta_{\text{PTO}} = 1$, the well known result in Eq. (3.54) may be used, yielding the optimal values of PTO spring term k_{PTO} and damping term B_{PTO} :

$$X_c = -X_i \quad \Rightarrow \quad k_{\text{PTO}} = (J_{\text{mech}} + J_{\text{add}}(\omega))\omega^2 - k_{\text{res}} \quad (3.55)$$

$$R_c = R_i \quad \Rightarrow \quad B_{\text{PTO}} = B_{\text{hyd}}(\omega) \quad (3.56)$$

The parameter values for the example are listed in Tab. 3.3.

If the efficiency of the PTO η_{PTO} is less than one, Eq. (3.53) has to be solved to get the optimal paramters, i.e.,

$$(B_{\text{PTO}}, k_{\text{PTO}}) = \arg \min_{B_{\text{PTO}}, k_{\text{PTO}}} \bar{P}_{\text{out}} \Big|_{\eta=\eta_{\text{PTO}}} \quad (3.57)$$

which may be performed numerically, which is computational easy as it is an algebraic equation. The function Eq. (3.53) for $\eta_{\text{PTO}} = 0.9$ is shown in Fig. 3.8, showing a smooth function with one maximum. The figure shows that when the reactive part (k_{PTO}) becomes large compared to the resistive part (B_{PTO}), the average power output becomes negative due to the losses in the PTO.

If the PTO system is non-reactive, the optimal linear damping is the equivalent damping of the system (length of the source/intrinsic impedance Z_i) at the given frequency:

$$B_{\text{PTO}} = |Z_i| = \sqrt{B_{\text{hyd}}(\omega)^2 + \left((J_{\text{arm}} + J_{\text{add}}(\omega))\omega + \frac{k_{\text{res}}}{\omega} \right)^2} \quad (3.58)$$

$$k_{\text{PTO}} = 0 \quad (3.59)$$

To compare the effect of including the efficiency of the PTO, Eq.(3.53) has been solved as a function of efficiency. The result is shown in Fig. 3.9, where the “ $\eta_{\text{PTO}} = 1$ ” parameters according to Eq.(3.55) and Eq.(3.56) also have been tested for all actual PTO efficiencies.

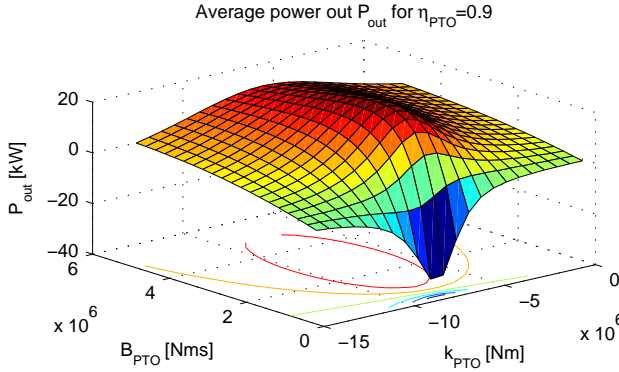


Figure 3.8: Average power output \bar{P}_{out} for different sets of PTO damping and spring term for a PTO efficiency $\eta_{PTO}=0.9$.

Table 3.3: Values used in regular wave example.

T_w	[s] :	5.5	ω_w	[rad/s]:	1.14
A_w	[m] :	0.5	$ H_{ext} $	[N]:	$1.15 \cdot 10^6$
A_{ext}	[Nm] :	$0.576 \cdot 10^6$	η_{PTO}	[-]:	0.9
J_{add}	[kgm ²]:	$2.01 \cdot 10^6$	B_{hyd}	[Nms]:	$0.983 \cdot 10^6$

At a PTO efficiency lower than approximately 80%, the use of the $\eta_{PTO}=1$ parameters from Eq. (3.54) will actually produce a negative average power output. However, if the efficiency is included in the control design using Eq. (3.53), the reactive control may produce 20kW at 80% efficiency, which is still 2.5 times more than linear damping, producing 8kW at 80% efficiency. Thus, reactive control is highly useful despite a non-ideal PTO, however, it is crucial that the PTO efficiency is included when determining the control parameters.

Looking at the actual control parameters, the optimal reactive control parameters go towards the linear damping coefficients when the efficiency goes towards zero. This is expected as the reactive part (the spring term) gets increasingly penalised. Likewise, as the efficiency goes toward one, the solution converges with the $\eta_{PTO}=1$ parameters as expected.

For the given regular wave, the $\eta_{PTO}=1$ parameters are only valid for PTO efficiencies above 95%. PTO efficiencies that high are currently not available in wave energy. Hence, the PTO efficiency must never be omitted in the optimisation of reactive control laws.

3.5 Tank Test Verification of Control Strategies

Control tests have been made in the wave tank presented in Sec. 2.5 for the 1:20 scale absorber. The purpose is general verification, and to verify the performance of the

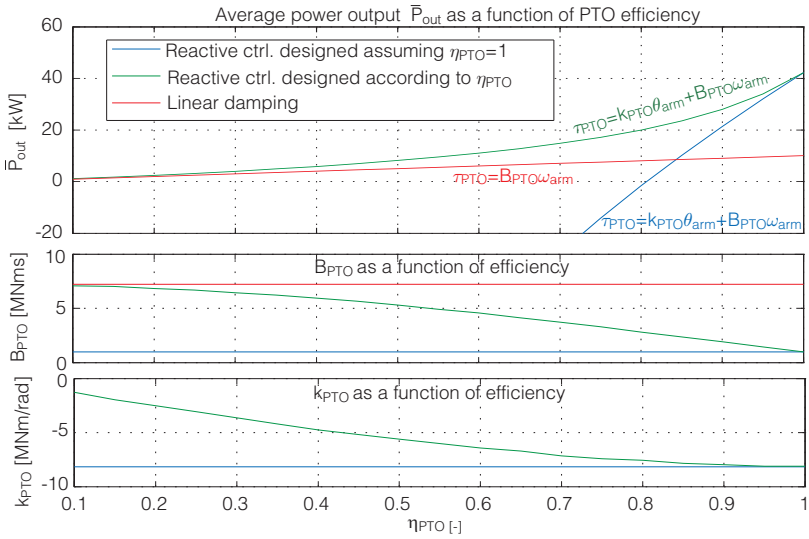


Figure 3.9: Power output for varying PTO efficiency for a regular wave with a period of 5.5 s. The curve with “x” shows the results if using the control parameters from Eq. (3.55) and Eq. (3.56), i.e. not taking the efficiency into account. The curve with dots is for optimal linear damping in Eq. (3.58), and the solid curve is parameters found taking into account the efficiency using Eq. (3.57).

reactive control strategy compared to linear damping. The used irregular wave is:

$$H_{m0,1:20}\lambda = 1.4\text{ m} , T_p = T_{p,1:20}\sqrt{\lambda} = 6.7\text{ s} \quad (3.60)$$

The tested controls are: Optimal linear damping with $B_{\text{PTO}} = 12\text{ kgm}^2/\text{s}$, and reactive control with $k_{\text{PTO}} = -35\text{ Nm/rad}$ and the corresponding optimal damping $B_{\text{PTO}} = 6\text{ kgm}^2/\text{s}$. Comparison of measured and simulated behaviour is seen Fig.3.10, where the measured incident wave has been used as input to the simulation model. Both simulation and tank test have been operated for some time to remove possible initial transients. The agreement between model and measurement is very good. As also the instantaneous power estimate agrees, the expected performance of reactive control according to theory is validated.

Looking at the measurements shows that by investing a small amount of energy in the reactive gives twice the average power extraction compared to linear damping. Note that the linear damping is optimised, whereas the shown reactive is actually only sub-optimal. For a 100% efficient PTO the optimal values would be $B_{\text{PTO}} = 1\text{ kgm}^2/\text{s}$ and $k_{\text{PTO}} = -60\text{ Nm/rad}$. For a 80% efficient PTO, $k_{\text{PTO}} = -80\text{ Nm/rad}$. Unfortunately at time of testing in the wave tank, the optimal reactive control parameters were not tested.

3.6 Summary

The purpose of the chapter to investigate optimal reactive control to find a causal implementation and show whether it is feasible for PTO with losses.

The well known optimal control (complex-conjugated) was presented, showing its inherit non-causality. Based on the complex-conjugated control, approaches to achieving causality are given. Replacing the non-causal part with a fixed damping revealed the sub-optimal causal control corresponding to the earlier suggested feedback-linearisation or inverse control. This inverse control was analysed, showing that the strategy cancels all the absorber dynamics, leaving the absorber operating as a pure damper. The analyses showed that though the control is causal, it is marginally stable (poles on the imaginary axis), rendering it very sensitive to plant and modelling inconsistencies, which will be present as the models are based on linear wave theory, which is an approximation. The inverse control is viewed as being the best sub-optimal causal version without using wave prediction, however not practical implementable in its raw form.

A new variant of the causal control was suggested, where the absorber dynamics is only partial cancelled determined by a coefficient α_J , which increases the robustness of the control (shown by a root locus plot). The suggested control flattens the absorber frequency response, and the coefficients are designed such that the remaining peak of the response is moved to the peak frequency of the wave spectrum. This is expected to a very good practical implementation of the control.

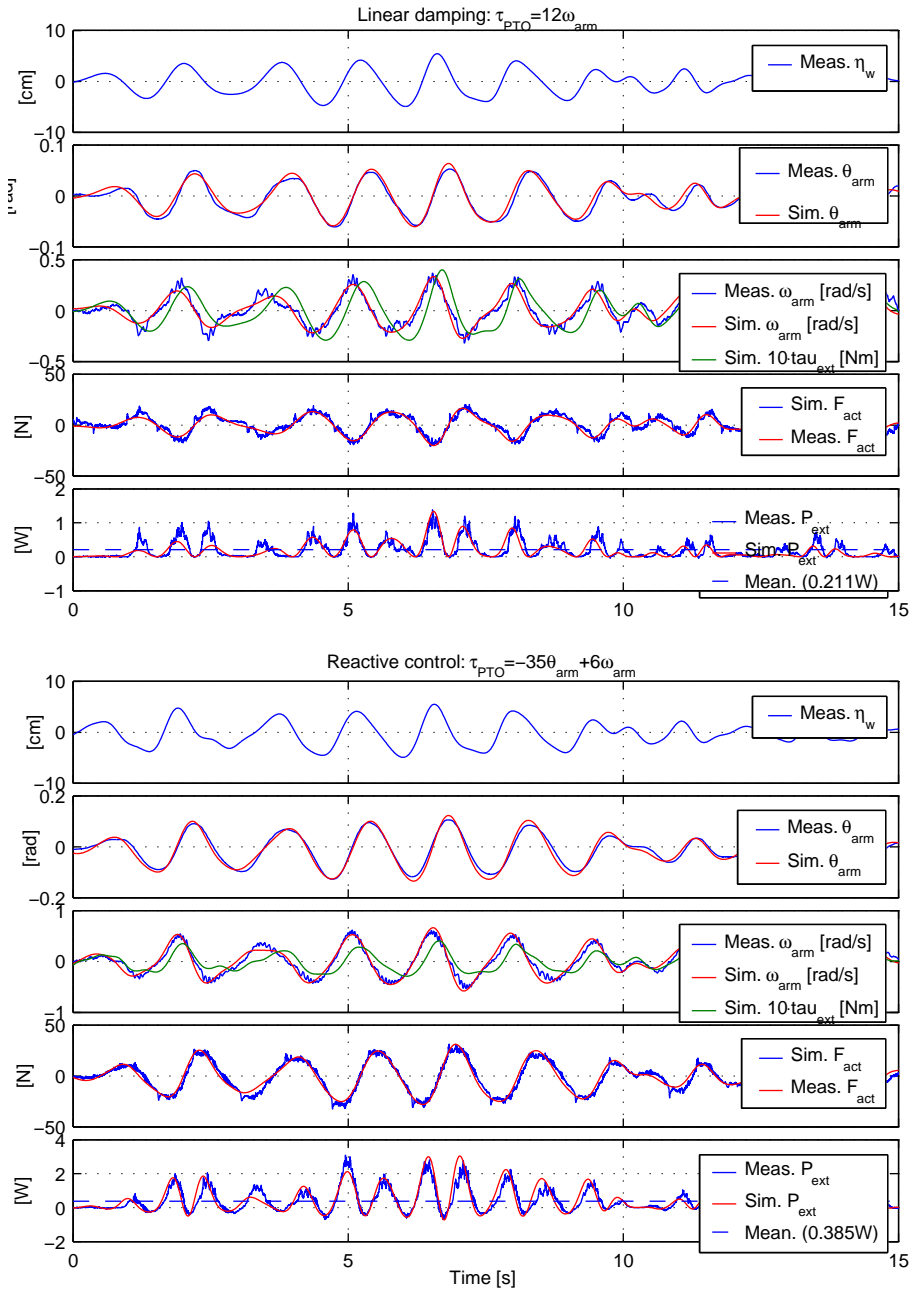


Figure 3.10: Measure and simulated behaviour of linear damping and reactive control.

If the acceleration feedback is unavailable, the optimal control reduces to a spring-based control, which still widens the frequency response compared to pure inertia based control.

Future work would be to test these suggested control strategies with partial cancellation of the absorber dynamics in wave tank test, and also perform simulation studies in irregular waves.

A key point in this chapter is the investigation on how a PTO with losses influence reactive control and how to design accordingly, which was formulated by cleverly relating extracted and out power of a PTO with conversion efficiency η as:

$$P_{\text{out}}(t) = \begin{cases} P_{\text{ext}}(t) \eta_{\text{PTO}} & ; P_{\text{ext}}(t) > 0 \\ P_{\text{ext}}(t) \frac{1}{\eta_{\text{PTO}}} & ; P_{\text{ext}}(t) \leq 0 \end{cases} \quad [\text{W}] \quad (3.61)$$

Using the map, the optimal reactive control for a given η_{PTO} was analytical solved in a regular wave for an arbitrary linear control strategy $Z_c(s)$,

$$\bar{P}_{\text{out}} = \frac{\frac{1}{2}A_{\text{ext}}^2}{(X_i + X_c)^2 + (R_i + R_c)^2} \left(\left(\eta - \frac{1}{\pi} \left(\eta - \frac{1}{\eta} \right) \arctan \left(\frac{X_c}{R_c} \right) \right) R_c + \frac{1}{\pi} \left(\eta - \frac{1}{\eta} \right) X_c \right)$$

where \bar{P}_{out} is average power output of the PTO and

$$\begin{aligned} R_i &= B_{\text{hyd}}(\omega), & X_i &= \omega(J_{\text{mech}} + J_{\text{add}}(\omega)) - k_{\text{res}} \frac{1}{\omega} \\ R_c &= \text{Re}\{Z_c(s)\}, & X_c &= \text{Im}\{Z_c(s)\} \end{aligned}$$

For an ideal PTO, $\eta = 1$, the expression reduces to the well known result for the average power output. Earlier work have suggested adding the PTO loss as an equivalent damping coefficient B_{loss} , such that $R_i = B_{\text{hyd}} + B_{\text{loss}}$. However, this does not affect the optimum value of X_c , meaning that the PTO is still using the necessary reactive power to bring ω_{arm} and τ_{ext} into phase. In this formulation, the value of X_c also gives penalty dependent of η .

By using the expression to design the reactive control according to efficiency, it was shown in an example that at a PTO efficiency of approximately 80%, the reactive still gives 2.5 times more than linear damping. It was also shown that as a rule of thumb that the efficiency of the PTO may only be disregarded in the reactive control design if it is above 95%, otherwise a very poor performing reactive control is obtained for the real PTO.

To conclude the chapter, verification of the control was obtained through tank testing, showing that both linear damping and reactive control performed according to theory, which increases the confidence in the applied models, which are heavily used in the coming chapters.

Chapter 4

Wave Power Extraction Algorithms

How to control a point absorber to maximise energy extraction from waves is an interesting subject which has undergone a lot of research the past 40 years, giving birth to a range of clever strategies - strategies ranging from discrete methods as latching and de-clutching (using relative simple PTOs), to reactive methods, requiring a full four-quadrant PTO with continuous control. These control methods are in this work referred to as Wave Power Extraction Algorithms (WPEA). All these strategies impose fundamentally different requirements on the PTO's controllability and properties, rendering the task of finding the best combination of WPEA and PTO system complex. An approach for solving the complex problem is the sought contribution of this chapter.

Most studies of WPEAs concentrate on optimisation based on power extraction criteria with reduced inclusion of the PTO - resultantly, the strategies do not guarantee that the PTO itself is operating in its best operating region. The approach in this work is to take the "classic" point absorber WPEAs and couple them to a generic PTO formulation. This allows optimising the WPEAs according to a given PTO with focus on the produced power (and not the extracted power), which is essential for reactive WPEAs.

The WPEAs are systematically optimised for a range of PTO characteristics, most notably PTO force capability and efficiency. Complete power output matrices are calculated for all WPEAs for all combination of investigated PTO characteristics. The obtained power matrices are mapped into a yearly production, which allows comparing all the WPEAs as a function of PTO characteristics. The comparison provides the insight into which WPEAs are best for a given PTO, and allows comparing expected performance of fundamentally different PTOs.

The basic idea of efficiency inclusion in the optimisation is given in paper [O], and the optimisation of some of the algorithms has led to the papers [N] and [B]. How the used causal reactive WPEA performs relative to the complex-conjugated is covered in [L].

4.1 Method for Optimising and Comparing WPEAs

Choosing a PTO topology fully couples to how the absorber should and can be controlled. Thus, performance comparison of PTO systems requires identifying best suited WPEA for each PTO system, and performing a mutual optimisation of PTO and WPEAs for each case. Examples of questions required answered when choosing PTO system may be:

- How large a latching torque should a PTO provide before yielding a higher output than a given continuous force control PTO?
- How efficient should a reactive PTO be before yielding a higher power output than a given resistive PTO?

In surveying state of the art, studies of WPEA algorithms for answering these questions have not been found. Resultantly, a method for answering these questions is presented and provides the frame work for the PTO evaluation. The method also adds the aspect of the PTO load force requirement, giving a more elaborate answer to the above questions.

Based on these primeters the following is performed in this chapter:

- Present method for optimising and comparing WPEAs based on PTO constraints.
- Show how each WPEA is optimised for the Wavestar absorber for a set of PTO constraints.
- Introduce a new non-linear resistive WPEA.
- Power output matrices are calculated for all WPEAs for all relevant combinations of load force limitations and PTO efficiency.
- Compare the performance of the WPEAs and their dependence on the PTO characteristics.

Theoretical and proven results often exist for finding the optimal parameters for a given WPEA when an ideal/unconstrained PTO system is assumed. Ideal PTO implies that infinite force is available and the PTO is 100% efficient. When moving to non-ideal PTO with force constraints and losses, the former results will at best only optimise the extracted power and not the actual power output to the grid.

Like the PTO in wind turbines, a wave energy PTO is expected to be designed to operate at full-load capacity a large portion of the time for having a cost-effective solution. Hence, a constrained and saturated PTO behaviour should be a natural part of the normal operation.

Few guidelines or results exist on designing the WPEA algorithms when having PTO constraints. Moreover, the results are often very specific for a given implementation. In [48] the electrical characteristics of the generator and inverter is taking into account, such that a WPEA compromising between power extraction and peak power load is found, yielding an overall better performing system. In [49] it is especially noted that attention should be given to the reactive part, as it greatly increases the peak load.

In [32] it is shown that if the PTO has a loss proportional to the absorber velocity, this may be reformulated as the ideal design case by formulating the loss as an increased damping coefficient in the intrinsic impedance of the absorber. However, as shown in the previous chapter this is inadequate and be difficult to describe and relate the PTO loss to an equivalent damping coefficient.

In [47] a larger comparison of different WPEAs is performed for the Archimedes Wave Swing, but seems not to take into account PTO efficiency when utilising reactive strategies. In [28] a brief survey of research to include PTO constraints for different WPEAs and WECs are given. The studies mostly concentrate on the absorber having constrained amplitude of motion, and not on a PTO with force limitations and losses. Considering the Wavestar absorber, the sea states where the amplitude constraint may be reached, the WEC will be in storm protection. Thus in this work, this is not of main interest.

The approach used in this work for inclusion of constraints is to base on numerical optimisation of simulation models. The overall setup is seen in Fig. 4.1. The applied model for optimisation is the time domain model of the single absorber model from the previous chapter, where a generalised PTO is included. In each iteration, the system is simulated in irregular waves for an adequate duration (>100 wave periods). Based on the calculated power output \bar{P}_{out} , the WPEA parameters are updated, and a new iteration is performed with new parameters. This is performed until the average power output has converged at a maximum.

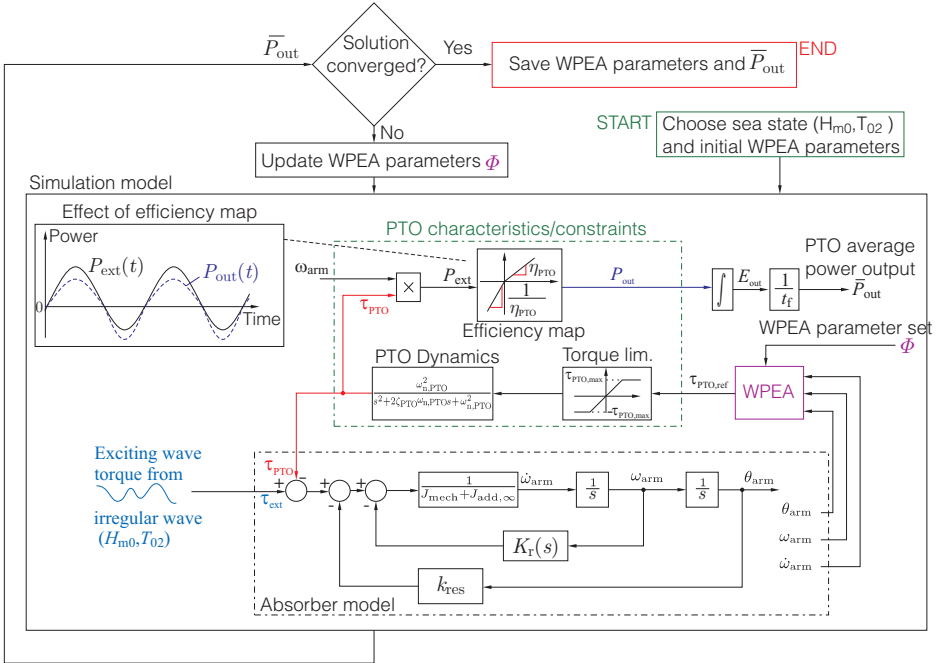


Figure 4.1: Outline of how the optimisation of WPEA algorithms is performed when PTO constraints are included.

In the single absorber model in Fig. 4.1, the wave excitation torque is assumed pre-computed by filtering the irregular wave signal. The WPEA algorithm computes a desired torque reference $\tau_{PTO, ref}$ based on absorber motion. This torque reference is tracked by the PTO, which is defined by some general characteristics, which (at

minimum) comprise a torque limit $\tau_{\text{PTO,max}}$, a tracking bandwidth of $\omega_{\text{n,PTO}}$ and a power conversion efficiency of η_{PTO} . The inclusion of power conversion efficiency is an essential part of the evaluation when evaluating reactive WPEAs, as having reactive power in the PTO dissipates energy. The instantaneous power output is calculated as suggested in [O],

$$P_{\text{out}}(t) = \begin{cases} P_{\text{ext}}(t) \eta_{\text{PTO}} & ; P_{\text{ext}}(t) > 0 \\ P_{\text{ext}}(t) \frac{1}{\eta_{\text{PTO}}} & ; P_{\text{ext}}(t) \leq 0 \end{cases} \quad [\text{W}] \quad (4.1)$$

and the average PTO output \bar{P}_{out} is calculated as,

$$\bar{P}_{\text{out}} = \frac{1}{t_f} \int_0^{t_f} P_{\text{out}}(t) dt \quad [\text{W}] \quad (4.2)$$

over the simulation duration t_f .

The non-linear scaling behaviour in Eq. (4.1) is also seen in Fig. 4.1. The presented efficiency map of Eq. (4.1) gives a very simple and generic inclusion of the PTO losses for calculating the power output. Also, efficiency is easily related to a system and is often the basic figure for losses in systems or components, e.g. generators.

The PTO torque tracking dynamics is included to give a realistic PTO behaviour,

$$\frac{\tau_{\text{PTO}}(s)}{\tau_{\text{PTO,ref}}(s)} = \frac{\omega_{\text{n,PTO}}^2}{s^2 + 2\zeta_{\text{PTO}}\omega_{\text{n,PTO}}s + \omega_{\text{n,PTO}}^2} \quad [-] \quad (4.3)$$

where the bandwidth is set to $\omega_{\text{n,PTO}} = 2\pi 3 \text{ rad/s}$, and the damping factor to $\zeta_{\text{PTO}} = 0.7$. A bandwidth of minimum 3Hz is realistic for hydraulic PTOs and easily realisable for electrical PTOs.

Given these PTO constraints and a WPEA algorithm, the optimal control parameter set Φ_{opt} for a given WPEA is then the parameters Φ maximising the energy output of the PTO:

$$\Phi_{\text{opt}} = \arg \max_{\Phi} \int_0^t P_{\text{out}}(t) dt \quad (4.4)$$

Thus, for each iteration of a parameter set Φ , a full simulation is performed in irregular waves to determine \bar{P}_{out} . As input to the model, an irregular wave sequence $\eta_{w,\text{base}}$ with mean wave period of $T_{02,\text{base}} = 1 \text{ s}$ and $H_{m0,\text{base}} = 1 \text{ m}$ has been designed. The sequence complies with the PM-spectrum and has been made with the white noise method presented in Sec. 2.2. This design wave is then reused for each optimisation. The different sea states are then created by scaling the time vector of the wave and the height, which is then pre-filtered to obtain the exciting wave torque.

The design wave has a length of 100 wave periods. According to [37], 100 periods are often too low for estimating average power. However, based on a number of generated shorter wave series, a short wave series has been found, which gives approximately the same average power extraction and PTO performance results compared to a long simulation of 1000 wave periods. Resultantly, this short wave series is used for optimisation and comparison purposes. The used short wave is seen in Fig. 4.2.

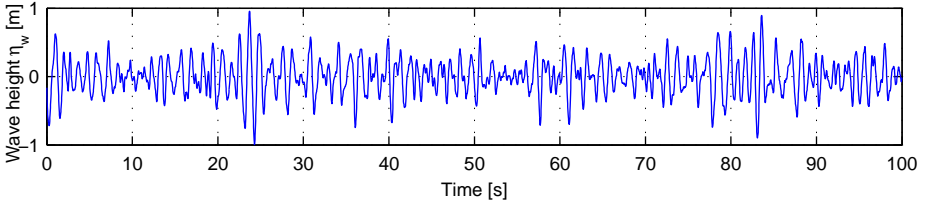


Figure 4.2: Used design wave of 100 periods.

The use of the design wave gives the following benefits:

- The cost function (average power output) in the optimisations becomes deterministic (no jitter from iteration to iteration due to wave perturbation).
- Time trajectories of absorber behaviour may be compared directly for different WPEAs.
- Reduced computational time, as a short wave is used, and repeated wave computation and force filtering is avoided.

The WPEA algorithms going to be explored are listed below:

- *Reactive control:* Apply torque as $\tau_{\text{PTO}} = k_{\text{PTO}}\theta_{\text{arm}} + B_{\text{PTO}}\omega_{\text{arm}}$
- *Linear damping:* Apply a linear damping torque $\tau_{\text{PTO}} = B_{\text{PTO}}\omega_{\text{arm}}$
- *Coulomb damping:* The PTO may only apply a constant damping torque in both directions.
- *OCIR:* A resistive algorithm, where phase control is achieved through non-linear damping.
- *Latching with linear damping:* The absorber is locked in parts of the oscillation cycle, and linear damping is applied during movement.
- *Latching with Coulomb damping:* The absorber is locked in parts of the oscillation cycle, and Coulomb damping is applied during movement.
- *De-clutching:* The absorber apply either no torque (de-clutched) or a constant damping torque (clutched).
- *Double ratchet:* Torque is applied when the absorber reach a certain speed, and controlled not to exceed this speed.
- *Single Ratchet:* Torque is only applied when the absorber reaches a certain positive speed, but no torque is applied in negative direction.

The classic algorithms are reactive control, linear damping, latching control, de-clutching control and Coulomb damping. The OCIR is a WPEA suggested in this work, which is a causal non-linear WPEA, where Oscillation Control is Implemented Resistively (OCIR). The “ratchet” methods are more a PTO type than an actual control method. Nevertheless, the ratchet mechanism dictates a control method and is therefore included as a WPEA for evaluating these types of PTO systems. An appetiser to the torque and absorber trajectories of the nine WPEAs is given in Fig. 4.3. Optimised implementation of each algorithm is going to be presented in this chapter, taking into account PTO efficiency, torque constraints and PTO bandwidth. Examples of time trajectories for all optimised WPEAs are presented for the same irregular wave with $H_{m,0} = 1.75$ m and $T_p = 5.5$ s. The common PTO setup used in these examples is an efficiency of $\eta_{PTO} = 0.8$ and maximum PTO torque $\tau_{PTO,max} = 1$ MNm.

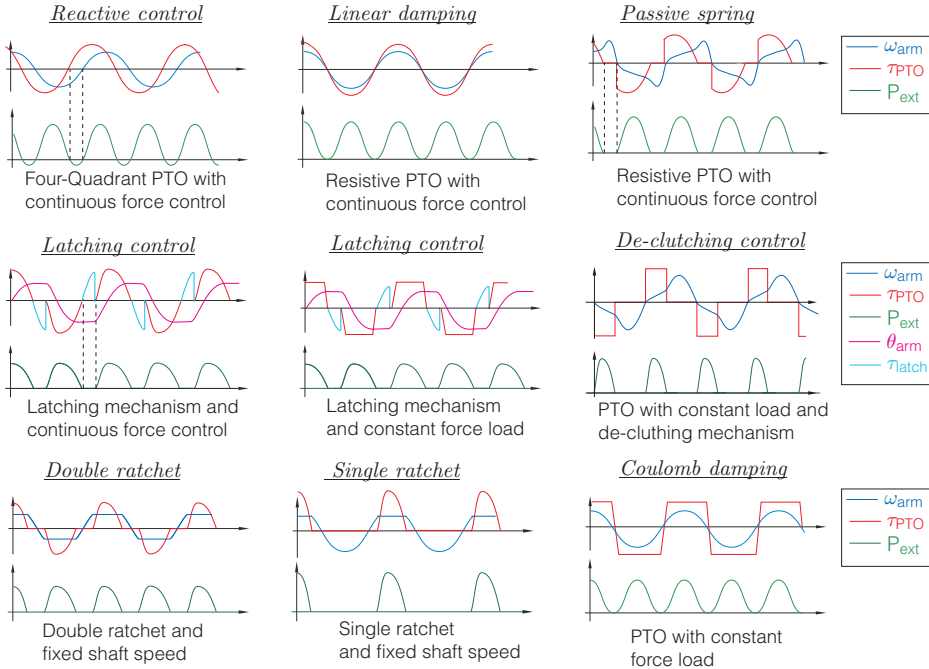


Figure 4.3: The explored WPEA algorithms and the corresponding PTO type.

To compare the performance of the WPEAs, average power output matrices \mathbf{P}_{mat} are generated for each WPEA for the C5 absorber for the sea states given in Tab. 4.1.

To avoid comparing power matrices and give a more apprehensible comparison, the power matrices will be converted into a yearly production E_{year} based on an assumption of sea state distribution for an installed WEC. The yearly production may be viewed as a weighted average of the power matrix entries.

Table 4.1: Sea states included in output power matrices \mathbf{P}_{mat} .

$H_{m,0}$ [m]	$T_{0,2}$ [s]					
	2.50	3.50	4.50	5.50	6.50	7.50
0.75						
1.25						
1.75						
2.25						
2.75						

Power matrix
= \mathbf{P}_{mat}

For the 5 m diameter absorber, which is used as the case, a valid wave climate is given in [50] for the Wavestar C5, and shown in Tab. 4.2. The C5 absorber is designed to be in production from a significant wave height from 0.5 m to 3.0 m. By calculating the amount of time spend at these sea states per year, and multiplying with the average power output produced for the individual sea states given in the found power matrices, the yearly production is obtained,

$$E_{\text{year}} = \sum_{i=1}^{n_H} \sum_{j=1}^{n_T} \mathbf{D}_{ij} \mathbf{P}_{\text{mat},ij} \cdot 365 \cdot 24 \cdot 60 \cdot 60 \quad [\text{J}] \quad (4.5)$$

using the distribution matrix \mathbf{D} defined in Tab. 4.2, and n_H and n_T are the number of discrete wave periods and wave heights in the matrices. The matrices are created such that their entries match, i.e. the entry ij corresponds to the same sea state in \mathbf{P}_{mat} and \mathbf{D} . The sea states in the calculation are $T_{0,2} \in \{2.5, 3.5, 4.5, 5.5, 6.5, 7.5\}$ s and $H_{m,0} \in \{0.75, 1.25, 1.75, 2.25, 2.75\}$ m.

Table 4.2: Typical annual distribution of the wave climate at the Wavestar prototype test site.

$H_{m,0}$ [m]	Mean wave period $T_{0,2}$ [s]						Sum [%]
	2-3	3-4	4-5	5-6	6-7	7-8	
0.0 - 0.5	2.65	8.18	1.84	0.38	0.14	0.04	13.2
0.5 - 1.0	1.22	19.2	11.4	2.21	0.18	0.08	34.4
1.0 - 1.5	0.00	6.84	13.0	2.96	0.30	0.04	23.2
1.5 - 2.0	0.00	0.33	9.58	3.05	0.29	0.04	3.3
2.0 - 2.5	0.00	0.02	3.34	4.60	0.20	0.04	8.2
2.5 - 3.0	0.00	0.01	0.22	3.89	0.21	0.02	4.4
3.0 - 3.5	0.00	0.00	0.00	1.38	0.51	0.02	1.9
3.5 - 4.0	0.00	0.00	0.00	0.17	0.57	0.03	0.8
4.0 - 4.5	0.00	0.00	0.00	0.00	0.24	0.07	0.3
4.5 -	0.00	0.00	0.00	0.00	0.07	0.27	0.3
Sum[%]	3.87	34.6	39.5	18.6	2.72	0.68	100

= \mathbf{D}
Production time
distribution matrix

4.2 Causal Reactive Control

Different approaches have been suggested to predict waves to overcome the non-causal behaviour of e.g. complex-conjugate control. In [51] a requirement of only 1 s prediction is proposed. The prediction control is shown to give a two-fold output compared to a causal linear damping control. However, the prediction control is used on a reactive

control scheme, making the comparison non-conclusive, as a casual reactive control may easily yield two-fold compared to linear damping [N]. Generally, the required prediction horizon is about the length of the impulse response of the absorber. Another method for wave prediction is to measure the waves up-stream of the absorber, where a filter may be calculated to estimate the future experienced wave excitation.

The use of prediction will often result in loss of robustness of the algorithms. Combining this with inclusion of the PTO constraints will further complicate the control design. Respecting the performed research within prediction, the approach used in this work is to use a non-predictive reactive control as presented in the previous chapter.

A robust and causal implementation is sought, hence acceleration feedback is avoided, leaving only velocity and position feedback. This corresponds to the control suggested in Eq. (3.34),

$$\Psi_k = k_{\text{PTO}}\dot{\theta}_{\text{arm}} + B_{\text{PTO}}\omega_{\text{arm}} \quad [\text{Nm}] \quad (4.6)$$

The idea is to pre-determine an optimal parameter set $\Phi = (k_{\text{PTO}}, B_{\text{PTO}})$ for all possible sea states, thereby generating a mapping between sea states and optimal parameters. When operating in a given sea state, the control will then tune the absorber to the fixed response yielding the highest energy output. The sea state is estimated by continuously gathering statistical information of wave period and wave height. If this simple reactive control shows sufficient performance to choose a reactive PTO, the improved reactive strategies suggested in the previous chapter may be implemented later on to improve performance.

4.2.1 Optimisation of Reactive Control with Realistic PTO in Irregular Waves

The optimisation of reactive control in irregular waves is a two dimensional problem of choosing the best suited set of B_{PTO} and k_{PTO} for each sea state, maximising the average power output. This is formulated below:

$$\begin{aligned} \max_{k_{\text{PTO}}, B_{\text{PTO}}} \quad & \frac{1}{t_f} \int_0^{t_f} P_{\text{out}}(t) dt & (4.7) \\ \text{s.t.} \quad & \dot{\mathbf{x}}(t) = \mathbf{f}(\mathbf{x}(t), \tau_{\text{PTO}}(t), \tau_{\text{ext}}(t)) \\ & \frac{\tau_{\text{PTO}}(s)}{\tau_{\text{PTO,ref}}(s)} = \frac{\omega_{\text{n,PTO}}^2}{s^2 + 2\zeta_{\text{PTO}}\omega_{\text{n,PTO}}s + \omega_{\text{n,PTO}}^2} \\ & \tau_{\text{PTO,ref}} = \text{sat} \left(B_{\text{PTO}}\dot{\theta}_{\text{arm}} + k_{\text{PTO}}\theta_{\text{arm}}, \tau_{\text{PTO,max}} \right) \\ & P_{\text{out}}(t) = \begin{cases} \tau_{\text{PTO}}\omega_{\text{arm}} \eta_{\text{PTO}} & ; \tau_{\text{PTO}}\omega_{\text{arm}} > 0 \\ \tau_{\text{PTO}}\omega_{\text{arm}} \frac{1}{\eta_{\text{PTO}}} & ; \tau_{\text{PTO}}\omega_{\text{arm}} \leq 0 \end{cases} \end{aligned}$$

The constraint $\dot{\mathbf{x}}(t) = \mathbf{f}(\mathbf{x}(t), \tau_{\text{PTO}}(t), \tau_{\text{ext}}(t))$ simply implies that the absorber movement is forced to obey the absorber dynamics defined in Eq. (2.37). The saturation function $\text{sat}(x, c)$ is defined as,

$$\text{sat}(x, c) = \begin{cases} x & ; |x| < |c| \\ c \cdot \text{sgn}(x) & ; |x| \geq |c| \end{cases} \quad (4.8)$$

i.e. $\text{sat}(\tau_{\text{PTO,ref}}, \tau_{\text{PTO,max}})$ limits the reference $|\tau_{\text{PTO,ref}}|$ to be less or equal to $|\tau_{\text{PTO,max}}|$.

To perform the optimisation, an initial value is found by calculating the optimal control parameters based on an regular wave with a period equal to the peak period by solving Eq. (3.57). For the example with $T_p = 5.5$ s, $\eta_{PTO} = 0.8$ and $\tau_{PTO,max} = 1$ MNm, this yields the parameters $k_{PTO} = -8.0$ MNm and $B_{PTO} = -2.6$ MNms.

To solve the optimisation, the simplex algorithm implemented in MATLAB is applied [52]. Note that the applied simplex algorithm performs unconstrained optimisation, which is adequate as the constraints in the problem are a part of the underlying model. E.g. the model implements the limit on the force. The optimisation is shown in Fig. 4.4. For this example a grid of points has been computed to show the actual cost function and how the algorithm performs. The function is nice and smooth (indicating that a gradient based optimisation algorithm may advantageously applied), and has only one maximum. The trajectory of the executed simplex algorithm from initial value to final value is shown in the contour plot of Fig. 4.4. The algorithm reaches the maximum of 19.7kW in approximately 10 iterations. The optimal control parameters are found to be $k_{PTO} = -7.0$ MNm and $B_{PTO} = 4.9$ MNms. The negative k_{PTO} value is expected in order to reduce the natural frequency of the absorber.

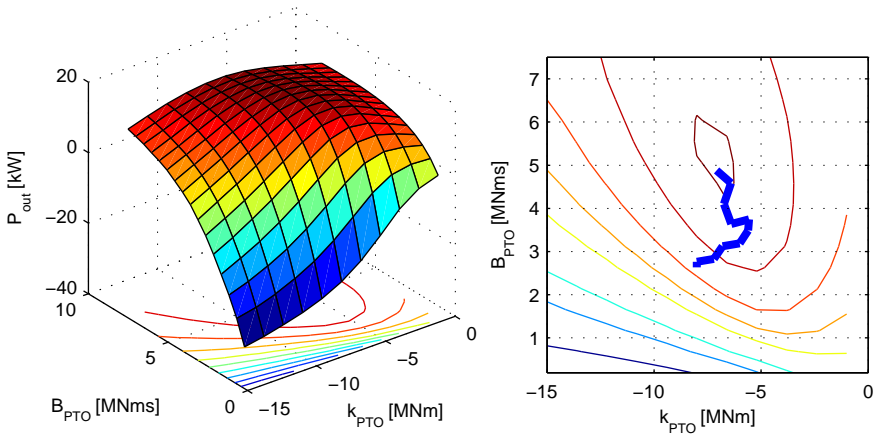


Figure 4.4: Optimisation reactive control for a sea state $H_{m0} = 1.75$, $T_p = 5.5$ s, a PTO torque limitation of $\tau_{PTO,max} = 1$ MNm and an efficiency of $\eta_{PTO} = 0.8$.

A small section of the simulation, which is performed in each iteration, is shown in Fig. 4.11 for the optimum value of k_{PTO} and B_{PTO} . With the optimum parameters the PTO torque reference is actually often saturated. The hydro-dynamics damping coefficient at a period of 5.5 s is about 1 MNms, however the found optimum PTO damping is 4.9 MNms. This indicates that the control is being penalised by efficiency and torque constraints and thereby partial resorts to over-damping.

As the efficiency enters non-linearly in the cost function, optimisation for each sea state has to be performed for each set of $\tau_{PTO,max}$ and η_{PTO} .

Regarding reactive control, the reactive power may only be processed in part of the

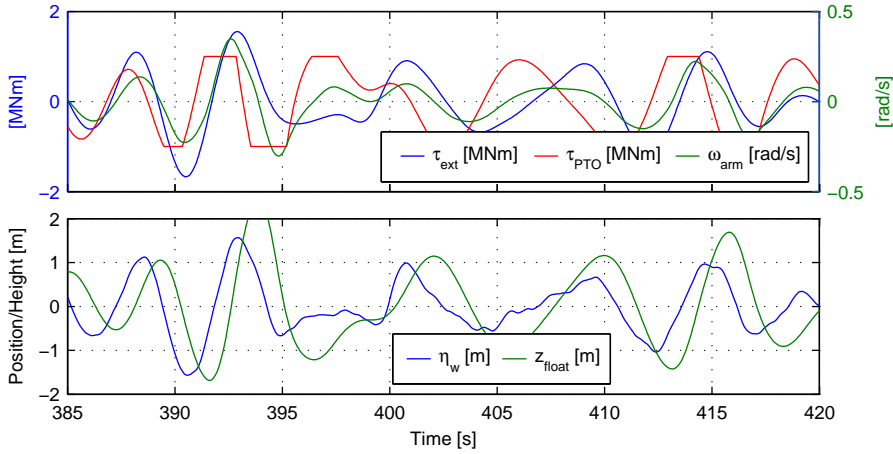


Figure 4.5: Simulation of reactive control for a sea state $H_{m0} = 1.75$, $T_p = 5.5$ s with $\tau_{PTO,max} = 1$ MNm, and $k_{PTO} = -7.0$ MNm and $B_{PTO} = 4.9$ MNms.

PTO. For example, if a temporary energy storage is integrated into the PTO system as illustrated in Fig. 4.6, then the reactive power is only processed through the first part of the PTO with efficiency $\eta_{PTO,1}$. Hence, only $\eta_{PTO,1}$ influences the control parameters and not $\eta_{PTO,2}$. Accordingly, the reactive control for such a system is optimised by maximising the average net power output to the energy storage \bar{P}_{stor} using efficiency $\eta_{PTO,1}$. The total average power output is then given as $\eta_2 \bar{P}_{stor}$. This is allowed as the power transfer from the energy storage to grid/output is always positive. Thus, the optimisation performed in Eq. (4.7) is actually also the optimal solution for a system, where the first part of the PTO has efficiency $\eta_{PTO,1}$. To obtain the average output for a system with $\eta_{PTO} = \eta_{PTO,1} \cdot \eta_{PTO,2}$, one may simply take the average output of Eq. (4.7) and multiply it with $\eta_{PTO,2}$.

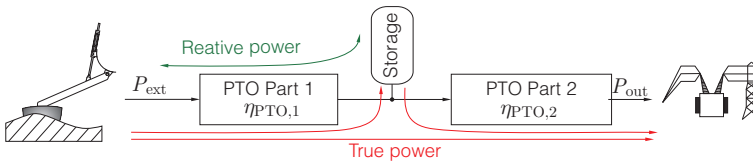


Figure 4.6: From mechanical power input to storage and vice versa the PTO has a power conversion efficiency of $\eta_{PTO,1}$. From storage to power output the PTO has a power conversion efficiency $\eta_{PTO,2}$. The reactive power only travels between storage and absorber.

4.3 Linear Damping Control

The linear damping control is defined as,

$$\Psi_k = B_{\text{PTO}}\omega_{\text{arm}} \quad [\text{Nm}] \quad (4.9)$$

and is optimised in the following.

4.3.1 Optimisation of Linear Damping Control with Realistic PTO

The optimisation of linear damping control is a one dimensional problem of choosing the best suited PTO damping coefficient B_{PTO} in a given sea state:

$$\begin{aligned} \max_{B_{\text{PTO}}} \quad & \frac{1}{t_f} \int_0^{t_f} P_{\text{out}}(t) dt & (4.10) \\ \text{s.t.} \quad & \dot{\mathbf{x}}(t) = \mathbf{f}(\mathbf{x}(t), \tau_{\text{PTO}}(t), \tau_{\text{ext}}(t)) \\ & \frac{\tau_{\text{PTO}}(s)}{\tau_{\text{PTO,ref}}(s)} = \frac{\omega_{\text{n,PTO}}^2}{s^2 + 2\zeta_{\text{PTO}}\omega_{\text{n,PTO}}s + \omega_{\text{n,PTO}}^2} \\ & \tau_{\text{PTO,ref}} = \text{sat} \left(B_{\text{PTO}}\dot{\theta}_{\text{arm}}, \tau_{\text{PTO,max}} \right) \\ & P_{\text{out}}(t) = \begin{cases} \tau_{\text{PTO}}\omega_{\text{arm}} \eta_{\text{PTO}} & ; \tau_{\text{PTO}}\omega_{\text{arm}} > 0 \\ \tau_{\text{PTO}}\omega_{\text{arm}} \frac{1}{\eta_{\text{PTO}}} & ; \tau_{\text{PTO}}\omega_{\text{arm}} \leq 0 \end{cases} \end{aligned}$$

To solve the optimisation, the simplex algorithm used in reactive control optimisation is utilised. The optimisation is shown in Fig. 4.7. For this example a grid of points have computed to show the actual cost function and how the algorithm performs. As initial guess, the damping coefficient is calculated according to Eq. (3.58) for a regular wave with the same period as the peak wave period:

$$B_{\text{PTO}} = \sqrt{B_{\text{hyd}}^2 + \left((J_{\text{arm}} + J_{\text{add}})\omega_{\text{P}} + \frac{k_{\text{res}}}{\omega_{\text{P}}} \right)^2} \bigg|_{\omega_{\text{P}} = \frac{2\pi}{T_{\text{P}}}} = 7.2 \text{ MNms} \quad (4.11)$$

The used values are listed in Tab. 3.3.

The function is nice and smooth with one maximum. The trajectory of the executed simplex algorithm is shown in the contour plot of Fig. 4.7. The initial guess is very close to the optimum. The algorithm reaches the maximum of 11.47 kW in just two iterations. The optimal control parameters are found to be $B_{\text{PTO}} = 6.9 \text{ MNms}$. A small section of the simulation for the optimum value is seen in Fig. 4.8. As the PTO efficiency enters linearly in the cost function, i.e. $\eta_{\text{PTO}} \frac{1}{t_f} \int_0^{t_f} \tau_{\text{PTO}}\omega_{\text{arm}} dt$, the optimisation only has to be performed for one value of η_{PTO} and the result may be scaled afterwards for different PTO efficiencies.

4.4 Coulomb Damping Control

The Coulomb damping control is applied for PTOs only allowing applying a constant damping force (in both positive and negative direction). The Coulomb damping force is often not directly controllable in such PTOs, but is a passive function of the absorber

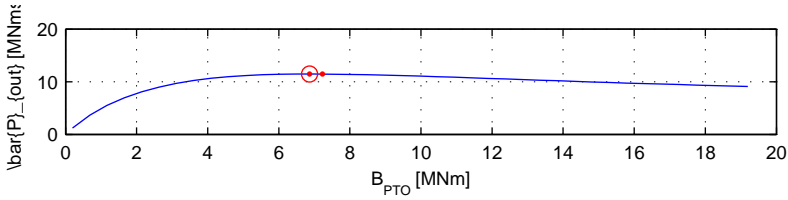


Figure 4.7: Optimisation linear damping control for a sea state $H_{m0}=1.75$, $T_p=5.5$ s, a PTO torque limitation of $\tau_{PTO,max}=1$ MNm and an efficiency of $\eta_{PTO}=0.8$.

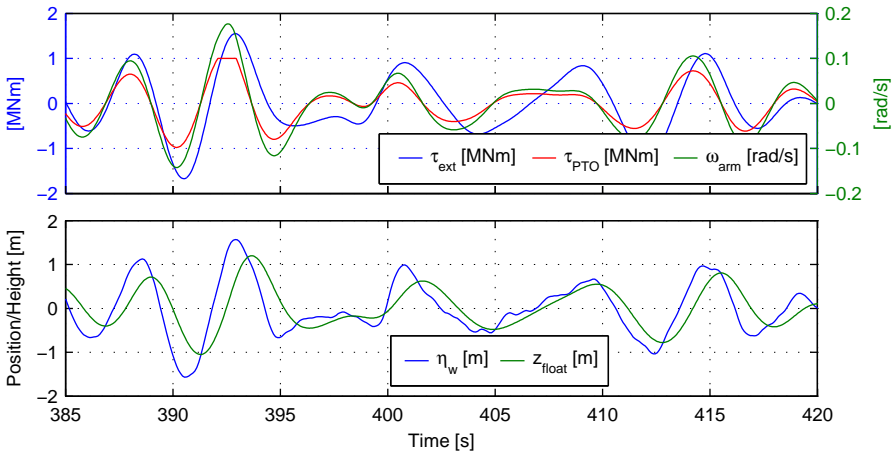


Figure 4.8: Simulation of linear damping control for a sea state $H_{m0}=1.75$, $T_p=5.5$ s with $\tau_{PTO,max}=1$ MNm, and $k_{PTO}=-7.0$ MNm and $B_{PTO}=4.9$ MNms.

velocity. This means that the constant damping force is not applied instantaneously. For a hydraulic system as in Fig. 4.9a, which is the typical PTO for Coulomb damping, the volume of fluid within the cylinder chamber has to be compressed each time the velocity changes direction. Also, power is first generated when the check valves opens to the hydraulic motor and generator. The dynamics of the cylinder force may according to Fig. 4.9a be expressed by using the flow continuity equation:

$$\dot{p}_A = \begin{cases} \frac{\beta_{\text{eff}}}{V_A} v_c A_c & ; p_A < p_M \wedge v_c > 0 \\ \frac{\beta_{\text{eff}}}{V_A} v_c A_c & ; p_T < p_A \wedge v_c < 0 \\ 0 & ; \text{else} \end{cases} \quad \left[\frac{\text{Pa}}{\text{s}} \right] \quad (4.12)$$

$$\dot{p}_B = \begin{cases} -\frac{\beta_{\text{eff}}}{V_B} v_c A_c & ; p_B < p_M \wedge v_c < 0 \\ -\frac{\beta_{\text{eff}}}{V_B} v_c A_c & ; p_T < p_A \wedge v_c > 0 \\ 0 & ; \text{else} \end{cases} \quad \left[\frac{\text{Pa}}{\text{s}} \right] \quad (4.13)$$

$$F_c = (p_B - p_A) A_c \quad [\text{N}] \quad (4.14)$$

where β_{eff} is the bulk modulus of the fluid, i.e. the fluid stiffness, V_A and V_B the chamber volumes, p_M is the hydraulic motor pressure, which is assumed constant for a given sea state. The pressure p_T is the tank pressure, and A_c is the cylinder area.

If V_A and V_B are assumed constant and equal with value denoted V_c , which is a fair assumption as the cylinder is operating around mid position, the resulting cylinder force may be expressed by an equivalent expression for the differential pressure $\Delta p = p_B - p_A$:

$$\dot{\Delta p} = \begin{cases} -2 \frac{\beta_{\text{eff}} A_c}{V_c} v_c & ; \Delta p < p_M - p_T \wedge v_c < 0 \\ -2 \frac{\beta_{\text{eff}} A_c}{V_c} v_c & ; \Delta p > -(p_M - p_T) \wedge v_c > 0 \\ 0 & ; \text{else} \end{cases} \quad (4.15)$$

$$F_c = \Delta p A_c \quad (4.16)$$

This description is shown as a block diagram in Fig. 4.9b, borrowing SIMULINK's notation for an integrator with a lower and a upper saturation limit. The equations may be rewritten as torque and angular velocity as shown in Fig. 4.9c,

$$\dot{\tau}_{\text{PTO}} = \begin{cases} \alpha_D \omega_{\text{arm}} & ; |\tau_{\text{PTO}}| < |\tau_{\text{Coulomb}}| \\ 0 & ; |\tau_{\text{PTO}}| = |\tau_{\text{Coulomb}}| \wedge \text{sgn}(\omega_{\text{arm}}) = \text{sgn}(\tau_{\text{PTO}}) \end{cases} \quad (4.17)$$

with $\alpha_D = 2 \frac{d_A^2 \beta_{\text{eff}} A_c^2}{V_c}$. Example of values for a hydraulic cylinder with a stroke of 2m for a Wavestar 5m absorber, producing 420kN at a differential pressure of 330bar, is shown in Tab. 4.3. Inserting into Eq. (4.17) yields $\alpha_C = 2d_A^2 \beta_{\text{eff}} A_c^2 / V_c = 142 \text{ MNm}$,

To simplify the expression, α_D is divided with $\tau_{\text{PTO,max}}$ to give α_C , yielding the following:

$$\omega_{\text{arm}} \rightarrow \boxed{\alpha_C} \rightarrow \boxed{\frac{1}{s} \int_{-1}^1} \rightarrow \boxed{\tau_{\text{Coulomb}}} \rightarrow \tau_{\text{PTO}} \quad (4.18)$$

Power is only generated by the PTO when the check valves are opened into the hydraulic motor, i.e. $\tau_{\text{PTO}} = \tau_{\text{Coulomb}}$. Thus the instantaneous power is calculated as shown in

Fig. 4.9d:

$$P_{\text{ext}} = \begin{cases} \tau_{\text{PTO}}\omega_{\text{arm}} & ; |\tau_{\text{PTO}}| = |\tau_{\text{Coulomb}}| \\ 0 & ; |\tau_{\text{PTO}}| \neq |\tau_{\text{Coulomb}}| \end{cases} \quad (4.19)$$

Table 4.3: Values used for describing Coulomb damping dynamics.

V_c	$[\text{m}^3]$	0.0127	β_{eff}	$[\text{MPa}]$	1000
A_c	$[\text{m}^2]$	0.0127	d_A	$[\text{m}]$	2.36

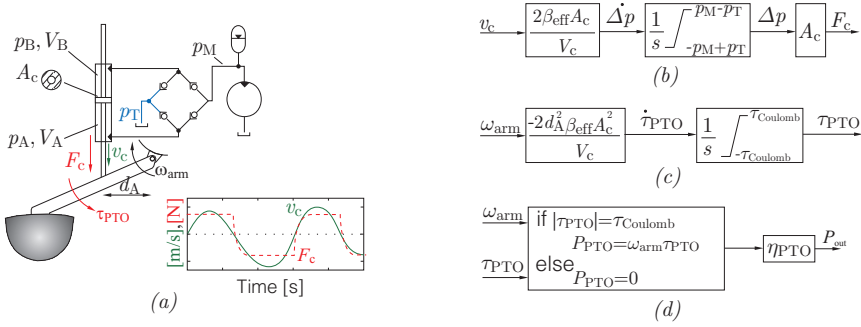


Figure 4.9: In (a) hydraulic PTO for Coulomb damping. In (b) corresponding dynamics, and in (c) formulated as angular velocity and PTO torque τ_{PTO} . In (d) a block diagram for calculating instantaneous power output.

4.4.1 Optimisation of Coulomb Damping with Realistic PTO

Given a torque limitation of the PTO $\tau_{\text{PTO,max}}$, the optimisation is a one dimensional problem of choosing the best suited Coulomb damping torque for a given sea state:

$$\begin{aligned} & \max_{\tau_{\text{Coulomb}} \in [0; \tau_{\text{PTO,max}}]} \frac{1}{t_f} \int_0^{t_f} P_{\text{out}}(t) dt \\ & \text{s.t.} \quad \dot{\mathbf{x}}(t) = \mathbf{f}(\mathbf{x}(t), \tau_{\text{PTO}}(t), \tau_{\text{ext}}(t)) \\ & \tau_{\text{PTO}}: \omega_{\text{arm}} \rightarrow \alpha_C \rightarrow \frac{1}{s} \int_{-1}^1 \rightarrow \tau_{\text{Coulomb}} \rightarrow \tau_{\text{PTO}} \\ & |\tau_{\text{PTO}}| \leq \tau_{\text{PTO,max}} \\ & P_{\text{out}}(t) = \begin{cases} \tau_{\text{PTO}}\omega_{\text{arm}} \eta_{\text{PTO}} & ; |\tau_{\text{PTO}}| = |\tau_{\text{Coulomb}}| \\ 0 & ; \text{else} \end{cases} \end{aligned}$$

As the Coulomb damping value is in the interval $\tau_{\text{Coulomb}} \in [0; \tau_{\text{PTO,max}}]$, the optimisation is performed by performing nine evaluations in the interval, whereafter the interval with the highest average power output is chosen. The found interval is divided into eight intervals, which are stepped through until the maximum is found. The optimisation is shown in Fig. 4.10, yielding a maximum of 7.8 kW.

A small section of the iteration with the optimum value $\tau_{\text{Coulomb}} = 0.375 \text{ MNm}$ is shown in Fig. 4.11. As the PTO efficiency enters linearly in the cost function, the optimisation only has to be performed for one value of η_{PTO} and the results may be scaled afterwards.

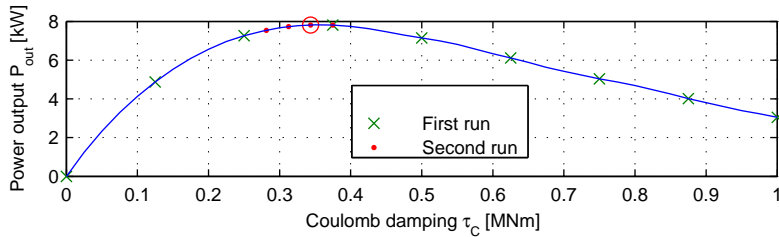


Figure 4.10: Optimisation of Coulomb damping for a sea state $H_{m0}=1.75$, $T_p=5.5$ s and an efficiency of $\eta_{PTO}=0.8$.

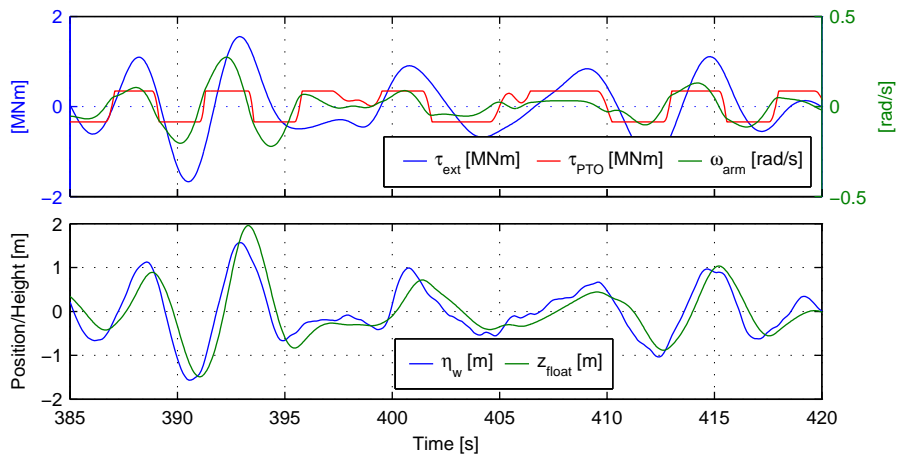


Figure 4.11: Simulation of Coulomb damping value for a sea state $H_{m0}=1.75$, $T_p=5.5$ s and $\tau_{Coulomb}=0.375$ MNm.

4.5 Latching Control

To improve the frequency response of point absorbers without using reactive power, a WPEA known as latching has been proposed and tested [53, 54, 28, 55, 56]. In the latching approach, the natural period of the absorber is non-linearly pro-longed by locking the absorber's movement in parts of its oscillation cycle. Depending on the implementation, the PTO may load with either a constant force or a linear damping force during the un-latched periods, where energy is generated.

An example of latching is seen in Fig. 4.12 for the Wavestar absorber in regular waves with a period of 4.5s. For the first 10s, the absorber is un-controlled whereafter latching is applied, locking the absorber's motion for 0.48s each time the absorber is at a top or bottom position (velocity equal to zero). As seen, the motion is greatly amplified, implying that resonant behaviour is achieved. A more direct evidence of the method is that the absorber velocity becomes in phase with excitation torque after latching control has been applied, which is consistent with the optimum conditions for power extraction.

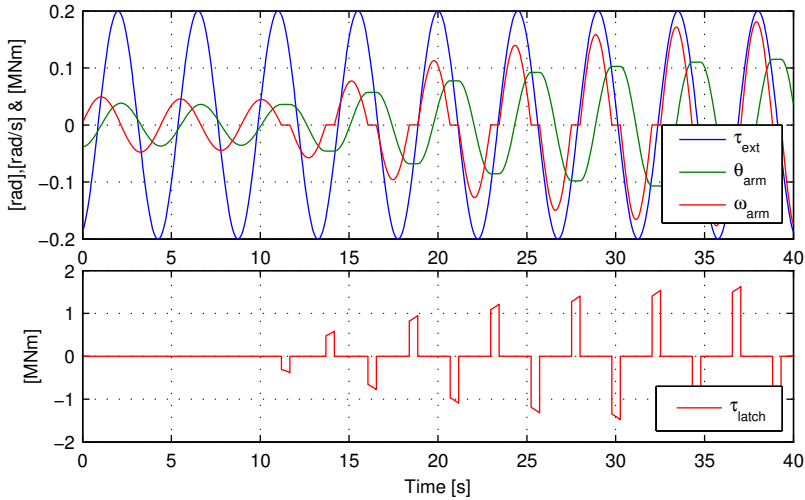


Figure 4.12: Example of latching on the C5 absorber in regular waves.

Inspecting the applied torque to hold the absorber fixed τ_{latch} , around 1.7MNm of latching torque is required for performing the optimal latching for an excitation torque amplitude of 0.2MNm. Even though the processed power is zero during the latching period, latching control imposes a large force requirement on the latching mechanism. Exploring the relation of available latching force and energy output is thus performed in this dissertation in order to evaluate the attractiveness of latching based PTOs.

During movement of the absorber, power may be extracted by the PTO τ_{PTO} by either applying a linear or constant damping force, depending on the PTO implementation.

As complex-conjugated control, determining the optimal latching control requires knowl-

edge of the future incoming waves [57, 54]. It is known that the latching instant always begin when the absorber velocity reaches zero, however, determination of the de-latching point requires future knowledge.

In order to make a just evaluation of latching, the future wave knowledge is assumed known such that the evaluation is not congested with more or less poorly implemented prediction algorithms by the author. Hence, a non-causal implementation is used.

The method used for optimising latching is based on the idea of Babarit et al. [54]. Optimisation is performed by “pausing” the time whenever the velocity becomes zero, which is where a latching period is initiated. In the pause, multiple simulations are performed on the available future to find the latching period optimising the motion amplitude for the next half oscillation. The “global” simulation is then resumed with this latching duration and next time the velocity vanishes, the procedure is repeated. The amplitude optimisation was in [54] found to give a higher yield than optimising the absorbed energy of each oscillation. Optimising the energy output on the next half oscillation causes the algorithm to focus on short term energy capture, which may not be optimal on successive periods. Maximising amplitude is in line with the resonance condition, which gives a higher output on successive oscillations as well.

During motion the PTO in [54] is set to behave as a linear damper with the same damping coefficient as the hydrodynamic damping coefficient. In this work the PTO damping coefficient is optimised as well. This is done with the experience that if optimum condition is not met due to force constraints, a better output is obtained by a slight over-damping. In [54], PTO constraints were not included.

The following two latching strategies are explored:

1. Latching with linear damping during motion
2. Latching with Coulomb damping during motion

These are both treated as these impose fundamental different requirements on a PTO.

In surveying state-of-the-art, studies exploring the available latching force versus extracted power have not been found. Accordingly, the allowed latching force is made finite in this work and formulated such, that if the required latching force is exceeded, the absorber is released. The used simulation model for optimising latching is illustrated in Fig.4.13. When the velocity is zero and the latching control algorithms decides to latch using the signal u_{latch} , a latching torque τ_{latch} is applied to the absorber, holding the absorber fixed. If the required latching torque $\tau_{\text{latch,req}}$ exceeds the threshold $\tau_{\text{latch,max}}$ the absorber is released, and may first be latched when the velocity ω_{arm} vanishes again.

During motion a PTO torque is applied, which is either a linear damper or a Coulomb damper, depending on the studied case. Given values of B_{PTO} or τ_{Coulomb} in a given sea state, the latching duration t_{latch} for each latching instance is found using the algorithm illustrated in Fig. 4.15. The global simulation of the model in Fig. 4.13 is started in an irregular wave. Each time the absorber velocity vanishes, the global simulation is paused. All state information of the model and future wave excitation torque is transferred to

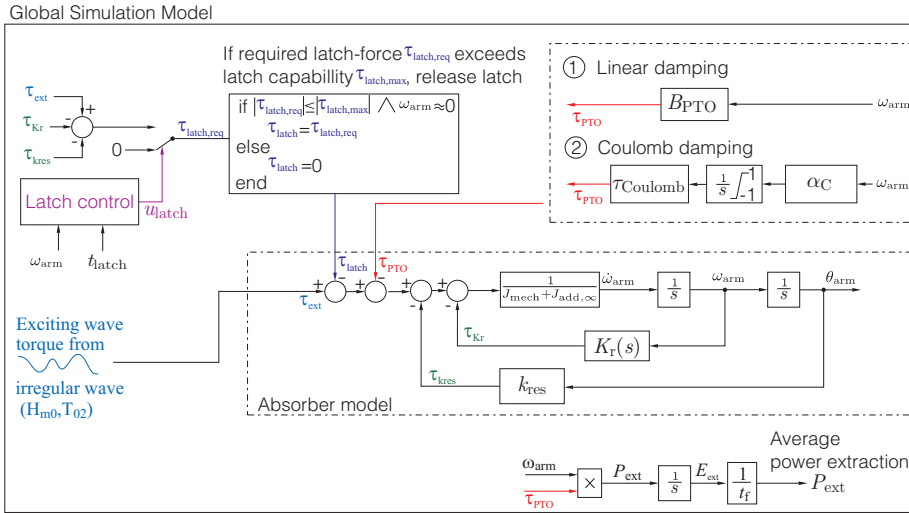


Figure 4.13: Simulation model of the latching control.

a copy of the model. This includes the current state information of the radiation force $K_r(s)$. The copy of the model is now tested for different t_{latch} values, identifying the t_{latch} leading to the highest motion amplitude of θ_{arm} . An example of the latching duration optimisation is given in Fig. 4.14. The sub-model is given an input consisting of repeated wave excitation of the next 8 second. For each repetition, the model resets itself to the initial condition and increments the latching duration. This allows executing one fast simulation and afterwards selecting the optimum. In the example of Fig. 4.14 the largest motion is obtained for a latching duration of $t_{latch} = 1.6$ s. The optimal value is fed back to the global simulation. The procedure is repeated each time the velocity vanishes.

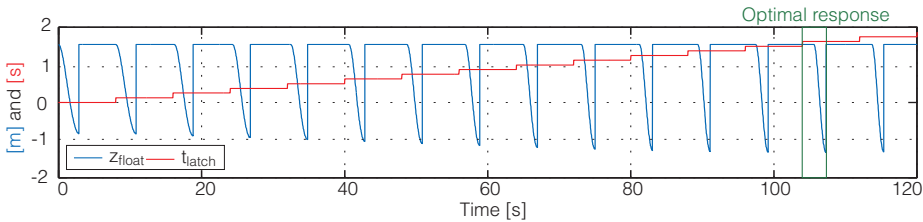


Figure 4.14: Optimising latching duration given a set of initial conditions and future wave excitation torque.

Finally, instead of using the PTO damping coefficient equal to the hydrodynamic damping as in [54], this parameter is also optimised. Note that each iteration of B_{PTO} require performing a complete irregular wave simulation with all the sub-optimisations of latching durations. The PTO damping coefficient is fixed for a given sea state. The same optimisation approach is used for the Coulomb damping parameter $\tau_{Coulomb}$.

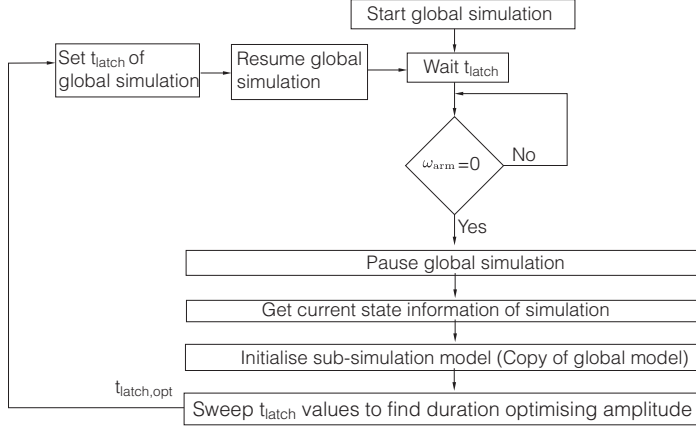


Figure 4.15: Algorithm for finding optimal latching period t_{latch} .

4.5.1 Optimisation of Latching with Realistic PTO

The problem to be solved is formulated below for the latching control with linear damping,

$$\begin{aligned}
 & \max_{B_{PTO}} \quad \frac{1}{t_f} \int_0^{t_f} P_{out}(t) dt \\
 \text{s.t.} \quad & \dot{\mathbf{x}}(t) = \mathbf{f}(\mathbf{x}(t), \tau_{PTO}(t), u_{latch}(t), \tau_{ext}(t)) \\
 & \tau_{PTO,ref} = \text{sat}(B_{PTO} \omega_{arm}, \tau_{PTO,max}) \\
 & \frac{\tau_{PTO}(s)}{\tau_{PTO,ref}(s)} = \frac{\omega_{n,PTO}}{s^2 + 2\zeta_{PTO} \omega_{n,PTO} s + \omega_{n,PTO}^2} \\
 & u_{latch} : \text{Controlled to maximise absorber amplitude} \\
 & |\tau_{latch}| \leq \tau_{latch,max} \\
 & |\tau_{PTO}| \leq \tau_{PTO,max} \\
 & P_{out}(t) = \tau_{PTO} \omega_{arm} \eta_{PTO}
 \end{aligned}$$

and the problem formulated for latching with Coulomb damping during motion:

$$\begin{aligned}
 & \max_{\tau_{Coulomb} \in [0; \tau_{PTO,max}]} \quad \frac{1}{t_f} \int_0^{t_f} P_{out}(t) dt \\
 \text{s.t.} \quad & \dot{\mathbf{x}}(t) = \mathbf{f}(\mathbf{x}(t), \tau_{PTO}(t), u_{latch}(t), \tau_{ext}(t)) \\
 & \tau_{PTO} : \omega_{arm} \rightarrow \left[\alpha_C \right] \rightarrow \left[\frac{1}{s} \int_{-1}^1 \right] \rightarrow \left[\tau_{Coulomb} \right] \rightarrow \tau_{PTO} \\
 & u_{latch} : \text{Controlled to maximise absorber amplitude} \\
 & |\tau_{latch}| \leq \tau_{latch,max} \\
 & |\tau_{PTO}| \leq \tau_{PTO,max} \\
 & P_{out}(t) = \begin{cases} \tau_{PTO} \omega_{arm} \eta_{PTO} & ; \tau_{PTO} = \tau_{Coulomb} \\ 0 & ; \tau_{PTO} \neq \tau_{Coulomb} \end{cases}
 \end{aligned}$$

To optimise with respect to B_{PTO} or $\tau_{Coulomb}$, a complete simulation of the model in

Fig. 4.13 for the given sea state is performed in each iteration. This includes performing all the sub-optimisations of the latching duration in each iteration.

The search algorithm for τ_{Coulomb} is to test nine points in the interval $\tau_{\text{Coulomb}} \in [0; \tau_{\text{PTO,max}}]$, whereafter the interval with the highest average power output is chosen. The chosen interval is divided into eight intervals, which is stepped through, until the maximum is found. This algorithm has been chosen instead of the simplex, as the value τ_{Coulomb} is bounded and easy to sweep.

For B_{PTO} , the initial values are initialised with $B_{\text{PTO}} = \frac{1}{2}B_{\text{hyd}}$ and incremented with large steps of $\frac{1}{2}B_{\text{hyd}}$ for each iteration until the average power output begins to decrease. At this point, eight values in the two last intervals are calculated to find maximum. The reason for using this method compared to the simplex method is that small local maxima have been experienced. Thus, the initial large steps ensure adequate step size for skipping local minima.

In the following, four optimised examples are given:

- Latching with linear damping where $\tau_{\text{PTO,max}} = 1 \text{ MNm}$ and $\tau_{\text{latch,max}} = 1 \text{ MNm}$.
- Latching with linear damping where $\tau_{\text{PTO,max}} = 1 \text{ MNm}$ and $\tau_{\text{latch,max}} = \infty$.
- Latching with Coulomb damping where $\tau_{\text{PTO,max}} = 1 \text{ MNm}$ and $\tau_{\text{latch,max}} = 1 \text{ MNm}$.
- Latching with Coulomb damping where $\tau_{\text{PTO,max}} = 1 \text{ MNm}$ and $\tau_{\text{latch,max}} = \infty$.

All examples are for $H_{m0} = 1.75$, $T_p = 5.5$ s. A small section of each simulation is shown for the optimum value of τ_{Coulomb} and B_{PTO} respectively.

In Fig. 4.16 latching with infinite latching torque is shown. The simulation shows that the latching duration is varying from wave to wave, and that the used optimisation algorithm of the latching period ensures that the exciting wave torque and absorber velocity are in phase as desired. The optimum damping coefficient is found to be $B_{\text{PTO}} = 1.68 \text{ MNs}$, which is close to the hydro-dynamic damping, which is 1 MNs at a wave period of 5.5 s. This also indicates that close to optimum conditions has been achieved as no over-damping is present.

In the simulation in Fig. 4.17 the latching torque is limited to 1 MNm . When the latching torque reaches 1 MNm , the absorber is released. Resultantly, the latching approach no longer brings the exciting wave torque and velocity into phase, and the absorber amplitude is reduced. The optimum damping coefficient in this case is found to be $B_{\text{PTO}} = 3.68 \text{ MNs}$, which is more than 3 times the hydro-dynamic damping coefficient. That over-damping is being resorted to increase power extraction indicates less resonant behaviour. Thus, when having finite latching torque, inclusion of the damping coefficient in the optimisation is very important, otherwise the used coefficient would have been less than a half the optimum value. Note that the average power output is reduced with about 35% compared to the unlimited case.

The Coulomb damping case with infinite latching torque is seen in Fig. 4.18. The phase condition is reasonable achieved, but the average power output is about 18% lower

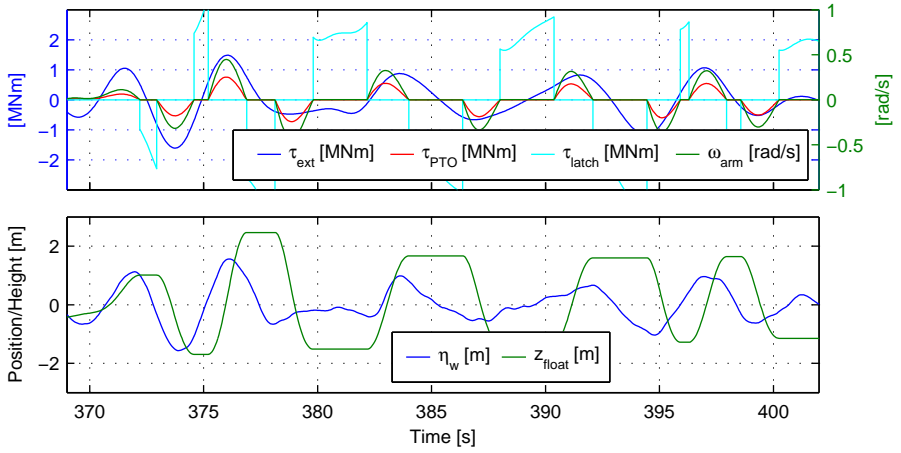


Figure 4.16: Simulation of optimal latching with linear damping for a sea state $H_{m0} = 1.75, T_p = 5.5$ s. PTO torque is limited to 1 MNm, whereas the latching torque τ_{latch} is unlimited. The optimal damping is found to be $B_{PTO} = 1.68$ MNs. For $\eta_{PTO} = 0.8$ the average power output is 22.2 kW.

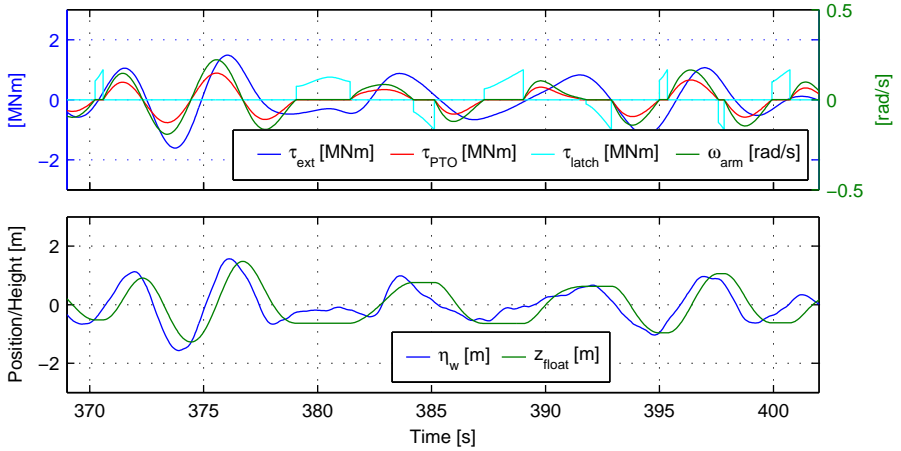


Figure 4.17: Simulation of optimal latching with linear damping for a sea state $H_{m0} = 1.75, T_p = 5.5$ s. PTO torque is limited to 1 MNm, whereas the latching torque τ_{latch} is limited to 1 MNm. The optimal damping is found to be $B_{PTO} = 3.98$ MNs. For $\eta_{PTO} = 0.8$ the average power output is 14.6 kW.

compared to the linear damping case. Moving to the Coulomb damping case with limited latching torque in Fig. 4.19, the phase condition is not satisfied. The average power output is reduced by 15% compared to the limited linear damping case.

Note that as latching is a resistive strategy, the PTO efficiency enters linearly in the output power. Hence, the shown optimisations only have to be performed for one value of η_{PTO} for each sea state and the results may be scaled afterwards for other PTO efficiencies.

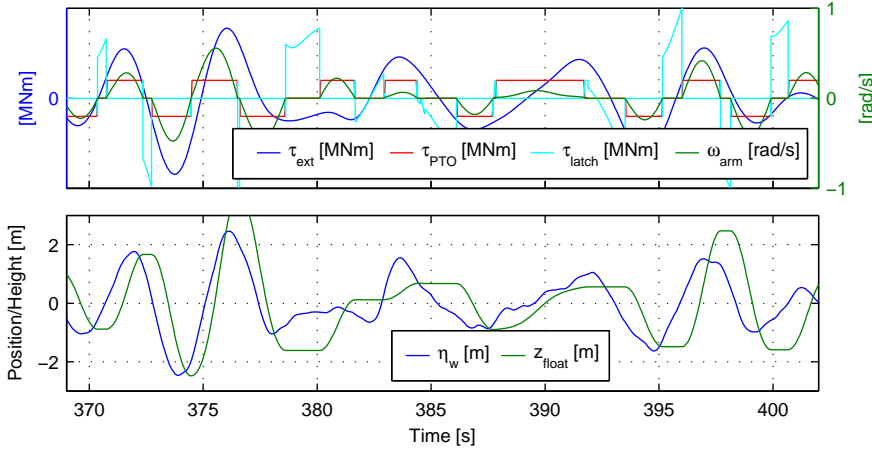


Figure 4.18: Simulation of optimal latching with Coulomb damping for a sea state $H_{m0}=1.75$, $T_p=5.5$ s. PTO and latching torque are limited to 1 MNm. The optimal Coulomb damping is found to be $\tau_{Coulomb}=0.3$ MNm. For $\eta_{PTO}=0.8$ the average power output is 18.3 kW.

4.6 De-Clutching Control

A method dual to latching has been proposed in [27] and [58] and is referred to as unlatching or de-clutching control. In de-clutching control the absorber motion is manipulated by shifting between applying full load force or no force. Like latching, de-clutching control is also non-causal. De-clutching control seems to have gotten less attention than latching control. In [58] it was shown that when using future knowledge, de-clutching control would lead to better power capture than linear damping, indicating that some phase manipulation is obtained through the method.

De-clutching control is tested on the Wavestar absorber for a regular wave in Fig. 4.20. Each time the velocity vanishes the PTO clutches and applies a constant PTO load force. After a duration t_{clutch} the PTO de-clutches and the absorber moves freely. Notice the motion amplification and that the control drives the excitation torque and velocity into phase as desired, i.e. the required optimum condition is being met.

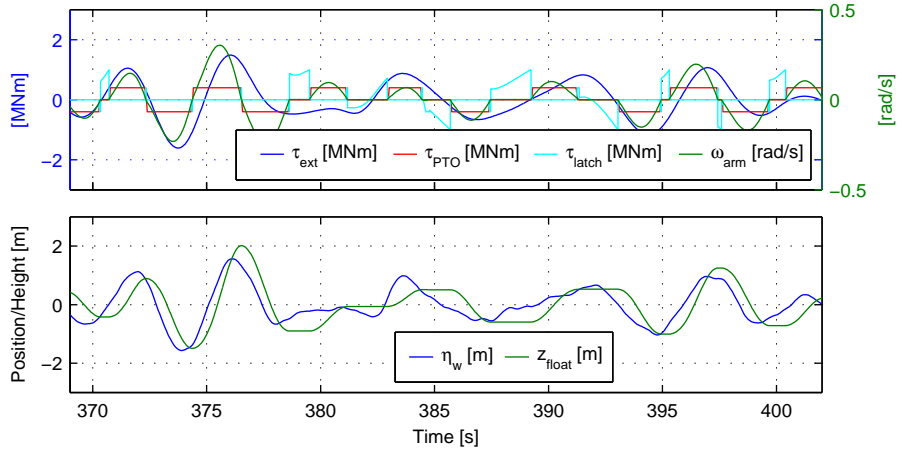


Figure 4.19: Simulation of optimal latching with Coulomb damping for a sea state $H_{m0}=1.75$, $T_p=5.5$ s. PTO and latching torque are limited to 1 MNm. The optimal Coulomb damping is found to be $\tau_{Coulomb}=0.4$ MNm. For $\eta_{PTO}=0.8$ the average power output is 12.4 kW.

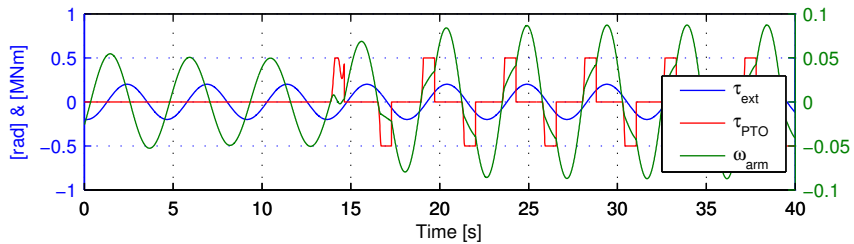


Figure 4.20: De-clutching control applied to the Wavestar absorber in regular waves.

To calculate the varying clutching duration in irregular waves a similar method as in latching control is defined. Each time the velocity vanishes, the simulation is paused, and different clutching durations t_{clutch} are tested. The algorithm and model is shown in Fig. 4.21. During the clutched period a constant damping force $\tau_{Coulomb}$ is applied, which is kept constant in magnitude for a given sea state. To ensure control stability and reflect a real PTO system, the Coulomb force “builds up” as a function of velocity as previously defined in Sec. 4.4, where the integration rate is determined by α_D . In the de-clutching instant, the integrator is reset to zero, which corresponds to assuming instant de-clutch.

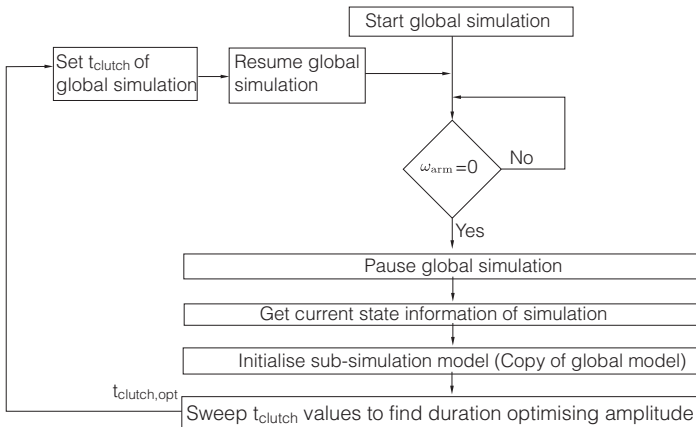
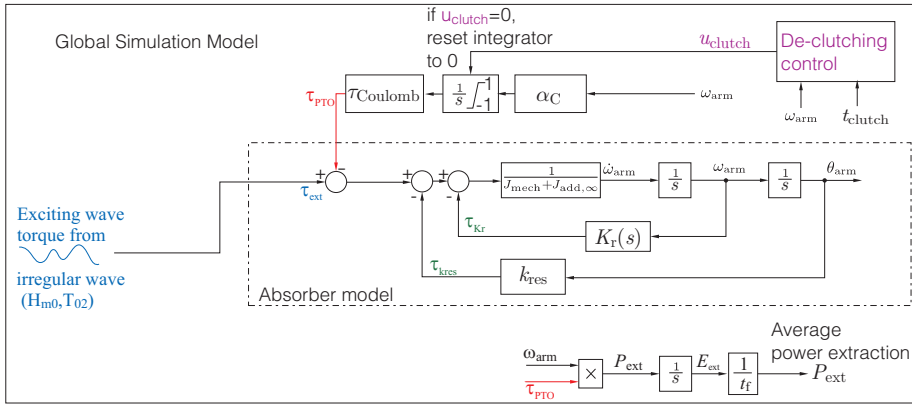


Figure 4.21: Model and control for simulating de-clutching control.

The assumption of the algorithm is that choosing the t_{clutch} maximising amplitude at each clutching instant will maximise energy extraction. To increase confidence in this assumption, a sweep of clutching durations has been performed in a regular wave with a period of 4.5s and a clutching force of $\tau_{Coulomb} = 1$ MNm. The resulting average power output from simulation of different clutch durations is given Fig. 4.22c, where the

optimum value is 0.88s. The same regular wave is applied to the system and algorithm in Fig. 4.20. The result is seen in Fig. 4.22a, showing that the algorithm settles on a clutch duration of 0.83s, equal to the optimum in the sweep. Hence, the approach of maximising amplitude is assumed valid for de-clutching control. The optimisation of clutch duration at each instant is seen in Fig. 4.22b.

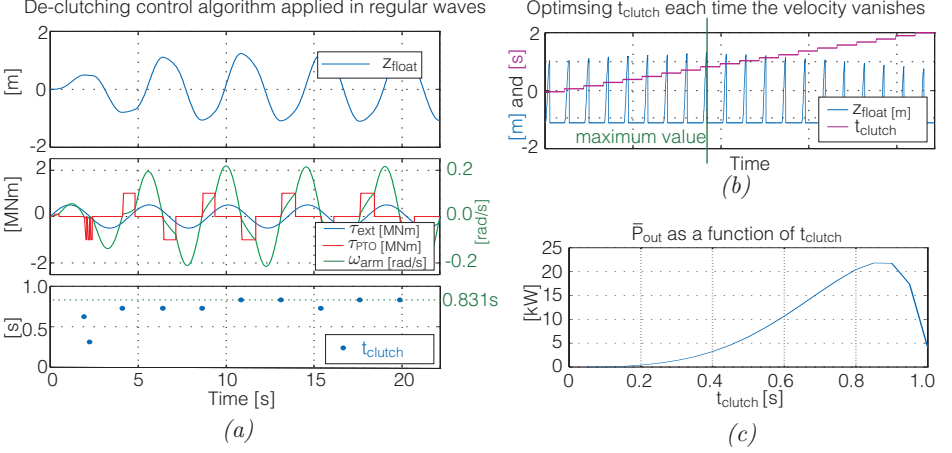


Figure 4.22: In (a) de-clutching algorithm applied in a regular wave. In (b) the optimisation performed for clutching duration for each instant. In (c) the average power output for different fixed clutching durations in the same regular wave.

4.6.1 Optimisation of De-Clutching with Realistic PTO

The optimisation problem to be solved for the de-clutching control is formulated below:

$$\begin{aligned}
 & \max_{\tau_{\text{Coulomb}} \in [0; \tau_{\text{PTO, max}}]} \frac{1}{t_f} \int_0^{t_f} P_{\text{out}}(t) dt \\
 \text{s.t.} \quad & \dot{\mathbf{x}}(t) = \mathbf{f}(\mathbf{x}(t), \tau_{\text{PTO}}(t), \tau_{\text{ext}}(t)) \\
 & \tau_{\text{PTO}}: \omega_{\text{arm}} \rightarrow \boxed{\alpha_C} \rightarrow \boxed{\frac{1}{s} \int_{-1}^1} \rightarrow \tau_{\text{Coulomb}} \rightarrow \tau_{\text{PTO}} \\
 & \quad \quad \quad u_{\text{clutch}}(t) \rightarrow \uparrow \text{reset int. to zero if } u_{\text{clutch}} = 0 \\
 & u_{\text{clutch}}: \text{Controlled to maximise absorber amplitude} \\
 & |\tau_{\text{PTO}}| \leq |\tau_{\text{PTO, max}}| \\
 P_{\text{out}}(t) = & \begin{cases} \tau_{\text{PTO}} \omega_{\text{arm}} \eta_{\text{PTO}} & ; |\tau_{\text{PTO}}| = |\tau_{\text{Coulomb}}| \\ 0 & ; \text{else} \end{cases}
 \end{aligned}$$

The used simulation of the model is given in Fig. 4.21. For each iteration of τ_{Coulomb} , a complete irregular wave simulation is performed with all the sub-optimisations of clutching durations.

The search algorithm for τ_{Coulomb} is to test nine points in the interval $\tau_{\text{Coulomb}} \in [0; \tau_{\text{PTO, max}}]$, whereafter the interval with the highest average power out is chosen. The

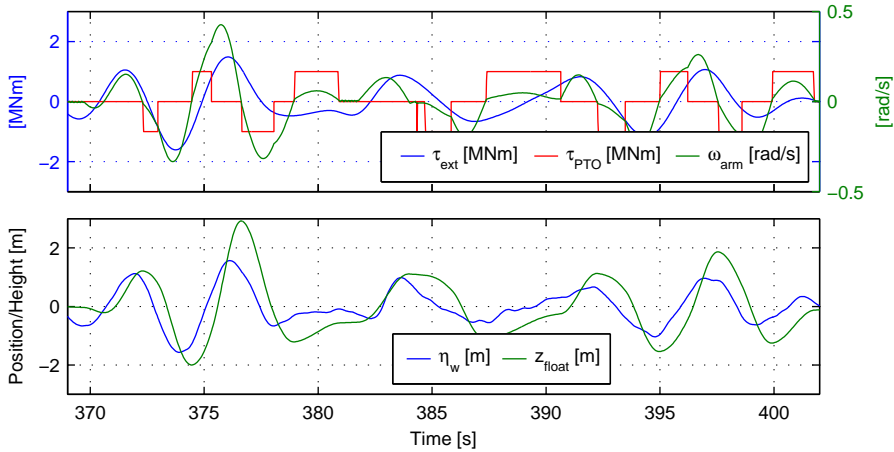


Figure 4.23: Simulation of optimal de-clutching for a sea state $H_{m0}=1.75$, $T_p=5.5$ s. The PTO torque is limited to 1 MNm. The optimal value is found to be $\tau_{Coulomb}=1$ MNm.

chosen interval is divided into eight intervals, which are stepped through, until the maximum is found.

In Fig. 4.23 the optimised de-clutching control is shown. The simulation shows that the clutching duration is varying from wave to wave. The optimum clutching torque $\tau_{Coulomb}$ is found to be 1 MNm, which is the limit in the example. This indicates that de-clutching control requires a very high load torque. The simulation also shows that with this torque limit, the control is unable to drive the excitation torque and velocity into phase. If the significant wave height is decreased to 1.25 m as in Fig. 4.24, running the same optimisation shows that the PTO has sufficient torque to force the excitation torque into phase with velocity. The reach phase condition also supports the validity of the used algorithm for finding the optimal clutching control. As other resistive strategies, the de-clutching control only has to be solved for one PTO efficiency.

4.7 Ratchet based PTO

As will be seen in state-of-the-art, a lot of PTO suggestions base on using a ratchet mechanism on the absorber motion, whereby the motion is rectified to drive a main shaft at a constant speed. Control wise, this means that the absorber will be free-wheeling until reaching the shaft speed where the ratchet clutches, locking absorber and shaft motion together. Hence the absorber is forced to move with the speed corresponding to the shaft speed. Most suggestions have a single ratchet, which means that the absorber will only be able to transfer power to the PTO in one direction. A functional illustration for the single ratchet PTO is given in Fig. 4.25a. The absorber is free-wheeling until ω_{arm} reaches the shaft speed ω_s in positive direction.

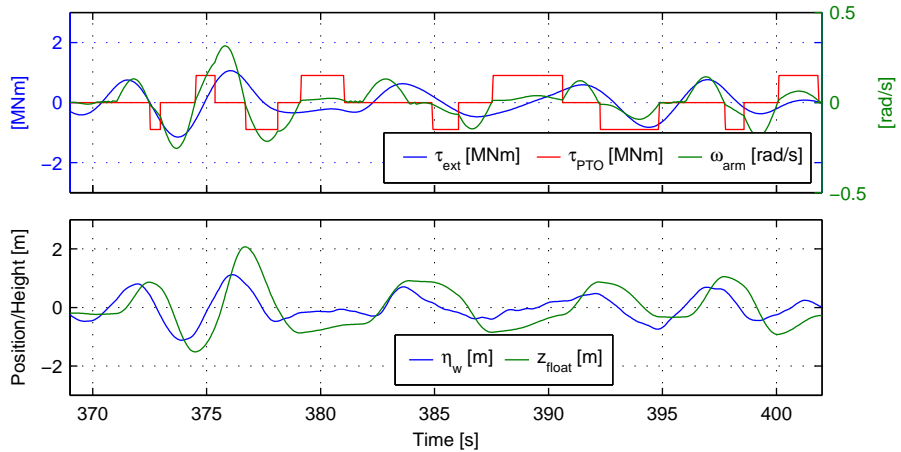


Figure 4.24: Simulation of optimal de-clutching for a sea state $H_{m0} = 1.25\text{ m}$, $T_p = 5.5\text{ s}$. PTO torque is limited to 1 MNm . The optimal value is found to be $\tau_{Coulomb} = 1\text{ MNm}$.

Some PTO implementations may also suggest having two ratchets (which may power the same generator shaft though some additional gears and mechanisms.) The functionality of the double-ratchet PTO is shown in Fig.4.25b. Here the PTO transfers power in both directions when $|\omega_s|$ reaches the speed of the shaft ω_s .

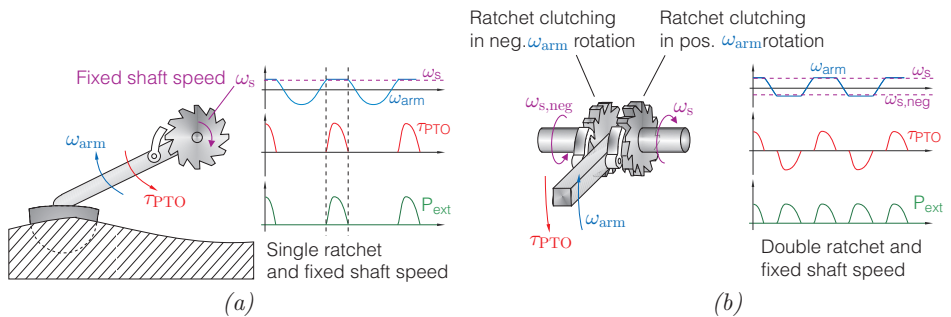


Figure 4.25: In (a) single ratchet PTO, and in (b) double ratchet.

To simulate the load induced by a single ratchet mechanism, the PTO torque is formulated as a very stiff spring when shaft and absorber motion is locked. At the instant ω_{arm} reaches ω_s , the ratchet will clutch (ideal ratchet) and the ratchet torque is applied as a

spring force based on defining a deflection θ_d between shaft and absorber movement:

$$\dot{\theta}_d = \begin{cases} \omega_{\text{arm}} - \omega_s & ; (\omega_{\text{arm}} \geq \omega_s \wedge \tau_{\text{PTO}} \leq \tau_{\text{PTO,max}}) \vee (\omega_{\text{arm}} \leq \omega_s \wedge \theta_d \neq 0) \\ 0 & ; \text{else} \end{cases} \quad (4.20)$$

$$\tau_{\text{PTO}} = \begin{cases} k_d \theta_d + B_d \omega_{\text{arm}} & ; \theta_d \neq 0 \\ 0 & ; \text{else} \end{cases} \quad [\text{Nm}] \quad (4.21)$$

$$P_{\text{out}} = \eta_{\text{PTO}} \tau_{\text{PTO}} \quad [\text{W}] \quad (4.22)$$

The parameter k_d determines the PTO torque as a function of deflection θ_d . The parameter is selected to be $k_d = \frac{1 \text{ MNm}}{0.005 \text{ rad}}$, corresponding to 1 MNm at 1.87° deflection (This is consistent with the torsion of a steel shaft required for transferring 1 MNm). To ensure a fast simulating and stable system, a coefficient B_d is added to dampen the introduced stiffness when the ratchet clutches. In the clutched period, the dynamics will be given as:

$$\omega_N = \sqrt{\frac{k_{\text{res}} + k_d}{J_{\text{mech}} + J_{\text{add}}}} \quad [\text{rad/s}] \quad (4.23)$$

$$\zeta = B_d + B_{\text{hyd}} \frac{1}{2\omega_N} \frac{1}{J_{\text{mech}} + J_{\text{add}}} \quad [-] \quad (4.24)$$

Thus, to model a stable clutch operation the damping factor ζ is selected to 1, yielding:

$$B_d = 2\omega_N \zeta (J_{\text{mech}} + J_{\text{add}}) - B_{\text{hyd}} = 60 \text{ MNms/rad} \quad (4.25)$$

Note that in Eq. (4.22) a maximum ratchet/PTO torque is included. The implemented saturation corresponds to that of an ideal slip-clutch, where a constant torque load is maintained, but the absorber motion is no longer limited to the shaft speed.

For the double-ratchet an extra equation is introduced similar to Eq. (4.21), describing the ratchet mechanism operating in reverse direction. The SIMULINK implementation of the double-ratchet is shown in Fig. 4.26.

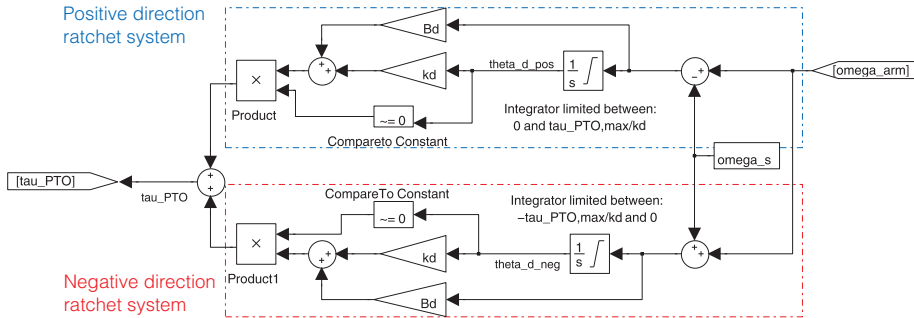
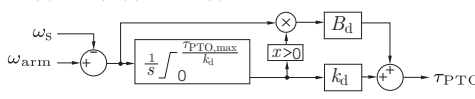


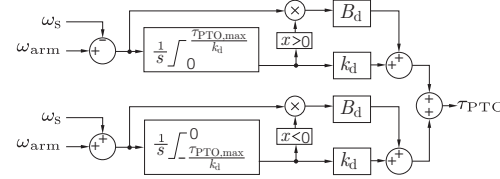
Figure 4.26: Double ratchet SIMULINK model.

4.7.1 Optimisation of Single and Double Ratchet based PTO

Given a torque limitation of the PTO $\tau_{\text{PTO,max}}$, the optimisation of the ratchet PTO is a one dimensional problem of choosing the best suited fixed shaft speed ω_s for a given sea state. The single ratchet problem is given in Eq. (4.26) and the double ratchet in Eq. (4.27).

$$\begin{aligned} \max_{\omega_s > 0} \quad & \frac{1}{t_f} \int_0^{t_f} P_{\text{out}}(t) dt \\ \text{s.t.} \quad & \dot{\mathbf{x}}(t) = \mathbf{f}(\mathbf{x}(t), \tau_{\text{PTO}}(t), \tau_{\text{ext}}(t)) \end{aligned}$$


$$P_{\text{out}}(t) = \tau_{\text{PTO}} \omega_{\text{arm}} \eta_{\text{PTO}} \quad (4.26)$$

$$\begin{aligned} \max_{\omega_s > 0} \quad & \frac{1}{t_f} \int_0^{t_f} P_{\text{out}}(t) dt \\ \text{s.t.} \quad & \dot{\mathbf{x}}(t) = \mathbf{f}(\mathbf{x}(t), \tau_{\text{PTO}}(t), \tau_{\text{ext}}(t)) \end{aligned}$$


$$P_{\text{out}}(t) = \tau_{\text{PTO}} \omega_{\text{arm}} \eta_{\text{PTO}} \quad (4.27)$$

To solve the optimisation the previously applied simplex algorithm is used. The optimisation is shown in Fig. 4.27. For this example a range of values has been computed to show the actual power output and how the algorithm performs. As initial value, a shaft speed of 0.01 rad/s is used. The optimisation finds the maximum in a few number of iteration at a value of $\bar{P}_{\text{out}} = 11.75 \text{ kW}$ and $\omega_s = 0.0585 \text{ rad/s}$.

A small section of the simulation is shown in Fig. 4.28 for the optimum value. As seen, the speed is limited in both directions, unless $\tau_{\text{PTO,max}}$ is exceeded.

Optimisation of the single ratchet system is seen in Fig. 4.30. The optimum is found at $\bar{P}_{\text{out}} = 11.86 \text{ kW}$ and $\omega_s = 0.025 \text{ rad/s}$. Thus, the single ratchet system yields the same output as the double ratchet system, but at approximately half the shaft speed. Whether this is general true will be seen in the WEPA comparison section. A section of the simulation is seen in Fig. 4.30. As seen, the velocity is only limited in positive direction.

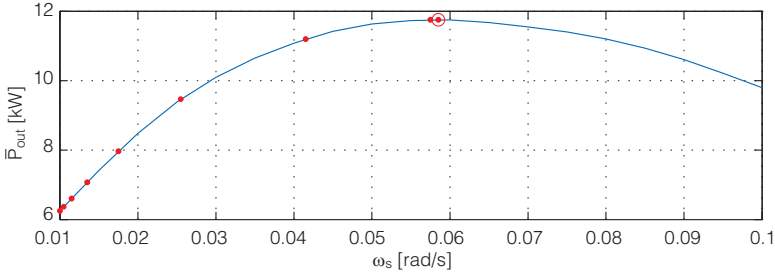


Figure 4.27: Optimisation of shaft speed for double ratchet PTO.

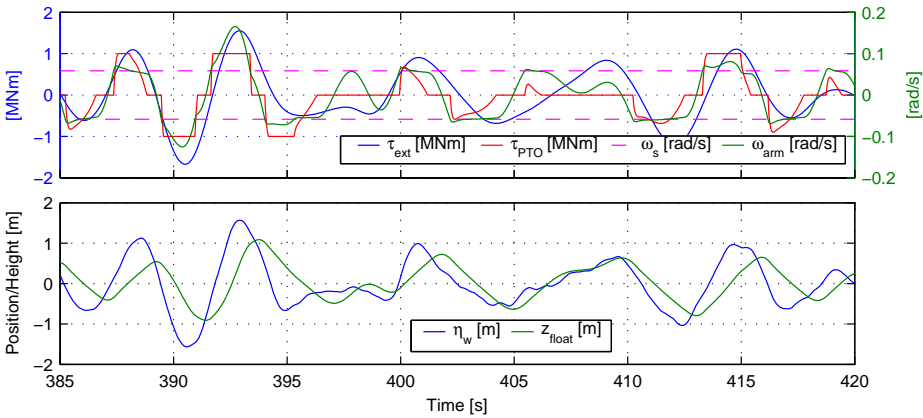


Figure 4.28: Iteration for the optimum shaft speed for the double ratchet PTO. The optimum is found at $\bar{P}_{out} = 11.75 \text{ kW}$ and $\omega_s = 0.0585 \text{ rad/s}$.

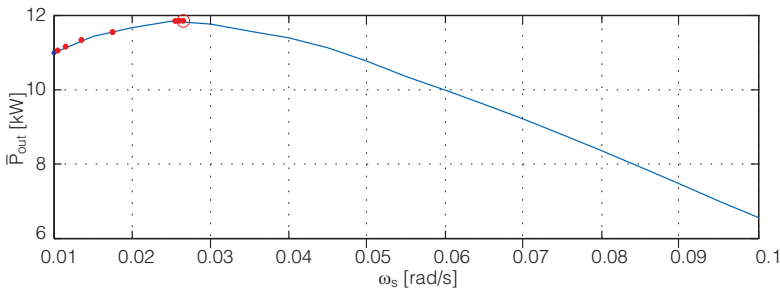


Figure 4.29: Optimisation of shaft speed for a single ratchet PTO.

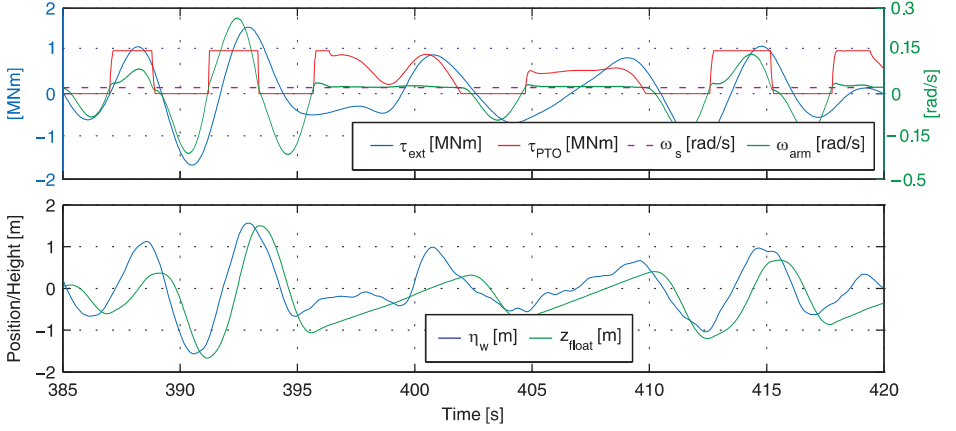


Figure 4.30: Iteration for the optimum shaft speed for the single ratchet PTO. The optimum is found at $\bar{P}_{out} = 11.86 \text{ kW}$ and $\omega_s = 0.025 \text{ rad/s}$.

4.8 OCIR Control

Motivated by the fact that non-linear resistive controls like latching may increase power extraction compared to linear damping, a new resistive WPEA is suggested. The idea of the new WPEA is to formulate a resistive law, which is causal in nature while approximating the energy output of reactive control laws through non-linear manipulation of the oscillation, i.e. the WPEA is characterised by having the Oscillation Control Implemented Resistively (OCIR).

Taking origin in the well-performing causal reactive control,

$$\tau_{PTO,ref} = k_{PTO}\theta_{arm} + B_{PTO}\omega_{arm} \text{ Nm} \quad (4.28)$$

the idea is first to remove the reactive part of this law. This leads to the formulation,

$$\Psi_{OCIR} = \begin{cases} k_{PTO}\theta_{arm} + B_{PTO}\omega_{arm} & ; (k_{PTO}\theta_{arm} + B_{PTO}\omega_{arm})\omega_{arm} \geq 0 \\ 0 & ; (k_{PTO}\theta_{arm} + B_{PTO}\omega_{arm})\omega_{arm} < 0 \end{cases} \quad (4.29)$$

where the periods with reverse power flow have been removed. This expression Ψ_{OCIR} is illustrated in Fig. 4.31a. The parts where the power flow become negative for the normal reactive law, the output of the Ψ_{OCIR} is zero. The next step is then to optimise the damping and “spring” coefficients accordingly.

To demonstrate the OCIR algorithm capability compared to reactive control an example is given for regular wave with period 4.5s and amplitude 0.3m. The PTO efficiency is set to $\eta_{PTO} = 0.8$ for both Ψ_k and Ψ_{OCIR} . Both are optimised to maximise energy output, yielding the results in Fig. 4.32. Both WPEAs are able to drive velocity and excitation torque into phase. The reactive control produces a perfect sinusoidal movement, whereas the OCIR control produces a distorted sinusoidal velocity due to the non-linear effects. Inspecting the average power output, the OCIR actually performs better with $\bar{P}_{out} =$

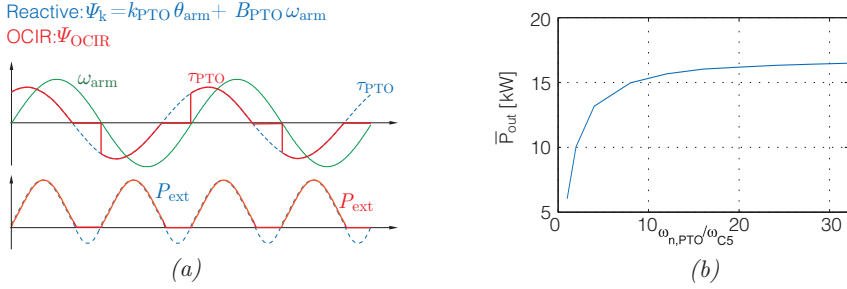


Figure 4.31: In (a) illustration of the OCIR control versus reactive control. In (b) average power out as a function of torque control bandwidth $\omega_{n,PTO}$ for the OCIR WPEA in regular waves with period 4.5s and amplitude 0.3m.

16.7kW compared to $\bar{P}_{out} = 14.7\text{kW}$ for the reactive law ($\eta_{PTO} = 0.8$). This may also be expected as the two WPEAs achieve same amplitude amplification, however, the OCIR method does it without reactive power. Note that the OCIR algorithm uses almost twice the PTO torque in the example.

The performance of the OCIR may be dependent on how rapid the torque is engaged. For the regular wave case, the natural frequency of the second order filter for describing the PTO's tracking dynamics has been varied, yielding the result in Fig. 4.31b. For adequate power production the bandwidth of the filter has to be about 10 times the natural frequency of the absorber, i.e. 3Hz for the C5.

4.8.1 Optimisation of OCIR control with Realistic PTO

The optimisation of the OCIR control is a two dimensional problem of choosing the best suited set of B_{PTO} and k_{PTO} :

$$\begin{aligned}
 \max_{k_{PTO}, B_{PTO}} \quad & \frac{1}{t_f} \int_0^{t_f} P_{out}(t) dt & (4.30) \\
 \text{s.t.} \quad & \dot{\mathbf{x}}(t) = \mathbf{f}(\mathbf{x}(t), \tau_{PTO}(t), \tau_{ext}(t)) \\
 & \frac{\tau_{PTO}(s)}{\tau_{PTO,ref}(s)} = \frac{\omega_{n,PTO}^2}{s^2 + 2\zeta_{PTO}\omega_{n,PTO}s + \omega_{n,PTO}^2} \\
 & \tau_{PTO,ref} = \begin{cases} k_{PTO}\theta_{arm} + B_{PTO}\omega_{arm} & ; (k_{PTO}\theta_{arm} + B_{PTO}\omega_{arm})\omega_{arm} \geq 0 \\ 0 & ; (k_{PTO}\theta_{arm} + B_{PTO}\omega_{arm})\omega_{arm} < 0 \end{cases} \\
 & P_{out}(t) = \begin{cases} \tau_{PTO}\omega_{arm} \eta_{PTO} & ; \tau_{PTO}\omega_{arm} > 0 \\ \tau_{PTO}\omega_{arm} \frac{1}{\eta_{PTO}} & ; \tau_{PTO}\omega_{arm} \leq 0 \end{cases}
 \end{aligned}$$

To perform the optimisation, an initial value is found by calculating the optimal control parameters based on an regular wave with a period equal to the peak period by solving Eq. (3.57).

To solve the optimisation the simplex algorithm is utilised. The optimisation is shown in Fig. 4.33. For this example a grid of values has been computed to show the actual power output and how the algorithm performs.

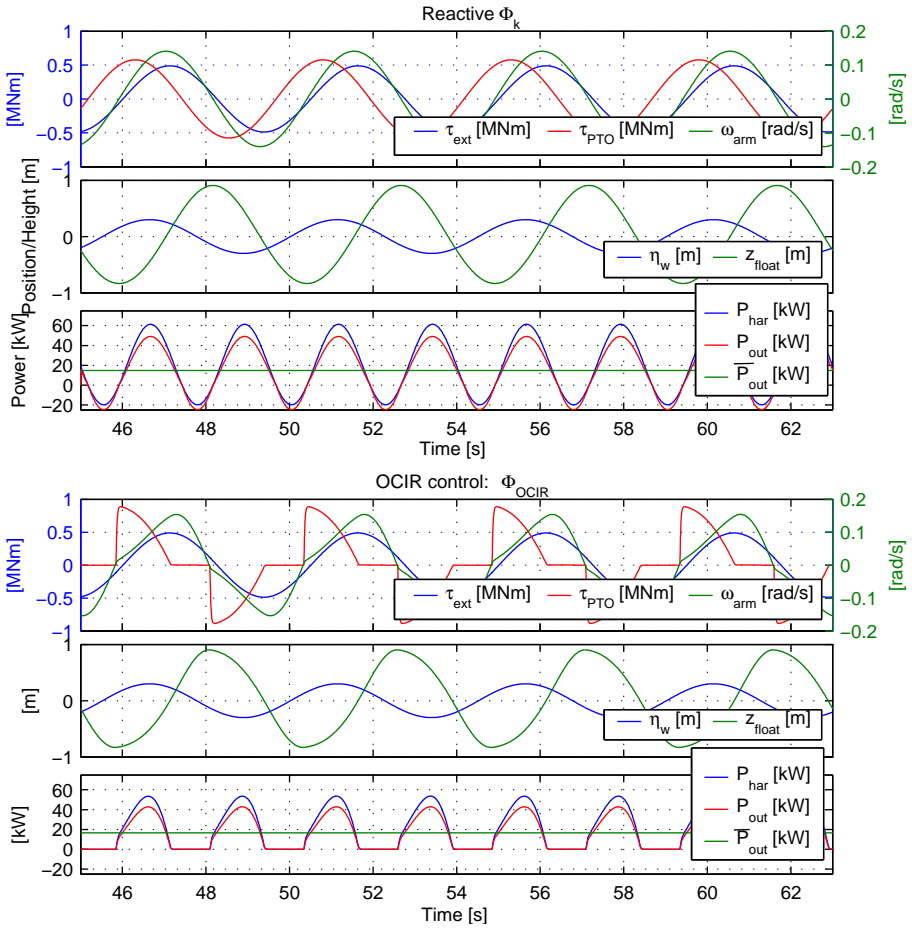


Figure 4.32: Simulation of the optimal OCIR control ($\bar{P}_{out} = 16.7 \text{ kW}$, $\bar{P}_{ext} = 20.8 \text{ kW}$) and reactive control ($\bar{P}_{out} = 14.7 \text{ kW}$, $\bar{P}_{ext} = 20.8 \text{ kW}$) in a regular wave for $\eta_{PTO} = 0.8$.

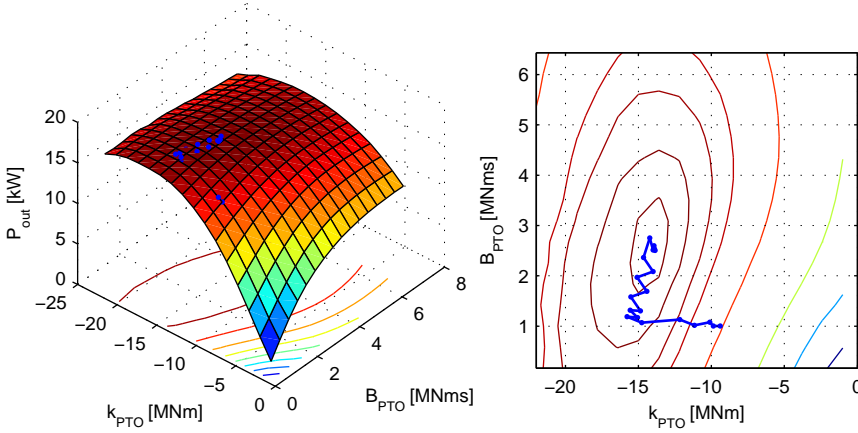


Figure 4.33: Optimisation of OCIR control for a sea state $H_{m0}=1.75$, $T_p=5.5$ s, a PTO torque limitation of $\tau_{PTO,max}=1$ MNm and an efficiency of $\eta_{PTO}=0.8$.

A small section of the simulation is shown in Fig. 4.34 for the optimum value of k_{PTO} and B_{PTO} . The optimum values often lets the PTO torque reference saturate. The average power output is $\bar{P}_{out}=18.7$ kW, where linear damping control gave 11.47 kW for the same wave. In this regard, linear damping may be seen as a waste of controllability, as the OCIR gives 63% more energy with the exact same PTO.

4.9 Comparison of WPEA Algorithms

For the nine wave energy extraction algorithms listed in Fig. 4.3 on page 72, power matrices of power output have been found for the following combinations of PTO characteristics:

Reactive control:

$$\begin{aligned} \tau_{PTO,max} &\in \{0.25, 0.375, 0.5, 0.625, 0.75, 0.875, 1.0, \dots \\ &\quad 1.125, 1.25, 1.375, 1.5, 1.625, 1.75, 2, 2.25, 2.5\} \text{ MNm} \\ \eta_{PTO,1} &\in \{0.40, 0.45, 0.50, \dots, 1.00\} \\ \eta_{PTO,2} &= 1 \\ \omega_{n,PTO} &= 2\pi \cdot 3 \text{ rad/s} \end{aligned}$$

Linear damping control:

$$\begin{aligned} \tau_{PTO,max} &\in \{0.25, 0.375, 0.5, 0.625, 0.75, 0.875, 1.0, 1.125, 1.25\} \text{ MNm} \\ \eta_{PTO} &= 1.0 \\ \omega_{n,PTO} &= 2\pi \cdot 3 \text{ rad/s} \end{aligned}$$

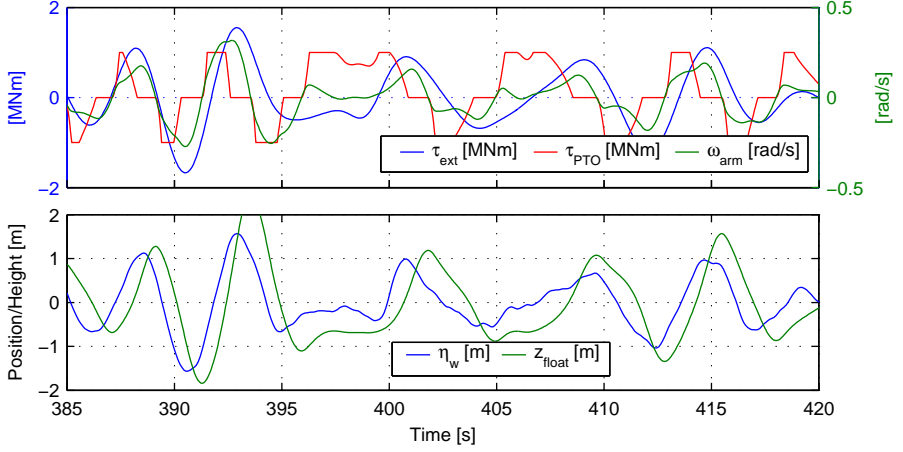


Figure 4.34: Simulation of OCIR control for a sea state $H_{m0} = 1.75$, $T_p = 5.5$ s with $\tau_{PTO,max} = 1$ MNm, and $k_{PTO} = -13.9$ MNm and $B_{PTO} = 2.5$ MNms.

OCIR control:

$$\begin{aligned}\tau_{PTO,max} &\in \{0.25, 0.375, 0.5, 0.75, 1.0, 1.25, 1.5, 1.75, 2, 2.25, 2.5\} \text{ MNm} \\ \eta_{PTO} &= 1.0 \\ \omega_{n,PTO} &= 2\pi \cdot 3 \text{ rad/s}\end{aligned}$$

Latching with linear damping:

$$\begin{aligned}\tau_{PTO,max} &\in \{0.25, 0.5, 0.75, 1.0, 1.25\} \text{ MNm} \\ \eta_{PTO} &= 1.0 \\ \omega_{n,PTO} &= 2\pi \cdot 3 \text{ rad/s} \\ \gamma_{latch} &= \frac{\tau_{latch,max}}{\tau_{PTO,max}} \in \{1, 2, 3\}\end{aligned}$$

Latching with Coulomb damping:

$$\begin{aligned}\tau_{PTO,max} &\in \{0.25, 0.5, 0.75, 1.0, 1.25\} \text{ MNm} \\ \eta_{PTO} &= 1.0 \\ \alpha_D &= 10001/\text{rad} \\ \gamma_{latch} &= \frac{\tau_{latch,max}}{\tau_{PTO,max}} \in \{1, 2, 3\}\end{aligned}$$

De-clutching control:

$$\begin{aligned}\tau_{PTO,max} &\in \{0.35, 0.5, 0.75, 1.0, 1.25\} \text{ MNm} \\ \eta_{PTO} &= 1.0 \\ \alpha_D &= 10001/\text{rad}\end{aligned}$$

Double ratchet PTO:

$$\begin{aligned}\tau_{\text{PTO,max}} &\in \{0.35, 0.5, 0.75, 1.0, 1.25\} \text{ MNm} \\ \eta_{\text{PTO}} &= 1.0 \\ k_d &= 200\text{e6 Nm/rad}, B_d = 60\text{e6 Nms/rad}\end{aligned}$$

Single ratchet PTO:

$$\begin{aligned}\tau_{\text{PTO,max}} &\in \{0.375, 0.5, 0.75, 1.0, 1.25\} \text{ MNm} \\ \eta_{\text{PTO}} &= 1.0 \\ k_d &= 200\text{e6 Nm/rad}, B_d = 60\text{e6 Nms/rad}\end{aligned}$$

Coulomb damping:

$$\begin{aligned}\tau_{\text{PTO,max}} &\in \{0.25, 0.375, 0.5, 0.625, 0.75, 0.875, 1.0, 1.125, 1.25\} \text{ MNm} \\ \eta_{\text{PTO}} &= 1.0 \\ \alpha_C &= 142 \text{ MNm}\end{aligned}$$

Note that γ_{latch} define the available latching torque relative to available damping torque. If $\gamma_{\text{latch}} = 3$, the PTO may use a latching torque 3 times the maximum damping torque $\tau_{\text{PTO,max}}$.

Note that only the reactive control has been required optimised for different PTO efficiencies. For the resistive laws, the optimum is independent of this property. All WPEAs have been evaluated in the sea states given by the combinations of $T_{0,2} = \{2.5, 3.5, 4.5, 5.5, 6.5, 7.5\}$ s and $H_{m0} = \{0.75, 1.25, 1.75, 2.25, 2.75\}$ m.

4.9.1 A Selection of Power Matrices

A selection of power output matrices \mathbf{P}_{mat} [kW] are shown in Tab. 4.4 for $\eta_{\text{PTO}} = 0.8$ and $\tau_{\text{PTO,max}} = 1$ MNm. For the reactive case, the efficiency is defined such that the reactive power travels through the entire PTO, $\eta_{\text{PTO},1} = 0.8$ and $\eta_{\text{PTO},2} = 1$. The blue numbers are the performance relative to the reactive control. The matrices are roughly sorted according to performance. From the table the following may be implied:

- Overall the OCIR control and latching with linear damping ($\tau_{\text{latch,max}} = 3$ MNm) have the highest power output.
- The performance of latching with linear damping outperforms the latching strategy using Coulomb damping.
- If the allowed latching torque is high, latching with linear damping is the best performing WEPA at wave periods longer than the natural period of the absorber (3.5s).
- If the allowed latching torque is the same as the allowed damping torque (1 MNm), latching produces approx. 20% less than reactive control, implying a high latching torque is required.

- The OCIR has the best utilisation of available torque, as latching with $\tau_{\text{latch,max}} = 1 \text{ MNm}$ performs poorly.
- If the available torque is 1 MNm , de-clutching control is a better choice than latching and linear damping. Also notice that de-clutching with 1 MNm and latching with Coulomb damping at $\tau_{\text{latch,max}} = 3 \text{ MNm}$ are performing equally. Thus, de-clutching is a good strategy when having a constant force damping.
- The single ratchet and double ratchet have approximately the same performance except at long periods, where the single ratchet is penalised, as it requires a higher PTO torque. Their performance is around 0.65 compared to reactive control.
- Linear damping performance is similar to the single and double ratchet control.
- Linear damping is the poorest utilisation of continuous torque control.
- Coulomb damping is the weakest strategy, having a performance of about 0.45 compared to reactive control.

4.9.2 Comparing Yearly Production of WPEAs

To compare the WPEAs as a function of efficiency and available PTO torque, the annual production is calculated according to Eq. (4.5) on page 73. The resistive strategies are presented for $\eta_{\text{PTO}} = 1$, as the efficiency enters linearly in the estimated production:

$$\bar{P}_{\text{out}}(\eta_{\text{PTO}}) = \frac{1}{t_f} \int_0^{t_f} \tau_{\text{PTO}} \omega_{\text{arm}} \eta_{\text{PTO}} dt = \frac{\eta_{\text{PTO}}}{t_f} \int_0^{t_f} \tau_{\text{PTO}} \omega_{\text{arm}} dt = \eta_{\text{PTO}} \bar{P}_{\text{out}} \Big|_{\eta_{\text{PTO}}=1}$$

Hence, for other efficiencies than 100%, the output may be obtained by multiplying with η_{PTO} . The 100% curves are plotted in Fig. 4.35 and are directly comparable. The next step is to also include the reactive control curves, such that direct comparison is allowed.

For the reactive strategies, the total efficiency was defined as $\eta_{\text{PTO}} = \eta_{\text{PTO},1} \eta_{\text{PTO},2}$, where $\eta_{\text{PTO},1}$ is the efficiency of the part in-which the reactive power travels. That the power does not travel the entire PTO is possible if some intermediate storage is present in the PTO, see Fig. 4.6 on page 76 where this is discussed. If the reactive power travels through the entire PTO, then $\eta_{\text{PTO}} = \eta_{\text{PTO},1}$. If denoting the power travelling between storage and absorber as P_{stor} , then

$$P_{\text{stor}} = \begin{cases} \eta_{\text{PTO},1} P_{\text{ext}}(t) & ; P_{\text{ext}}(t) > 0 \\ \frac{1}{\eta_{\text{PTO},1}} P_{\text{ext}}(t) & ; P_{\text{ext}}(t) \leq 0 \end{cases} \quad (4.31)$$

$$\bar{P}_{\text{stor}} = \frac{1}{t_f} \int_0^{t_f} P_{\text{stor}} dt \quad (4.32)$$

$$\bar{P}_{\text{out}} = \eta_{\text{PTO},2} \bar{P}_{\text{stor}} \quad (4.33)$$

Accordingly, $\eta_{\text{PTO},2}$ was set to one in the optimisations as this may be post multiplied for other efficiencies of the secondary part of the PTO. The calculated output \bar{P}_{out} is thus for $\eta_{\text{PTO}} = \eta_{\text{PTO},1}$. The curves of actual output \bar{P}_{out} for the reactive WPEAs

Table 4.4: Average power output matrices \mathbf{P}_{mat} [kW] for $\tau_{PTO,max}=1MNm$ and $\eta_{PTO}=0.8$. Blue numbers denote the performance relative to reactive control.

		Reactive control					
H_{m0} [m]		T_{02} [s]					
		2.50	3.50	4.50	5.50	6.50	7.50
0.75		1.00	2.75	4.23	4.82	5.50	6.27
1.25		2.91	7.63	10.92	11.45	10.87	10.04
1.75		5.70	15.00	19.47	19.40	17.93	16.56
2.25		9.43	24.18	29.33	28.39	25.78	23.40
2.75		14.08	34.85	40.24	38.20	34.14	30.51

H_{m0} [m]		Latching w. linear damping: $\eta_{latch} = \frac{\eta_{latch,max}}{\tau_{PTO,max}} = 3$					
		T_{02} [s]					
		2.50	3.50	4.50	5.50	6.50	7.50
0.75		0.80	2.47	3.74	4.25	5.35	4.95
		0.80	0.90	0.88	0.88	0.97	0.79
1.25		2.24	7.67	11.35	12.99	13.72	11.39
		0.77	1.01	1.04	1.14	1.26	1.13
1.75		3.69	15.69	20.63	21.62	23.11	20.30
		0.65	1.05	1.06	1.11	1.29	1.23
2.25		5.79	22.85	31.55	33.95	33.40	28.22
		0.61	0.94	1.08	1.20	1.30	1.21
2.75		9.29	34.33	43.17	45.33	43.72	32.21
		0.66	0.98	1.07	1.19	1.28	1.06

H_{m0} [m]		OCIR control					
		T_{02} [s]					
		2.50	3.50	4.50	5.50	6.50	7.50
0.75		1.08	3.24	5.20	5.88	5.85	5.68
		1.07	1.18	1.23	1.22	1.07	0.91
1.25		3.00	8.83	12.23	12.93	12.49	11.34
		1.03	1.16	1.12	1.14	1.15	1.12
1.75		5.94	16.38	20.68	20.95	18.64	16.91
		1.04	1.09	1.06	1.08	1.04	1.02
2.25		9.82	25.41	30.29	29.79	27.46	22.37
		1.04	1.05	1.03	1.05	1.07	0.96
2.75		14.67	35.71	40.93	39.28	31.13	27.86
		1.04	1.02	1.02	1.03	0.91	0.91

H_{m0} [m]		De-clutching control					
		0.91	2.81	3.88	3.88	3.59	2.93
0.75		0.90	1.02	0.92	0.81	0.65	0.47
1.25		2.46	7.03	10.16	10.48	9.60	7.84
		0.85	0.92	0.93	0.92	0.88	0.78
1.75		4.91	13.74	18.19	17.50	16.10	14.56
		0.86	0.92	0.93	0.90	0.90	0.88
2.25		7.99	19.97	26.64	26.40	24.31	19.63
		0.85	0.83	0.91	0.93	0.94	0.84
2.75		12.05	28.19	35.22	33.90	30.08	26.70
		0.86	0.81	0.88	0.89	0.88	0.88

H_{m0} [m]		Latching w. Coulomb damping: $\eta_{latch} = \frac{\eta_{latch,max}}{\tau_{PTO,max}} = 3$					
		0.56	2.37	3.08	3.94	4.22	4.24
0.75		0.56	0.86	0.73	0.82	0.77	0.68
1.25		1.62	6.33	9.68	10.01	10.82	10.32
		0.56	0.83	0.89	0.88	1.00	1.03
1.75		3.70	13.12	18.29	19.26	17.94	17.11
		0.65	0.88	0.94	0.99	1.00	1.03
2.25		5.79	21.87	25.30	29.02	26.97	26.01
		0.61	0.90	0.86	1.02	1.05	1.11
2.75		8.31	30.63	37.58	39.45	37.19	34.05
		0.59	0.88	0.93	1.03	1.09	1.12

H_{m0} [m]		Latching w. linear damping: $\eta_{latch} = \frac{\eta_{latch,max}}{\tau_{PTO,max}} = 1$					
		0.69	2.56	3.30	3.73	3.50	3.39
0.75		0.69	0.93	0.78	0.77	0.64	0.54
1.25		1.91	7.09	8.59	8.77	7.87	6.69
		0.66	0.93	0.79	0.77	0.72	0.67
1.75		4.05	11.98	14.59	14.92	13.31	11.36
		0.71	0.80	0.75	0.77	0.74	0.69
2.25		8.88	19.25	22.80	22.42	20.43	17.98
		0.94	0.80	0.78	0.79	0.79	0.77
2.75		14.05	27.55	31.68	30.12	28.39	25.77
		1.00	0.79	0.79	0.79	0.83	0.84

H_{m0} [m]		Latching w. Coulomb damping: $\eta_{latch} = \frac{\eta_{latch,max}}{\tau_{PTO,max}} = 1$					
		0.59	2.48	3.02	3.22	3.20	2.99
0.75		0.59	0.90	0.72	0.67	0.58	0.48
1.25		1.94	6.01	7.03	7.15	6.74	6.14
		0.67	0.79	0.64	0.63	0.62	0.61
1.75		4.19	10.39	12.37	12.33	11.46	10.26
		0.74	0.69	0.64	0.64	0.64	0.62
2.25		7.93	16.15	19.12	19.19	17.63	15.84
		0.84	0.67	0.65	0.68	0.68	0.68
2.75		11.57	23.14	27.58	27.57	25.60	22.99
		0.82	0.66	0.69	0.72	0.75	0.75

H_{m0} [m]		Double ratchet					
		0.85	1.75	1.98	1.99	1.84	1.67
0.75		0.85	0.64	0.47	0.41	0.34	0.27
1.25		2.37	4.87	5.61	5.77	5.47	5.04
		0.81	0.64	0.51	0.51	0.50	0.50
1.75		4.65	9.86	11.62	11.75	11.13	10.24
		0.82	0.66	0.60	0.61	0.62	0.62
2.25		7.84	16.89	19.69	19.49	18.23	16.72
		0.83	0.70	0.67	0.69	0.71	0.71
2.75		12.08	25.70	29.33	28.60	26.53	24.17
		0.86	0.74	0.73	0.75	0.78	0.79

H_{m0} [m]		Single ratchet					
		0.89	1.95	2.16	2.02	1.79	1.60
0.75		0.89	0.71	0.51	0.42	0.33	0.26
1.25		2.61	5.72	6.33	5.90	5.25	4.68
		0.90	0.75	0.58	0.52	0.48	0.47
1.75		5.42	11.04	11.94	11.54	10.37	9.08
		0.95	0.74	0.61	0.59	0.58	0.55
2.25		9.10	17.67	18.98	17.57	15.48	13.60
		0.97	0.73	0.65	0.62	0.60	0.58
2.75		13.50	25.39	26.51	23.67	20.81	18.16
		0.96	0.73	0.66	0.62	0.61	0.60

H_{m0} [m]		Linear damping					
		1.03	1.91	2.11	0.52	0.30	0.18
0.75		1.02	0.70	0.50	0.11	0.05	0.03
1.25		2.93	5.32	5.85	5.75	5.44	5.11
		1.01	0.70	0.54	0.51	0.50	0.51
1.75		5.75	10.43	11.47	11.29	10.67	9.90
		1.01	0.70	0.59	0.58	0.59	0.60
2.25		9.50	17.25	18.98	18.53	17.39	16.05
		1.01	0.71	0.65	0.65	0.67	0.69
2.75		14.19	25.80	28.14	27.22	25.33	23.22
		1.01	0.74	0.70	0.71	0.74	0.76

H_{m0} [m]		Coulomb damping					
		0.78	1.16	1.11	1.07	1.05	1.01
0.75		0.78	0.42	0.26	0.22	0.19	0.16
1.25		2.38	3.58	3.65	3.68	3.68	3.51
		0.82	0.47	0.33	0.32	0.34	0.35
1.75		4.76	7.35	7.77	8.02	7.97	7.54
		0.84	0.49	0.40	0.41	0.44	0.46
2.25		7.98	12.52	13.57	14.09	13.88	12.98
		0.85	0.52	0.46	0.50	0.54	0.55
2.75		11.99	19.06	20.98	21.97	21.56	19.90
		0.85	0.55	0.52	0.57	0.63	0.65

for different $\eta_{\text{PTO}} = \eta_{\text{PTO},1}$'s may not directly coexist in the same plot as the resistive strategies as these are for $\eta_{\text{PTO}} = 1$. Hence, direct comparison of the yearly production would not be possible. To this end the reactive results are scaled with $\frac{1}{\eta_{\text{PTO},1}}$, which allow direct comparison with the resistive laws.

That this make sense may seen as follows. If the total efficiency of PTO for linear damping control is $\eta_{\text{PTO}} = 0.8$, the curves values is read and multiplied with 0.8, yielding the actual output as:

$$E_{\text{year}}|_{\eta_{\text{PTO}}=0.8} = 0.8 \underbrace{E_{\text{year}}|_{\eta_{\text{PTO}}=1}}_{\text{curve value}} \quad (4.34)$$

Likewise, if the reactive control is imagined implemented with $\eta_{\text{PTO},1} = 0.9$, but with the same total efficiency $\eta_{\text{PTO}} = 0.8$ as the linear case, then the expected output of this reactive control is found by taking the $\eta_{\text{PTO},1} = 0.9$ curve times 0.8:

$$\begin{aligned} E_{\text{year}} \left| \begin{array}{l} \eta_{\text{PTO},1}=0.9 \\ \eta_{\text{PTO},2}=0.889 \end{array} \right. &= \underbrace{0.8}_{\eta_{\text{PTO}}} \underbrace{\frac{1}{\eta_{\text{PTO},1}} \left(E_{\text{year}}|_{\eta_{\text{PTO}}=0.9} \right)}_{\text{curve value}} \\ &= \eta_{\text{PTO},1} \eta_{\text{PTO},2} \frac{1}{\eta_{\text{PTO},1}} E_{\text{year}}|_{\eta_{\text{PTO}}=0.9} = \eta_{\text{PTO},2} E_{\text{year}}|_{\eta_{\text{PTO}}=0.9} \end{aligned}$$

The above shows that multiplying the shown reactive curve with η_{PTO} gives the actual average output, similar to reading the linear damping curve and multiplying with η_{PTO} . As a result, the curves of yearly production may be directly compared, as they all scale linearly with η_{PTO} . Hence, if a reactive PTO is imagined to have a conversion efficiency of $\eta_{\text{PTO},1}$ of the reactive part, this curve is picked and may be compared to the resistive curves.

From Fig. 4.35 the following may be seen:

- Coulomb damping is the poorest performing WPEA, producing approximately one third of the best methods.
- Of WPEAs using Coulomb damping, de-clutching control is far the best choice, especially when looking at utilising available torque.
- As the available torque increases, the single and double ratchets systems reaches the same performance. Generally, the double ratchet system seems to requires only half the torque for the same performance as the single ratchet.
- Latching with linear damping is approximately 15% better than latching with Coulomb damping with the same torque capabilities.
- The benefit of the simple causal reactive control is highly dependent on the PTO efficiency. However, already at an efficiency of $\eta_{\text{PTO},1} = 0.8$, the system performs better than latching with Coulomb damping and de-clutching control. Also latching with linear damping require $\gamma_{\text{latch}} = 2$ to compete with reactive at an efficiency of 0.8.

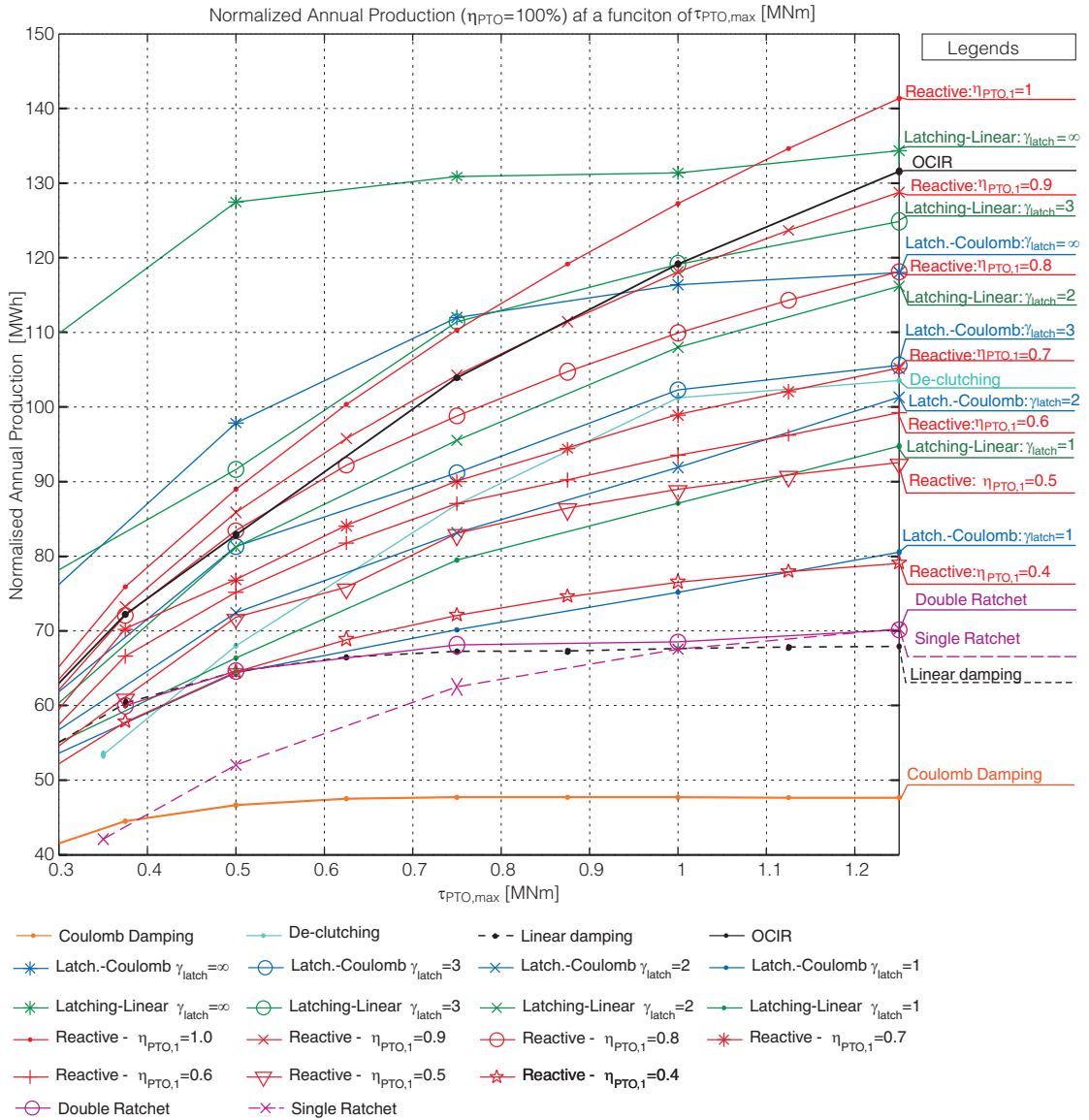


Figure 4.35: Calculated annual production for WPEAs normalised to $\eta_{PTO}=1$. The resistive strategies (all except reactive) is the actual annual production for $\eta_{PTO}=1$. The reactive curves are scaled such, that when multiplied with η_{PTO} they give the actual annual production. Hence, all curves are directly comparable.

- At an efficiency of $\eta_{\text{PTO},1}=0.9$, latching with linear damping require $\gamma_{\text{latch}}=3$ to compete with reactive control.
- The OCIR control performs similar to the reactive control at an efficiency of $\eta_{\text{PTO},1}=0.9$.
- Linear damping, ratchet based PTOs, and latching with Coulomb damping, $\gamma_{\text{latch}}=1$, have similar performance.
- Latching control require at minimum $\gamma_{\text{latch}}=2$ before being better than de-clutching control.

The overall conclusion from Fig. 4.35 is that despite non-ideal efficiency, the simple causal reactive control is still a good performing WPEA compared to the non-causal latching strategies, which require high latching torques. Comparing algorithms requiring continuous torque control, the OCIR seems to be the best choice, only exceeded by latching if having infinite latching torque or reactive control with a 100% efficient PTO.

4.9.3 Yearly Production of WPEAs based on PTO Part-load Performance

The efficiency of a PTO is often dependent of the power level, such that efficiency increases as the PTO approaches its rated power. Thus, as the available PTO torque $\tau_{\text{PTO,max}}$ is increased, the PTOs becomes bigger and rated power will increase, which will reduce its efficiency at lower power levels. This was not included in the analysis of Fig. 4.35, resulting in that increased PTO torque never affects the annual production negative.

To include this aspect in the analysis, a function is required, describing how increased PTO size $\tau_{\text{PTO,max}}$ affects PTO efficiency η_{PTO} as a function of power level. To get this relation, origin is taken in the efficiency of wind turbines. A typical PTO efficiency curve as a function of power is given in Ch. 2 of [59] for a 5MW turbine. The curve is the total power conversion efficiency of the turbine and is reproduced in Fig. 4.36a. By plotting the curve as a function of power, a typical relation of efficiency and power level is obtained, Fig. 4.36b. An accurate fit of Fig. 4.36b, where the maximum efficiency is scaled to 1, is given as:

$$\text{eff}(P) = 0.90 \tanh \left(11.18 \sqrt{\frac{P}{P_{\text{PTO,rated}}}} - 2.5 \right) + 0.1008 \sqrt{\frac{P}{P_{\text{PTO,rated}}}}$$

Wind turbines are a highly matured technology compared to WECs, resultantly, the developed PTOs of WECs are more likely to reach their “zero-efficiency” point sooner. Resultantly, this points is moved to 0.1 of rated power instead of 0.05 in Fig. 4.36b. This gives the following relation $\tilde{\eta}_{\text{PTO}}$ of average power load and efficiency:

$$\tilde{\eta}_{\text{PTO}}(P) = \eta_{\text{PTO,base}} \cdot \left(0.90 \tanh \left(11.18 \sqrt{\frac{P}{P_{\text{PTO,rated}}}} - 0.05 - 2.5 \right) + 0.1 \sqrt{\frac{P}{P_{\text{PTO,rated}}}} - 0.05 \right) \quad (4.35)$$

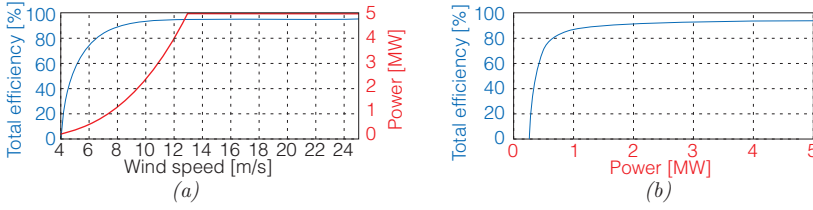


Figure 4.36: In (a) total power conversion efficiency of a 5 MW wind turbine from [59]. In (b) efficiency plotted as a function of power.

The quantity $\eta_{\text{PTO,base}}$ denotes the base efficiency of the PTO, which is the efficiency at rated power. The equation is plotted in Fig. 4.39a.

To connect the maximum PTO torque $\tau_{\text{PTO,max}}$ to rated power of the PTO $P_{\text{PTO,rated}}$, a 90%-peak absorber velocity $\omega_{\text{peak,90}}$ is used to define the PTO's peak power. The $\omega_{\text{peak,90}}$ is defined as the absorber velocity for which the absorber is below 90% of the time. Based on [60], the annual distribution of cylinder velocity of the C5 is estimated in Fig. 4.37, yielding $\omega_{\text{peak,90}} = 0.5d_{\text{arm}} = 0.21$ rad/s. If the PTO has no force overload capability, the rated power of the PTO will be the peak power. The rated PTO power is accordingly defined as,

$$P_{\text{PTO,rated}} = \omega_{\text{peak,90}} \frac{\tau_{\text{PTO,max}}}{1 + k_{\text{overload}}} \quad (4.36)$$

where k_{overload} describes the PTO's torque overload capacity. If $k_{\text{overload}} = 1$, the PTO's force overload capacity is 100%.

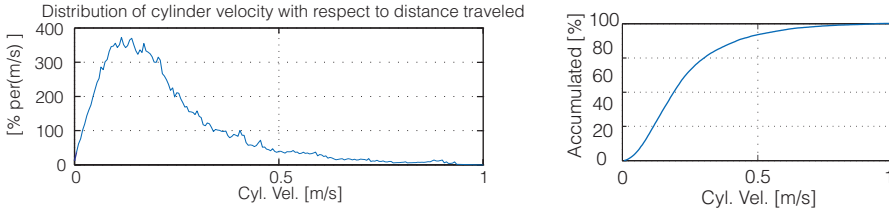


Figure 4.37: Annual distribution of cylinder velocity for reactive control.

To calculate the power production including the relation in Eq.(4.35), new power matrices \tilde{P}_{mat} are calculated based on the normal power matrices P_{mat} as:

$$\tilde{P}_{\text{mat,ij}} = P_{\text{mat,ij}} \tilde{\eta}_{\text{PTO}} \left(\frac{P_{\text{mat,ij}}}{P_{\text{PTO,rated}}} \right) \quad [\text{W}] \quad (4.37)$$

Equation 4.37 is allowed for restive strategies, as the PTO efficiency does not affect the amount of extracted power \tilde{P}_{ext} . However, for the reactive strategies, the PTO efficiency affects the extracted power output, as the control parameters changes with η_{PTO} . Resultantly, the following have to be solved, where $\eta_{\text{PTO,base}}$ denotes the base

efficiency of the PTO (the maximum efficiency of the PTO where the reactive power is processed)

$$\bar{P}_{\text{proc}}(\eta_{\text{PTO}}) = \tilde{\eta}_{\text{PTO}}^{-1}(\eta_{\text{PTO}}) \quad (4.38)$$

Power processed by reactive control as a function of η_{PTO} *The PTO power level as a function of η_{PTO}*

For reactive control, the processed power \bar{P}_{proc} is the actual power being processed, and not the calculated extracted power \bar{P}_{ext} , as this does include the reactive part. Resultantly, \bar{P}_{proc} determines the operating point of the PTO, and therefore its conversion efficiency in Eq. (4.38). When calculating the average power output of reactive control \bar{P}_{out} , the extracted power was also saved \bar{P}_{ext} . As the efficiency of the PTO was known, the processed power may be calculated as:

$$\bar{P}_{\text{proc}} = \frac{\bar{P}_{\text{ext}} \left(\frac{1}{\eta_{\text{PTO}}} + \eta_{\text{PTO}} \right) - 2\bar{P}_{\text{out}}\eta_{\text{PTO}}}{\frac{1}{\eta_{\text{PTO}}} - \eta_{\text{PTO}}} \quad (4.39)$$

Solving Eq. (4.38) is performed numerically, and an example is given in Fig. 4.38 for $\tau_{\text{PTO,max}} = 0.625 \text{ MNm}$, $\eta_{\text{PTO,base}} = 0.9$, $H_{m0} = 1.75 \text{ m}$, $T_{0,2} = 3.5 \text{ s}$ and $k_{\text{overload}} = 0$. The figure shows that the actual PTO efficiency for a reactive control with base efficiency $\eta_{\text{PTO,base}} = 0.9$ is going to be 0.81 at that specific sea state, due to operating away from rated power level of the PTO. Hence, the k_{overload} parameter may also be viewed as defining the part-load efficiency curve of the PTO.

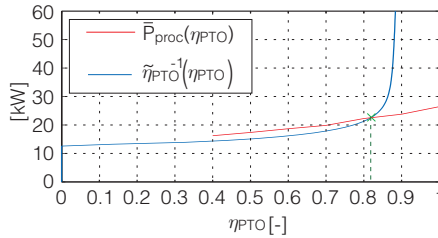


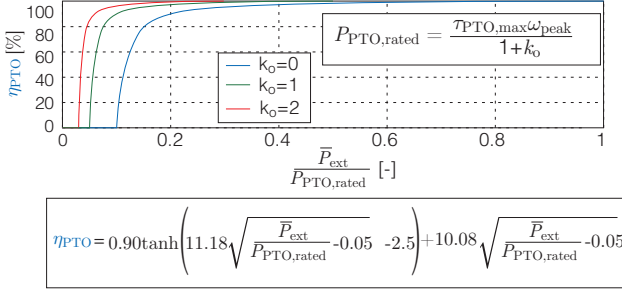
Figure 4.38: Example of solving Eq. (4.38).

New curves of expected power output of different WPEAs as a function of efficiency and available PTO torque are seen in Fig. 4.39 for different overload capabilities of the PTO. These are also normalised to $\eta_{\text{PTO}} = 1$.

Introducing Eq. (4.35) has given the sought effect as the WPEAs now having clear optimum values as a function of $\tau_{\text{PTO,max}}$. As the allowed PTO torque overload is increased, the energy production increases and higher $\tau_{\text{PTO,max}}$ values are optimal. The figure roughly shows that a PTO allowing 200% torque overload may be designed to have twice the yearly production compared to a PTO not allowing overload. This strongly emphasises that a good part load performance is essential to a good PTO design. Likewise, a PTO should have a power smoothing storage as close to the extracted power as possible to avoid dimensioning the entire PTO for the peak load.

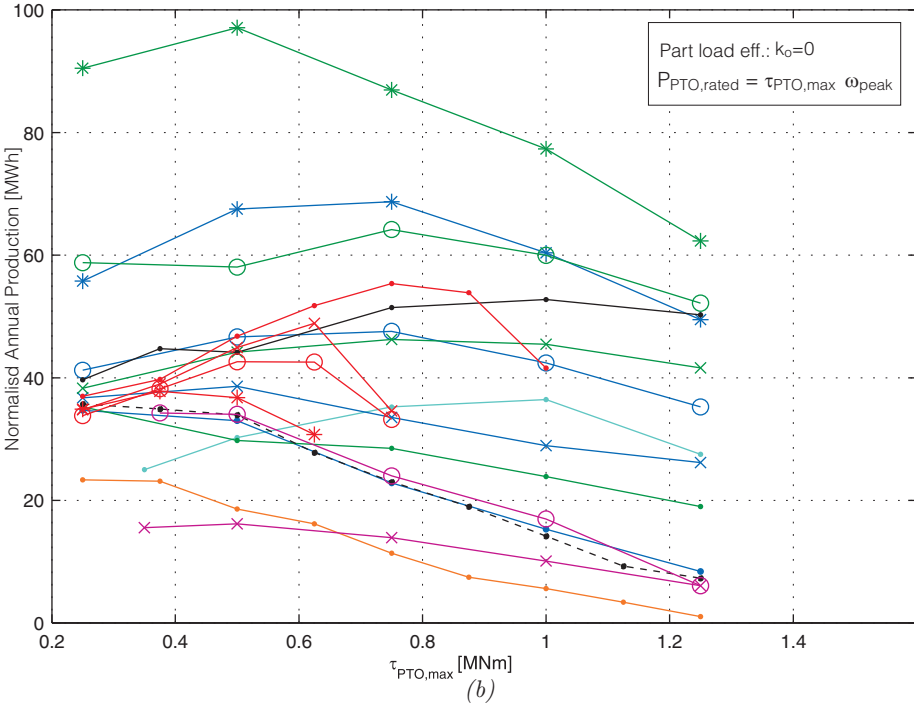
Figure 4.39: In (a) Eq. (4.35) is shown for $\eta_{PTO,base} = 1$. In (b), (c) and (d) the annual power production of different WPEAs for different PTO overload capabilities $k_{overload}$.

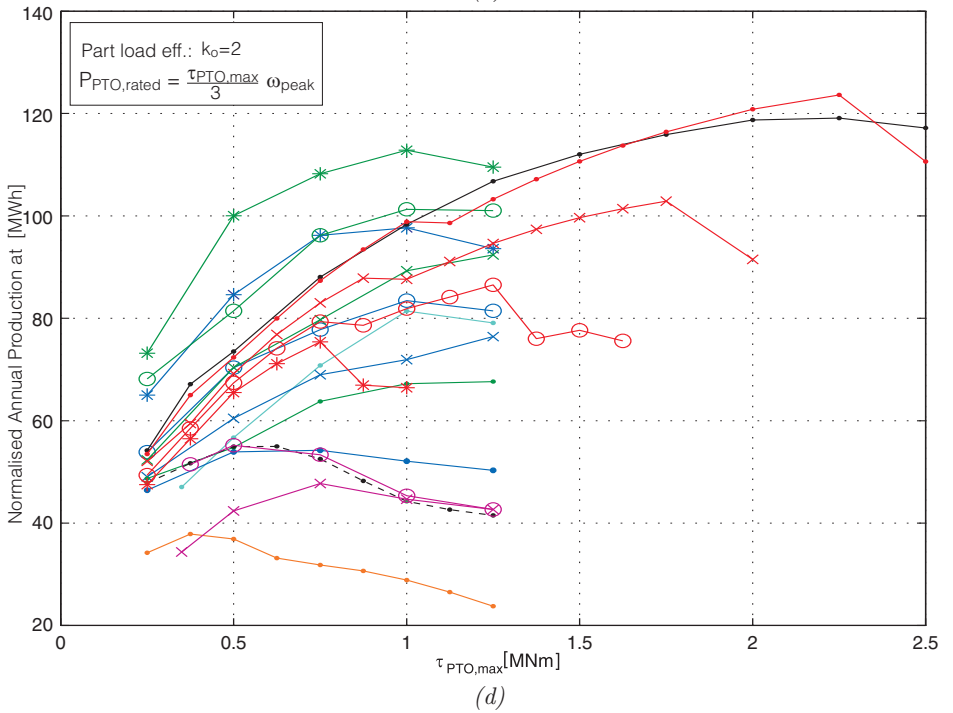
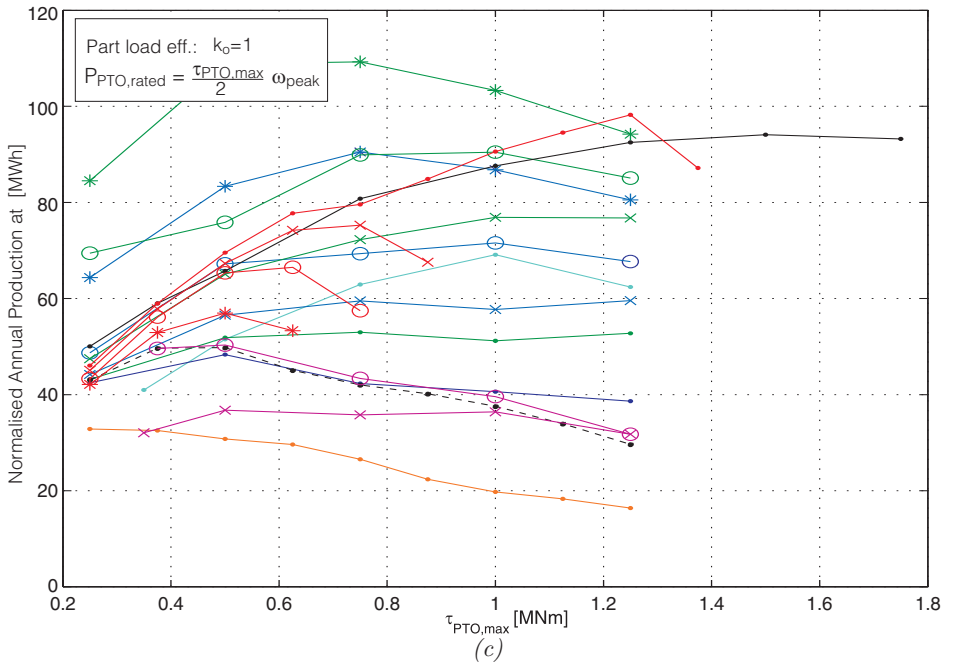
Used relation of $\tau_{PTO,max}$ and efficiency η_{PTO}



(a)

- Coulomb Damping
- De-clutching
- - - Linear damping
- OCIR
- * Latch.-Coulomb $\gamma_{latch}=\infty$
- Latch.-Coulomb $\gamma_{latch}=3$
- * Latch.-Coulomb $\gamma_{latch}=2$
- Latch.-Coulomb γ_{latch}
- * Latching-Linear $\gamma_{latch}=\infty$
- Latching-Linear $\gamma_{latch}=3$
- * Latching-Linear $\gamma_{latch}=2$
- Latching-Linear γ_{latch}
- Reactive - $\eta_{PTO,1}=0.9$
- * Reactive - $\eta_{PTO,1}=0.8$
- Reactive - $\eta_{PTO,1}=0.7$
- * Reactive - $\eta_{PTO,1}=0.6$
- Double Ratchet
- * Single Ratchet





The figure also shows that the OCIR control and the reactive control are the WPEAs with highest production potential. The optimum points of Fig. 4.39 have been summarised in Tab. 4.5. For a given PTO with base efficiency $\eta_{\text{PTO,base}}$, the annual production is obtained by multiplying the production in Tab. 4.5 with $\eta_{\text{PTO,base}}$. Additionally for the reactive WPEAs: One must first determine the base efficiency $\eta_{\text{PTO},1}$ of the part in which the reactive power is processed and choose the corresponding curve. The read value of the curve is then multiplied with the PTO's total base efficiency, i.e. $\eta_{\text{PTO,base}} = \eta_{\text{PTO},1}\eta_{\text{PTO},2}$.

To choose between the different WPEAs, the following rule-of-thumbs for the C5 absorber may be given:

- For a resistive PTO with continuous control the OCIR control is the best choice - for latching control to be able to compete requires adding a latching mechanism with about a factor 3 in torque capability, while having the same PTO as the OCIR for providing linear damping.
- If the system only allows applying a constant force damping, de-clutching control is the best choice - latching approach with Coulomb damping would only be better with three times the torque capacity of the latching mechanism.
- Choosing a four-quadrant PTO for the suggested reactive control is only better than the OCIR control if the conversion efficiency of the reactive part is above 90%.
- Linear damping should never be used as it is a waste of controllability - apply a non-linear damping strategy as the OCIR.
- Ratchet-mechanisms and pure Coulomb damping should be avoided unless the PTO and WEC may be made extremely cheap.

Table 4.5 is going to be essential in the next chapter for evaluating different PTO concepts, as by inferring a PTOs base efficiency and WPEA options may estimate its annual production potential.

Table 4.5: Optimum points in Fig.4.39 for the different WPEAs for three different PTO overload capabilities. The annual production results are given in MWh and are the normalised values. By multiplying with the total base PTO efficiency the actual annual production is obtained.

WPEA	No overload		100% overload		200% overload	
	$\tau_{\text{PTO,max}}$	$\frac{E_{\text{year}}}{\eta_{\text{PTO,base}}}$	$\tau_{\text{PTO,max}}$	$\frac{E_{\text{year}}}{\eta_{\text{PTO,base}}}$	$\tau_{\text{PTO,max}}$	$\frac{E_{\text{year}}}{\eta_{\text{PTO,base}}}$
	[MNm]	[MWh]	[MNm]	[MWh]	[MNm]	[MWh]
Reactive- $\eta_{\text{PTO,1}} = 0.9$	0.75	55.4	1.25	98.2	2.25	123.6
Reactive- $\eta_{\text{PTO,1}} = 0.8$	0.625	48.9	0.75	75.3	1.75	102.9
Reactive- $\eta_{\text{PTO,1}} = 0.7$	0.50	42.6	0.625	66.5	1.25	86.5
Reactive- $\eta_{\text{PTO,1}} = 0.6$	0.375	37.8	0.50	57.0	0.75	75.4
Latch.-linear $\gamma_{\text{latch}} = 3$	0.75	64.2	0.75	89.9	1.00	101.3
Latch.-linear $\gamma_{\text{latch}} = 2$	0.75	46.3	1.00	76.8	1.25	92.35
Latch.-linear $\gamma_{\text{latch}} = 1$	0.25	35.2	0.75	53.0	1.00	67.2
Latch.-Coulomb $\gamma_{\text{latch}} = 3$	0.75	47.6	1.00	71.6	1.00	83.4
Latch.-Coulomb $\gamma_{\text{latch}} = 2$	0.50	38.6	0.75	59.5	1.25	76.4
Latch.-Coulomb $\gamma_{\text{latch}} = 1$	0.25	34.8	0.50	48.3	0.75	54.3
De-clutching	1.00	36.4	1.00	69.1	1.00	81.4
OCIR	1.00	52.8	1.50	94.1	2.25	119.1
Linear damping	0.25	35.7	0.50	49.8	0.625	55.0
Double ratchet	0.375	34.3	0.50	50.3	0.50	55.2
Single ratchet	0.50	16.2	0.50	36.8	0.75	47.7
Coulomb damping	0.25	23.3	0.25	32.8	0.375	37.8

Top five WPEAs indicated with colours: 1. 2. 3. 4. 5.

4.10 Summary

A method was presented for determining the optimal control parameters for a general Wave Power Extraction Algorithm (WPEA) for point-absorbers when having a non-ideal PTO. The non-ideal PTO characteristic included force limitations, finite control bandwidth and a power-conversion efficiencies below 100%.

The following WPEAs were optimised according to the mentioned PTO constraints: Causal reactive control, OCIR control, Coulomb damping, Non-causal latching with linear damping, Non-causal latching with Coulomb damping, Linear damping, Non-causal de-clutching, Ratchet mechanism with fixed shaft speed and Double-Ratchet mechanism with fixed shaft speed.

The latching strategies were also evaluated as a function of both allowed damping force and allowed latching force. The WPEAs were optimised by iterated simulations in irregular wave simulations. A complete expected average power output matrix were made for each WPEA algorithms for all relevant combinations of PTO efficiency, torque limitation and latching torque limitation.

The power matrices were converted into yearly production and normalised to 100%

efficiency. The normalisation gives that for different PTO efficiencies, the expected PTO efficiency may be multiplied with the showed results for obtaining the actual annual production.

The realistic constraint that a larger PTO will have a poorer performance at low power levels was introduced. The shape of the part load efficiency curves were based on wind turbines, and were coupled to the PTO torque limit, as this defined the peak power rating of the PTO. These made the different WPEAs have a clearly defined optimal point, representing the optimal PTO size under these assumptions.

A new WPEA was suggested in the chapter, the OCIR control, which is a causal non-linear resistive approach. The control showed to be one of the best choices. It is left for future work to verify the control in e.g. wave tanks, however, based on that the reactive control was successfully verified in the wave tank, the OCIR is believed to perform as calculated.

Based on the chapter, the following rule-of-thumbs were given:

- For a resistive PTO with continuous control the OCIR control is the best choice - for latching control to be able to compete requires adding a latching mechanism with about a factor 3 in torque capability, while having the same PTO as the OCIR for providing linear damping.
- If the system only allows applying a constant force damping, de-clutching control is the best choice - latching approach with Coulomb damping would only be better with three times the torque capacity of the latching mechanism.
- Choosing a four-quadrant PTO for the suggested reactive control is only better than the OCIR control if the conversion efficiency of the reactive part is above 90%.
- Linear damping should never be used as it is a waste of controllability - apply a non-linear damping strategy as the OCIR.
- Ratchet-mechanisms and pure Coulomb damping should be avoided unless the PTO and WEC may be made extremely cheap.

The presented framework gives a background for choosing the PTO topology, as it may answer design questions as:

If a resistive PTO capable of constant force loading and free floating (WPEA: De-clutching) may be made with a given conversion efficiency, which efficiency and torque level is a continuous force control PTO (WPEA: OCIR) required to have to yield a better yearly production?

The presented framework is going to be essential in the following chapter, where PTOs are evaluated. The framework may estimate the yearly production of PTOs based on its force control method, conversion efficiency and part load performance. Resultantly, PTOs with fundamental different control options may be qualitative compared.

Evaluation of State-of-the-Art in PTO Systems

A large variety of PTO systems has been suggested throughout the years with fundamental different characteristics, ranging from using direct drive solutions to using various transmissions based on hydraulics, mechanical gears or magnetic gears. Their properties like efficiency, overload capabilities and force control abilities various, making direct comparison nearly impossible. However, based on the framework presented in the previous chapter, an assessment is going to be performed of the different PTOs.

The assessment is going to be a combination of expected power-production, PTO size, durability and storage capability. Based on the assessment, best potential technologies are identified which are further explored and development in the next chapter to identify the most promising PTO technology for the Wavestar.

5.1 PTO Assessment Chart

The chart seen in Tab. 5.1 has been defined to structure the assessment and be able to provide an overview at the end of the chapter. The chart contains a scoring system, where the score in each category is -1,1,2 or 3, with three being the best. Furthermore, the chart contains expected power production, used WPEA algorithm for extracting wave power, the optimum value of the maximum torque $\tau_{PTO,max}$ and energy storage type. The “overload capability” or “part load performance” k_o is also given, which was introduced in the previous chapter. This determines which part load efficiency distribution is expected in Fig. 4.5, i.e. $k_o = 1, 2$ or 3 .

The size value is a rough estimate of the size of the primary part of the PTO, i.e. the part required installed on the Wavestar arm to absorb the linear motion. E.g. for a linear generator, the whole generator (except for converter) has to be mounted on the arm, whereas for a hydraulic solution, only the cylinder has to be mounted on the arm, and the remaining parts may be inside. This is illustrated in Fig. 5.1a.

The “part sized for peak load” of the chart indicates that if viewing the PTO as a chain of conversion steps, how much of this chain sees the peak power of the absorber. This is illustrated in Fig. 5.1b. The efficiency $\eta_{PTO,1}$ denotes the efficiency of the PTO part, where reactive power will be processed. The $\eta_{storage}$ is the round trip efficiency of the storage and η_{tot} is the overall or base efficiency of the PTO. Note that the base efficiency η_{tot} and the part load performance k_o determine the assumed efficiency curve of the PTO. Using this curve together with the best WPEA choice possible by the PTO

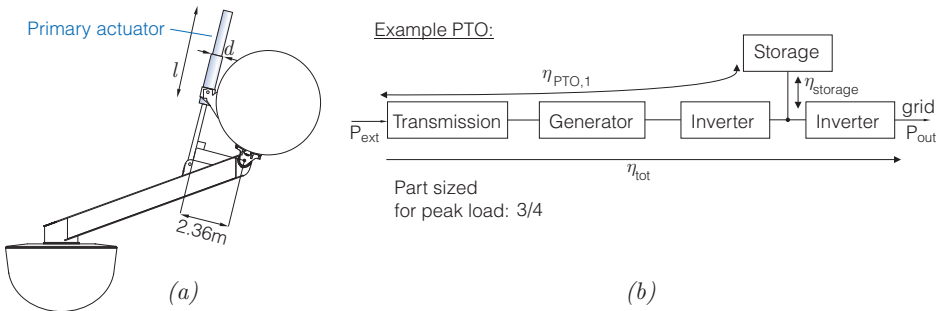


Figure 5.1: Illustration of evaluation chart quantities.

yields using Tab. 4.5 the expected annual energy output for a C5 absorber.

Table 5.1: Used evaluation chart for PTOs.

PTO NAME Illustration	Prod.	Size	Durability	Storage	Total
	Points:				
WPEA:			Storage:		
Part sized for peak load:		Optimum maximum force:	$\tau_{PTO,max} =$	$F_{PTO,max} =$	
Part load perform. k_o :		Size of primary gen./actuator:	$d =$	$l =$	
$\eta_{PTO,1}$	$\eta_{storage}$		η_{tot}	Annual prod. [MWh]	

Before entering evaluation of the different PTOs, the different energy storage technologies are discussed to aid in this aspect of the evaluation.

5.2 Energy Storage Technologies

In wave energy, energy smothering using storage may be required in two levels: Wave-to-wave and wavegroup-to-wavegroup. The first requires storage capable of charging/discharging in couple of seconds and the second type requires cycle-time in tens of seconds.

Different storage technologies are show in Fig. 5.2 in the form of Ragone plots, where the energy density is plotted versus power density in a logarithmic scale. The sloped lines indicate the relative time required to charge or discharge the device. Storages delivering power in form of electrical power is given in Fig. 5.2a. The Ragone plot in Fig. 5.2b also contains systems delivering mechanical power like flywheels.

In Fig. 5.3 a new Ragone plot has been made based on Fig. 5.2 where the hydraulic accumulator has been added. The accumulator is added according to Ragone plots found in [63] and [64]. Figure 5.3 also agrees with the Ragone plot found in [65], which however show a much larger operating area of the hydraulic accumulator. Compared to the conventional fly-wheels, the advanced fly-wheels (based on low density high strength

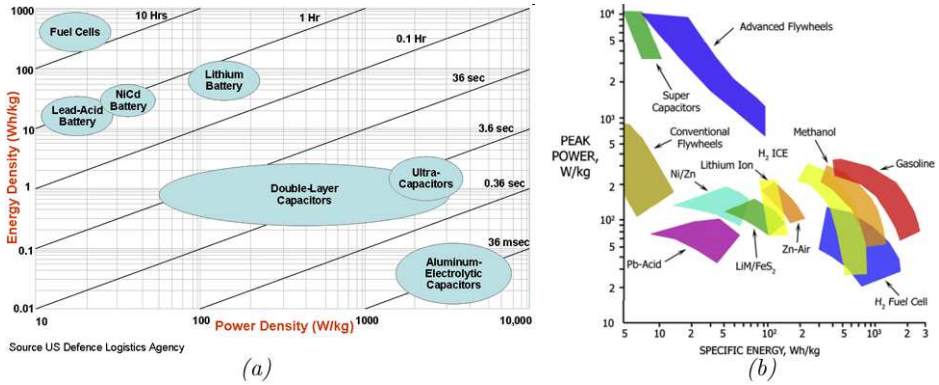


Figure 5.2: In (a) Ragone plot from [61] of storages with electrical output. In (b) Ragone plot of different storage from [62].

material, advanced bearings, etc.) may operate at much higher speed.

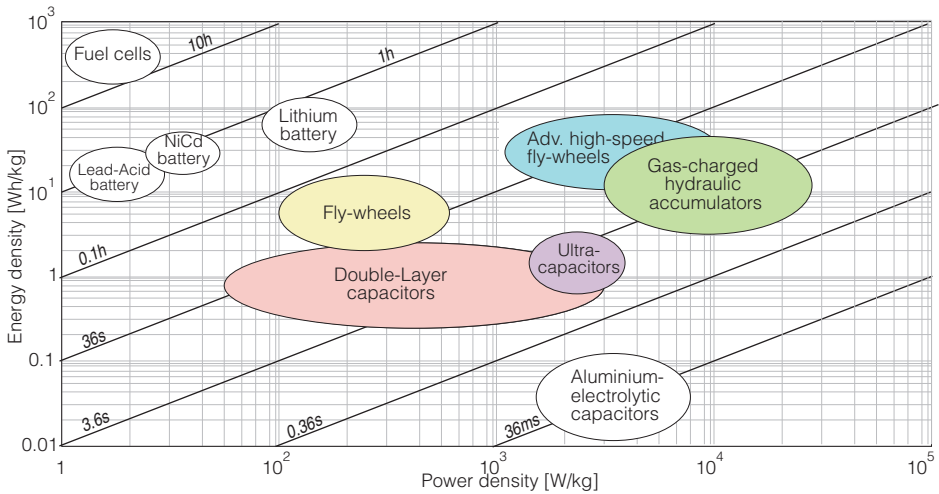


Figure 5.3: Ragone plot of different energy storage technologies.

In motor sports, implementations of the advanced fly-wheels are often used in Kinetic Energy Recovery Systems (KERS). Here high speed fly-wheels are used together with a Continuously Variable Transmission (CVT) between a main drive shaft and the fly-wheel shaft. This is illustrated in Fig. 5.4. This allows storage control independent of main shaft speed, and also allows increasing the fly-wheel speed. The system is for regenerative use of brake energy. According to [66], a 100kW-unit by Flybrid LtD weighs 25 kg, including the CVT. This gives 4kW/kg. According to [67] the unit may store 400kJ, i.e. the energy density is 4.4Wh/kg. This agrees with Fig. 5.2. The speed of the fly-wheel may be up to 60000rpm.

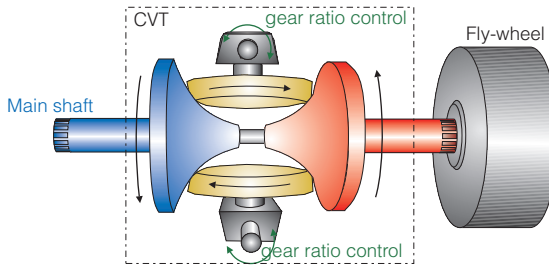



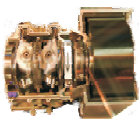


Figure 5.4: Illustration of KERS, consisting of a CVT with a fly-wheel.

According to [68], the current round-trip efficiency is about 70% in KERS used for Formula 1. The round-trip efficiency is expected to approach 80% for KERS being developed for the auto-mobile sector [68].

Based on the table presented by Dr. Rampen at a keynote speech at FPMC2010 [69], which also may be found in [63], Tab. 5.2 has been constructed, showing average characteristics of different storage technologies. Round trip efficiencies and densities of super capacitors may be found in [70] and [71], indicating 95% efficiency of a charge or discharge, i.e. 90% round-trip efficiency. Round-trip efficiency of both super capacitors (ultra and double layer capacitors) and accumulators are highly dependent on charge and discharge times.

Table 5.2: Average values of different storage technologies based on [69] and [63].

	Accumulator	LiON battery	Supercap module	KERS
				
Power density	20 kW/kg	0.5 kW/kg	2 kW/kg *	4 kW/kg
Energy density	3 Wh/kg	40 Wh/kg	1 Wh/kg *	4 Wh/kg
Round-trip eff.	94%	81%	92%	70-80%
Cost	<1€/kJ		approx. 20€/kJ	

*including internal wiring and cooling

Looking at wave-to-wave smoothing, super capacitors and hydraulic accumulators are in right time range of 1-5 seconds to charge and discharge according to Fig. 5.3, where the hydraulic accumulators are superior in regard to both power and energy density. The conventional fly-wheels are on the slower side for wave-to-wave smoothing, however, the advanced fly-wheels or KERS have the required response time.

Recalling that the ratio of mean and peak power of wave energy is about 10, the high power density of the hydraulic accumulator makes it the best solution for short term

power smoothing if a hydraulic circuit is a natural part of the PTO. Unlike the KERS, if the hydraulic circuit is properly designed an accumulator may be utilised without use of an intermediate conversion step corresponding to a CVT or power converter. Furthermore, accumulators have a high round-trip efficiency of 94%.

Super-capacitors for WECs are explored in [72], which by assuming a power period of 5s reaches that 21,000,000 cycles are performed every 5 years. In [72] it is also mentioned that leading manufacturers quote lifetimes of super capacitors up to one million cycles or less, which means that it is uncertain if super-capacitors will reach the required life-time. [72] also shows as in Fig. 5.7a that using the super-capacitor module requires an extra converter module attached to the DC-line in the converter to control the stored power.

Accumulators operating at full pressure of 360 bar guarantee more than 2,000,000 cycles according to data-sheet [73, 74]. Fatigue-wise, infinite life-time is possible if the dynamic loads are dimensioned correctly as shown in Fig. 5.5, showing worst case scenario for fatigue.

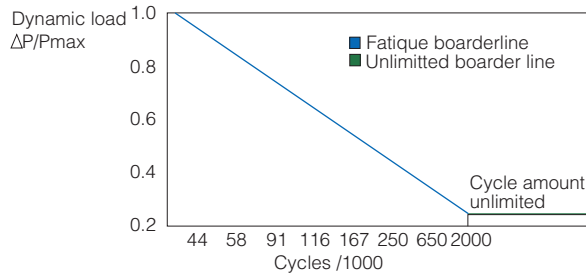


Figure 5.5: Worst-case structure fatigue life-time for piston accumulators [75].

Looking at wavegroup-to-wavegroup smoothing, conventional fly-wheels, super capacitors and accumulators are in the right time range according to Fig. 5.3. Here, fly-wheels and accumulators are best at both energy and power density. Conclusively, accumulators are a good overall solution as they may cover both wave-to-wave and wave-group smoothing. Super capacitors and KERS may also cover both areas, but at a higher cost and a heavier system (and with a lower round-trip efficiency). Conventional fly-wheels may also be used for wave-group smoothing, but with a higher mass compared to accumulators.

5.3 Power Converters

Most PTO designs will drive a generator at varying speeds and loads, generating electricity with varying frequency and voltage. Resultantly, a power converter is required to connect the system to the grid. The converter may also be required to comply with grid-codes. The converter often comprises two inverters back-to-back, where an inverter unit allows converting a DC-voltage to an almost arbitrary frequency and voltage level. This is efficiently implemented using power transistors, operating as switches. A full-power converter used for e.g. wind turbines is shown in Fig. 5.6.

For detailed analysis of losses in a converter see e.g. [76]. Including filters, a converter for a wind turbine is in [77] estimated to have an efficiency of approximately 97% at rated power.

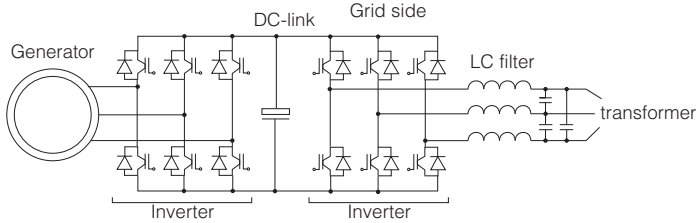


Figure 5.6: Illustration of a full-power converter used in e.g. wind turbines [76].

For industrial inverters, the Danfoss FC300 series has efficiencies of 98% at rated power for 10-1000kW [78]. The load dependence of the efficiency is given in Fig. 5.7a, where the base efficiency of 0.98 should be multiplied to get the actual inverter efficiency.

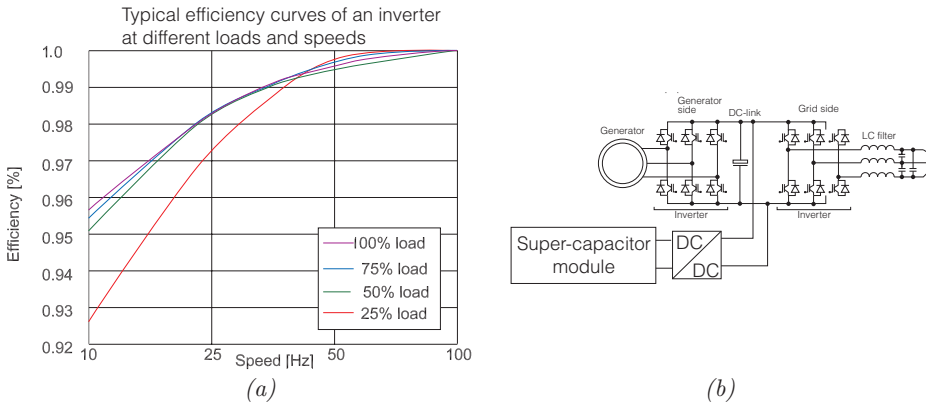


Figure 5.7: In (a) inverter efficiency dependency from [78] and in (b) connection of super-capacitor module to DC-line [72].

In the coming evaluation, the converter is considered to consist of two inverters, each having a base efficiency of 0.975, yielding a total converter efficiency of 95%.

5.4 Direct Drive

Several investigations have been performed on using generators driven directly by the absorbers' movement. As most WECs produce linear motions, most effort has been put into designing linear generators, directly converting the slow linear motion (peak linear velocity about 2m/s) to electricity. The generators are mainly designed as Linear Permanent Magnet Machines (LPMM) or Linear Variable Reluctance Permanent Magnet Machines (VLPMM).

Figure 5.8a illustrates typical LPMMs, consisting of a stator with slot embedded wound coils. The translator consists of permanent magnets on an iron yoke. The air-gap between stator and translator is 2-5 mm. As the translator is translated by the absorber, so is the magnetic field created by the permanent magnets, inducing an electromotive force in the stator coils due to the flux change. A power converter is attached to the LPMM phases, converting the varying frequency of the induced voltage to a fixed voltage level and frequency. Also, the order of the phases in the generators is interchanged when the translator movement reverses, which is handled by the power converter.

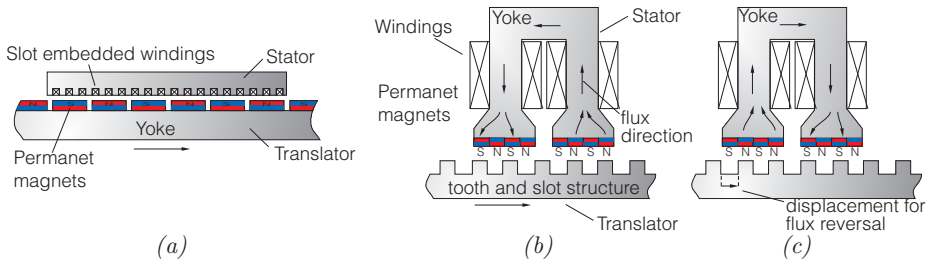


Figure 5.8: In (a) illustration of a LPMM and in (b) and (c) illustration of the VLPMM principle [79].

Implementations of LPMMs for wave energy have been widely tested with both rectangular versions [80, 81, 82, 83, 84] and tubular types [85, 86, 87, 88, 89].

One of the largest experimental tested versions on a WEC is for the Archimedes Wave Swing (point absorber) with a 1MW linear generator with a 7m stroke and a peak capacity of 2MW [80]. The weight of the WEC prototype was 7000 tons, including ballast water of 5000 tons [90, 1]. The linear generator has four 8m high iron cored translators with surface mounted permanent magnets and two 5m high double sided stators. Fig. 5.10c shows technicians working on the generator. This provides 20m² of active surface area [90]. According to [91] the linear generator itself exhibits a efficiency above 90% over a wide range of wave amplitudes and periods. This is seen in Fig. 5.9 where the plot on right shows the total efficiency with inclusion of converter, which reduces the part load efficiency. The indicated peak efficiency of 85% is a best attempt read off.

In [87] a smaller 10kW LPMM prototype is tested. The expected efficiency of the prototype is 83% in regular waves. The generator has a rated force of 1.3kN.

Another realised LPMM is the 8kW prototype for the Seabased [92] WEC presented in [84] with a 5mm air-gap and a translator of height 650mm and width of 400×400mm (1.04m² air-gap area). At rated speed (0.7m/s) an efficiency of 86.0% is expected for a 10kW unit, and the system may be operated at 300% overload. The mass of permanent magnets (NdFeB) for a 10kW unit are 115kg, stator steel weight 766kg and piston steel weight 432kg. The system is currently being tested as sea [93]. A prototype is seen in Fig. 5.10e, with surface mounted magnets on the four sides of the translator.

Different direct drive concepts are also explored by Columbia Power Technologies in

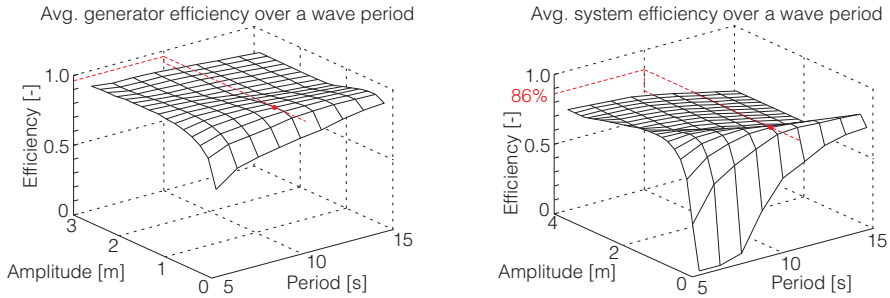


Figure 5.9: Efficiency of generator and total efficiency of generator and converter based on [90].

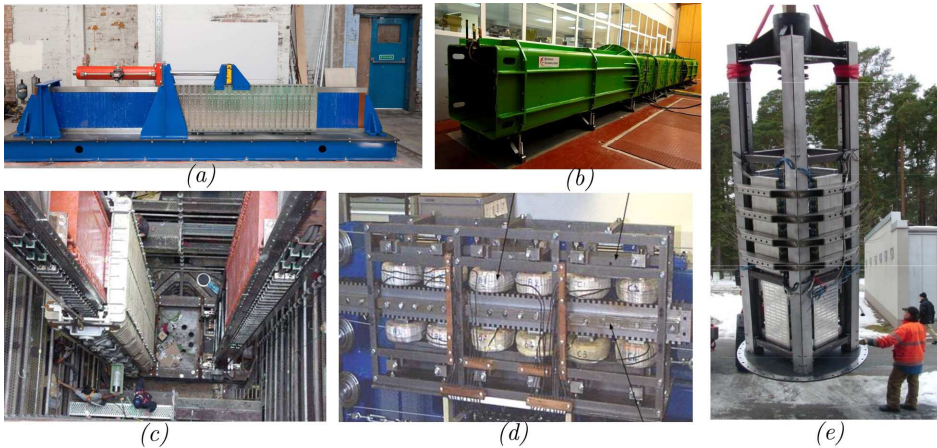


Figure 5.10: Different prototypes of linear generators. In (a) 50kW air-cored LPMM generator [94], (b) 160kW VPRMM generator [95], (c) 1MW iron cored LPMM generator [91], (d) 3kN VRPMM prototype and (e) Seabased iron cored 10kW prototype [12].

[96, 97, 98, 99, 100]. Their conclusion through cost of energy analysis is that bi-directional rotary motion is preferable to linear motions. Resultantly, their idea is to design an absorber producing bi-directional angular motion, which powers two direct drive generators. This is illustrated in Fig. 5.11 with the two large generators contained in the nacelle. During 2012 a 1:7 scale system driving two 5-kW permanent magnet generators were tested [97]. Obtained or predicted size and efficiency have not been shown. However, for producing 100kW two generators with torque capability of 1 MNm seems to be required based on the simulation results in [96] and as seen in Fig. 5.11. This is two generators with approximately the torque capability of a 2MW direct-drive wind turbine generator, having a rated torque of 1 MNm [101].

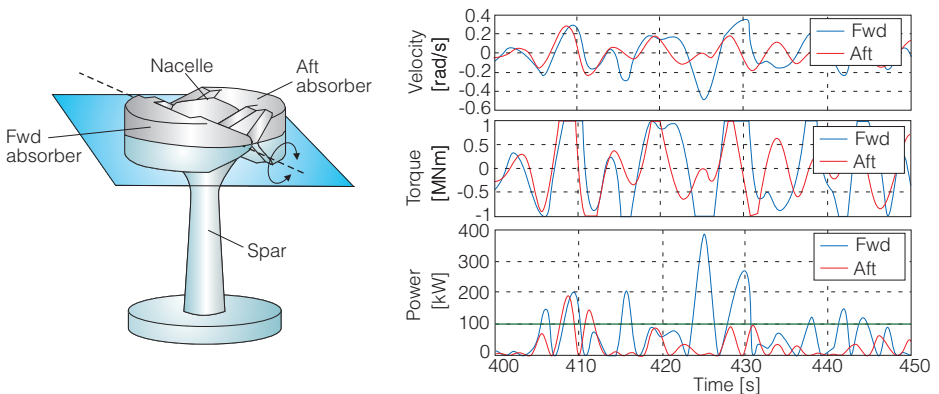


Figure 5.11: Illustration of Columbia Power Technologies WEC and typical operation fitted from [96].

The advantages of the LPMs are good overall efficiency, continues force control and four quadrant behaviour, and has a simple design in the sense of a few moving parts and directly converting the absorber motion into electricity. The main drawback is that the design results in very large machines with a low power to weight ratio. In [102] conventional LPMs are estimated to have a power to weight ratio of maximum 4kW/ton. Also, heavy support structures are required to maintain the small air-gap due to magnetic attraction of stator and translator.

To avoid the magnetic attraction of stator and translator, air-cored coils have been investigated for the Archimedes Wave Swing. In [103] a 2MW design is calculated, yielding a 24ton generator of average efficiency 87%, where 4.5ton are PM-magnets. A 50-kW prototype has been constructed and tested [94, 104], showing an efficiency of 70%. The prototype is shown in Fig. 5.10a. Note the size compared to the smaller hydraulic actuator, actuating the generator. Another example of an air-cored design is the linear generators used in the Trident WEC [105, 106], having a peak velocity of 2.1m/s and peak force of 16kN. Air-cored design is also being explored for direct drive wind turbines [107, 101] to reduce the structural mass of the design. However, the dominant solution is the radial flux PM synchronous generator [108, 109] with typical shear stress levels 25-50kN/m² in the air-gap [101]. In [109] a 10 MW design is discussed with 40kN/m².

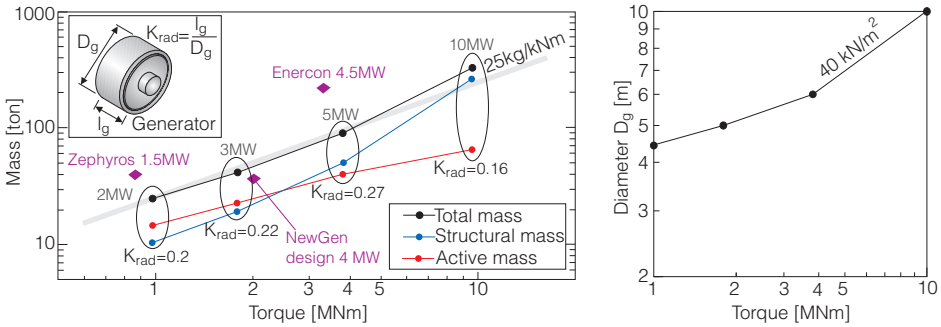


Figure 5.12: Figure based on [108] of generator sizes.

Fig. 5.12 is based on [108]. This illustrates the size of generators versus torque, where the ratio of diameter and length has been optimised to minimise mass.

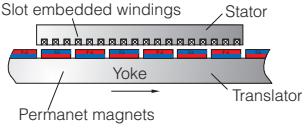
The reason for the poor weight to power ratio of LPPMs is the slow velocities, e.g. the flux lines are only cut with a speed of 2m/s, which is 15-50 times slower compared to a conventional rotational generator [1]. For the LPPM the achievable air-gap shear-stress, i.e. the maximum force possible to generate to resist relative translation of translator and stator, is about 20-25kN/m² [110]. In [90] the weight of active magnetic material alone (copper, iron laminations, magnets and back-iron) is estimated to be 1500kg/m².

To increase the force density, generators based on Linear Variable Reluctance Permanent Magnet Machines may be used (VRPMM). The basic concept is illustrated in Fig. 5.8b, which is a combination of reluctance (magnetic resistance) principle and magnetic gearing. The translator is a teathed structure of low-reluctance material. This will at high force try to reach a position, minimising the reluctance of the magnetic circuit. Secondly, the magnetic gearing is utilised by splitting a single stator pole with a coil into multiple smaller poles, e.g. using surface mounted permanent magnets with a small pole pitch. [110]

In Fig. 5.8b the translator’s multiple poles are fully aligned with the stator teeth, minimizing the reluctance and generating a flux in the stator yoke through the windings. When the translator moves just one tooth pitch, the direction of the flux is reversed, generating rapid flux changes in the stator and thereby inducing a high emf in the windings. Thus, the slow motion of the translator is converted into a higher rate of flux changes. As power is exchanged with the coils for each pole pitch instead of full main pole displacement, a higher linear force may be generated [110]. However, this type of design requires small air-gap spaces, e.g. for avoiding short-circuiting of flux at the teeth.

A design example of a VRPM for wave energy is given in [82], showing an expected force density of 48kN/m². In [91, 110] a 3 kN prototype is constructed, showing 100kN/m² prototype. However, an issue with the VRPM design is to rely on small air-gaps (<1mm), which in combination of stoke lengths of meters is difficult to manufacture and requires heavy guide structures. For the prototype, the attractive force

Table 5.3: Assessment of linear PM generator.

<i>Linear PM Machines</i>		Prod.	Size	Durability	Storage	Total
		3	-1	2	1	5
WPEA: <i>Reactive or OCIR</i>				Storage: <i>Super capacitors</i>		
Part sized for peak load:	3/4	Optimum maximum force:		$\tau_{PTO,max} = 1.25 \text{ MNm}$ $F_{PTO,max} = 530 \text{ kN}$		
Part load perform. k_o :	1	Size of primary gen./actuator:		$d = 2.1 \text{ m}$ or $2 \times d = 1.05 \text{ m}$ $l = 4 \text{ m}$ + <i>linear guide</i> $l = 4 \text{ m}$		
$\eta_{PTO,1}$	0.89	$\eta_{storage}$	0.92	η_{tot}	0.87	Annual prod. [MWh] 86

The efficiency of a linear PM generator from input power to grid is assumed to maximum 90%. If storage is installed, this would be in form of super capacitors on the DC-line of the converter. These have a round-trip efficiency of 92%. If 1/3 of the power is processed in the storage, then the expected overall efficiency would be 87%. If the converter between generator and grid consist of two inverters back to back, each operating at about 97.5% efficiency, the first part of the PTO with storage (where reactive power would be processed) would have an efficiency up to 89% at rated power. About 2/3 of the PTO will see and be designed for the peak power.

Control wise, the linear generator is capable of continues and 4-quadrant force control, thus both the OCIR and reactive control methods would be possible. Overload wise, the generator is assumed to be able to operate at twice the current at medium-term duration. This is consistence with [80], describing that Archimedes Wave Swing has 1 MW nominal power and peak power of 2MW.

Assuming the use of reactive control, the optimum torque level is going to be 1.25 MNm with an annual production of $98.2 \cdot 0.87 = 88.2 \text{ MWh}$ according to Tab. 4.5. The 1.25 MNm corresponds to $F_{PTO} = 1.25 \text{ MNm} / 2.36 \text{ m} = 530 \text{ kN}$ on the current cylinder mounting of the C5. Assuming a force density of $\kappa_{FA} = 40 \text{ kN/m}^2$, the diameter d of a linear generator with a 2m stroke would be given as,

$$d = \frac{F_{PTO}}{\pi l \kappa_{FA}} \text{ m} \quad (5.1)$$

yielding $d = 2.1 \text{ m}$. Note that the actuator would be 4m long to ensure having 2m of overlapping stator and translator, plus additional heavy mechanical linear guides to maintain air-gap. Durability is given a 2 due to the complication with the heavy linear guides required to maintain air-gap.

The required air-gap area is 13 m^2 . At 1500 kg/m^2 , 19500kg of copper, iron laminations, magnets and back-iron is required for producing an average of 55kW. Additionally, the required linear guides should be added to the weight.

Due to the extreme size and weight of the linear generator, the PTO is viewed as an infeasible solution.

of stator and translator is 2.7 times greater than the useful force [82, 91]. The design also has very poor power factors, typically in the range of 0.35-0.55 [89] due to the high inductance. Resultantly, an overrated power converter is required to process the reactive power.

Another implementation of the VRPM is given by the Wedge Company, [95, 111, 112, 113, 114]. In [114] a full-scale 160kW version is tested, capable of 160kN, stroke of 2m and rated speed 1m/s. Efficiencies up to almost 80% have been reported [114] for the system. The obtained force density is not recorded, by according to [91], if the air gap is increased beyond the 1mm, the system begins to re-assemble the characteristics of the LPMM. An air-gap of 2mm is used in the prototype. Wavebob has suggested a VRPM design in [115], and in [116] an arc-based design is suggested for direct conversion of angular oscillations.

5.5 Magnetic Transmission

Compared to using linear generators, better utilisation of the total magnetic mass and increased compactness have been suggested by using magnetic gears to perform a step up in velocity before driving a generator.

The idea of the following concepts is to use the principle of magnetic couplings, having very high shear stress values at near zero loss. According to [102] the coupling surface of two facing arrays of permanent magnets locks with shear stress values up to 10 times those in wound electrical machines. According to [117] a magnetic coupling shows torque densities of 300-400kNm/m³, which is equivalent to 150-200kN/m².

This is utilised in the PTO of the Snapper WEC [118, 102, 119, 120]. The combined magnetic gearing concept and generator is shown in Fig. 5.13a. The translator consists of two sides with permanent magnets. These magnets face corresponding magnets on the armature/oscillator, creating a magnetic coupling. The oscillator also comprises the wounded coils as a normal linear generator, and is spring-mounted to a fixed base. Using this configuration, the translator and oscillator will move together, tensioning the springs until the spring force is able to overcome the shear stress of the magnetic coupling. At this point, the coupling breaks and a rapid relative movement of translator and armature is obtained, inducing a high burst of emf. Hence, the system transforms a slow motion into a series of rapid relative movements as illustrated in Fig. 5.13b.

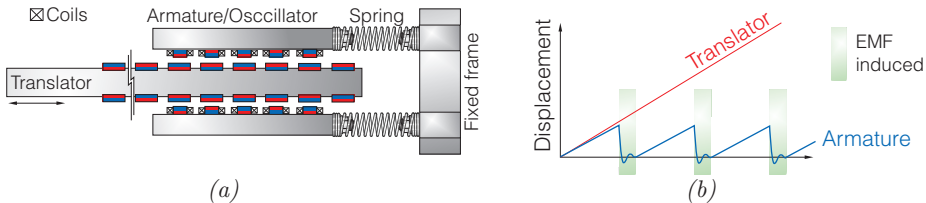


Figure 5.13: Illustration of Snapper PTO based on [121] and [122].

A Snapper PTO generating 19kW at an average translator movement of 1m/s is simu-

Table 5.4: Assessment of linear variable reluctance PM-Machines.

<i>Linear VRPM Machines</i>		Prod.	Size	Durability	Storage	Total	
		Points:	2	1	2	1	6
		WPEA: <i>Reactive or OCIR</i>		Storage: <i>Super capacitors</i>			
		Part sized for peak load:	3/4	Optimum maximum force:	$\tau_{PTO,max} = 1.50 \text{ MNm}$ $F_{PTO,max} = 636 \text{ kN}$		
		Part load perform. k_o :	1	Size of primary gen./actuator:	$d = 1.2 \text{ m}$ $d = 0.60 \text{ m}$ $l = 4 \text{ m}$ or $2 \times l = 4 \text{ m}$ + linear guide		
		$\eta_{PTO,1}$	0.87	$\eta_{storage}$	0.92	η_{tot}	0.85

The efficiency of a linear VRPM generator from input power to grid is assumed at best to be 85% as a lower efficiency is expected compared to the conventional PM generator due to the lower power factor of the VRPM. If storage is installed, this would be similar to the conventional linear generator with super capacitors, meaning about 2/3 of the PTO chain (including the VRPM) will be designed for the peak power. With storage, a total efficiency is expected around 82%. The efficiency of the part of PTO from input to storage is expected to be around 87%.

Control wise, the VRPM generator is capable of continuous and 4-quadrant force control, thus both the OCIR and reactive control methods would be possible. Overload wise, the generator is assumed to be able to operate at twice the current at medium-term duration.

Assuming the use of OCIR control, the optimum torque level is going to be 1.50 MNm with an annual production of $94.1 \cdot 0.82 = 77 \text{ MWh}$ according to Tab. 4.5. The 1.50 MNm corresponds to $F_{PTO} = 1.50 \text{ MNm} / 2.36 \text{ m} = 636 \text{ kN}$ on the current cylinder mounting of the C5. Assuming a force density of $\kappa_{FA} = 85 \text{ kN/m}^2$, the diameter d of a linear generator with a 2m stroke would be 1.2m plus additional linear guides to maintain air-gap, which would be heavier than the conventional linear generator due to smaller air-gap requirements of VRPM.

To reduce the size of the VRPM generator, it may be implemented as two parallel generators, each providing 318kN. This would give a minimum diameter of 0.60m of each generator, which will also make the implementation of linear guides easier.

Given the small air-gap requirement combined with the large size and weight, also making the linear guide design very difficult, the PTO is viewed as an infeasible solution for the C5.

lated in [119]. The efficiency is estimated to be 88.5% and the force density is estimated to be 132 kN/m^2 , which is higher than the typical linear generators.

In [120] a 143kW unit at an estimated efficiency of 71% is calculated to use half the material for a linear generator. In [102], a conventional linear generator is estimated to give a power to weight ratio of about 4kW per tonne compared with about 30kW per tonne for the Snapper. In [123] it is claimed that the Snapper may be reduced to require 4.1 tonnes/MW of copper and iron.

In [124, 121, 125] simulation and test of a prototype with 1.5m stroke and a peak force of 5.5kN is presented. The setup is shown in Fig. 5.14a. According to [124] a velocity amplification of up to 12 from wave energy device to armature relative velocity has been achieved in the testrig. In [121] it is discussed that the spring has to be carefully matched, otherwise the armature may oscillate without snapping to the translator. In [124] the Snapping event has also been recorded, showing the complex force produced. The data have been fitted and shown in Fig. 5.14b. As seen the PTO load force will build up to the 5.5kN, and reset to zero with some complex transients before the cycle repeats.

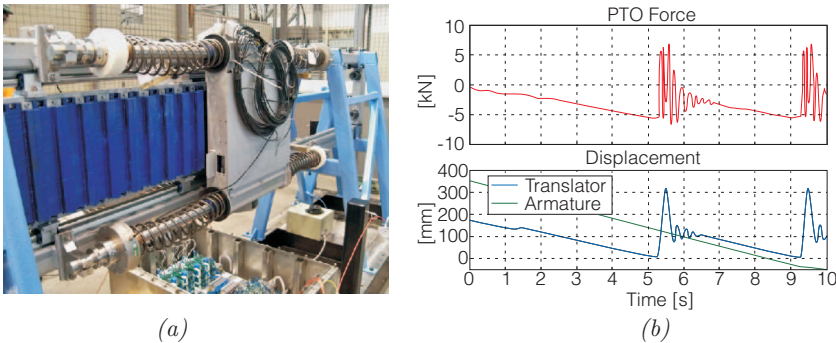
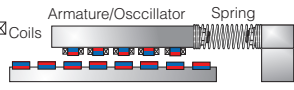


Figure 5.14: In (a) Snapper prototype in [124] and in (b) fitted data of a measured force response in [124].

Another PTO system based on the characteristics of the magnetic coupling is the magnetic lead screw. The idea is that of a screw and a nut, where the thread is created as a magnetic field by permanent magnets placed in a helical screw pattern. Thus, there is no physical contact between the rotor (“nut”) and translator (“screw”), but instead a frictionless power transfer through the interaction of the magnetic fields of screw and nut. This is illustrated in Fig. 5.15. Due to the frictionless design, the screw and nut are not self-locking, and translation of the screw will cause rapid rotation of the nut.

PTOs based on this design have been suggested in [126, 127] and are shown in Fig. 5.16. The designs are presented with permanent magnets only on the nut-part (1370) as in Fig. 5.16a and (b), whereas the screw (1376) is made of a low-reluctance material. Based on the principle that the rotor will position itself to minimise the reluctance of the magnetic circuit, the rotor will operate as a screw.

Table 5.5: Assessment of Snapper™ based PTOs.

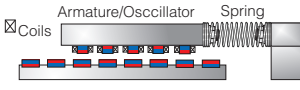
<i>Snapper™ Linear Generator</i>		Prod.	Size	Durability	Storage	Total	
	Points:	-1	3	1	1	4	
	WPEA: <i>Coulomb damping</i>			Storage: <i>Super capacitors</i>			
	Part sized for peak load:	3/4	Optimum maximum force:	$\tau_{PTO,max} = 0.25 \text{ MNm}$ $F_{PTO,max} = 106 \text{ kN}$			
	Part load perform. k_o :	1	Size of primary gen./actuator:	$d = 0.13 \text{ m}$ + linear guide $l = 4 \text{ m}$			
	$\eta_{PTO,1}$	N/A	$\eta_{storage}$	0.92	η_{tot}	0.80	Annual prod. [MWh]

A mature design is assumed to have an efficiency up to 80% with a force density of 130 kN/m^2 . The Snapper PTO is assumed allowing use of super capacitors for power smoothing. An overload capability of 2 is also assumed like previous linear generators, and also to 2/3 of design of the Snapper PTO is expected to see the peak power.

The load force of the Snapper™ is produced by repeatedly kipping a magnetic coupling, thus the force load of the Snapper would resemble a modulated constant force, i.e. Coulomb damping. Also note that the size of Coulomb force is not controllable from sea-state to sea-state but fixed, which is more restrict than the analysis in the previous chapter.

Assuming using the Coulomb damping WPEA, the optimum force capability would be 0.25 MNm with an annual production of $32 \cdot 0.8 = 26 \text{ MWh}$. To produce 106 kN , the diameter d of a tubular Snapper design would be 0.13 m .

Regarding durability, the mechanical spring is considered a weak part of the Snapper design.

<i>Snapper™ Linear Generator with latching mechanism</i>		Prod.	Size	Durability	Storage	Total *	
	Points:	1	2	1	1	5	
	WPEA: <i>Latching w. Coulomb</i>			Storage: <i>Super capacitors</i>			
	Part sized for peak load:	2/3	Optimum maximum force:	$\tau_{PTO,max} = 1.00 \text{ MNm} (424 \text{ kN})$ $\tau_{latch,max} = 3.00 \text{ MNm}$			
	Part load perform. k_o :	1	Size of primary gen./actuator:	$d = 0.52 \text{ m}$ + latching mech. $l = 4 \text{ m}$ + linear guide			
	$\eta_{PTO,1}$	N/A	$\eta_{storage}$	0.92	η_{tot}	0.80	Annual prod. [MWh]

De-clutching control would not be possible for Snapper, thus to improve power capture, latching control with Coulomb damping remains as the only way to improve power extraction. If a latching mechanism is added to the design with three times the force capability of the Snapper, the yearly production is increased to $72 \cdot 0.8 = 57 \text{ MWh}$, c.f. latching control with Coulomb damping. The optimum torque load is 1 MNm , i.e. 424 kN , which gives a diameter of 0.52 m . However, the latching mechanism is also required, which applies three times the production load force. This will increase the loading on the structure, and also the latching mechanism itself will be a very heavy construction.

As 3 MNm latch torque is required to get a decent production along with the Snapper design, the PTO seems as a poor solution for the C5.

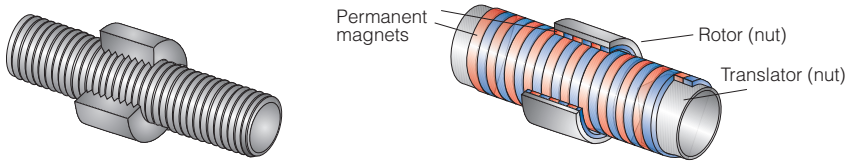


Figure 5.15: Illustration of the magnetic lead screw.

The complete WEC is shown in Fig. 5.16b, where translation of the float (1323) will thus cause the screw (1360) to be rotated, causing the generator (1392) to be driven. The clutch (1391) functions as a ratchet. Prototypes or simulations of the magnetic lead screw performance have not been found.

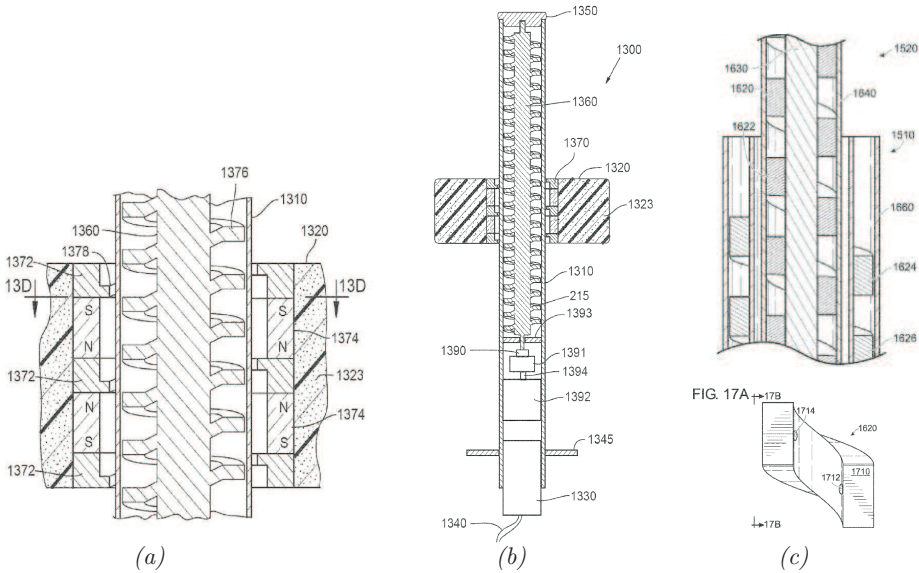


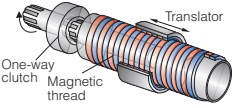
Figure 5.16: From patent application [126, 127].

The idea of the magnetic screw dates back to 1945, see Fig. 5.17d, from [128], but the design has first become interesting with the introduction of rare-earth magnets. In [129] in Fig. 5.17a the magnetic screw is suggested as an actuator for a heart pump. The screw is also mentioned in [130] and in [131] as shown in Fig. 5.17b and Fig. 5.17c respectively.

The lead screw may drive a conventional generator. Typical efficiency of a 4-pole 55kW squirrel cage asynchronous generator is seen in Fig. 5.18 where it is operated up to 100% overload. The peak efficiency is about 95%. A 96.4% peak efficiency is possible if the size is increased to 200kW of this particular series [132]. For permanent magnet machines the peak efficiency may be slightly higher and have better part load efficiency.

Other types of magnetic gears are shown in Fig. 5.19, however these are from rotation to

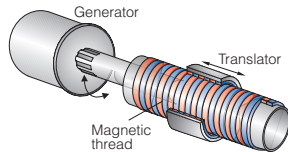
Table 5.6: Assessment of magnetic lead screw PTOs.

<i>Magnetic Lead Screw w. ratchet</i>		Prod.	Size	Durability	Storage	Total
	Points:	1	3	2	2	8
	WPEA: Single-ratchet			Storage: Fly-wheels		
	Part sized for peak load:	1/3	Optimum maximum force:		$\tau_{PTO,max} = 0.50 \text{ MNm}$ $F_{PTO,max} = 212 \text{ kN}$	
	Part load perform. k_o :	2	Size of primary gen./actuator:		$d = 0.19 \text{ m}$ $l = 4 \text{ m}$ + linear guide	
	$\eta_{PTO,1}$	N/A	$\eta_{storage}$		η_{tot} 0.81	Annual prod. [MWh] 41

Force density wise the magnetic lead screw would assemble that of a magnetic coupling, i.e. 200 kN/m^2 is assumed. No prototypes have been made, but as no friction exist in the screw besides linear guide and required axial thrust bearing, the efficiency from conversion from linear to rotation motion is assumed to be approximately 95%. The screw is assumed able to give a speed increase to operate a conventional generator. The generator’s base efficiency is assumed to be 95% and the converter 95%. Hence a total efficiency of around 85% is obtained.

With the one way clutch, the generator will always rotate in one direction. This allows adding fly-wheels to the generator shaft for power smoothing. In this case, only the magnetic lead screw will see the peak power of the absorber. As there is no idle consumption of the screw, the system is expected to have an excellent part load efficiency, i.e. $k_o = 3$.

Due to the one-way clutch, the design would load the absorber motion like the single-ratchet WPEA. Resultantly, the yearly production would be $47.7 \cdot 0.85 = 41 \text{ MWh}$ with an optimum torque of 0.75 MNm corresponding to 320 kN , which at 200 kN/m^2 yields a machine diameter of 0.25 m . Durability wise, the weak point is the linear guide system required, as rotor and translator are attracting each other, and both rotation and translation have to be allowed simultaneously.

<i>Magnetic Lead Screw</i>		Prod.	Size	Durability	Storage	Total
	Points:	3	3	2	1	9
	WPEA: OCIR or Reactive			Storage: Super-capacitors		
	Part sized for peak load:	2/3	Optimum maximum force:		$\tau_{PTO,max} = 1.50 \text{ MNm}$ $F_{PTO,max} = 636 \text{ kN}$	
	Part load perform. k_o :	2	Size of primary gen./actuator:		$d = 0.51 \text{ m}$ or $2 \times d = 0.25 \text{ m}$ $l = 4 \text{ m}$ or $l = 4 \text{ m}$ + linear guide & generator	
	$\eta_{PTO,1}$	N/A	$\eta_{storage}$ 0.92	η_{tot} 0.81	Annual prod. [MWh] 95	

If the one-way clutch was removed from the design, continuous load force control would be possible using the generator and inverter. An issue would be inertia of the screw and generator rotor, as the inertia has to be de-accelerated and accelerated each time the absorber movement reverses. Moreover, the generator would see the peak load as the fly-wheels are gone.

If the inertia of rotor and generator is assumed sufficient small, the system would be able to implement the OCIR control. As a high speed generator may be made and given the assumed flat efficiency curve of the MLS, the part load efficiency is still assumed corresponding to the $k_o = 3$ curve. Resultantly, the yearly production would be $113.2 \cdot 0.86 = 95 \text{ MWh}$ with an optimum torque of 1.5 MNm .

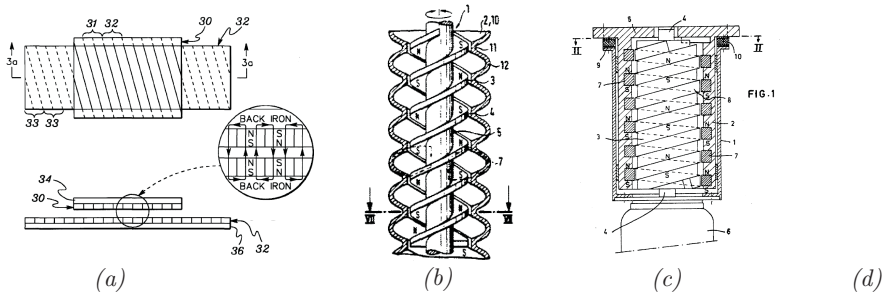


Figure 5.17: Magnetic helical screws for converting linear motion to rotational motion are disclosed in (a) [129] (1997), in (b) [130], in (c) [131] (1967) and in (d) [128] (1945).

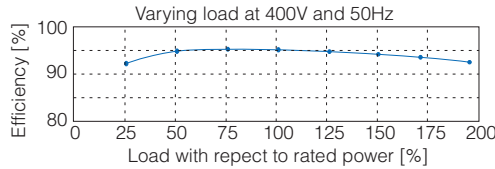


Figure 5.18: Typical efficiency of a conventional generator operating at 1500rpm.

rotation. The first two are gears inspired by mechanical gears and gives a poor utilisation of magnets. The third gear is from [133] and is based on modulating the magnetic field. The outer rotor has many poles whereas the inner rotor has few poles. The stationary low reluctance segments transmit the flux between the two rotors, such that a small movement of the outer rotor reverses the poles seen by the inner rotor. The advantage of this magnetic gear is the high utilisation of magnets, providing torque densities of $50\text{-}150\text{ kNm/m}^3$ [133]. This is mentioned to be one fourth of the density of the magnetic coupling. One-half is lost as the segments only cover half of the available area [117]. Other contributions are the effect of a double air-gap. A prototype was made in [117] with a gearing ratio of 1:5.5 with a measured stall torque of 16Nm, equivalent to only 15 kNm/m^3 . If construction problems were solved and with special designed magnets, 108 kNm/m^3 is estimated possible. Force wise, this is equivalent to 54 kN/m^2 of shear stress. For the prototype the efficiency was only 81%, however the efficiency is expected to increase to 96%.

The concept of magnetic modulation has also been presented as a linear-to-linear gear [135] as shown in Fig. 5.20a. In [136] a linear magnetic gear for wave energy with a 1:3.86 gearing ratio was suggested using the design shown in Fig. 5.20b. The design is tubular, where the gear is combined with the linear generator by having an inner set of magnets on the high speed translator. The high speed translator then induces emf in the windings of an iron cored stator placed in the centre of the construction. A FEM analysis is made of a design yielding a maximum force of 5564N. The diameter of the outer rotor is not given, however using the same diameter as the stator yields 47 kN/m^2 .

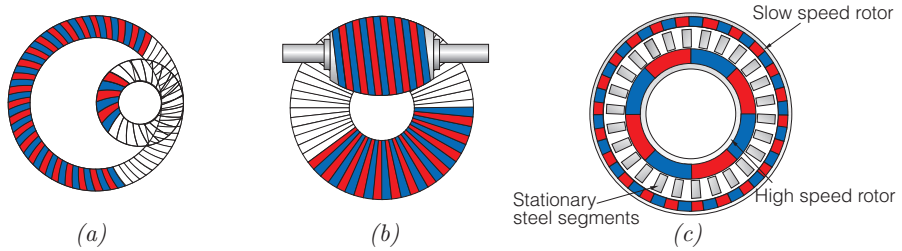


Figure 5.19: Different magnetic gear concepts [134].

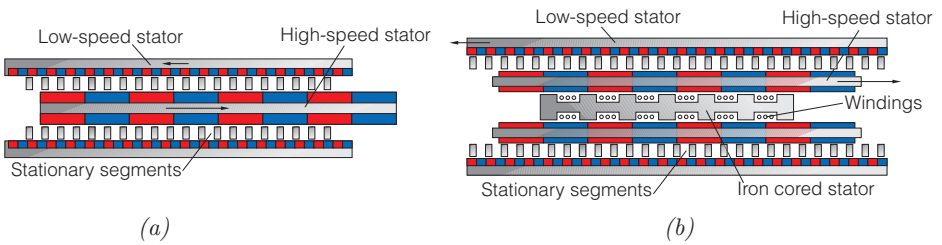


Figure 5.20: In (a) linear magnetic gear [135] and in (b) linear magnetic gear with integrated generator [136].

Table 5.7: Assessment of linear magnetic-geared PM machine.

Lin. Magnetic-Geared PM Mach.	Prod.	Size	Durability	Storage	Total
	Points:	2	1	2	1
	WPEA: Reactive or OCIR		Storage: Super capacitors		
Part sized for peak load:	2/3	Optimum maximum force:	$\tau_{PTO,max} = 1.50 \text{ MNm}$ $F_{PTO,max} = 636 \text{ kN}$		
Part load perform. k_o :	1	Size of primary gen./actuator:	$d = 1.68 \text{ m}$ + linear guide $l = 4 \text{ m}$		
	$\eta_{PTO,1}$ 0.87	$\eta_{storage}$ 0.92	η_{tot} 0.85	Annual prod. [MWh]	80

The machine’s gear part is expected to reach an efficiency of 95%. If linear generator and converter are added, a total efficiency is assumed to be 85%. Control wise, the PTO is capable of continues and 4-quadrant force control. Assuming the use of OCIR control and an overload capability of 100%, the optimum torque level is going to be 1.50MNm with an annual production of $94.1 \cdot 0.85 = 80 \text{ MWh}$. Assuming a force density of 60kN/m^2 , the diameter d would be 1.68m.

Given the small air-gap requirement combined with the large size and weight, also making the linear guide design very difficult, the PTO is viewed as an infeasible solution for the C5.

5.6 Mechanical Transmission

Many early PTO designs suggest different mechanical transmissions. The designs often include a mechanism for rectifying the bi-directional motion of the absorber to avoid continuously reversing the rotation for the generator. The mechanical transmission is either from angular-to-rotary or linear-to-rotary depending on the WEC system.

One of the active WEC projects relying on mechanical transmission is the WEPTOS WEC [137], which is a duck-inspired system. Other systems producing angular motion are e.g. the Wavestar, Pelamis, Oyster and Waveroller. However, all of these systems are basically floating body hinged on a lever arm, thereby reducing the amplitude of the angular motion.

Figure 5.21a shows a wave tank test of a WEPTOS prototype [138], where the sea is a scale 1:15 relative to the Danish Hanstholm site [139]. The WEC consists of a floating structure with multiple duck-shaped absorbers, driving a common shaft using a ratchet mechanism as illustrated in Fig. 5.21b. Power is transferred to the shaft in one direction when the absorber catches up with the shaft speed.

This is a similar ratchet system as disclosed in [140] for early designs of the Wavestar, see Fig. 5.22a. The floats of the Wavestar drive a common shaft through the ratchet mechanism. The ratchet system was tested in a Wavetank as shown in Fig. 5.22b before being abandoned in favour of hydraulics in later designs.

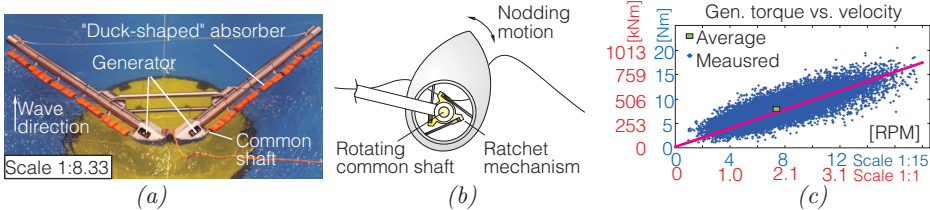


Figure 5.21: In (a) WEPTOS tank test, (b) side-view of a single absorber, (c) speed and torque curves measured on the common shaft.

From scales tests performed by WEPTOS, trajectories of shaft speed and generator torque is shown in Fig. 5.21c, where the blue axes are the measured values for a sea state $H_s = 0.118\text{m}$ and $T_P = 1.51\text{s}$. The red axes values correspond to up-scaling both WEC and sea with 15 according to the scaling laws. Resultantly, the peak wave period would be $T_P = 1.51\text{s}\sqrt{15}$, correspondingly reducing the shaft speed with a factor of $\sqrt{15}$.

The idea is to directly attach a generator to the shaft [141]. The mean expected mean speed in Fig. 5.21c is about 2.1 RPM, which is a factor of 5-10 lower than the typical rotor speed of MW-class wind turbines. Typical rotor speeds as a function of power rating is given in Fig. 5.23a. Hence, a larger direct drive generator than currently employed by some wind turbines is required. Confer for size a prototype 3.4WM direct drive generator for Siemens Windpower in Fig. 5.23c. For similar power rating, a 5-10 times greater torque capability is required, corresponding to either 5-10 times larger air-gap area, or the radius of the generator must be increased for a higher peripheral speed in

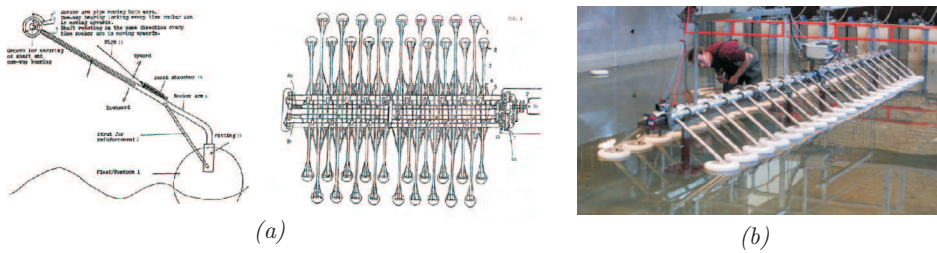


Figure 5.22: (a) mechanical PTO in [140] and in (b) test of system in wavetank.

the air-gap. The latter is structural expensive due to the small air-gap requirement.

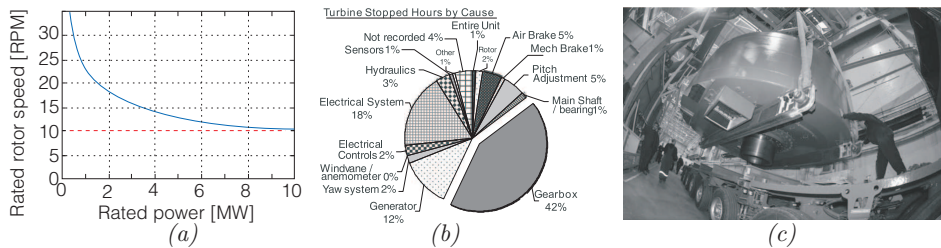


Figure 5.23: In (a) typical rotor speeds [142], (b) down time for turbines in Germany [143] and (c) prototype 3.4 WM direct drive generator for Siemens Windpower.[142]

To avoid the large slow operating generator, a step-up gearbox could be used. The gearbox would probably need a 5 times higher gearing-ratio than the three-stage gearboxes used in turbines today. As these gear-boxes already have durability challenges as seen in Fig. 5.23b, this is probably not a good solution. For wind-turbines in Germany 42% of the down-time is due to gearbox failures.

For mechanical transmission systems converting linear motion to rotary, examples may be found in patents and patents applications. These include systems based on rack and pinion, wire systems, helical screws and ball screws.

Examples of rack and pinion are given in [144, 145, 146]. The PTO disclosed in [146] and shown in Fig. 5.24a consists of multiple pairs of rack and pinions with different pinion sizes, providing multiple available gearing ratios. Using the forked rack, each pair of pinions will rotate in opposite direction, and by adding a ratchet mechanism between each pinion and generator shaft, power will be transferred to the generator in both up and down strokes. Different pinion pairs may then be enabled depended on the sea state. In [145] the pinion diameter required for delivering a thrust of 500kN is estimated to be 150mm, yielding 127rpm at 1m/s. Thus, a decent speed increase is obtained. A rack and pinion design is also suggested in [115], where the pinion drives a switches reluctance machine. The ratio of the rotor and pinion determines the air-gap speed of the generator, i.e. having a ratio 4:1, gives at a peak rack speed 1m/s an air-gap speed of

Table 5.8: Assessment of ratchet mechanism with direct drive.

Direct Drive Generator		Prod.	Size	Durability	Storage	Total
Points:		1	0	1	1	3
WPEA: Single-ratchet			Storage: Super-capacitors			
Part sized for peak load:	3/4	Optimum maximum force:		$\tau_{PTO,max} = 0.50 \text{ MNm}$		
Part load perform. k_o :	2	Size of primary gen./actuator:		$d = 3.5 \text{ m}$ $l = 0.77 \text{ m}$		
$\eta_{PTO,1}$	N/A	$\eta_{storage}$		η_{tot} 0.90	Annual prod. [MWh]	33

Assuming a high total efficiency of 90% and 100% overload, $k_o = 2$, the single ratchet load will for a C5 absorber produce $36.8 \cdot 0.90 = 33 \text{ MWh}$ at an optimum torque of 0.5 MNm . This will required a generator of the size of a 1 MW direct drive turbine, i.e. at 40 kN/m^2 a diameter of 3.5 m and a length of 0.77 m . If the ratchet was removed, the OCIR WPEA could be used yielding $94.1 \cdot 0.90 = 84.7 \text{ MWh}$ at a torque of 1.0 MNm . According to Fig.5.12, this gives a generator diameter of 4.5 m .

The large size combined with low power production renders this system infeasible.

4 m/s , which is similar to air-gap speed of direct drive turbine generator at rated speed. However, the biggest challenge with the rack and pinion is life time, and is probably the reason why no larger implementations have been performed on WECs. The efficiency of the gears is typical that of spur or helical gears, i.e. 97% [147, 148].

In [99] a small rack and pinion setup of peak capacity of 200 W is tested, having a 15:1 step-up gearbox between pinion and generator. At sinusoidal excitation the transmission efficiency from input mechanical power to generator shaft showed was reported to be between 50%-83%, with the 50% being at 50% rated force and 100% rated speed.

In Fig. 5.24b a rack and tooth belt driven WEC [149] and in Fig. 5.25a a belt driven PTO. In Fig. 5.24c [150] a helical screw or lead screw is suggested for driving a generator. However, only a low gearing ratio is possible due to the self-locking nature of a lead screw if the thread pitch becomes too low.

To avoid the friction of lead screws, suggestions have been given to use ball-screws [151, 127, 152, 153]. An illustration of a ball-screw is given in Fig. 5.25, where the rolling balls between nut and screw thread greatly reduce the thread friction. A mechanism is added for re-circulating the balls. A high gearing ratio may be obtained as a low thread pitch is allowed without self-locking. Systems implemented with ball-screws are seen in Fig. 5.25b and Fig. 5.25c. In [152] the ball screw is suggested combined with a one way clutch to achieve a uni-directional shaft-rotation, avoiding acceleration and de-acceleration of gear and generator inertia.

The expected efficiency of a ball-screw is seen in Fig. 5.25d. A ball-screw rated for a dynamic load of 200 kN in a WEC will at minimum require a $\text{Ø}100 \text{ mm}$ screw [154]. At

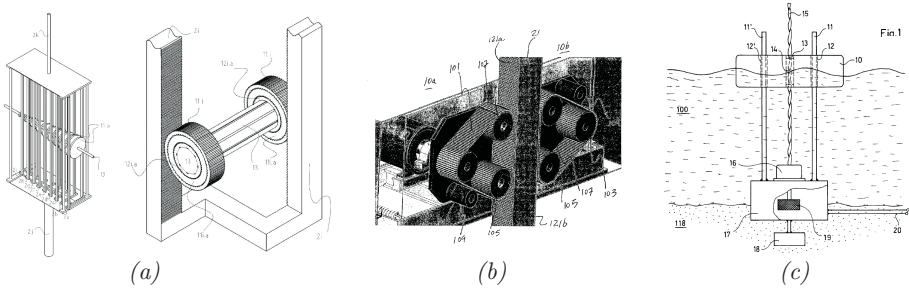
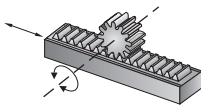


Figure 5.24: In (a) rack and pinion PTO [146], (b) rack and tooth belt PTO [149], (c) lead screw PTO [150].

Table 5.9: Assessment of rack and pinion PTO.

Rack and Pinion	Prod.		Size	Durability	Storage	Total
		Points:	2	2	1	1
WPEA: OCIR			Storage: Super capacitors			
Part sized for peak load:		3/4	Optimum maximum force:	$\tau_{PTO,max} = 0.50 \text{ MNm}$ $F_{PTO,max} = 212 \text{ kN}$		
Part load perform. k_o :		2	Size of primary gen./actuator:	Pinion diameter: 150mm + linear guide & generator		
$\eta_{PTO,1}$		N/A	$\eta_{storage}$	η_{tot}	0.86	Annual prod. [MWh]

If the transmission itself from linear to rotational is assumed to be 95% efficient, and yield sufficient speed not requiring an extra gear, the total efficiency with generator and converter would be 86%. As the gear is passive, it will have a good part load efficiency, i.e. the $k_o=2$ curves are used.

Assuming the use of OCIR control, the optimum torque level is going to be 1.50 MNm with an annual production of $94.1 \cdot 0.86=80$ MWh according to Tab. 4.5. This corresponds to 424kN, which according to state-of-the-art analysis requires a pinion diameter of 150mm. A low durability is expected, rendering the design infeasible. Also, the design is expected to be very cumbersome for the C5.

a lead-angle of 6° this will give a pitch of 26mm/rev, i.e. at a linear velocity of 0.5m/s this gives 1150RPM, which is a sufficient speed increase.

The main reason for no active projects using ball screws is the durability, as the expected number of rotations is more than 5 times greater than for the current most demanding application of roller screws like the injection moulding industry, where 50 million screw revolutions per year [155] is expected. According to [156] lifetime of a ball-screw is expected to be 25-100 million revolutions depending on load cycles and design. Similar to ball-screw design, also roller screw design exists, where helical rollers in a planetary arrangement replace the balls.

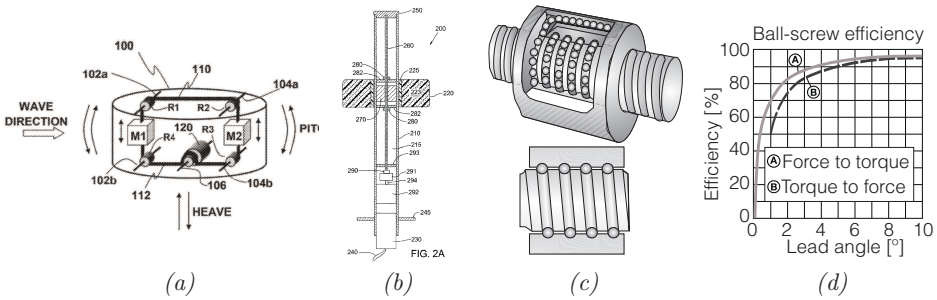


Figure 5.25: In (a) belt driven PTO [157], (b) [127], (c) illustration of a ball-screw, (d) typical ball-screw efficiency [158, 156].

Table 5.10: Assessment of ball or roller screw PTO.

Ball(Roller) Screw	Prod.		Size	Durability	Storage	Total
		Points:	-1	3	1	2
WPEA: Single-ratchet			Storage: Fly-wheels			
Part sized for peak load:		1/3	Optimum maximum force:		$\tau_{PTO,max} = 0.50 \text{ MNm}$ $F_{PTO,max} = 212 \text{ kN}$	
Part load perform. k_o :		2	Size of primary gen./actuator:		$d = 0.10 \text{ m}$ + linear guide & generator	
$\eta_{PTO,1}$		N/A	$\eta_{storage}$	η_{tot}	0.81	Annual prod. [MWh]

Similar evaluation as the magnetic lead screw with ratchet mechanism, except a low durability score. Also the overall efficiency is expected a bit lower due to friction in the ball screw. A ball-screw rated for a dynamic load of 200kN will at minimum require a $\varnothing 100\text{mm}$ screw [154]. For the C5, the screw is durability wise assumed to be infeasible.

5.7 Hydraulic Transmissions

Hydraulic solutions are interesting for wave energy as low weight actuators (cylinders) are capable of producing the high controllable forces at low velocities, and the bidirectional

input may be easily “rectified” with valves. Unfortunately, fluid power systems are often characterised by poor efficiencies when operating at part load, which is crucial with the highly fluctuating power levels of waves.

Force density wise, hydraulic actuators are unmatched compared to other technologies. In the hydrostatic transmissions, the hydraulics is typically allowed operated at a continuous pressure of 350 bar (35000kN/m²).

The hydraulic pressure is converted into mechanical work by applying the pressure to displaceable pistons, which is used for creating both linear and rotary actuators. Double acting hydraulic cylinders are shown in Fig. 5.26. By applying a differential pressure across the piston, force is generated, and flow is entering and exiting the cylinder chambers as the piston displaces. A cylinder may both be created asymmetric or symmetric, where the symmetric cylinder may produce equal sizes positive and negative forces.

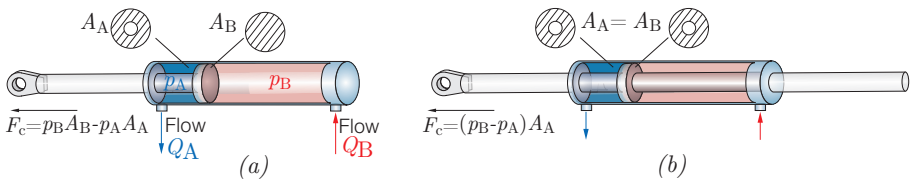


Figure 5.26: Asymmetric (a) cylinder and (b) symmetric cylinder.

Compared to the linear electric actuator, where the active or force producing area is parallel to the force direction, the active areas in the cylinder is normal to the force direction. Resultantly, the length of a hydraulic cylinder is ideally equal to the required stroke, whereas a linear generator has to be longer to have overlapping stator and translator area. Often two times the stroke is chosen for electrical actuators for best utilisation of materials. By applying 350bar pressure to an area, a hydraulic cylinder produces 35000kN/m² per active area, which is a factor of about 1000 compared electrical machines. A visualisation of size comparison of a hydraulic and electric actuator is given in Fig. 5.27, where the electric actuator produces 50kN/m² and the hydraulic cylinders operates at 340bar differential pressure. Both are capable of producing minimum ± 400 kN. The efficiency of a hydraulic cylinder with proper choice of seals is typically 95% [159, 160, 161].

For converting between hydraulic energy and rotary motion different types of high speed hydraulic motors exist, allowing speeds from 450rpm up to 3500rpm. A typical topology is the axial piston motors, which may be capable of variable displacement, i.e. adjustable ratio between flow and speed. As illustrated in Fig. 5.28 the pistons are located in a rotating barrel, which is connected to the drive shaft. By applying pressure to the pistons on one side of the barrel, a component of the normal force acting on the pistons will generate a net torque on the barrel. The useful components of the normal force are generated because the piston shoes are resting on an inclined plate. As the pistons rotates with the barrel, a commutating unit, the valves-plate, ensures that only pistons on one side are connected to high pressure. As the pistons moves on the inclined plate, they make a reciprocating movement inside the barrel, thereby producing flow. By having

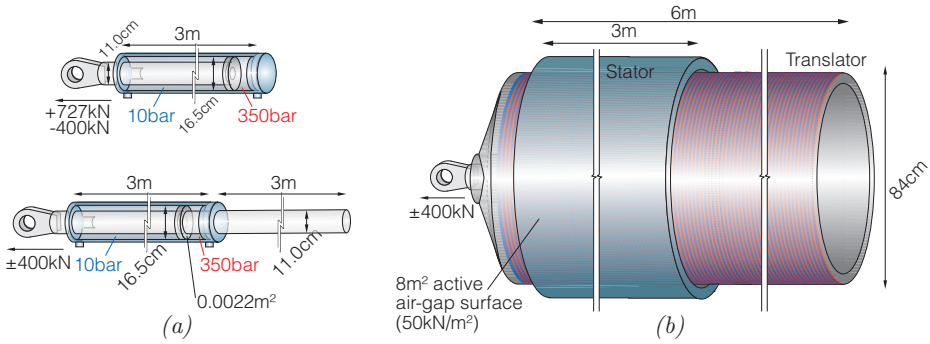


Figure 5.27: Cylinders of 3 m stroke producing minimum ± 400 kN and corresponding electrical actuator.

a small actuator adjusting the angle of the inclined plate, the swash-plate, torque and flow of the motor may be controlled. By swashing the plate to an opposite angle, the motor may reverse flow while maintaining same rotational direction. These variable displacement units are the main components of a hydro-static transmission, consisting of one unit functioning as a pump and one functioning as a motor. By adjusting the displacement, the gearing ratio may be controlled continuously.

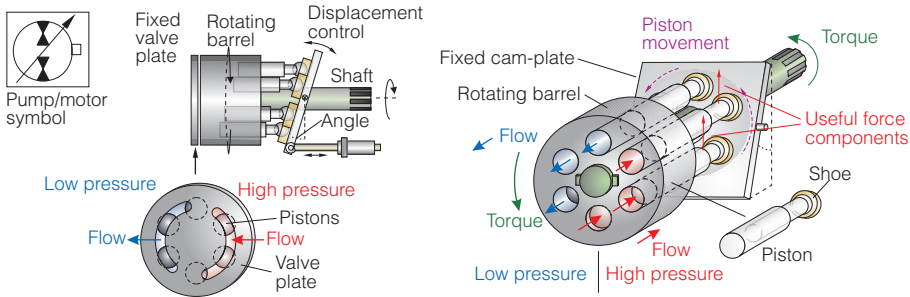


Figure 5.28: Illustration of closed circuit variable displacement pump/motor.

Based on the conventional hydrostatic transmission for mobile hydraulics, these have in wide range been suggested for use in wave energy, especially in patent literature [162, 163, 164, 165, 166, 167, 168, 163, 164, 165, 167, 168] with the oldest patent being for the Duck [166] in 1977. An illustration of the circuit is shown in Fig.5.29a. A symmetric cylinder is applied as pump, producing a bi-directional flow, which is in closed-circuit connection with a hydraulic pump/motor. The hydraulic pump/motor adapts to the incoming flow, running the generator at a fixed speed. When the flow changes direction, the hydraulic motor swashes to an opposite angle. Hence, the hydraulic implements a reversible transmission with continuously variable gearing ratio between float and generator. By controlling the displacement of the hydraulic motor α_{disp} , the differential pressure of the cylinder Δp may be controlled, thereby also implementing continuous force control of the cylinder. The system is capable of 4-quadrant control. The charge

pump is for maintaining a minimum charge pressure and ensures adequate flushing of the fluid in the closed circuit. The relief valves limit the pressure in the circuit in case the flow produced by the cylinder exceeds the capability of the motor. In Fig. 5.29b an open circuit version is given, where check valves rectify the bidirectional flow instead of the pump/motor. Note that the rectifier bridge prevents reverse power flow, meaning that reactive control is not possible.

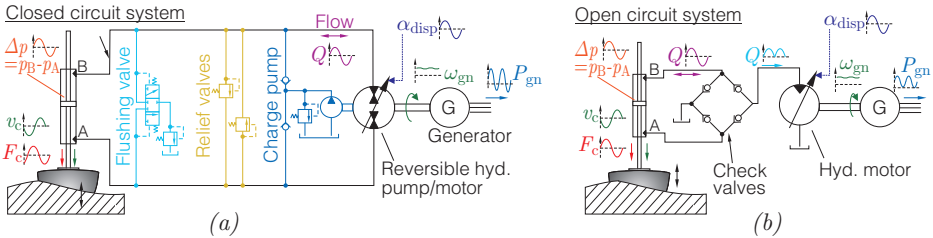


Figure 5.29: In (a) closed circuit hydraulic transmission and in (b) open circuit version.

One of the main drawbacks of the above system is that all components, i.e. cylinder, motor, generator, etc. has to be sized for handling the peak power load conditions as no temporary storage is part of the conversion chain. If a gas charged accumulator as illustrated in Fig. 5.30 is added to the pressure line, energy is stored a function of the hydraulic pressure. When the hydraulic pressure exceeds the gas' pre-charge pressure $p_{acc,0}$, the accumulator fills with fluid, compressing the gas to the hydraulic pressure. To have good utilisation the accumulator storage capacity, the hydraulic pressure should vary between $p_{acc,0}$ and $2p_{acc,0}$. Thus, adding accumulators to the lines of the hydraulic transmission will not be possible, as the stored energy and force control are not decoupled.

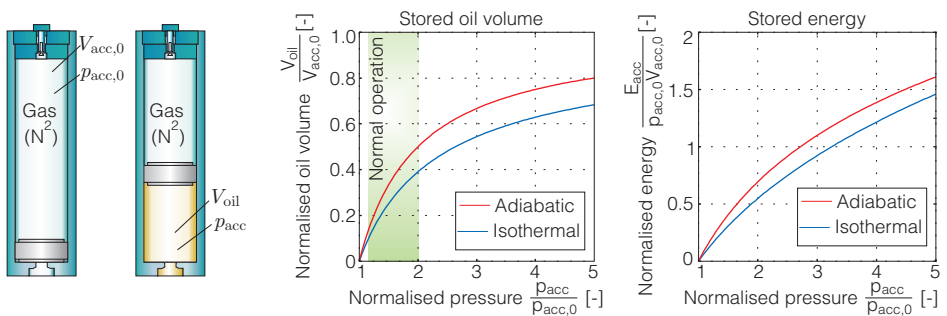


Figure 5.30: Illustration of a gas charged piston accumulator. Normalised operation curves with N^2 -gas are shown for adiabatic and isothermal processes respectively.

The component suffering the most of being sized for handling the peak power load is the variable displacement hydraulic motor, having poor part load efficiencies. Typical

efficiencies for a swash-plate motor operating at part displacement are shown in the left plot in Fig. 5.31. Dependent on pressure and speed, the motor may at full displacement perform up to 88%, however, as the displacement is reduced, the efficiency drops at an increasing rate. At 25% part displacement the efficiency has dropped to 60%.

More efficient commercial hydraulic motors exist, e.g. bent-axis type. The efficiency of this type of unit is shown for variable and fixed displacement respectively in the mid and right plot in Fig. 5.31. At fixed displacement the motor may actually operate at up-to 95% efficiency and stay above 90% in a very large range. Hence, the main problem with hydraulics is not being capable of high efficiencies, but not offering high efficiencies at part load. The reason for not using the bent axis-motor instead of the swash-plate unit in Fig. 5.29a is due to response time. From zero to full displacement a bent-axis uses more than 1s for larger units [169], whereas swash-plate units is often below 50ms with bandwidths above 10Hz [170, 171, 172, 173]. Thus pressure control is not possible with bent-axis. Another aspect is that bent-axis motors are normally not designed to reverse flow direction.

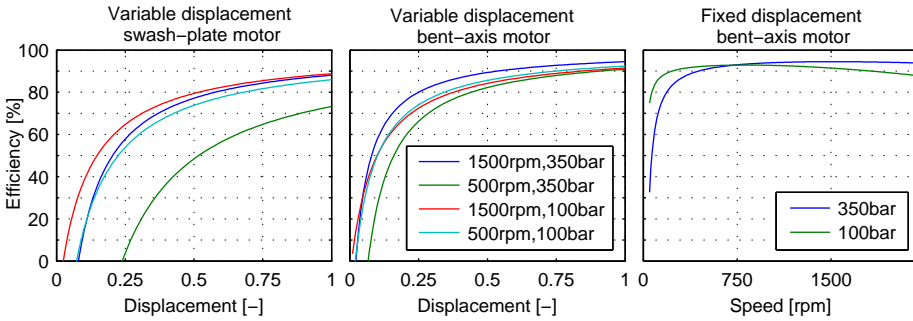


Figure 5.31: Typical efficiency curves for 250 cm³/rev pump/motors.

Evaluation of the concept in Fig. 5.31 based on simulation was performed in [174] for Wavebob. When optimising power production, the efficiency from cylinder to generator shaft was found to be 65% at the best sea state, when operating the generator at a fixed speed. Thus, adding efficiency of generator and auxiliaries will further reduce the overall efficiency.

A similar PTO system has also been tested at Wavestar [175] on the prototype. As seen in Fig. 5.32a each absorber is driving a symmetric cylinder with 3m stroke. A zoomed view of the cylinders is given in Fig. 5.32b. Each cylinder is connected to a 250 cm³/rev motor inside the machine hull as shown in Fig. 5.32c, driving a 55kW asynchronous generator. A maximum of 58% efficiency from hydraulic cylinder to generator output is reported in [175].

The Wavestar PTO is slightly modified compared to the system in Fig. 5.29a. When the cylinder flow exceeds the motor’s flow capability, instead of dissipating the extra flow across a relief valve, a check-valve opens to a common “overflow” line with accumulators as illustrated in Fig. 5.32a. All 20 floats supply this line when in overflow, thereby

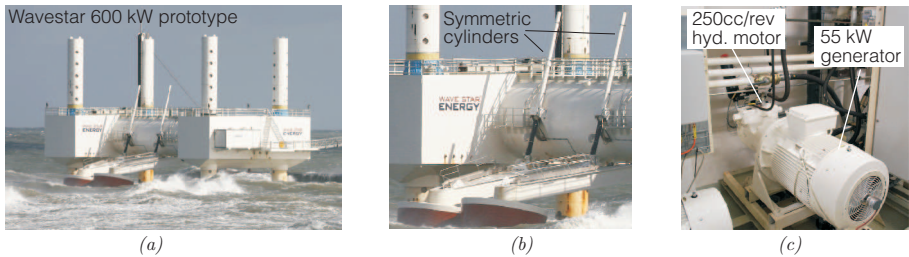


Figure 5.32: Wavestar prototype and hydraulic PTO. The prototype is a test section of a 600kW 20 float system,

providing power an extra generator. In [O] the efficiency of such a system is estimated to be between 60% and 70% from input to grid.

In [176] a similar system is suggested for a single absorber, where the overflow motor drives the same generator as shown in Fig. 5.32b. In low flow regimes the damping force may be controlled using motor 1, and as the flow exceeds this level, the pressure saturates, and excess flow enters the accumulator connected to the second motor. Resultantly, the average load of the units may be increased. An estimated efficiency is not disclosed.

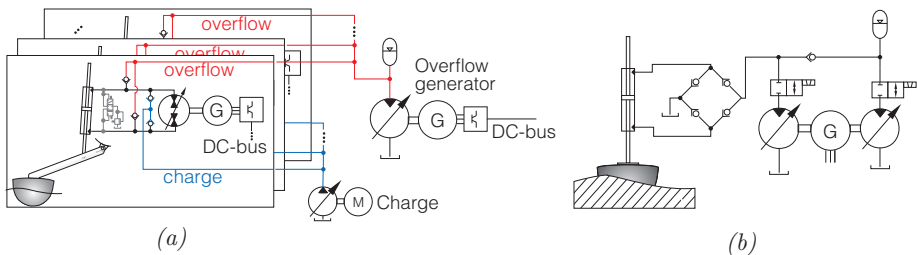
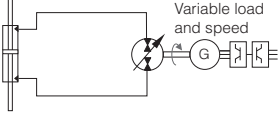


Figure 5.33: In (a) Wavestar PTO and in (b) PTO shown in [176].

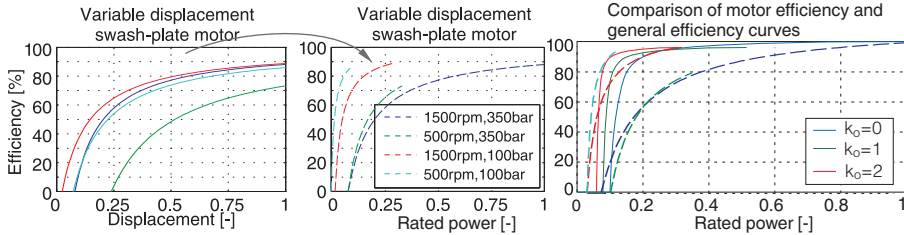
To overcome the poor part load performance of conventional variable displacement motors, new types of hydraulic pump and motors known as discrete displacement or Digital Displacement[®] are being developed, primarily by Artemis Intelligent Power [178, 179, 180, 181, 182, 183]. The idea of the DDPM is to achieve variable displacement by electronically activated poppet valves (on/off valves) instead of mechanically varying the stroke length of pistons. The concept was developed during the 1970s and 1980s [184] by the Edinburgh team working on the Duck as a solution for the PTO This later lead to establishment of the company Artemis Intelligent Power in 1994, which is the forerunners in developing the technology. The first patent was filled 1989 [180]. In 2010 the company was acquired by Mitsubishi Power Systems Europe, with the aim of developing multi-megawatt wind-turbine transmissions [185] .

Based on [186], an illustration of the Discrete Displacement Pump/Motor (DDPM) is given in Fig. 5.34 and for a single piston in Fig. 5.35. The pistons make a full stroke

Table 5.11: Assessment conventional hydrostatic transmission.

Conventional Hydrostatic Trans.	Prod.	Size	Durability	Storage	Total
	Points:	1	3	1	1
	WPEA: OCIR (or reactive)			Storage: Super capacitors	
	Part sized for peak load:	4/4	Optimum maximum force:	$\tau_{PTO,max} = 1.00 \text{ MNm}$ $F_{PTO,max} = 424 \text{ kN}$	
	Part load perform. k_o :	0	Size of primary gen./actuator:	$d = 0.22 \text{ m}$ $l = 4 \text{ m}$	
	$\eta_{PTO,1}$	$\eta_{storage}$	0.92	η_{tot}	0.65

An overall efficiency from mechanical to grid of 65% is assumed. The efficiency at part load will be dominated by the variable displacement motor. Converting the swash-plate motor plots in Fig. 5.31 to efficiency versus rated power has been performed below. As seen, if the speed of the hydraulic motor may be varied, the part load efficiency may be increased. Comparison of these to the curves in the Fig. 4.39 has also been performed below. Based on the efficiency curves, and the system is operating a high force/pressure, the part load efficiency is still poor, the $k_o = 0$ curves are used for annual production evaluation.



The power-converter will continuously be controlling the generator to adapt the speed of hydraulic motor and generator to incoming power. This is covered in [177]. Resultantly, fly-wheels as storage are not possible, i.e. only super-capacitors are possible. Cylinder, motor, generator and inverter have to process peak power, thus the components are size accordingly. Hence 4/4 of the PTO sees the peak power load.

Control wise, the PTO is capable of continues and 4-quadrant force control, thus both the OCIR and reactive control methods would be possible. Assuming the use of OCIR control, the optimum torque level is going to be 1.0MNm with an annual production of $52.8 \cdot 0.65 = 34 \text{ MWh}$ according to Tab. 4.5. The 1.00MNm corresponds to $F_{PTO} = 424 \text{ kN}$. Assuming a piston rod diameter of $\varnothing 1180 \text{ mm}$, a piston diameter of 224.5mm would be required at a differential pressure of 300 bar. Note that with with the chosen rod diameter, additional linear guides are not required to support the cylinder.

Durability wise, cylinder are highly tested, however the hydraulic motor with the varying load and extreme high amount of swash-cycles would might not have sufficient life-time.

for each rotation of the eccentric drive shaft/crankshaft. To control the displacement, a piston stroke is either fully used or left idling by controlling the two poppet valves placed at each piston outlet. By leaving the low pressure poppet open, the piston is idling by breathing low pressure fluid, i.e. in turns sucking and pumping low pressure fluid with very little energy consumption.

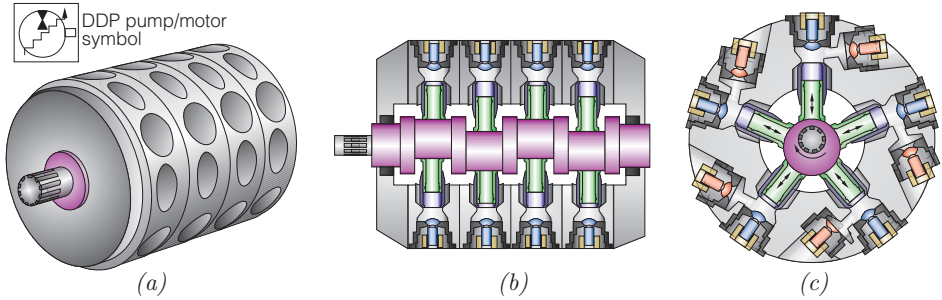


Figure 5.34: DDPM motor in radial design.

If an active pumping stroke is required, the low pressure poppet is closed at bottom top position and the high pressure poppet opened. By controlling the number of active strokes over time of all pistons, the average flow and thereby displacement may be discretely controlled. By reversing the poppet activation cycle and instead opening the high pressure poppet at the top piston position, the unit operates as a motor, as the high pressure acting on the piston delivers torque to the crankshaft.

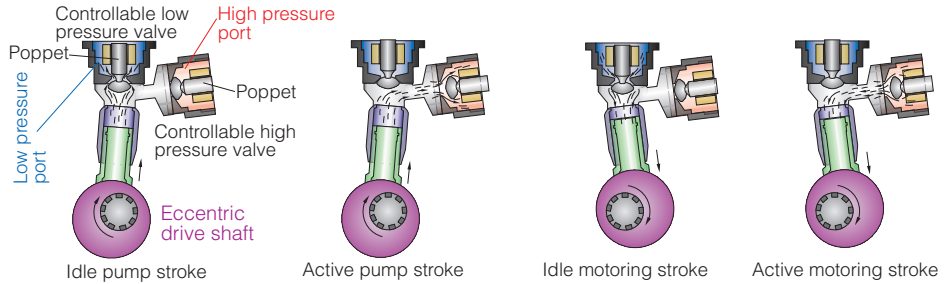


Figure 5.35: Different modes of piston operation in the DDPM.

As shown in Fig. 5.34 the DDPMs are normally based on a radial pump/motor design for best space for the valves at the pistons outlet, allowing large flow connection for low breathing losses. The design also reduces the linear velocities at the pistons shoes compared to the axis piston design. Finally, the design allows banking “slices” of DDPMs onto a common crankshaft, allowing higher displacement resolution and load distribution. The construction of the DDPM in slices has also given it the name, the “Wedding-Cake” machine [187, 188, 189]. One of challenges in digital/discrete hydraulics is the fast switching times required of valves. In [190] it is reported that for a DDP operating at 1800-2800 rpm, valve opening closing time should be kept below 5 ms.

The core property of the DDPM is providing high part load efficiency by using either full or idle strokes, whereas the conventional swash-plate or bent-axis machines distribute the part displacement on all strokes, meaning that all pistons are pressurised and loaded despite performing reduced useful work. In [191] a complete hydraulic wind turbine transmission based on a DDP pump and a DDM motor is reported to shown idle power loss powers in the range of 7W/(litre/min). Discrete displacement based transmission for wind turbines are also explored in [192, 193] and for tidal energy in [194]. One of the first suggestions for DDPM in turbines is given [184], which as the current concept suggest having the turbine rotor directly driving a ring-cam pump with valves for discrete displacement. In [195] a ring-cam pump is also suggested for wave-energy.

Achieved efficiency for a 196cm³/rev Digital Displacement[®] machine made by Artemis [196] is shown in Fig. 5.36. As seen the peak efficiency is above 95% at full displacement and is in [191] reported to be 97%. At 20% displacement the machine maintain an efficiency above 90% for a large range of pressure and speed. Sauer-Danfoss, having a license for the technology in mobile hydraulic, has reported the results in Fig. 5.37 for a 175kW-unit (approx. 116cm³/rev at 300bar,3000rpm) [197]. As seen, the DDPM excels in part load efficiency compared to the conventional variable displacement technologies.

Bandwidth of the DDPM is explored in [198, 196, 199]. Flow wise, depending on the speed, the DDPM is shown to be able to go from idle to full flow in 25ms [196], i.e. faster response time than the swash-plate design.

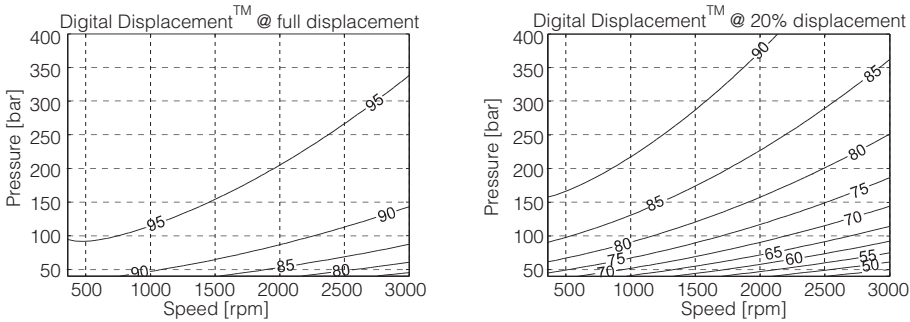
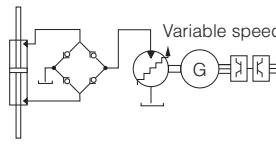


Figure 5.36: Efficiency curves for a 196cm³/rev Digital Displacement[®] machine disclosed in [196].

Directly replacing the closed circuit variable displacement swash plate motor Fig. 5.29a with a DDPM is evaluated in [174] based on simulation with the efficiency curves in Fig. 5.36. The DDPM based transmission is shown to maintain an average of 82% efficiency from cylinder input to generator shaft. However, the DPDM is an open circuit machine, meaning that it has one pressure port, and the other port must always be connected to tank or low boost pressure. The PTO in Fig. 5.29a requires a closed circuit motor, i.e. both ports are in change pressurised. Thus to make an evaluation, the system should be evaluated as an open circuit as in Fig. 5.29b with an external valve arrangement for shifting which port of the cylinder is connected to tank and which is connected to the DDPM. This is suggested in Ehsan et. al. [187] for the IPS buoy.

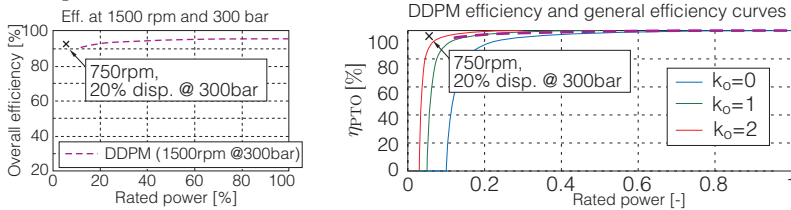
Table 5.12: Assessment of DDPM Transmission.

	Prod.	Size	Durability	Storage	Total	
	Points: 3	3	3	1	10	
	WPEA: OCIR			Storage: Super capacitors		
	Part sized for peak load:	4/4	Optimum maximum force:	$\tau_{PTO,max} = 1.50 \text{ MNm}$ $F_{PTO,max} = 635 \text{ kN}$		
	Part load perform. k_o :	2	Size of primary gen./actuator:	$d = 0.24 \text{ m}$ $l = 4 \text{ m}$		
$\eta_{PTO,1}$	$\eta_{storage}$	0.92	η_{tot}	0.83	Annual prod. [MWh] 98	

Assuming 95% efficiency for the cylinder, 97% for the DDPM and 95% of the generator, along with 95% of the power converter,

$$\eta_{tot} = \eta_{cyl} \eta_{hyd,m} \eta_{gn} \eta_{conv} = 0.95 \cdot 0.97 \cdot 0.95 \cdot 0.95 = 0.83 \tag{5.2}$$

, a base efficiency of 83% is obtained. The efficiency plot of Fig. 5.37 is compared to the general efficiency curves below. If the speed of the DDPM is controllable using the inverter, the DDPM may maintain above 90% efficiency down to 10% of rated power at full pressure, i.e. at full torque τ_{PTO} . Adding the converter and generator to the system will also affect the overall shape of the curve, but a part load performance of $k_o=3$ is assumed to be valid.



Control wise, the PTO is capable of continues force control (but not reactive), thus OCIR control would be used. Assuming the use of OCIR WPEA, the optimum torque level is going to be $\tau_{PTO,max} = 1.50 \text{ MNm}$, yielding an annual production of $119.1 \cdot 0.83 = 98 \text{ MWh}$. The 1.50 MNm corresponds to $F_{PTO} = 635 \text{ kN}$. Assuming a piston rod diameter of $\varnothing 180 \text{ mm}$, a piston diameter of 244 mm would be required at a differential pressure of 300 bar.

Durability wise, the DDPM motor is being developed for wind turbines and is therefore assumed to reach required durability. Overall the PTO will be highly suitable for the C5, except for requirement of one generator per absorber and that storage would be performed using super capacitor. Another aspect is, that the DDPM is not commercially available yet.

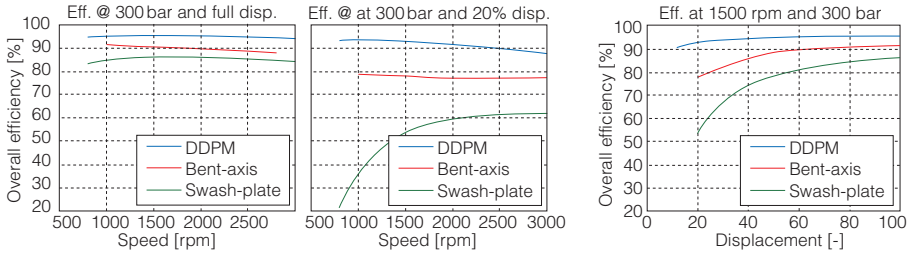


Figure 5.37: Efficiency curves for a 175kW DDPM unit in pumping mode by Sauer-Danfoss [197]

The PTO concept proposed by Ehsan et. al. uses the multiple-slices or “wedding-cake machine”, where one section operates as a motor connected to the cylinder and the second section is connected to hydraulic gas-charged accumulators for temporary energy storage.

Thus, the second section operates both in motoring and pumping mode. This is illustrated in Fig. 5.38a. Using this system the generator may be operated at both fixed speed and steady load. At high instantaneous wave power the second slice is in pumping mode, storing energy in the hydraulic accumulator. When the wave power drops, the second slice shifts to motoring, transferring the stored energy back to the generator shaft. The simulated results obtained in [187] are reproduced in Fig. 5.38b, showing how the PTO is capable of completely smoothing the fluctuating power input. The figure also shows how the second slice in turns stores and retrieves energy from the accumulators. Achieved total conversion efficiency is not reported, however some additional loss will be present in second slice, as the power is processed twice. A similar transmission is suggested for injection moulding in [199, 200].

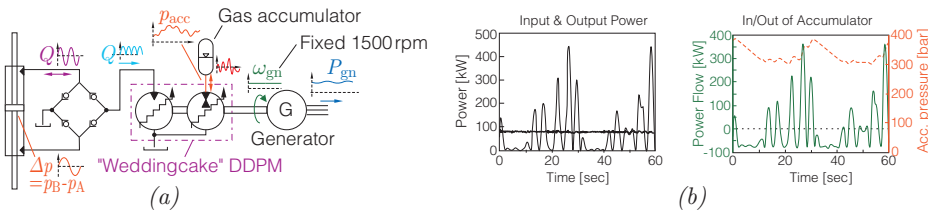
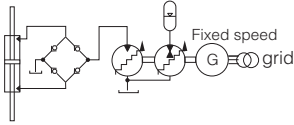


Figure 5.38: In (a) “weddingcake”-PTO for wave energy suggested in [187], and in (b) the simulated results.

To sum up the status of the DDPM technology, many prototypes have been implemented since the 1990’s, with some of the largest units being prototype wind turbine transmissions. In 2009 a 1.6MW prototype turbine transmission was completed by Artemis, comprising a ring-cam discrete displacement pump driven at rotor speed and two 800kW DDM’s operating at 1500rpm [69]. Mitsubishi have reported in 2012, that a 2.4MW “MWT100” gear-driven wind turbine have been retrofitted and tested with a

DDT hydraulic drive train, comprising one pump operating at 10rpm and two hydraulic motors operating at fixed 1000RPM [201]. A 7 MW-class transmission is reported for testing by Mitsubishi in 2013 for their upcoming 7 MW Sea Angel turbine.

Table 5.13: Assessment of wedding-cake transmission.

Weddingcake Trans. (DDPM)		Prod.	Size	Durability	Storage	Total	
		Points:	2	3	3	3	11
WPEA: OCIR			Storage: Accumulator				
	Part sized for peak load:	2/3	Optimum maximum force:		$\tau_{PTO,max} = 1.50 \text{ MNm}$ $F_{PTO,max} = 635 \text{ kN}$		
	Part load perform. k_o :	1	Size of primary gen./actuator:		$d = 0.24 \text{ m}$ $l = 4 \text{ m}$		
	$\eta_{PTO,1}$	$\eta_{storage}$	0.94	η_{tot}	0.79	Annual prod. [MWh]	79

As a fixed speed of 1500rpm may be obtained, a full-power converter may be avoided depending on grid requirements. Accordingly, from generator to grid, the efficiency is assumed to be 0.98 for e.g. filters.

The power passing the accumulator storage will experience the round-trip efficiency of the accumulator, i.e. 94%, and pass the DDPM conversion efficiency twice.

If 2/3 of the power is assumed passing in and out of the accumulator storage, the base efficiency of the PTO is:

$$\eta_{tot} = \frac{\eta_{cyl}\eta_{hyd,m}\eta_{gn}\eta_{conv} + 2\eta_{cyl}\eta_{hyd,m}\eta_{hyd,m}\eta_{acc,round-trip}\eta_{hyd,m}\eta_{gn}\eta_{conv}}{3} = 79 \tag{5.3}$$

Looking at the DDPM efficiency curves in Fig. 5.37 the $k_o = 2$ curves are used for annual production evaluation. Control wise, the PTO is capable of continues force control, thus OCIR control would be used as WPEA. The optimum torque level is going to be 1.50MNm with an annual production of $94.1.8 \cdot 0.79 = 74 \text{ MWh}$. A piston diameter of 244mm would be required at a differential pressure of 300 bar.

Overall the PTO will be highly suitable for the C5, except for requirement of one generator per absorber. The storage capacity using accumulator is also a big advantage.

A hydraulic PTO system having common properties with the weddingcake-PTO is PTOs employing a hydraulic transformer. This PTO is illustrated in Fig. 5.39a, and has been suggested in [202, 176, 203]. The PTO is capable of controlling the force of the cylinder, while having a fixed system pressure with energy smoothing accumulators. However, the part load efficiency of the hydraulic transformer in Fig. 5.39a is poor, as it is basically two variable displacement pump/motors on a common shaft, where both are rated for the peak power flow.

The concept was simulated in [203] using regular waves and employing reactive control. For a hydraulic transformer capable of handling the peak load, only the largest waves were resulted in a positive energy output of the PTO, where the conversion efficiency was only 30% from cylinder to the high pressure side. The work also shows how PTO losses penalises the benefit of reactive control schemes.

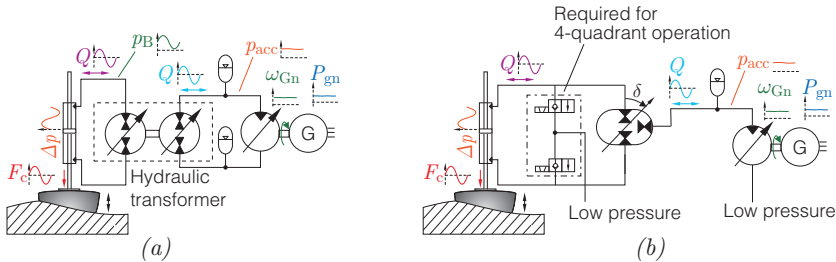


Figure 5.39: In (a) suggested hydraulic transformer for wave energy. In (b) modified concept for the Innas transformer.

To improve the performance of a hydraulic transformer, the company Innas has suggested a new design as shown in Fig. 5.40 [204, 205, 206, 207, 208, 209, 210]. Here the pumping and motoring have been combined in one axial piston unit. This is achieved by adding a third port or “kidney” in the valve plate, which gives the unit an A-port, a B-port and a T-port. By adjusting the angle of the valve plate, the ratio of flow consumed by A Q_A and produced by B Q_B port may be controlled. This is illustrated in Fig. 5.40b, where one piston is followed through a rotation. By the given location of the valve plate, a larger volume of flow is produced at B then consumed by A. To replenish the flow imbalance, a volume of flow is added to the piston during the T-port transit.

The illustration is based on a fixed displacement swash-plate machine, but the transformer may be designed on other hydraulic-machine concepts as well. Currently, Innas is working on a transformer based a floating-cup axial piston machine, which is fixed displacement unit with a peak efficiency of 97-98% [207, 205].

In Fig. 5.41 estimates of performance for a conventional and the Innas transformer is

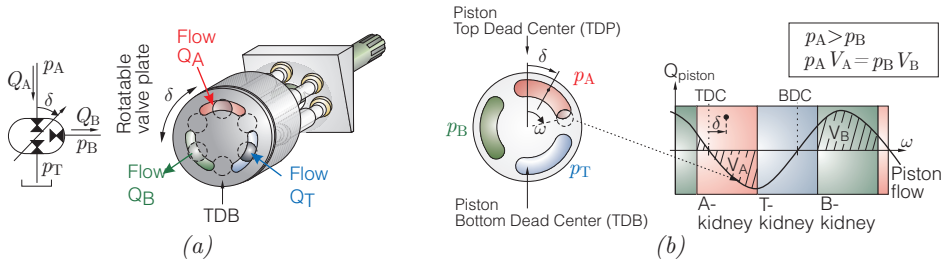
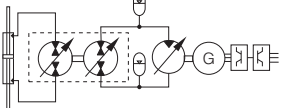


Figure 5.40: In (a) illustration of Innas transformer and in (b) illustration of working principle. Figures based on [209].

Table 5.14: Assessment of conventional hydraulic transformer.

Conventional Hyd. Transformer		Prod.	Size	Durability	Storage	Total	
		Points:	1	3	1	3	7
		WPEA: OCIR			Storage: Accumulator		
		Part sized for peak load:	1/2	Optimum maximum force:		$\tau_{PTO,max} = 1.00 \text{ MNm}$ $F_{PTO,max} = 420 \text{ kN}$	
		Part load perform. k_o :	0	Size of primary gen./actuator:		$d = 0.24 \text{ m}$ $l = 4 \text{ m}$	
$\eta_{PTO,1}$	$\eta_{storage}$	0.94	η_{tot}	0.60	Annual prod. [MWh]	32	

The part load efficiency will be dominated by the two hydraulic swash-plate pump/motors, i.e. the efficiency curves in Fig. 5.31. Resultantly, the $k_o = 0$ curves are used for production evaluation, despite them being too optimistic, as there are now two swash-plate units.

If the efficiency of the swash-plate motor assumed to be is 0.88 and 2/3 of the power is processed in the accumulator, the following base efficiency is obtained,

$$\eta_{tot} = \frac{\eta_{cycl} \eta_{hyd,m} \eta_{hyd,m} \eta_{bent} \eta_{gn} \eta_{conv} \eta_{hyd,m}}{3} + \frac{2 \eta_{cycl} \eta_{hyd,m} \eta_{hyd,m} \eta_{acc,round-trip} \eta_{bent} \eta_{gn} \eta_{conv}}{3} = 0.60$$

where the motor driving the generator is chosen as a fix-displacement bent-axis with an efficiency of $\eta_{bent} = 0.95$.

Control wise, the PTO is capable of continues and 4-quadrant force control, thus both the OCIR and reactive control methods would be possible. Assuming use of OCIR control, the optimum torque level is going to be 1.00 MNm with an annual production of $52.8 \cdot 0.65 = 32 \text{ MWh}$. Assuming a piston rod diameter of $\emptyset 180 \text{ mm}$, a piston diameter of 224mm would be required at a differential pressure of 300 bar.

Giving the very poor efficiency, the system is a poor solution.

given [206], showing the estimated benefit of the design. Based on results given in for a $45\text{ cm}^3/\text{rev}$ machine for different operating points in [208, 211], the graphs of Fig. 5.41 have been constructed. The targeted performance for a matured design based on the floating-cup principle is also shown.

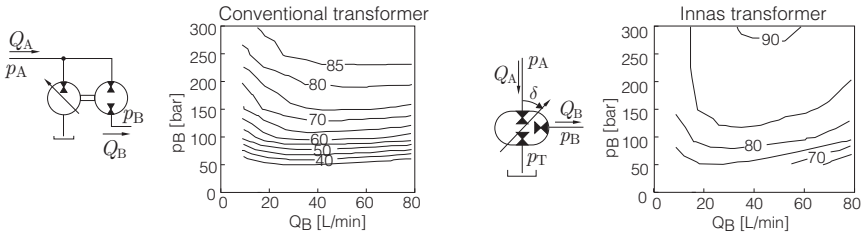


Figure 5.41: Left a conventional hydraulic transformer, and right the Innas transformer ($p_A = 300\text{ bar}$). Efficiency estimates from [206].

The transformer is being developed for a 4-quadrant drive drain for automotive [204]. In [212] the average performance of a $60\text{ cm}^3/\text{rev}$ transformer in automotive drive cycles is estimated to be about 92%. Based on this, the PTO for wave energy based on this transformer would look like the system in Fig. 5.39b. The valve arrangement is required for handling the flow imbalance when operating in 4-quadrant mode.

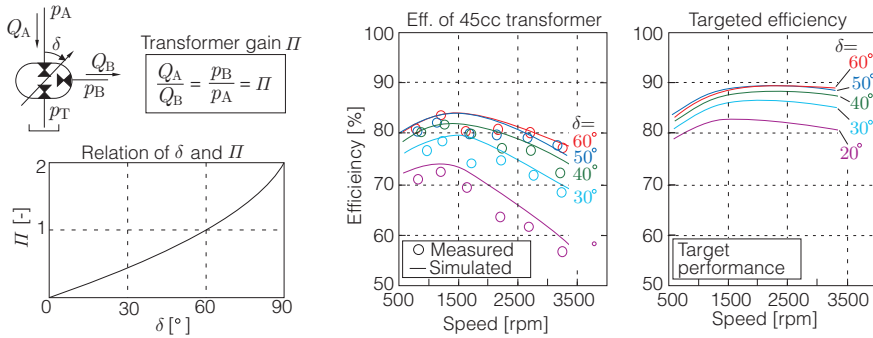
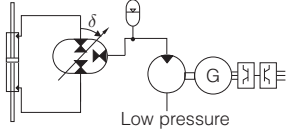


Figure 5.42: Test results and targeted performance, $p_A = 200\text{ bar}$. [208, 211]

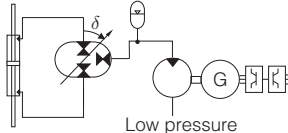
More simple hydraulic PTOs have also been suggested and explored in [213, 58, 55, 214, 215, 216, 217, 218, 219, 220, 221], often consisting of a valve arrangement for rectifying the bi-directional flow produced by a cylinder. The flow is fed directly into accumulators. This is illustrated in Fig. 5.43a. The accumulator smoothes the energy input, leaving the hydraulic motor to be sized for the average power level, reducing the degree of part load operation. However, the accumulators also prevent rapid pressure control, c.f. Fig. 5.30, but instead stabilises the pressure to be slowly varying as a function of stored energy. In effect, the load force applied by the cylinder has the characteristics of a Coulomb damping. As shown in Fig. 1.10, this control type has a tendency to extract less energy compared to continuous control schemes. Regarding power conversion efficiency, the PTO performs well.

Table 5.15: Assessment of PTO with Innas' transformer.

Hydraulic Transformer - Innas	Prod.	Size	Durability	Storage	Total
		2	3	2	3
WPEA: <i>Passive Spring</i>			Storage: Accumulator		
Part sized for peak load:	1/2	Optimum maximum force:	$\tau_{PTO,max} = 1.00 \text{ MNm}$ $F_{PTO,max} = 424 \text{ kN}$		
Part load perform. k_o :	1	Size of primary gen./actuator:	$d = 0.24 \text{ m}$ $l = 4 \text{ m}$		
$\eta_{PTO,1}$	$\eta_{storage}$	0.94	η_{tot}	0.70	Annual prod. [MWh] 65

The part load efficiency curves of the Innas have been estimated from Fig. 5.42, yielding the curves below. For the $\delta = 60^\circ$ -curve, the pressure transformation is 1, i.e. same pressure on A and B-side. Thus, at 3500rpm, $\delta = 60^\circ$ and maximum pressure, the transformer is operating at rated power. Resultantly, the $\delta = 60^\circ$ curve may be easily converted to the efficiency as a function of rated power. If $\delta = 30^\circ$, the pressure ratio is 2 between A and B-side, i.e. half the rated power is being processed at e.g. 3500rpm.

Comparing efficiency curves, the transformer will agree with $k_o = 2$, if the targeted efficiencies of Innas are met.

Hydraulic Transformer - Innas	Prod.	Size	Durability	Storage	Total
		2	3	2	3
WPEA: <i>OCIR</i>			Storage: Accumulator		
Part sized for peak load:	1/2	Optimum maximum force:	$\tau_{PTO,max} = 1.00 \text{ MNm}$ $F_{PTO,max} = 424 \text{ kN}$		
Part load perform. k_o :	1	Size of primary gen./actuator:	$d = 0.24 \text{ m}$ $l = 4 \text{ m}$		
$\eta_{PTO,1}$	$\eta_{storage}$	0.94	η_{tot}	0.70	Annual prod. [MWh] 65

If the peak efficiency of the transformer is 0.90, 0.95 for the bent-axis motor, and 2/3 of the power is processed in the accumulator, the following base efficiency is obtained:

$$\eta_{tot} = \frac{\eta_{cyl}\eta_{trans}\eta_{bent}\eta_{gn}\eta_{conv} + 2\eta_{cyl}\eta_{trans}\eta_{acc,round-trip}\eta_{bent}\eta_{gn}\eta_{conv}}{3} = 0.70 \tag{5.4}$$

Using OCIR control, the annual production is $94.1 \cdot 0.65 = 65 \text{ MWh}$ at $\tau_{PTO,max} = 1.5 \text{ MNm}$. Assuming a piston rod diameter of $\varnothing 180 \text{ mm}$, a piston diameter of 0.24m would be required at a differential pressure of 300 bar.

If Innas reaches their targeted efficiencies, the solution may become an option for wave energy.

By Plummer et al. [216, 217, 218, 215] a PTO system as in Fig. 5.43 was simulated, showing a conversion efficiency from movement to generator shaft of 75% over a wide range of sea states. In regular waves the Coulomb damping was shown to perform better than linear damping, however, when moving to realistic irregular waves, the liner damping methods would produce 10%-30% more depending on the sea state. This is in agreement with Fig. 1.10.

In [56] Falcão simulates a similar PTO and discloses the same type PTO in [55], with the addition of a locking mechanism for performing latching control. Latching may be implemented using a valve for shutting the cylinder off as shown in Fig. 5.43b. For waves with more than twice the period as the natural period of the absorber, the latching control was shown to extract twice the power as Coulomb damping. However, the locking force required was at these circumstances 16 times the normal damping force of the cylinder.

By Ringwood et al. [222, 174] the system in Fig. 5.43a is also explored by simulation. If a swash-plate motor is used, the conversion efficiency from cylinder movement to generator shaft is found to be 75.5% for the best wave, where the generator operates at a fixed speed (1500rpm). A bent-axis motor could have been utilised with improved results, as only slow variation of the displacement is required. If a DDPM is used, [174] reports that an efficiency of 91.4% from cylinder to generator shaft is possible.

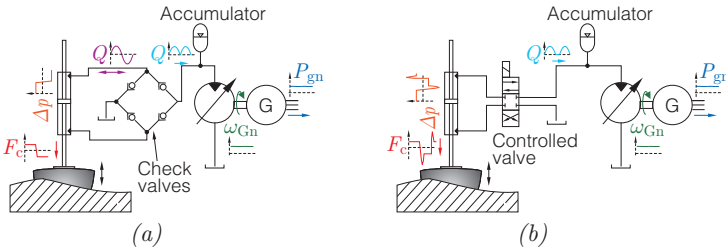
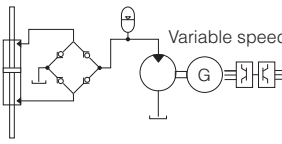


Figure 5.43: In (a) hydraulic PTO with passive valves for rectifying flow and in (b) active valve, allowing latching control by locking cylinder.

A slightly modified PTO is given by Eidsmoen in [223, 224, 225, 226]. The origin is the PTO in Fig. 5.44a, which differs from Fig. 5.43 by using a single acting cylinder. To provide a load force in both directions, the buoyancy is biased such that the cylinder pulls with 175kN to maintain the float in equilibrium. The drawback of this design is that non-useful power is in change delivered to and from the cylinder to provide this bias force as the float is oscillating. However, otherwise the system is similar to Fig. 5.43a, providing a Coulomb damping characteristic. The finding by Eidsmoen et al. is that the movement or phase of the absorber may be controlled by adding an accumulator “A” with a controllable on/off valve. This circuit is shown in Fig. 5.44b. By in change storing and releasing energy from the accumulator, the motion amplitude of the absorber may be improved. The cycle is illustrated in Fig. 5.44c. By simulation of a 3.3m diameter absorber, the yearly production was in [223, 224] estimated to be 3 times greater with system Fig. 5.44b compared to the Coulomb damping system Fig. 5.44a. The conversion efficiency of the PTO was not reported. Also note that the control required predicting

Table 5.16: Assessment of a simple fixed pressure PTOs.

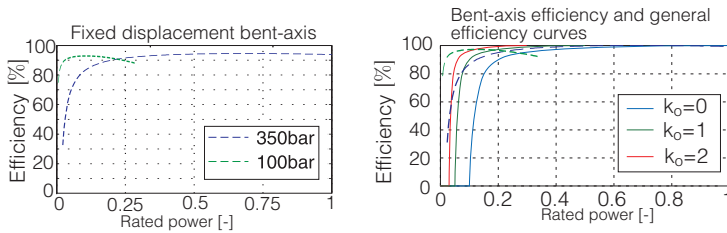
Simple Fixed Pressure PTO	Prod.	Size	Durability	Storage	Total	
	Points:	-1	3	3	8	
	WPEA: <i>Coulombng damping</i>			Storage: Accumulator		
	Part sized for peak load:	1/3	Optimum maximum force:		$\tau_{PTO,max} = 0.375 \text{ MNm}$ $F_{PTO,max} = 159 \text{ kN}$	
	Part load perform. k_o :	2	Size of primary gen./actuator:		$d = 0.24 \text{ m}$ $l = 4 \text{ m}$	
	$\eta_{PTO,1}$	$\eta_{storage}$	0.94	η_{tot}	0.78	Annual prod. [MWh]
						29

The PTO in Fig. 5.43a is assumed with a fixed-displacement bent-axis hydraulic motor. This motor will operate at a steady-load with due to the accumulators, where the power level is controlled by setting the speed of the generator appropriately according to the sea state using a converter.

The efficiency curves of the bent-axis motor from Fig. 5.31 have been mapped to a function of rated power below. Inspecting the curves, the part load is very good, resultantly the $k_o = 3$ curves are used.

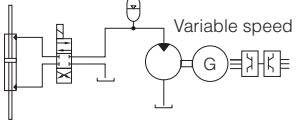
Assuming a peak efficiency of 0.95 for the bent-axis motor, and that 2/3 of the power is processed in the storage, the following total efficiency is estimated:

$$\eta_{tot} = \frac{\eta_{cyl}\eta_{bent}\eta_{gn}\eta_{conv} + 2\eta_{cyl}\eta_{acc,round-trip}\eta_{bent}\eta_{gn}\eta_{conv}}{3} = 0.78 \quad (5.5)$$



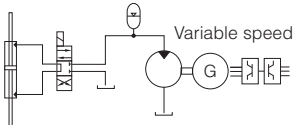
Control wise, the PTO is only capable of Coulomb damping, yielding the annual production $37.8 \cdot 0.78 = 29 \text{ MWh}$ at $\tau_{PTO,max} = 0.375 \text{ MNm}$. Assuming a piston rod diameter of $\varnothing 180 \text{ mm}$, a piston diameter of 0.20 m would be required at a differential pressure of 300 bar . Despite the simplicity and durability of the PTO, the production is too low for being a good solution.

Table 5.17: Different fixed pressure PTOs with control valve.

<i>Simple hyd. w. latching</i>		Prod.	Size	Durability	Storage	Total *
		Points: 1	3	2	3	9
WPEA: OCIR			Storage: Accumulator			
Part sized for peak load:	1/3	Optimum maximum force:		$\tau_{PTO,max} = 0.75 \text{ MNm}$ $F_{PTO,max} = 318 \text{ kN}$		
Part load perform. k_o :	2	Size of primary gen./actuator:		$d = 0.21 \text{ m}$ $l = 4 \text{ m}$		
$\eta_{PTO,1}$	$\eta_{storage}$	0.94	η_{tot}	0.70	Annual prod. [MWh]	42

The PTO in Fig. 5.43b is similar, except latching is now possible using the active valve. The latching force will have the same size as the production force, i.e. $\gamma_{latch} = 1$ in Tab. 4.5. This gives a yearly production of $54.3 \cdot 0.78 = 42 \text{ MWh}$. The system may also be designed, where the cylinder size is increased compared to the hydraulic motor, such that the motor operates up-to 150 bar, but the cylinder may go up to 300 bar during latching. In this case $\gamma_{latch} = 2$ and the yearly production will be $76.4 \cdot 0.78 = 60 \text{ MWh}$ at $\tau_{PTO,max} = 1.25 \text{ MNm}$, i.e. the latching torque will load with up to 2.5 MNm.

Given the extra mechanism requires for latching, and that some reduced performs will be experienced when the control is made causal, the solution is not considered optimal.

<i>Simple hyd. w. de-clutching</i>		Prod.	Size	Durability	Storage	Total *
		Points: 2	3	3	3	11
WPEA: De-sclutching			Storage: Accumulator			
Part sized for peak load:	1/3	Optimum maximum force:		$\tau_{PTO,max} = 1.00 \text{ MNm}$ $F_{PTO,max} = 424 \text{ kN}$		
Part load perform. k_o :	2	Size of primary gen./actuator:		$d = 0.24 \text{ m}$ $l = 4 \text{ m}$		
$\eta_{PTO,1}$	$\eta_{storage}$	0.94	η_{tot}	0.78	Annual prod. [MWh]	63

The valve of the PTO in Fig. 5.43b is replaced with a valve short-circuiting the cylinder chambers, allowing use of de-clutching control. This gives a yearly production of $81.4 \cdot 0.78 = 63 \text{ MWh}$ at $\tau_{PTO,max} = 1.0 \text{ MNm}$. Thus, the design is favourable compared to the latching design, as additional latching mechanism is not required. Note that some performance reduction may be experienced when the control is made causal.

4 seconds of future waves.

A modified version for the Wavestar WEC was suggested in [227]. Instead of just having one extra accumulator for phase control, the system comprises multiple accumulators at different levels. As a float has passed a wave crest, the idea is to use the on/off valves to apply the accumulators in sequel to force the float further into the water, increasing the amplitude of motion. The accumulators would then be charged in a similar sequence at an upstroke of the float. However, the PTO was abandoned as not performing sufficient.

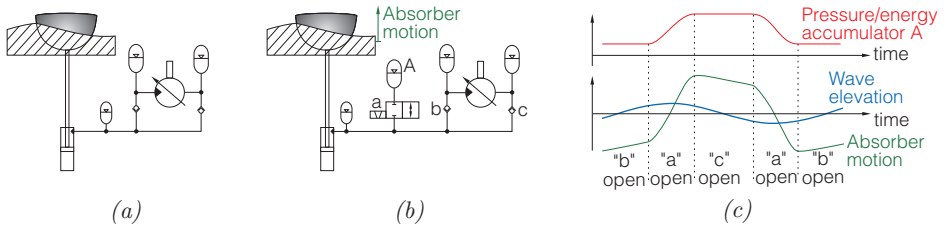


Figure 5.44: PTOs disclosed in [223]. The operation of the PTO in (b) is illustrated in (c).

Based on the system suggested by Eidsmoen, a similar design was explored in [228, 229], however the modelling, system sizing and results seem non-consistent. E.g. the cylinder is shown as asymmetric but modelled symmetrically and 50 L gas-accumulators are used to model the oil compressibility of the cylinder. Also the extreme of a total accumulator capacity of 12000 L is suggested for a system outputting an average of about 5 kW.

Another group of hydraulic PTO concepts are based on a discrete gearing between a fixed pressure supply and cylinder movement. This is realised by switching between the active numbers of cylinders. One suggestion is disclosed in the patent application [230], where three different sized cylinders are mounted in parallel as shown in Fig. 5.45. Each cylinder is connected in to an arrangement of check valves for rectifying the flow. The flow output from each circuit is again using a check valve connected to a fixed high pressure line with accumulator for energy smoothing. To be able to control the resulting damping force, the individual cylinder may be de-activated by opening the valves “140”, whereby the cylinder is idling by breathing fluid from the tank connection. By performing different combination of activated cylinders, ± 7 different resulting damping forces may be produced as illustrated.

For producing electricity parallel sets of hydraulic motors and generators are connected to the high pressure circuit. Depending on the sea state, an adequate number of motors and generators are activated. Thus, the circuit allows a pressure circuit with accumulators for energy smoothing, while providing a discrete controllable damping force. The expected efficiency is not disclosed.

Pelamis has disclosed a similar PTO system in [231, 232] as shown in Fig. 5.46. Each pair of cylinders (33) and (35) gives a resulting torque about axis 1 and 2 respectively. Check valves (72) and (82) are used to rectify the flow, which enters high pressure accumulators (71). Two motors (74) may be separately activated and drive separate generators (75).

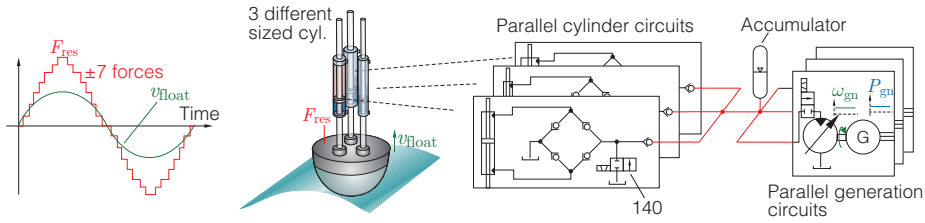


Figure 5.45: Illustration of the PTO disclosed in [230] for Wavebob.

The cylinders may be separately disengaged by using hydraulic switches (83) to open the piloted inlet valves (82), resulting in the cylinder breathing low pressure oil. Thus, as the previous PTO system, the resulting damping torque may be discretely controlled. Due to the check valves, 4-quadrant control is not possible.

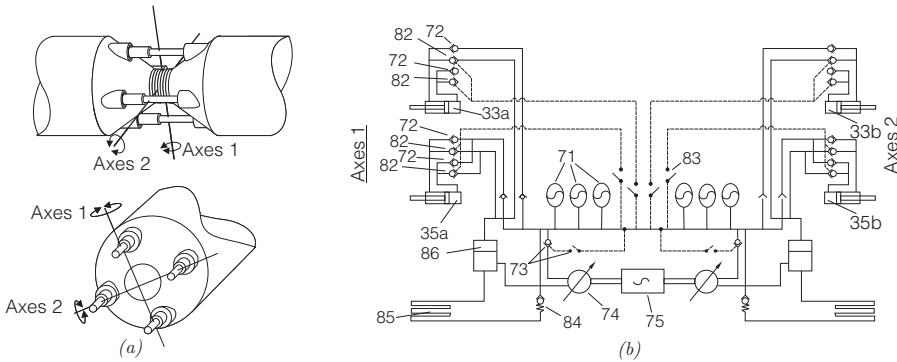


Figure 5.46: In (a) illustration of the Pelamis PTO cylinder arrangement and in (b) PTO disclosed in [232].

The lack of 4-quadrant behaviour is not a hindrance for this particular WEC. Instead the Pelamis WEC changes the systems natural period by varying the ratio of applied damping restraints in the two coupled axes [233]. This is illustrated in Fig. 5.47, where the damping ratio of the axes determines the angle of the inclined response, which relates to the natural period of the response.

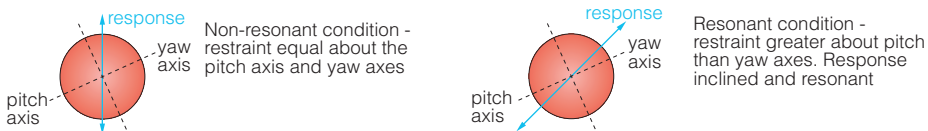


Figure 5.47: Illustration of Pelamis response control [233].

The PTO by Pelamis has during the past 14 years been tested in test-benches and used in Pelamis prototypes installations. A Pelamis 1/7 scale prototype was constructed and tested in 2001. The prototype was 17m long with a diameter of 0.5m and featured three

active degree-of-freedom joints [234]. The prototype is shown in Fig.5.48. The model was equipped with a scaled hydraulic PTO, where the only difference was that no hydraulic motor-generator set was included due to the lower power scale. By performing different combination of enabled cylinder chambers, the resulting torque is varied. Experimental results for a wave cycle is shown in Fig.5.48, showing the quantified torque as the cylinder chambers are in turns pressurised and de-pressurised.

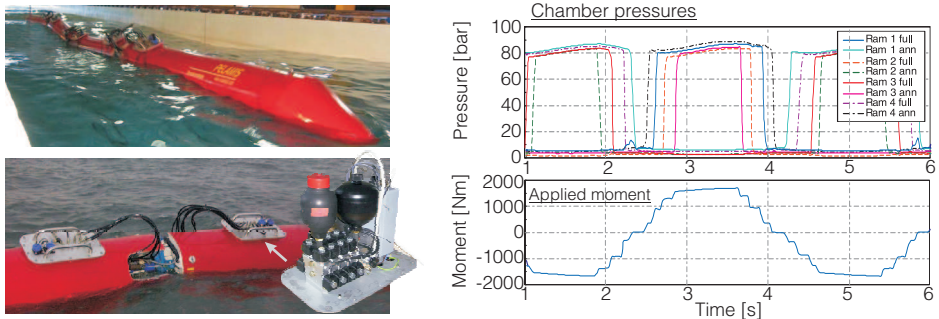


Figure 5.48: Prototype 1:7 scale Pelamis WEC. Scaled hydraulic PTO in each joint and test result from a cycle [234].

Following the scaled model, testing of a full scale 250kW-PTO joint module was performed in early 2003 and results reported in [235]. The setup is seen in Fig. 5.49, with the yellow cylinders mounted on the module's exterior, simulating the joint motion. A total conversion efficiency of 75-85% was reported in [235] across the tested power range.

The efficiency between the hydraulic cylinders and the storage accumulators was found to be between 88% and 94%, and the losses due to seal friction in cylinders were estimated to be around 5% [161]. The pressure drop/line-losses alone of valves, hoses and manifold were reported to be 1-2% [235]. The motor-generator set provided a conversion efficiency of $\approx 75\%$ at 150 bar with efficiency rising to 85%-90% at full flow and 300 bar [235]. One of the important aspects of the test regards the valve durability, as these will see a very large number of cycles ($>10^7$), where standard industrial valves are tested for 10^6 cycles. The dominant inefficiency is concluded to be the hydraulic motor/generator sets. An advantage of the PTO is employing tested "off the shelf" components.

From 2004-2007 a full-scale prototype machine (P1A) was tested at Orkney with three power-modules as shown in Fig. 5.49. The prototype was refitted and updated in 2006. The test results given in Fig. 5.50 are from 2007, showing the fluctuating wave power and the smoothed electrical output. A conversion efficiency of 64% was achieved over a 30 minutes average for the total machine at an average electrical output of 150 kW [233]. The machine had a rated capacity of 750kW [1]. Following the first prototype, three additional P1 machines similar to the upgraded machine were constructed and installed in Portugal in 2008 [1]. However, the project ended early due to financial collapse of a Portuguese electricity utility.

In 2010 Pelamis installed an upgraded machine, P2, for E.ON at the European Marine

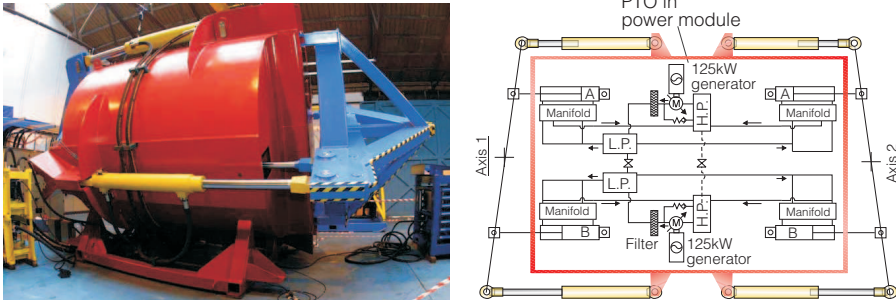


Figure 5.49: Full-scale test of a PTO module [235].

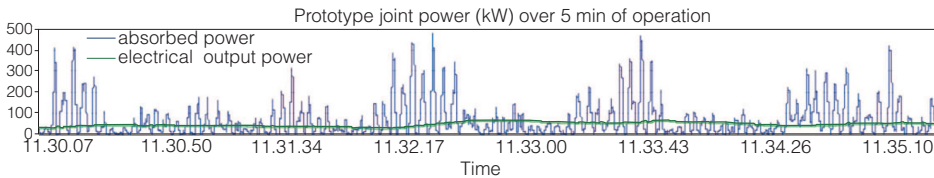


Figure 5.50: Test results from prototype P1A, generating to the UK grid in 2007. [233]

Energy Centre (EMEC) in Scotland. A similar machine 2012 was installed at the same location for Scottish Power Renewables [7]. Both P2 prototype are in operation and are undergoing 3 years test programmes [233]. The A 3D visualisation of the P2 is showed. Compared to the P1, the P2 incorporates and extra PTO joint and an increased diameter from 3.5m to 4m. The total machine is rated to 750kW. The conversion efficiency of the motor-generators sets are seen in Fig. 5.51 as reported in [233], where the total conversion efficiency of the PTO is typically 70%.

According to [7] the E.ON machine have reported 30 minute average electrical output of 270kW. Measured conversion efficiency is reported about 70% across a range of sea conditions.

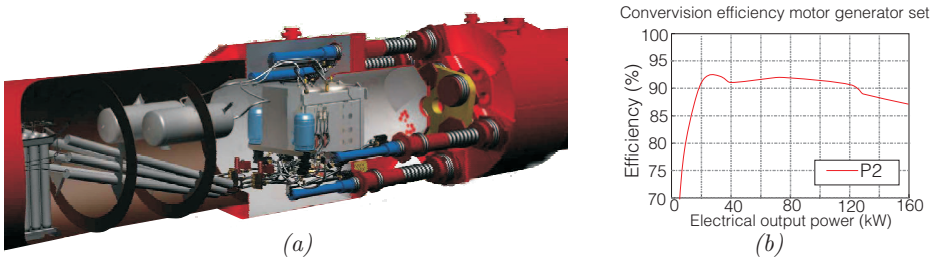


Figure 5.51: In left cutaways of the P2 joint and power take-off (PTO) system [233] and in right measured efficiency of motor-generator sets at 250bar [233].

A similar PTO is disclosed in [236, 237, 238] and is shown in Fig. 5.52. The multiple cylinders are employed where the resulting braking torque may be varied by in turns disabling different cylinder chambers. Moreover, the cylinder moments arm may be varied using fixation systems (5.2). A scaled PTO capable of braking with 16kN is presented in [237]. The PTO is tested in a test-rig, simulating regular waves. The overall efficiency is estimated to be from 69% to 80%. Estimates were given, as the test-rig was not fully operational.

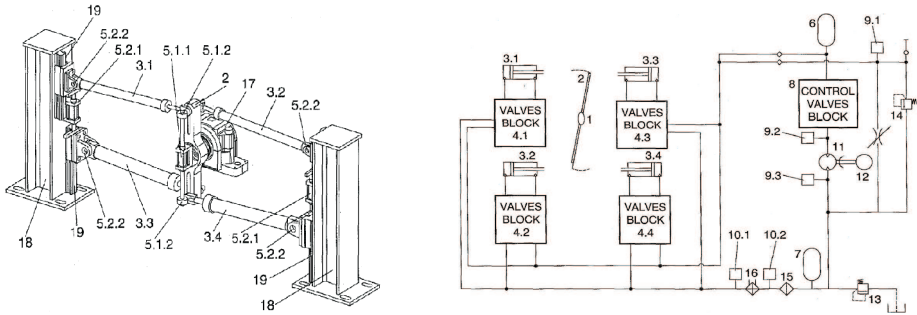


Figure 5.52: PTO disclosed in [236].

The concept of controlling a cylinder by activating and deactivating chambers has also been suggested for mobile hydraulics in [239, 240]. The system is shown in Fig. 5.53, where the main difference compared to previous PTOs is that the system is made as an actuation system, i.e. the power flow is reversed compared to wave-energy. Another detail is the use of multi-chambered cylinders with up to four chambers, which are employed to increase force resolution without installing multiple or larger cylinders than the conventional asymmetric cylinders. As shown in Fig. 5.53 a drawback of the design is that the cylinder produces a non-symmetric force distribution, which increases with the required rod diameter. Tests have showed promising energy saving compared to e.g. conventional load sensing systems used in mobile hydraulics.

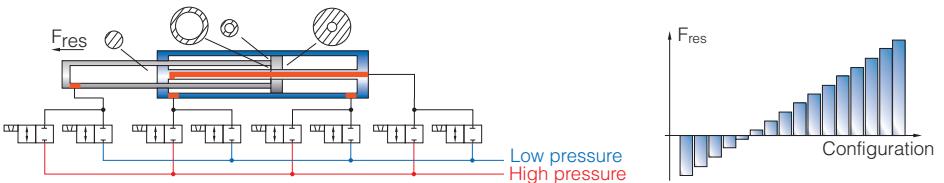
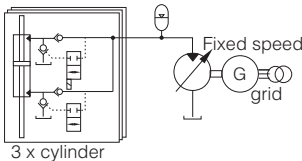


Figure 5.53: Actuation system suggested for mobile hydraulic in [240] and [239], and typical force distribution of the cylinder design.

A type of PTO adapting PWM modulation to hydraulic is suggested in [241] as shown in Fig. 5.54a. The 2/2-way valve (18) is used to control the pressure in the cylinder by pulse-width modulation of the system pressure. The reference damping force (201) is shown with the signal (202) to the valve (18). As the previous PTO, this enables employing a fixed pressure line with accumulator for energy smoothing, while having a

Table 5.18: Assessment of a discrete cylinder control PTOs.

Discrete Cylinder Control PTO		Prod.	Size	Durability	Storage	Total
		Points: 3	2	2	3	10
WPEA: OCIR			Storage: Accumulator			
Part sized for peak load:	1/4	Optimum maximum force:		$\tau_{PTO,max} = 2.25 \text{ MNm}$ $F_{PTO,max} = 953 \text{ kN}$		
Part load perform. k_o :	2	Size of primary gen./actuator:		$d_1 = 0.24 \text{ m}$, $d_2 = 0.18 \text{ m}$ $d_3 = 0.14 \text{ m}$, $l = 4 \text{ m}$		
$\eta_{PTO,1}$	$\eta_{storage}$	0.94	η_{tot}	0.75	Annual prod. [MWh]	90

A PTO as in Fig. 5.45b for a single float requires multiple cylinders for an adequate number of discrete force values.

As the part between cylinder and accumulator storage consists only of check-valves, which are either opened or closed, there efficiency will not decrease at low power levels. Additional losses exist to due pressurisation and de-pressurisation of chambers, but due to having storage so early in the PTO chain, the $k_o = 3$ curves of part load performance are assumed valid.

Assuming the same conversion efficiency possible as reported by the Pelamis, i.e. 75%, a yearly production of $119.1 \cdot 0.75 = 89 \text{ MWh}$. The $\tau_{PTO,max} = 2.25 \text{ MNm}$, i.e. $F_{PTO,max} = 953 \text{ kN}$. Using a binary distribution, such that their sizes have the ratio $\{1, 1/2, 1/4\}$, yields three cylinders of size 544 kN, 272 kN and 136 kN respectively.

Size wise, having three cylinders will be a bit cumbersome, also considering load distribution on the structure. Durability wise, the high cycles of the valve is also an issue. Overall, the PTO still seems as a good solution of the Wavestar C5.

potential low loss force control of the cylinder.

Most research on PWM adopted techniques for hydraulic drives has been performed by Scheidl et al, [242, 243, 244, 245, 246], adopting the concept of the electrical switch-mode converter to hydraulics, Fig. 5.54b. A fast on/off valves with switch times less than 2ms [244] implements the switch and the volume corresponds to the capacitor, and the pipe implements the inductor. The inductance is due to effect the inertia of the fluid in the pipe, which gives a phase shift between applied pressure and flow. The minimum require switching frequency is 50Hz [245]. A prototype of about 1kW is shown in Fig. 5.54c, and has shown efficiencies of approximately 80% in a wide range. In [246] at 50L/min unit was tested, which at a pulse width of about 55% showed 76% efficiency.

The challenge of the PWM type systems is developing larger valves with switch times less than 2ms to increase power level. Most industrial valves have response times greater than 15ms and most commonly about 40-50ms. In comparison to the valves used in DDPM motors, opening at near zero differential pressure, the valves in PWM must be able to open and close at full pressure differential, increasing the actuation power requirement. Resultantly, pilot stages are required, which complicates the design. Another aspect of PWM hydraulics is implementing sufficient inductance compare to capacity, as the hose often has a much higher capacitive energy storage compared to inductive [247]. Also, even though using valves of 1ms, according to [247], the switching time is only a number of times faster than the time constant of the hydraulic circuit, whereas the MOSFET transistor is typically about 1000 times faster than the time constant of the electrical circuit [247].

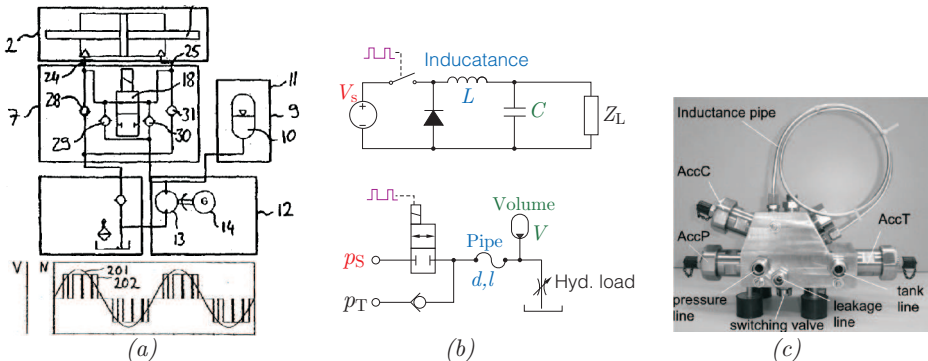


Figure 5.54: In (a) PTO disclosed in [241], (b) illustration of analogy between electrical and hydraulic buck converter and (c) 1kW prototype hydraulic buck converter given in [242].

Given the current power level of the prototypes of a few kW, combined with the requirements of ultra-fast valves, the system requires a lot of development before reaching the range required in wave power.

5.8 Overall Discussion and Summary of PTO Systems

Looking at the largest implemented PTO prototypes, the landscape looked as:

- The only WEC build so-far rated for 1MW was the 7000ton Archimedes Wave Swing with two direct-driven 500kW linear generator, together producing a load force up to 1000kN.
- The two Pelamis P2 machines with their discrete cylinder control are rated for an average of 750kW, where the four joint section each have a PTO capable of 250kW. Similar PTOs were installed in four P1 versions.
- A 160kW direct driven linear variable reluctance PM machines have been implemented by the Wedge company, producing a load force of 160kN.
- Wavestar's two-float C5 prototype had a conventional hydrostatic transmission with a rated generator capacity of 110kW. Each hydraulic actuator may load with 420kN and generate a peak power of 110kW.

Generally, most PTO research deal with the sub 1MW range and test results beyond 50kW are limited to the selection given above. The remaining PTOs presented have prototypes rated below 50kW, most often in the region of 10kW. Often it is difficult to see to what extent the PTOs are developed with attention to how the WPEA affects the design, which may give non-optimised designs.

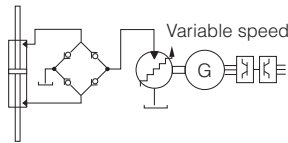
The performed evaluation identified the available WPEAs for the different PTO concepts, their peak efficiency and an estimate of their part load performance. The latter is often more important for the production capability than the actual efficiency at full load. Reliability and maintenance have not been the primary aspect of the review as the information is limited, however, an indication is given with the durability score, which is based on the challenges in the design.

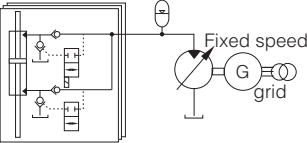
To provide an overview of the evaluated PTOs and the results, the obtained assessment tables have been collected into the tables showed on page 165 to page 167. The red “*” indicates that the production estimate is based on a non-causal WPEA, i.e. the production will most likely reduce when implementing the required prediction for achieving causality

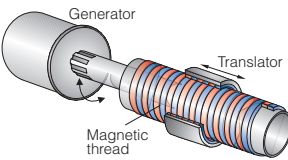
The PTOs are sorted into four groups according to their expected annual production, which is based on three parameters: PTO efficiency at rated power, an assumption of part load performance ($k_o = 0, 1$ or 2 , with 2 being the best) and the available WPEA. The groups are defined according to the production score:

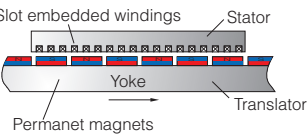
- Group 1: Annular production greater than 85MWh.
 - Group 2: Annular production of 61-85MWh.
 - Group 3: Annular production of 31-60MWh.
 - Group 4: Annular production less than 31MWh.
-

PTOs with a production score of 3 - annual production greater than 85 MWh

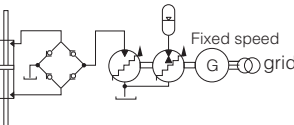
 <p>Variable speed</p>	Prod.	Size	Durability	Storage	Total	
	Points:	3	3	3	1	10
	WPEA: OCIR			Storage: Super capacitors		
	Part sized for peak load:	4/4	Optimum maximum force:	$\tau_{PTO,max} = 1.50$ MNm $F_{PTO,max} = 635$ kN		
	Part load perform. k_o :	2	Size of primary gen./actuator:	$d = 0.24$ m $l = 4$ m		
$\eta_{PTO,1}$	$\eta_{storage}$	0.92	η_{tot}	0.83	Annual prod. [MWh] 98	

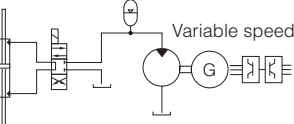
 <p>Fixed speed 3 x cylinder</p>	Prod.	Size	Durability	Storage	Total	
	Points:	3	2	2	3	10
	WPEA: OCIR			Storage: Accumulator		
	Part sized for peak load:	1/4	Optimum maximum force:	$\tau_{PTO,max} = 2.25$ MNm $F_{PTO,max} = 953$ kN		
	Part load perform. k_o :	2	Size of primary gen./actuator:	$d_1 = 0.24$ m, $d_2 = 0.18$ m $d_3 = 0.14$ m, $l = 4$ m		
$\eta_{PTO,1}$	$\eta_{storage}$	0.94	η_{tot}	0.75	Annual prod. [MWh] 90	

 <p>Generator Translator Magnetic thread</p>	Prod.	Size	Durability	Storage	Total	
	Points:	3	3	2	1	9
	WPEA: OCIR or Reactive			Storage: Super-capacitors		
	Part sized for peak load:	2/3	Optimum maximum force:	$\tau_{PTO,max} = 1.50$ MNm $F_{PTO,max} = 636$ kN		
	Part load perform. k_o :	2	Size of primary gen./actuator:	$d = 0.51$ m $l = 4$ m or $2 \times d = 0.25$ m $l = 4$ m + linear guide & generator		
$\eta_{PTO,1}$	N/A	$\eta_{storage}$	0.92	η_{tot}	0.81	Annual prod. [MWh] 95

 <p>Slot embedded windings Stator Yoke Permanent magnets Translator</p>	Prod.	Size	Durability	Storage	Total	
	Points:	3	-1	2	1	5
	WPEA: Reactive or OCIR			Storage: Super capacitors		
	Part sized for peak load:	3/4	Optimum maximum force:	$\tau_{PTO,max} = 1.25$ MNm $F_{PTO,max} = 530$ kN		
	Part load perform. k_o :	1	Size of primary gen./actuator:	$d = 2.1$ m or $2 \times d = 1.05$ m $l = 4$ m + linear guide		
$\eta_{PTO,1}$	0.89	$\eta_{storage}$	0.92	η_{tot}	0.87	Annual prod. [MWh] 86

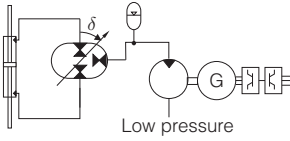
PTOs with a production score of 2 - annual production from 61-85 MWh

 <p>Fixed speed</p>	Prod.	Size	Durability	Storage	Total	
	Points:	2	3	3	3	11
	WPEA: OCIR			Storage: Accumulator		
	Part sized for peak load:	2/3	Optimum maximum force:	$\tau_{PTO,max} = 1.50$ MNm $F_{PTO,max} = 635$ kN		
	Part load perform. k_o :	1	Size of primary gen./actuator:	$d = 0.24$ m $l = 4$ m		
$\eta_{PTO,1}$	$\eta_{storage}$	0.94	η_{tot}	0.79	Annual prod. [MWh] 79	

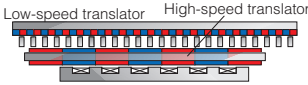
 <p>Variable speed</p>	Prod.	Size	Durability	Storage	Total *	
	Points:	2	3	3	3	11
	WPEA: De-sclutching			Storage: Accumulator		
	Part sized for peak load:	1/3	Optimum maximum force:	$\tau_{PTO,max} = 1.00$ MNm $F_{PTO,max} = 424$ kN		
	Part load perform. k_o :	2	Size of primary gen./actuator:	$d = 0.24$ m $l = 4$ m		
$\eta_{PTO,1}$	$\eta_{storage}$	0.94	η_{tot}	0.78	Annual prod. [MWh] 63	

PTOs with a production score of 2 - annual production from 61-85 MWh - continued

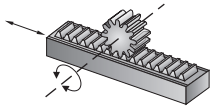
<i>Hydraulic Transformer - Innas</i>		Prod.	Size	Durability	Storage	Total
		Points:	2	3	2	3
WPEA: OCIR			Storage: Accumulator			
Part sized for peak load:	1/2	Optimum maximum force:	$\tau_{PTO,max} = 1.00 \text{ MNm}$ $F_{PTO,max} = 424 \text{ kN}$			
Part load perform. k_o :	1	Size of primary gen./actuator:	$d = 0.24 \text{ m}$ $l = 4 \text{ m}$			
$\eta_{PTO,1}$		$\eta_{storage}$	0.94	η_{tot}	0.70	Annual prod. [MWh] 65



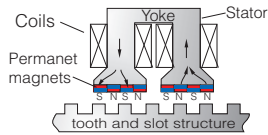
<i>Lin. Magnetic-Geared PM Mach.</i>		Prod.	Size	Durability	Storage	Total
		Points:	2	1	2	1
WPEA: Reactive or OCIR			Storage: Super capacitors			
Part sized for peak load:	2/3	Optimum maximum force:	$\tau_{PTO,max} = 1.50 \text{ MNm}$ $F_{PTO,max} = 636 \text{ kN}$			
Part load perform. k_o :	1	Size of primary gen./actuator:	$d = 1.68 \text{ m}$ + linear guide $l = 4 \text{ m}$			
$\eta_{PTO,1}$	0.87	$\eta_{storage}$	0.92	η_{tot}	0.85	Annual prod. [MWh] 80



<i>Rack and Pinion</i>		Prod.	Size	Durability	Storage	Total
		Points:	2	2	1	1
WPEA: OCIR			Storage: Super capacitors			
Part sized for peak load:	3/4	Optimum maximum force:	$\tau_{PTO,max} = 0.50 \text{ MNm}$ $F_{PTO,max} = 212 \text{ kN}$			
Part load perform. k_o :	2	Size of primary gen./actuator:	Pinion diameter: 150mm + linear guide & generator			
$\eta_{PTO,1}$	N/A	$\eta_{storage}$		η_{tot}	0.86	Annual prod. [MWh] 80

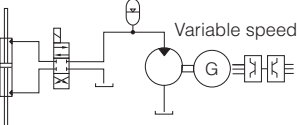


<i>Linear VRPM Machines</i>		Prod.	Size	Durability	Storage	Total
		Points:	2	1	2	1
WPEA: Reactive or OCIR			Storage: Super capacitors			
Part sized for peak load:	3/4	Optimum maximum force:	$\tau_{PTO,max} = 1.50 \text{ MNm}$ $F_{PTO,max} = 636 \text{ kN}$			
Part load perform. k_o :	1	Size of primary gen./actuator:	$d = 1.2 \text{ m}$ or $2 \times d = 0.60 \text{ m}$ $l = 4 \text{ m}$ + linear guide			
$\eta_{PTO,1}$	0.87	$\eta_{storage}$	0.92	η_{tot}	0.85	Annual prod. [MWh] 77

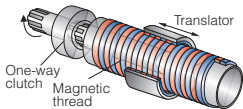


PTOs with a production score of 1 - annual production from 31-60 MWh

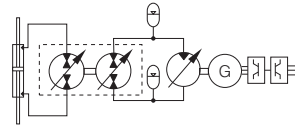
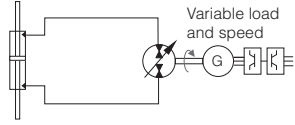
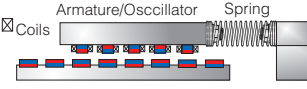
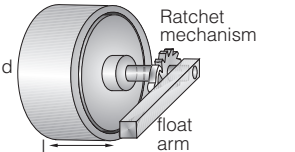
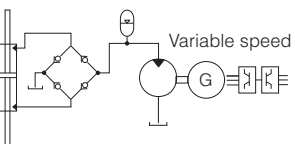
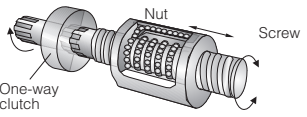
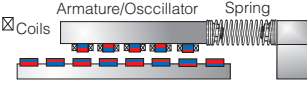
<i>Simple hyd. w. latching</i>		Prod.	Size	Durability	Storage	Total *
		Points:	1	3	2	3
WPEA: OCIR			Storage: Accumulator			
Part sized for peak load:	1/3	Optimum maximum force:	$\tau_{PTO,max} = 0.75 \text{ MNm}$ $F_{PTO,max} = 318 \text{ kN}$			
Part load perform. k_o :	2	Size of primary gen./actuator:	$d = 0.21 \text{ m}$ $l = 4 \text{ m}$			
$\eta_{PTO,1}$		$\eta_{storage}$	0.94	η_{tot}	0.70	Annual prod. [MWh] 42



<i>Magnetic Lead Screw w. ratchet</i>		Prod.	Size	Durability	Storage	Total
		Points:	1	3	2	2
WPEA: Single-ratchet			Storage: Fly-wheels			
Part sized for peak load:	1/3	Optimum maximum force:	$\tau_{PTO,max} = 0.50 \text{ MNm}$ $F_{PTO,max} = 212 \text{ kN}$			
Part load perform. k_o :	2	Size of primary gen./actuator:	$d = 0.19 \text{ m}$ + linear guide $l = 4 \text{ m}$			
$\eta_{PTO,1}$	N/A	$\eta_{storage}$		η_{tot}	0.81	Annual prod. [MWh] 41



PTOs with a production score of 1 - annual production from 31-60 MWh - continued

<i>Conventional Hyd. Transformer</i>		Prod.		Size		Durability		Storage		Total	
		1		3		1		3		7	
		WPEA: OCIR						Storage: Accumulator			
Part sized for peak load:		1/2		Optimum maximum force:		$\tau_{PTO,max} = 1.00 \text{ MNm}$		$F_{PTO,max} = 420 \text{ kN}$			
Part load perform. k_o :		0		Size of primary gen./actuator:		d = 0.24 m		l = 4 m			
$\eta_{PTO,1}$				$\eta_{storage}$		0.94		η_{tot}		0.60	
				Annual prod. [MWh]						32	
<i>Conventional Hydrostatic Trans.</i>		Prod.		Size		Durability		Storage		Total	
		1		3		1		1		6	
		WPEA: OCIR (or reactive)						Storage: Super capacitors			
Part sized for peak load:		4/4		Optimum maximum force:		$\tau_{PTO,max} = 1.00 \text{ MNm}$		$F_{PTO,max} = 424 \text{ kN}$			
Part load perform. k_o :		0		Size of primary gen./actuator:		d = 0.22 m		l = 4 m			
$\eta_{PTO,1}$				$\eta_{storage}$		0.92		η_{tot}		0.65	
				Annual prod. [MWh]						34	
<i>Snapper™ Linear Generator with latching mechanism</i>		Prod.		Size		Durability		Storage		Total *	
		1		2		1		1		5	
		WPEA: Latching w. Coulomb						Storage: Super capacitors			
Part sized for peak load:		2/3		Optimum maximum force:		$\tau_{PTO,max} = 1.00 \text{ MNm}$		$F_{PTO,max} = 424 \text{ kN}$			
Part load perform. k_o :		1		Size of primary gen./actuator:		d = 0.52 m + latching mech.		l = 4 m + linear guide			
$\eta_{PTO,1}$		N/A		$\eta_{storage}$		0.92		η_{tot}		0.80	
				Annual prod. [MWh]						57	
<i>Direct drive though ratchet</i>		Prod.		Size		Durability		Storage		Total	
		1		0		1		1		3	
		WPEA: Single-ratchet						Storage: Super-capacitors			
Part sized for peak load:		3/4		Optimum maximum force:		$\tau_{PTO,max} = 0.50 \text{ MNm}$					
Part load perform. k_o :		2		Size of primary gen./actuator:		d = 3.5 m		l = 0.77 m			
$\eta_{PTO,1}$		N/A		$\eta_{storage}$				η_{tot}		0.90	
				Annual prod. [MWh]						33	
<i>PTOs with a production score of -1 - annual production less than 31 MWh</i>											
<i>Simple Fixed Pressure PTO</i>		Prod.		Size		Durability		Storage		Total	
		-1		3		3		3		8	
		WPEA: Coulombng damping						Storage: Accumulator			
Part sized for peak load:		1/3		Optimum maximum force:		$\tau_{PTO,max} = 0.375 \text{ MNm}$		$F_{PTO,max} = 159 \text{ kN}$			
Part load perform. k_o :		2		Size of primary gen./actuator:		d = 0.24 m		l = 4 m			
$\eta_{PTO,1}$				$\eta_{storage}$		0.94		η_{tot}		0.78	
				Annual prod. [MWh]						29	
<i>Ball (Roller) Screw</i>		Prod.		Size		Durability		Storage		Total	
		-1		3		1		2		5	
		WPEA: Single-ratchet						Storage: Fly-wheels			
Part sized for peak load:		1/3		Optimum maximum force:		$\tau_{PTO,max} = 0.50 \text{ MNm}$		$F_{PTO,max} = 212 \text{ kN}$			
Part load perform. k_o :		2		Size of primary gen./actuator:		d = 0.10 m		+ linear guide & generator			
$\eta_{PTO,1}$		N/A		$\eta_{storage}$				η_{tot}		0.81	
				Annual prod. [MWh]						30	
<i>Snapper™ Linear Generator</i>		Prod.		Size		Durability		Storage		Total	
		-1		3		1		1		4	
		WPEA: Coulomb damping						Storage: Super capacitors			
Part sized for peak load:		3/4		Optimum maximum force:		$\tau_{PTO,max} = 0.25 \text{ MNm}$		$F_{PTO,max} = 106 \text{ kN}$			
Part load perform. k_o :		1		Size of primary gen./actuator:		d = 0.13 m		+ linear guide			
$\eta_{PTO,1}$		N/A		$\eta_{storage}$		0.92		η_{tot}		0.80	
				Annual prod. [MWh]						26	

Basically, all direct drive systems (linear generator variants) have been found in-feasible due to the poor torque-densities, which yielded machines requiring 7.5m^2 - 13m^2 of active air-gap area in the machines. To relate this area requirement, the weight of active magnetic material alone (copper, iron laminations, magnets and back-iron) is estimated to be $1500\text{kg}/\text{m}^2$ in [90]. Without the guides for absorbing axial load and maintaining the air-gap between mutual attracting stator and translator, between $11,000\text{kg}$ and $20,000\text{kg}$ active magnetic material is required for an absorber producing an average of up to 55kW .

Systems using a single hydraulic cylinder for converting motion to hydraulic pressure and flow are size-wise considered a good solution, as a cylinder around $\text{Ø}25\text{cm}$, weighing about 1600kg , may give the required force, and the produced flow may be sent to the second part of the PTO inside the WEC, converting the pressure/flow to electricity. Also note that the cylinder does not require additional linear guides for support.

Considering systems using mechanical transmission to convert linear to rotational motion and give a speed increase, these are generally considered to have insufficient durability.

Generally, the systems employing a ratchet mechanism in the design suffer heavily in production, producing 50% less than the best performing systems.

Groups with high annual production, 1 and 2, are seen as the main interest, as the Wavestar system is based on being a high performance system, i.e. the PTO is not the main cost - accordingly, an advanced PTO with a high performance is of preference.

The highest production with a reliable and compact system is obtained using a hydraulic to drive a DDPM based transmission. The drawback of this design is power smoothing, which is only possible using super-capacitors, which are considered to have insufficient lifetime for wave-to-wave smoothing.

The discrete displacement cylinder PTO also has a good production and inherently incorporates accumulators, making robust and low cost smoothing of fluctuations due to wave-to-wave and wavegrouping. Also, high peak powers may be absorbed, as the only component between storage and cylinder are simple on/off valves. The main drawback is that multiple cylinders are required, which makes the design cumbersome, as the load of three cylinders has to be distributed symmetrically on the float-arm. Also, the durability of the valves is of concern.

The magnetic lead screw without ratchet is viewed as a good solution in its simplicity, as it at a reasonable size may directly drive a conventional generator. However, obtainable gearing ratio and inertia of the screw is unknown, which highly affects the feasibility of the design. If the inertia is too high, the repeated acceleration/de-acceleration will give a too high inertial load on the system.

The wedding-cake transmission is considered a very good design for the Wavestar, having storage using accumulators, which allows fixed-speed operation of generator at steady load. The only concern is that the systems require similar DDPM capacity for operating the accumulator as for operating the cylinder. This may reduce part load performance, especially when considering operating the DDPMs at fixed speed.

The simple hydraulic system with de-clutching control is viewed as a simple solution with reasonable production, but the production is still about 30% lower compared to the best performing systems. Some production reduction may also be experienced when implemented the de-clutching strategy causally. The de-clutching version is preferable compared to the latching version, having 50% higher production, unless a much higher latching torque is used.

Despite the relative high force density of the Snapper PTO, the PTO has a surprisingly poor production for the Wavestar due to the Coulomb like damping. To improve the production a latching mechanism might be added, but this requires a 3MNm latching torque for reaching just above half the production of the best systems.

Three Potential PTO Systems

Based on evaluating state-of-the-art of PTOs, promising technologies for the Wavestar C5 have been found. These concepts are in this chapter adopted and developed to the Wavestar WEC. The treated PTO technologies are DDPM, the discrete cylinder control, and the magnetic lead screw. These are investigated in the following for the Wavestar C5.

6.1 DDPM based PTO

The DDPM based PTO concept had high production due to allowing force control with high part load efficiency. In the following, layouts for the C5 are discussed.

6.1.1 PTO Layout

One suggestion is to use a DDPM to directly power the generator. With this transmission, the generator is rated for peak power, however, the efficiency is increased by varying the speed of the generator according to power. To assess this PTO compared to the Wedding-cake-PTO, basis is taking in the paper [O].

In [O] a completely similar PTO is investigated for the C5, except using an axial piston swash-plate pump instead of the DDPM, see Fig. 6.1. The system also incorporates an energy over-flow if the cylinder speed exceeds the hydraulic motor capacity. The system was modelled completely from wave-to-grid, including all components losses and main PTO dynamics.

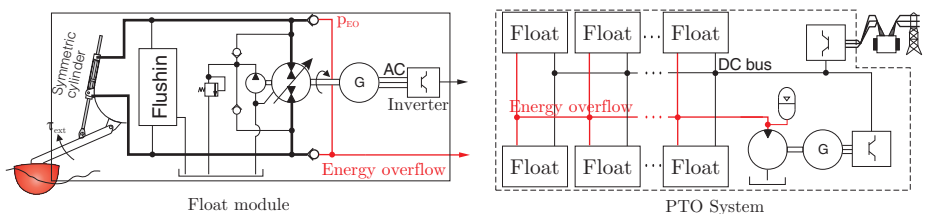


Figure 6.1: Figure from [O] of evaluated PTO.

Three different strategies were explored for generator speed, namely a fixed speed, a slow speed variation (adapting to wave groups), and a wave-to-wave speed control. This

is illustrated in Fig. 6.2. The results for strategy 2 are given in Tab. 6.1, where SS abbreviates sea state, where SS1-SS3 are $H_{m0} = \{1, 1.75, 2.5\}$ m. The table shows that the slow speed variation actually gives a fair performance of the hydraulic swash-plate motor. Thus, when inspecting the difference between a DDPM and a swash-plate unit in Fig. 6.3, this gives confidence in that a slow speed variation gives adequate part load performance of the DDPM. However, the generator and inverter are not operating optimally according to Tab. 6.1. This is due to the wave-to-wave fluctuating loads, i.e. changing from generating peak power to delivering idle power every half wave period.

With the high efficiency of the DDPM, it is considered better to move to the Wedding-cake PTO, allowing steadier load of generator and power smoothing.

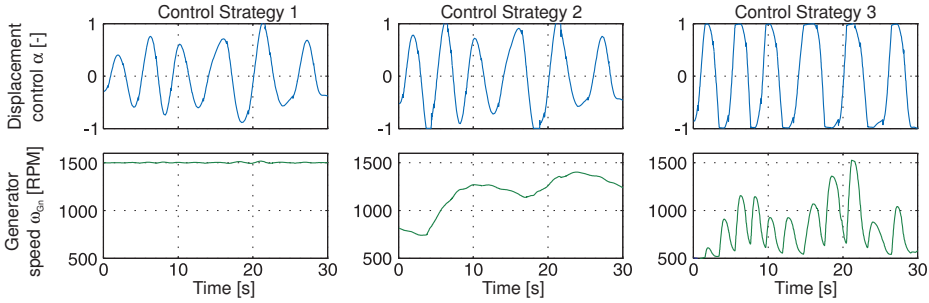


Figure 6.2: Figure from [O] of generator speed control strategies.

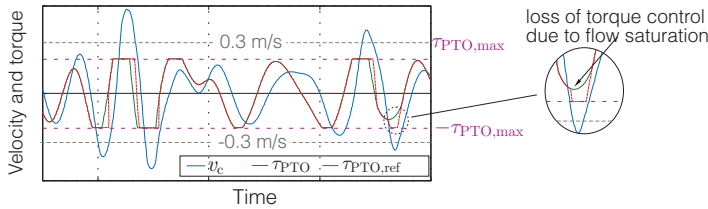


Figure 6.3: In (a) efficiency of DDPM and swash-plate motor from Ch. 5, and in (b) loss of torque control due to flow saturation in a hydro-static transmission.

Table 6.1: Optimised system with control strategy 2.

SS	Cylinder		Motor		Flush	Generator		Inverter		EO	Total		
	P_L	η	P_L	η	P_{flush}	P_L	η	P_L	η	P_L	P_{in}	P_{out}	η
1	0.30	94.4	1.18	76.5	0.28	0.86	75.9	0.25	90.6	0.00	5.45	2.45	44.9
2	1.04	94.5	2.57	83.4	0.35	1.22	90.3	0.77	93.2	0.47	18.9	12.1	64.0
3	2.05	94.7	3.92	85.0	0.37	1.52	93.0	1.27	93.8	2.32	38.8	26.7	68.9

To allow storage, the wedding-cake principle introduces an extra DDPM-slice on the shaft, which may in turns deliver and recover power from an accumulator battery. To avoid having a generator per absorber in the Wavestar C5, the idea is to connect a group of four neighbouring absorbers to one generator. This is illustrated in Fig. 6.4. Two sets

of stacked DDPM slices are connected to either side of a central generator, having a through-going shaft. As the Wavestar offers some amount of power smoothing due to phase difference in the absorbers' motions, half the DDPM capacity is assumed required for power smoothing compared to the cylinder connected DDPM capacity.

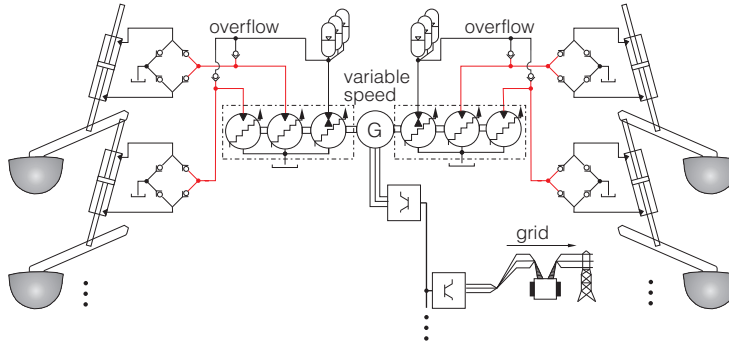


Figure 6.4: DDPM concept for the C5.

To avoid sizing both cylinder and storage DDPMs for peak power, an overflow line is added such that if the DDPM slices 1A,1B,2A or 2B saturate, the cylinder pressure will build up to the pressure $p_{acc,1}$ and excess power will be fed directly to the accumulator storage, whereby the 1C and 2C units may be downsized. Furthermore, this allows downsizing the 1A,1B,2A and 2B units to have a displacement corresponding to e.g. 0.3m/s cylinder velocity at the cost of cylinder control at high speeds.

Above this speed, torque control is lost, as the pressure in the cylinder will build-up and the load torque will go to $\tau_{PTO,max}$. This is illustrated in Fig. 6.3b. Noting that high damping forces are normally applied at high cylinder velocities, the effect of this torque control loss will be reduced. Finding the size of the DDPM is a problem of finding best trade-off between extracted power and DDPM performance.

To improve part load performance, an inverter is added to the generator, such that an appropriate speed may be set according to the current sea state. Note that reducing speed of the generator reduces the allowable cylinder velocity before force control is lost. This will also affect power production at low to medium energetic sea states.

An aspect of the design is that the applicable force becomes dependent on current storage pressure, as the cylinder cannot exceed this pressure.

Another issue regarding the DDPM solution is that the motor types are not commercially available yet, and self-development of such units within a reasonable time horizon seems infeasible.

6.2 Discrete Displacement Cylinder PTO

Having multiple cylinders on a single float is mechanically undesired for the Wavestar WEC. To overcome this issue, the idea is to introduce multi-chambered cylinders.

Different multi-chambered cylinder design may be made. A 4-chambered cylinder from patent application [248] is seen in Fig. 6.5a. However, this rather complex design will have an asymmetric force balance as the area sum in positive direction is much larger than negative direction unless the rod-diameter is small, which is not possible due to buckling. For optimal power extraction, the available force should be symmetric.

Fundamentally, a cylinder not having a trough-going rod will always have a higher positive force. To have symmetric forces and a mechanically simple cylinder, the design in Fig. 6.5b is suggested. If the rear chamber is left idle, breathing e.g. nitrogen gas for avoiding corrosion, active areas A_1 , A_2 and A_3 may be made such that $A_1 + A_3 = A_2$. However, three areas give $2^3 = 8$ combinations, i.e. 8 different load forces, which may be a too low resolution. To modify this aspect, an extra pressure line may be introduced, increasing the combination to $3^3 = 27$.

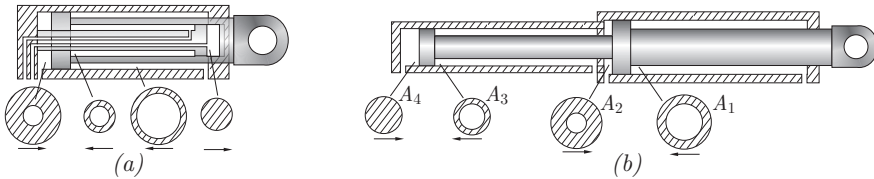


Figure 6.5: In (a) multi-chambered cylinder from [248], and in (b) suggested cylinder design.

Using the design, all absorbers may be directly connected to the same accumulator storage. This allows using a few numbers of central generators instead of one per absorber. The imagined system is shown in Fig. 6.6. A valve manifold with on/off valve is mounted on each cylinder, which may enable or disable the individual chambers. The effect may be interpreted as discrete variation of the displacement of the cylinder. Resultantly, the technology is going to be referred to as a Discrete Displacement Cylinder (DDC).

Compared to the PTO mentioned in state-of-the-art, active on/off valves are used instead of check valves. This allows a higher number of combinations, as cylinder volumes that are expanding also may be pressurised. For example, if check-valves are mounted on each chamber, the cylinder may only deliver one positive resistive force, $p_H A_2$, and three negative resistive forces $\{p_H A_1, p_H A_2, p_H (A_1 + A_2)\}$. Using active valves, the combinations $\{p_H (A_2 - A_1), p_H (A_2 - A_3), p_H (A_2 - A_1 - A_2)\}$ also becomes available.

The use of active valves allows performing reactive control. This is seen as a great property in this PTO, as the reactive power only travel between cylinder and storage.

The chosen hydraulic motor to drive the generator will be a bent-axis type, having a high efficiency of 95%, which it will maintain, as it operates at almost fixed load. Overall, the PTO has the best integration of storage as no additional conversion mechanisms are

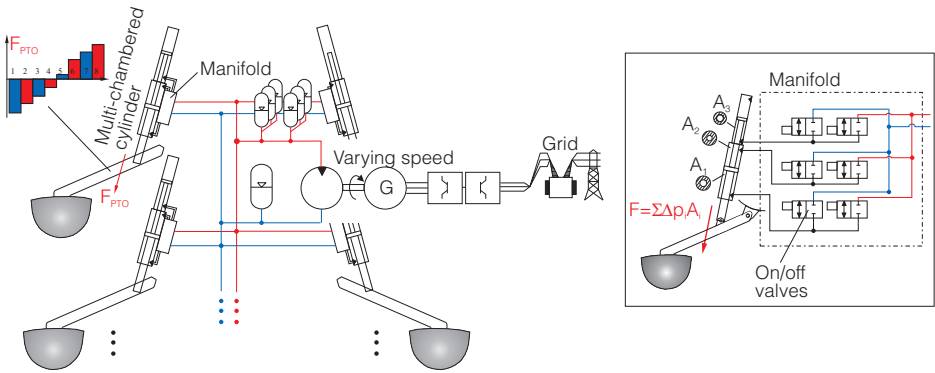


Figure 6.6: PTO for the C5 based on discrete displacement cylinder .

required to connect accumulators to the PTO. Accumulators may be added as desired based on the requested power smoothness. Thereby, the accumulator actually de-couples the PTO as illustrated in Fig. 6.7.

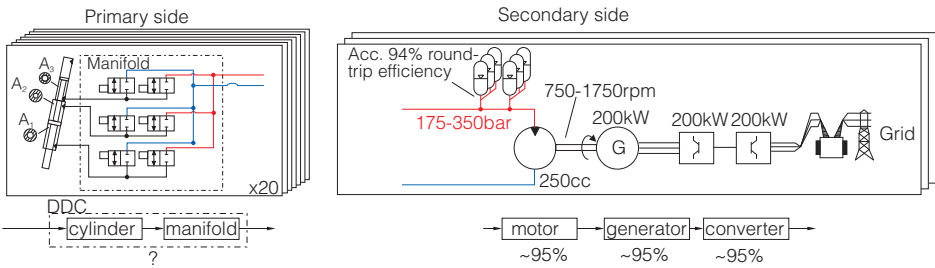


Figure 6.7: The PTO consists of primary side or DDC, and a secondary side.

The secondary side of the PTO, comprising a bent-axis motor, a generator and a converter, is a combination of standard components operating in their optimal operating regions. In Fig. 6.8 the pressure in the accumulator is imagined varied slowly between 175-350bar for good utilisation of storage capacity. Accordingly, the hydraulic motor and generator will always operate at minimum 50% torque load. The adaption to the overall power level is achieved by controlling the speed of the generator using the inverter, varying the speed between e.g. 750rpm-1750rpm. At low energetic sea states, one or two of the motor-generator sets may be disengaged to further adapt to the power level. Figure 6.8 shows that all components will operate in their best performance region.

Looking at primary side, the used cylinder is of rather simple design, being basically a series connection of two cylinders. The main problem is viewed as implementing the discrete control of the cylinder. Assessing whether suitable on/off valves exist requires investigating required size and response time. A study is also going to be required to see if the required power production is obtained when loading with only 8 forces, or additional chambers or pressure lines is required. Different losses and problems may

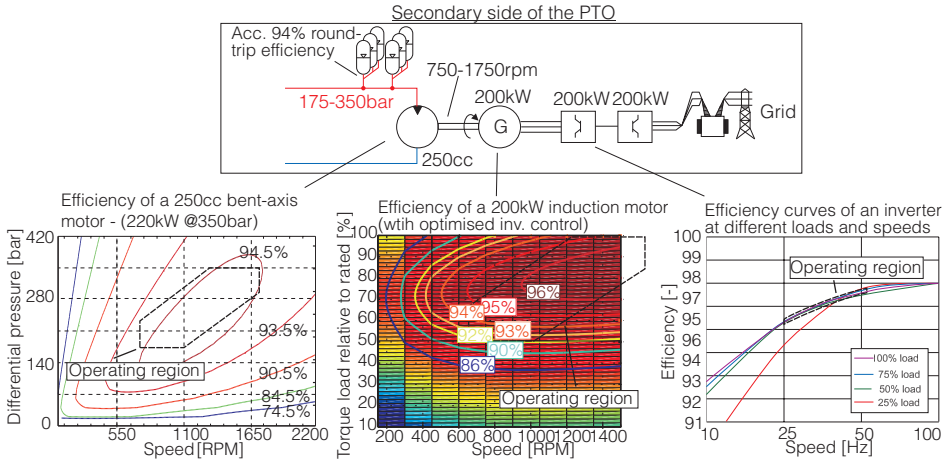


Figure 6.8: The secondary part of the DDC PTO, showing the operating region of the components. The efficiency curves were calculated in [A].

arise during shift transient, which also must be investigated.

The DDC PTO is viewed as providing high performance while having an overall very sound structure. Based on the above discussion, the validity comes down to proofing if the discrete force control affects power extraction, and if the DDC may be implemented reliable and with an adequate efficiency. This is illustrated in Fig. 6.7.

6.2.1 Investigation of DDC Performance

Investigation of the feasibility of the DDC for the Wavestar WEC is also performed in the four papers [M] , [I] , [G] and [E] .

Shifting Losses

The first aspect is to understand the fundamental losses in the DDC and if three chambers give sufficient performance. This is the main concern of [M] , where different configurations of pressure lines and cylinder chambers are investigated. In Fig. 6.9 a system with three pressure lines and three areas is shown. The cylinder is controlled by shifting pressure within the different chambers, generating F_{PTO} as sum of forces,

$$F_{PTO} = A_1 p_{A1} + A_2 p_{A2} + \dots + A_n p_{An} \quad [N] \quad (6.1)$$

where A_i is the i 'th cylinder area with sign according to force direction and p_{Ai} is the pressure of the i 'th cylinder chamber, which is connected to one of the system pressures $p_{Ai} \in \{p_0, \dots, p_{np}\}$.

Inspecting one chamber of the cylinder as in Fig. 6.9, where the cylinder velocity is assumed zero, it is proven in [M] that shifting from one pressure to another is associated with a minimum energy loss due to the compressibility of the fluid. The minimum loss

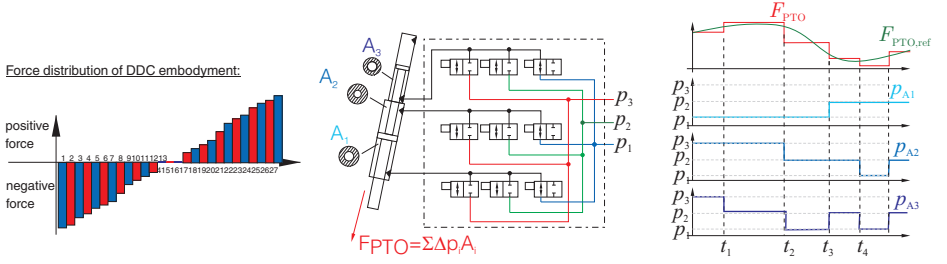


Figure 6.9: A DDC with three areas and three pressure lines.

is independent on how and how fast the valves are opened. In Fig. 6.10 a fixed chamber with volume V with initial pressure $p_v = p_0$ is illustrated. The chamber is about to be shifted to a second pressure p_1 by opening of the corresponding valve. When opening the valve to pressure p_1 at time t_0 , a flow will appear to build up the pressure in the volume as shown, where the volume of flow V_β required is:

$$V_\beta = \frac{V}{\beta_{\text{eff}}} \Delta p \quad [\text{m}^3] \quad (6.2)$$

Comparing the energy stored in the volume at t_f and the energy supplied from pressure line p_1 , the following amount of energy $E_{\beta\text{-loss}}$ has been lost,

$$E_{\beta\text{-loss}} = \frac{1}{2} (p_1 - p_0)^2 \frac{V}{\beta_{\text{eff}}} \quad [\text{J}] \quad (6.3)$$

where V is the volume and β_{eff} is the effective bulk-modules of the chamber, expressing the oil-stiffness. Note that Eq. (6.3) assumes a pressure-independent bulk-modulus, which is not true, however for pressures above 20bar, the variation is reduced.

The proof for Eq. (6.3) in [M] omits hose dynamics (inertia of the fluid within the hose). This is however included in paper [I]!, proving that Eq. (6.3) still holds.

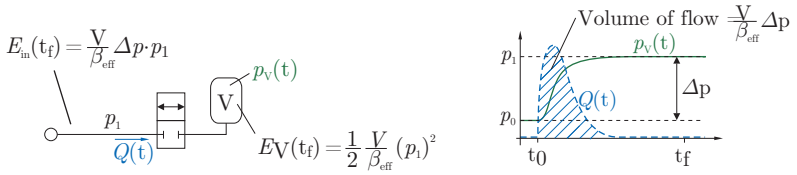


Figure 6.10: Illustration of compression loss based on [M].

Using the minimum loss in Eq. (6.3), a frame work is developed in [M] where the DDCs efficiency may be easy estimated in irregular waves as illustrated in Fig. 6.11. A Wavestar absorber is simulated in irregular wave where a continuous force reference is generated using a WPEA (reactive control). Based on the available discrete forces of the DDC $\{F_1, \dots, F_n\}$, the continuous reference $F_{\text{PTO,ref}}$ is approximated using some strategy implemented in the Force Shifting Algorithm (FSA). All shifts performed during the simulation is counted and saved as illustrated in Fig. 6.11. Afterwards, Eq. (6.3) may be

applied to calculate the total shifting losses $E_{\beta\text{-loss,tot}}$, and efficiency of the DDC may be determined as,

$$\eta_{\text{DDC}} = \frac{E_{\text{ext}} - E_{\beta\text{-loss,tot}} - E_{\text{tot,v}}}{E_{\text{ext}}} \quad [-] \quad (6.4)$$

Between shifts the flow going through the manifold will be throttled by the valves, dependent on their opening area. As a cylinder chamber is always connected to one pressure line through one valve, and if all valves used for that given chamber have an opening area A_o , the throttling losses $P_{v,i}(t)$ for a chamber with A_i piston area may be calculated based on the orifice equation as:

$$P_{v,i} = \frac{Q_i(t)^2}{A_{o,i}^2 C_d^2} \frac{\rho_{\text{fluid}}}{2} |Q_i(t)| = \frac{|v_c^3 A_i^3|}{A_{o,i}^2 C_d^2} \frac{\rho_{\text{fluid}}}{2} \quad [\text{W}] \quad (6.5)$$

where C_d is the discharge coefficient and ρ_{fluid} is the hydraulic-fluid density. The applied orifice equation, determining flow across a valve, is given as,

$$Q = C_d A_o \sqrt{\frac{2}{\rho_{\text{fluid}} |\Delta p|}} \quad \left[\frac{\text{m}^3}{\text{s}} \right] \quad (6.6)$$

where Δp is the differential pressure across the valve.

Integrating $P_{v,i}$ for each chamber and summing the values yields the total steady-state throttling loss $E_{\text{tot,v}}$ in Eq. (6.4).

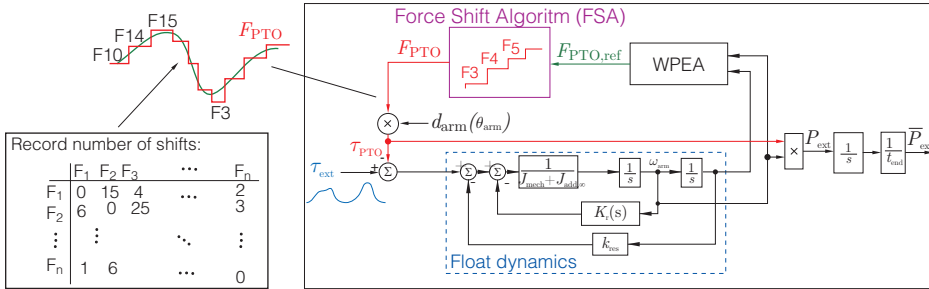


Figure 6.11: Evaluation of a DDC unit's efficiency in irregular waves.

In [M] it is discovered that controlling the DDC by choosing the force closest to the continuous reference is not energy wise optimal. Some force-shifts are more energy-expensive than others. This is illustrated in Fig. 6.12. The figure shows the shifting loss matrix, containing the compression losses experienced when shifting between forces. The forces are sorted according to size. As illustrated, if the current force is force number 9 and an increase in force is desired, it cost less energy to shift to force number 11 instead of 10. Likewise, from number 11 it is cheaper to shift to number 14, and skip 12 and 13. Thus, to avoid doing very expensive force shifts, a more suitable strategy is to calculate the energy expense of possible force-shifts, and make a compromise between tracking and energy-cost. Note, that the loss matrix in Fig. 6.12 changes with system pressures and cylinder position.

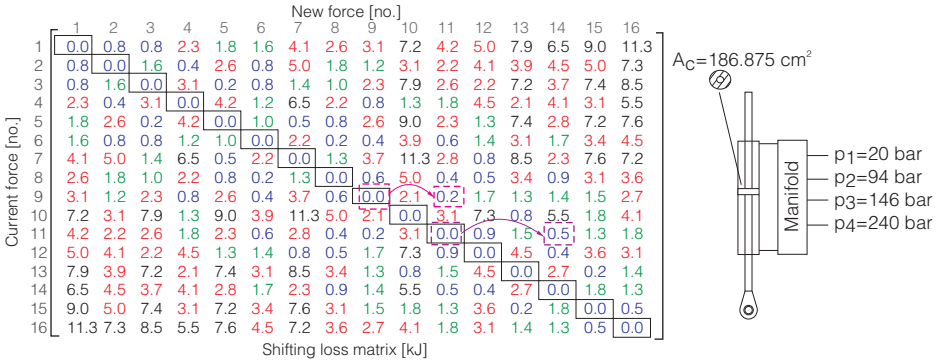


Figure 6.12: The shifting losses according to Eq. (6.3) for a DDC system consisting of 4 system pressures and a symmetric cylinder.

The method shown in [M] is to define a maximum allowed tracking error F_b , meaning that F_{PTO} must stay within a band of $\pm F_b$ about $F_{PTO,ref}$. However, within the band, the algorithm may choose the force steps with the lowest shift cost. A fixed time limit T_{min} on how frequently switching is allowed was also added. If the current force number is denoted k_0 , the control law may be stated as,

$$\{F_{PTO}(t) = \mathbf{F}[k] \mid k = \arg \min_{k \in \{k_-, k_0, k_+\}} |F_{ref}(t) - \mathbf{F}[k]| \} \quad (6.7)$$

where k_- and k_+ are the two cheapest forces to shift to within the band $\pm F_b$:

$$k_+ = \arg \min_{k \in S_+} E_{sh}(k_0, k), \quad S_+ = \{k \mid F_{PTO,ref}(t) < \mathbf{F}[k] < F_{ref}(t) + F_b\} \quad (6.8)$$

$$k_- = \arg \min_{k \in S_-} E_{sh}(k_0, k), \quad S_- = \{k \mid F_{PTO,ref}(t) - F_b < \mathbf{F}[k] < F_{ref}(t)\} \quad (6.9)$$

Hence, the tracking band is always defined around the value of $F_{PTO,ref}$. The algorithm is illustrated in Fig. 6.13. As the system pressure and volumes varies, the shifting losses are updated at each decision.

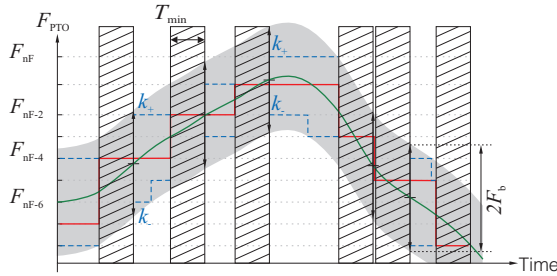


Figure 6.13: Tracking the continuous force within a band (grey), where forces with the less expensive shift costs (blue) are chosen.

To investigate the performance of different DDC configuration, the systems in Fig. 6.14 are explored based on the framework in [M] for three sea states:

- Sea state 1: $H_{m0} = 1.00\text{m}$, $T_{0,2} = 3.51\text{s}$
- Sea state 2: $H_{m0} = 1.75\text{m}$, $T_{0,2} = 4.23\text{s}$
- Sea state 3: $H_{m0} = 2.50\text{m}$, $T_{0,2} = 4.89\text{s}$

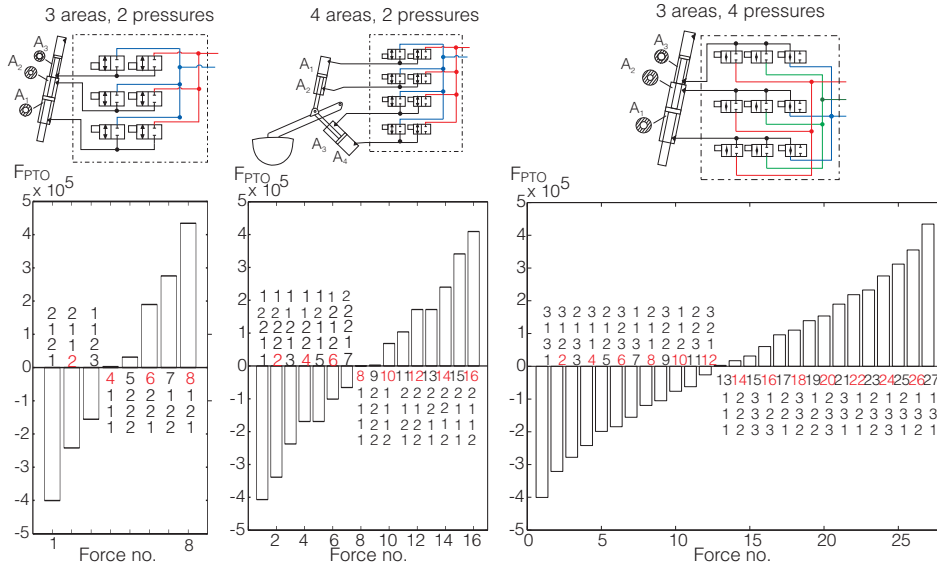


Figure 6.14: The three DDC configurations evaluated.

The simulations are made for a fixed bulk-modulus of 10000 bar, which is quite conservative energy-wise as an oil volume may be much stiffer as seen in Fig. 6.15, showing bulk-modules when assuming 1% free air the oil in a rigid chamber. However, if hoses are added, these reduce the stiffness, and hence the bulk-modulus is limited to 10000 bar to be conservative. The cylinder used in the simulation has a stroke of 3m, which penalises the results as only 2m is used in production. The last 1m is for storm protection, and the added volume requires extra energy for pressurisation. Extra capacity is required for lifting the absorbers into storm protecting, resulting in a layout with 420kN force at 240bar, which gives sufficient lifting capacity at 350 bar.

The results are shown on page 183, where the manifold efficiency η_{DDC} results have been highlighted. The efficiency is calculated as Eq. (6.4). Also the extracted power relative to applying continuous control has been highlighted.

The values of T_{min} and F_b have been found through iteration to find best compromise between adequate power extraction and high efficiency. In sea state 1 the high pressure is reduced to 180bar to improve efficiency as high forces are not required.

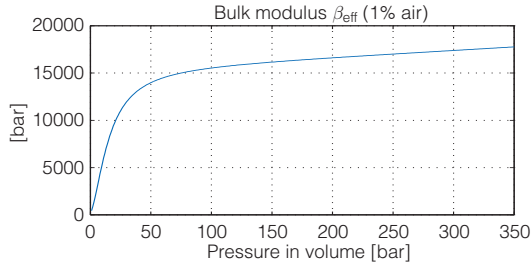


Figure 6.15: Bulk-modulus with 1% air, see e.g. for reference [249].

For sea state 2 and 3 the results show that all configurations yield approximately the same power extraction as the continuous control. In sea state 1, the energy extraction is about 91% of the continuous control. This could be increased if the lock-down time T_{\min} and force-band F_b was reduced to improve tracking. From the study it may be concluded that for all three DDCs, the discrete force approximation of the continuous force does not affect the power extraction. The main reason for this result is that the float has a natural frequency around 0.3Hz, thereby implementing an effective low pass filter on the discrete force variation.

Efficiency wise, configuration one with the 3 chambers and 2 pressure performs very poor with efficiencies η_{DDC} of 0.28, 0.64 and 0.71 for the three sea states. Adding an extra chamber as in configuration 2 improves the result to 0.60, 0.73 and 0.80. In configuration 3, adding the third pressure line to the three chambered cylinder has a huge effect. The efficiencies read 0.88, 0.89 and 0.90, which is viewed as being required for feasibility of the DDC PTO. An important feature of the design is maintaining efficiency for smaller sea states as well.

The greater effect of adding the third pressure line than increasing number of chambers is not a surprise. According to the shifting loss expression Eq. (6.3), this loss is proportional to volume size, but depends on the square of pressure difference.

The actual conversion efficiency of the manifold will also be a bit higher, as a reactive control was used which is not accounted for in the efficiency calculation.

An important discovery when adding the mid-pressure is that the net flow is close to zero (high-lighted blue box on page 183). This means that the DDC-modules actually operate as a sort of loss-less pressure transformer. For example, the DDC first lets the float motion supply flow into the mid pressure line. An instant later, the DDC shift configuration such that the mid pressure and float force now are combined through the cylinder to produce a high pressure flow.

An example of such a cycle is illustrated in Fig. 6.16. The cylinder is pumping fluid in to the mid pressure at time instance (1). At instance (2), the DDC increases the load force F_{PTO} using a configuration where the second chamber is now pumping fluid into the high pressure line, while the first chamber now consumes flow from the mid pressure. In instance (3), the force is further increased, such that the cylinder is pumping flow into

high pressure without use of the mid pressure.

As the system naturally delivers almost zero net-flow to the mid-pressure, only a small amount of extra control of the manifold is required to ensure that the net-flow is zero. Hence, no hydraulic motors and generators are required for the mid pressure line.

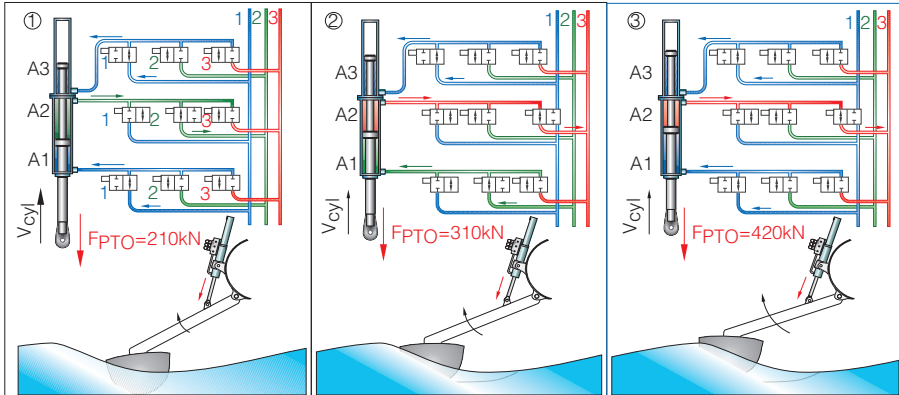


Figure 6.16: An example on how the DDC system operates during a wave, having zero net-flow to the mid pressure.

The efficiency may also be further increased as shown in Fig. 6.17. If a volume is undergoing displacement, a shift may be performed without energy loss if the displacement flow is in agreement with the desired pressure build up as shown in case 2 in Fig. 6.17. The displacement is contracting the volume, thus if the valve u_1 is closed, the pressure will up, and when the pressure has reached p_1 , the valve u_2 can be opened.

In case 1, an up-shift in pressure is performed, however, the displacement causes a decrease in pressure as it is expanding the volume. Resultantly, the opening and closing of valves needs to be performed very quickly to avoid cavitation, and the minimum loss will appear. This also illustrates that shifting pressure in chambers undergoing displacement increases the requirements of valve response time.

Having determined the overall DDC configuration and shown its feasibility with respect to efficiency and power extraction, the following section explores the required opening and closing time of the on/off valves.⁷

6.2.2 Required Valve Performance

Assuming only the minimum compression loss in Eq. (6.3) corresponds to assuming both infinite fast and large valves, or assuming that the cylinder piston is not moving. Identifying required valves opening and closing time with non-zero piston velocity is the main focus of paper [E]. This section gives a brief summary of the applied methods and results.

In [E] the investigation focus on the set-up in Fig. 6.18, where a chamber is undergoing

Evaluation of 3 chambers and 2 pressure lines

```

--- System ---
Stroke      : 3.0 m
A_vec [m^2]: [-0.011118 0.01962 -0.007194]

F_neg      = -400kN and F_pos = 434kN
(p_1 = 240bar and p_0 = 20bar)

F_lift     = 664kN
(p = 350bar)

Q_rated [L/min] = [333.54 588.6 215.82]
(v_cyl=0.5m/s)
Valve loss at rated flow = 3.00 bar

Sea State : 1 (H_m0=1.00 m, T_02=3.51 s, T_P=4.62 s)
Sea State : 2 (H_m0=1.75 m, T_02=4.23 s, T_P=5.57 s)
Sea State : 3 (H_m0=2.50 m, T_02=4.89 s, T_P=6.44 s)
--- Simulation ---
          SeaState1 SeaState2 SeaState3
p_vec [bar] : [20 180] [20 240] [20 240]
T_min      : 450 ms 450 ms 350 ms
Force_band : +- 100 kN+- 150 kN +- 150 kN

Total Loss      : 1549 kJ 3553 kJ 4695 kJ
Average manifold loss: 4.41 kW 8.40 kW 9.59 kW
Average power input : 6.09 kW 23.33kW 41.90 kW
Avg. compression loss: 4.31 kW 7.89 kW 8.36 kW
Average valve loss  : 0.10 kW 0.51 kW 1.24 kW
Manifold efficiency : 27.6 % 64.0 % 77.1 %
Average cylinder loss: 0.39 kW 1.47 kW 2.55 kW
Cylinder efficiency : 94.0 % 94.1 % 94.3 %

-- Gylander and manifold --
Harvested power : 6.48 kW 24.80 kW 44.45 kW
Power out       : 1.68 kW 14.94 kW 32.31 kW
Efficiency total : 25.95 % 60.23 % 72.68 %

Extracted power relative to continues ctrl: 90.6 % 99.6 % 98.5 %

-- Flow sum --
Low pressure    : -0.138 m^3 -0.467 m^3 -0.975 m^3
High pressure   : 0.138 m^3 0.467 m^3 0.975 m^3
    
```

Evaluation of 4 chambers and 2 pressure lines

```

--- System ---
Stroke      : 3.0 m
A_vec [m^2]: [0.016275 -0.008085 -0.01134 0.003255]

F_neg      = -427kN and F_pos = 430kN
(p_1 = 240bar and p_0 = 20bar)

F_lift     = 680kN
(p = 350bar)

Q_rated [L/min] = [488.25 242.55 340.2 97.65]
(v_cyl=0.5m/s)
Valve loss at rated flow = 3.00 bar

Sea State : 1 (H_m0=1.00 m, T_02=3.51 s, T_P=4.62 s)
Sea State : 2 (H_m0=1.75 m, T_02=4.23 s, T_P=5.57 s)
Sea State : 3 (H_m0=2.50 m, T_02=4.89 s, T_P=6.44 s)
--- Simulation ---
          SeaState1 SeaState2 SeaState3
p_vec [bar] : [20 180] [20 240] [20 240]
T_min      : 450 ms 450 ms 350 ms
Force_band : +-100 kN +-150 kN +-150 kN

Total Loss      : 854 kJ 2667 kJ 4009 kJ
Average manifold loss: 2.43 kW 6.30 kW 8.19 kW
Average power input : 6.12 kW 23.4 kW 42.1 kW
Avg. compression loss: 2.33 kW 5.81 kW 6.95 kW
Average valve loss  : 0.10 kW 0.49 kW 1.24 kW
Manifold efficiency : 60.2 % 73.0 % 80.5 %
Average cylinder loss: 0.42 kW 1.56 kW 2.62 kW
Cylinder efficiency : 93.6 % 93.7 % 94.1 %

-- Cylinder and manifold --
Harvested power : 6.54 kW 24.92 kW 44.73 kW
Power out       : 3.68 kW 17.06 kW 33.92 kW
Efficiency total : 56.4 % 68.45 % 75.82 %

Extracted power relative to continues ctrl: 91.4 % 100.0 % 99.1 %

-- FFlow sum --
Low pressure    : -0.139 m^3 -0.470 m^3 -0.982 m^3
High pressure   : 0.139 m^3 0.470 m^3 0.982 m^3
    
```

Evaluation of 3 chambers and 3 pressure lines

```

--- System ---
Stroke      : 3.0 m
A_vec [m^2]: [-0.011118 0.01962 -0.007194]

F_neg      = -400kN and F_pos = 434kN
(p_2 = 240bar and p_0 = 20bar)

F_lift     = 664kN
(p = 350bar)

Q_rated [L/min] = [333.54 588.6 215.82]
(v_cyl=0.5m/s)
Valve loss at rated flow = 3.00 bar

Sea State : 1 (H_m0=1.00 m, T_02=3.51 s, T_P=4.62 s)
Sea State : 2 (H_m0=1.75 m, T_02=4.23 s, T_P=5.57 s)
Sea State : 3 (H_m0=2.50 m, T_02=4.89 s, T_P=6.44 s)
--- Simulation ---
          Sea State 1 Sea State 2 Sea State 3
p_vec [bar] : [20 100 180] [20 130 240] [20 130 240]
T_min      : 450 ms 450 ms 350 ms
Force_band : +-100 kN +-150 kN +-150 kN

Total Loss      : 257 kJ 1082 kJ 2077 kJ
Average manifold loss: 0.73 kW 2.56 kW 4.24 kW
Average power input : 6.13 kW 23.6 kW 41.3 kW
Avg. compression loss: 0.64 kW 2.02 kW 3.06 kW
Average valve loss  : 0.09 kW 0.53 kW 1.19 kW
Manifold efficiency : 88.1 % 89.2 % 89.7 %
Average cylinder loss: 0.40 kW 1.54 kW 2.57 kW
Cylinder efficiency : 93.9 % 93.9 % 94.2 %

-- Cylinder and manifold --
Harvested power : 6.53 kW 25.13 kW 43.90 kW
Power out       : 5.40 kW 21.03 kW 37.09 kW
Efficiency total : 82.65 % 83.70 % 84.48 %

Extracted power relative to continues ctrl: 91.3 % 100.9 % 97.3 %

-- Flow sum --
Low pressure    : -0.083 m^3 -0.512 m^3 -0.964 m^3
Mid pressure    : -0.036 m^3 0.080 m^3 -0.000 m^3
High pressure   : 0.119 m^3 0.432 m^3 0.964 m^3
    
```

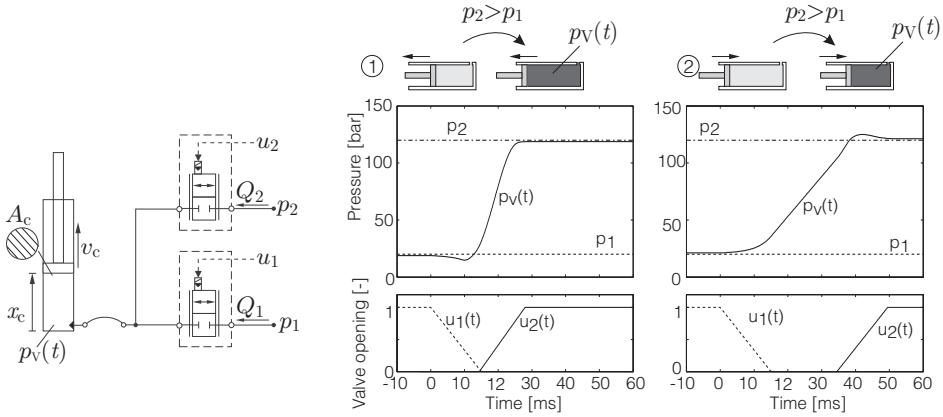


Figure 6.17: Shifting pressure in a chamber undergoing displacement.

displacement ($v_c \neq 0$), and has to shift connection from p_L to p_H or vice versa. When one valve closes, the fluid inside will be confined, causing an unstable pressure gradient until the second valve opens. Accordingly, the valves need to be fast, otherwise the fluid volume inside may either cavitate or “explode”.

The transient behaviour of the valve is modelled as a ramp function in order to have a very simple definition of valve requirements, see Fig. 6.18c. The model is preferred compared to e.g. a linear first order model as on/off valves do not tend to slow down near their set point, confer a seat valve. A linear second order model could also have been utilised, however, the response of a on/off valve also tends to saturate quite fast, making the ramp model more representative. The ramp model is also assumed to be the most conservative definition of a valve’s opening time. In the study the valve is assumed to be equally fast at opening and closing.

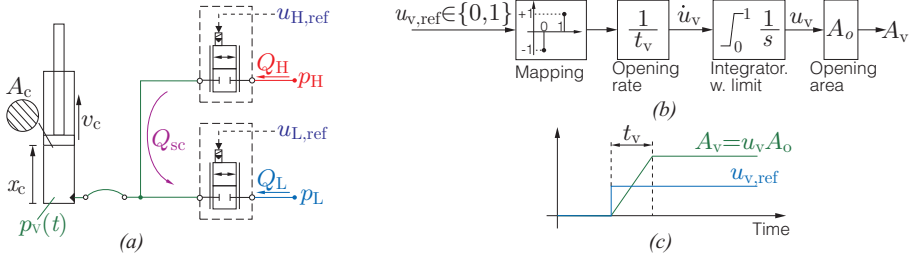


Figure 6.18: Set-up from [E] for investigating required valve response time.

The paper defines the four cases in Fig. 6.19 for investigation, which are the different pressure and velocity cases. In case 3 and 4 the pressure build up caused by the displacement flow is in agreement with the desired pressure change, where it is most efficient to close the first valve, and then open the second valve when the pressure has reached the desired level. This is referred to as a passive shift. For case 1 and 2 the displacement

causes a pressure gradient in disagreement with the desired pressure change. This is referred to the active shift, and the energy defined in Eq. (6.3) will at minimum be lost.

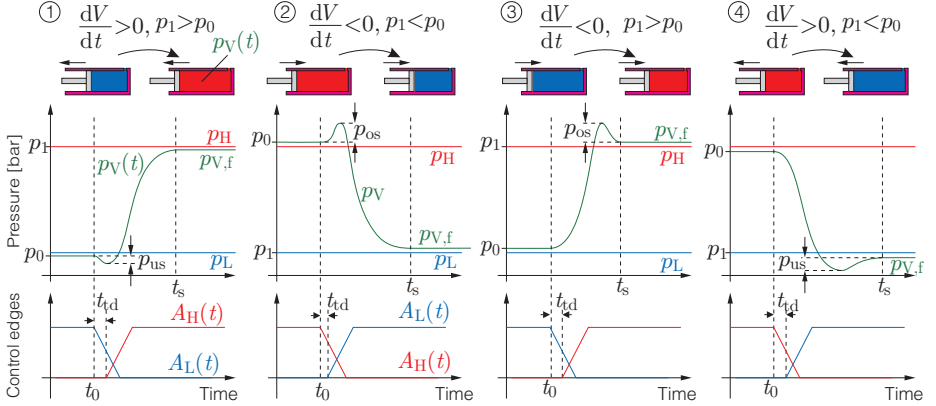


Figure 6.19: The four shift cases.

The required valve response time t_v is a trade-off between accepted energy loss and allowed pressure peaks p_{os} and p_{us} . The value of t_v for meeting these requirements is dependent on operating points, i.e. combination of cylinder position x_c and velocity v_c . The worst combination is a high velocity v_c and a small volume as this gives large pressure gradients when the fluid volume is confined.

To identify worst case operating points for the Wavestar WEC, the cylinder movement was analysed for a 30 min simulation in one of the largest production sea states for the Wavestar C5. The sea state had a significant wave height of 2.50m and a mean wave period of 5.5s. A view of the simulation results is seen in Fig. 6.20a. To describe the cylinders operating region, a density function $f(x_c, v_c)$ is calculated from the cylinder movement, showing how often the cylinder is in different position and velocity combinations. From the density function $f(x_c, v_c)$, the percentage F_{op} of time spend in a given region R_{op} may be found as:

$$F_{op}(R_{op}) = \iint_{R_{op}} f(x_c, v_c) dx_c dv_c \quad (6.10)$$

By dividing the cylinder position and velocities into discrete intervals, and integrating the time spend in each interval, the time trajectory in Fig. 6.20a is transformed into the density function in Fig. 6.20b. As expected, high velocities near the cylinder ends never occurs, thus, choosing the valves according to the worst case velocity and position would be over-conservative. Instead, the worst-case points are selected as the red trajectory in Fig. 6.20, as the cylinder is within this area more than 99% of the time. A more narrow operating region in Fig. 6.20b could have been chosen, as the control may be designed such that shifts at peak velocities are avoided.

To assess the size of the shifting loss, a loss coefficient γ_{Λ_o} is defined, which expresses

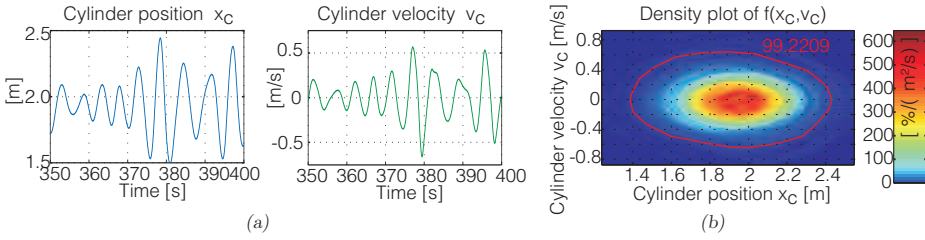


Figure 6.20: Cylinder movement for the Wavestar WEC and its density function.

the simulated shifting loss E_{shift} compared to having an infinite fast valve,

$$\gamma_{A_o} = \frac{E_{\text{shift}}}{E_{\text{shift},\infty}} - 1 \quad [-] \quad (6.11)$$

where $E_{\text{shift},\infty}$ is the shifting loss for $t_v \rightarrow 0$. Thus, as γ_{A_o} approaches zero, no benefit is obtained from having a faster valve.

To avoid performing the evaluation of required valve response time for all different area sizes of a given cylinder, the results are normalised by careful definition of the valve opening area as a function of chamber size.

Setting the maximum allowed undershoot and overshoot p_{us} and p_{os} to 7 bar, the loss ratio is evaluated along the red trajectory in Fig. 6.20 for different valve response times. The timing of closing and opening of valves t_d is optimised for each case such that pressure peaks below p_{us} and p_{os} are met, while minimising E_{shift} . The parameter t_d is defined in Fig. 6.19, controlling the amount of overlap between closing and opening of the valves.

The results are seen in Fig. 6.21. Due to the symmetric characteristics of the operating points, the results from shifting up and down in pressure become symmetric. The used opening area of the valves is such that a 5 bar pressure drop will be present when the cylinder is moving at 0.5 m/s.

If a valve with $t_v \leq 15$ ms is used, then an extra shifting loss of only 20% is present at the worst case points compared to using infinite fast valves. Benefit from increasing the valve's response time beyond this value will be reduced. Accordingly, the efficiencies in the feasibility's study of the PTO is valid if on/off valves with 15 ms opening and closing times are used.

Large on/off valves with 15 ms opening and closing time is commercial available, see e.g. Fig. 6.22 for a pilot operated 2/2 way valve. The data shows that for this series, valves with 850, 1500 and 3600 L/min are available at response times of 12 ms, 14 ms and 17 ms. Note that the data is for proportional controlled valve, which it not required for the DDC system, i.e. a simpler and cheaper valve should be used. This may be obtained by using a valve having the same cartridge type of e.g. Fig. 6.22, but with a much simpler pilot stage and without spool position feedback. An option is also to use a set of parallel valves of smaller size, which may be a more cost effective solution.

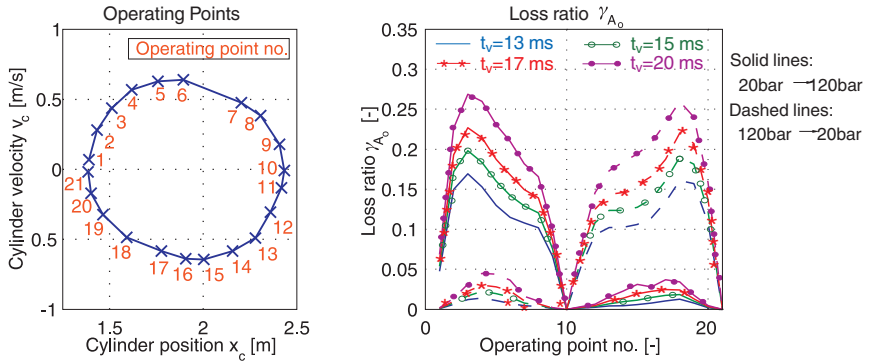
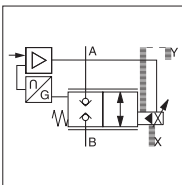
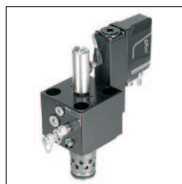


Figure 6.21: Performance of four valve response times evaluated along the border of the operating region.



General				
Design: Proportional throttle valve, slip-in cartridge according to ISO 7368				
Nominal size	DIN	NG32	NG40	NG63
Hydraulic				
Max. operating pressure	[bar]	Ports A, B, X, XX and SP up to 350		
Fluid temperature	[°C]	-20 ... +60		
Nominal flow at $\Delta p=5$ bar	[l/min]	850	1500	3600
Recommended max. flow	[l/min]	2000	3000	8000
Flow direction		B to A and A to B		
Static/dynamic				
Step response at pilot press. >140bar	[ms]	12	14	17
Frequency response at pilot press. >140bar				
Amplitude -3dB; 10% \pm 5%	[Hz]	80	74	52
Phase -90°; 10% +5%	[Hz]	63	59	56

Figure 6.22: Series TDP 2/2 way valve from Parker [250].

6.3 Magnetic Lead Screw based PTO

The magnetic lead screw has a high potential on both force-density and power production. Resultantly, the PTO is further explored in this section. The basic design of the MLS is based on papers [C] and [F]. This works extends on how the MLS interacts with the Wavestar absorber and conducts a general feasibility study.

6.3.1 MLS PTO Layout

Imagined implementation of the magnetic lead screw PTO on the C5 is shown in Fig.6.23. Compared to [126, 127] permanent magnets are placed both on rotor and translator to achieve the force-density of the magnetic coupling. In [126, 127] the rotor is suggest being the longer part, which is found undesirable due to the increased inertia of the rotating part. Resultantly, the design is made with rotor as the shortest part, also allowing all magnets to be placed internally. This design suggestion is credited to P.O.Rasmussen [C].

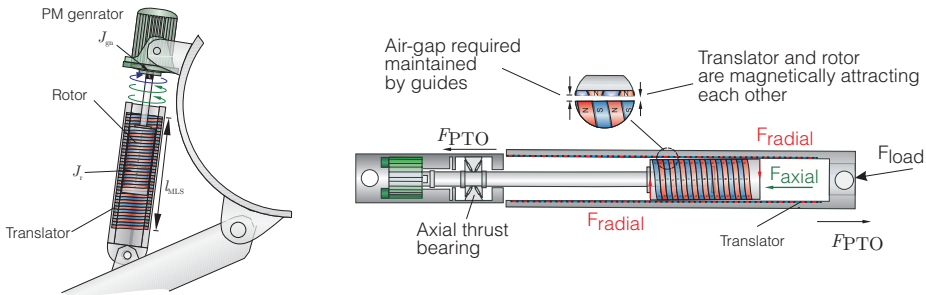


Figure 6.23: *MLS concept implementation on the Wavestar C5.*

Mechanically, the design is rather complex. The translator and rotor are magnetically attracting each-other, thus, the rotor will be pulled to one of the side of the translator if no external support is given. Hence, guides and bearing have to made, maintaining air-gap and absorbing radial loads, while allowing the rotor to rotate at a high speed, while being displaced relative to the translator.

The design must be stiff enough to avoid buckling when under compressional load. A trust bearing is also required for providing the reaction force for the applied force F_{PTO} , otherwise, this axial load will be applied to the generator shaft.

Realising such a design for the Wavestar WEC is the concern of the paper [C] and [F], where a design is explored. The design is summarised in Fig. 6.24. Both rotor and translator magnets are encapsulating in a non-magnetic sleeve. First the rotor shaft is supported by bearings in both ends of the rotor. These bearings are then mounted inside bushings, implementing the linear guide as these slides inside the translator. As the bearing supports the rotation, the bushings will ideally only experienced translational

motion. The rotor shaft is connected to the generator through an axial thrust bearing, absorbing the axial load.

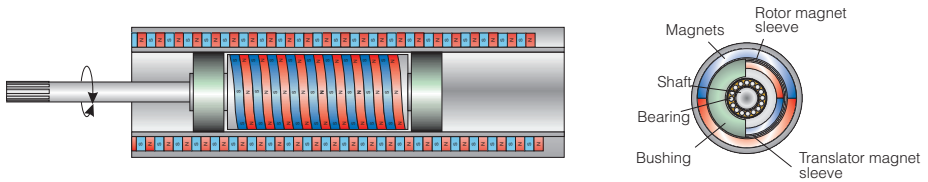


Figure 6.24: Mechanical implementation of a MLS.

Based on the design, a 17kN prototype was constructed and tested in a test-bench, see Fig. 6.25, with the parameters listed in Tab. 6.2. The magnetic thread was implemented using standard disc magnets, which was glued into a non-magnetic stainless steel retainer. Verification of the stall force of the prototype showed a deviation of only 2.3% between calculated (17kN) and measured stall force (16.6kN) [C]. Taking the rotor length and diameter, a sheer-stress of $16.6 \text{ kN} / (0.105 \text{ m} \cdot \pi \cdot 0.410 \text{ m}) = 204 \text{ kN/m}^2$ has been achieved. The 20mm lead of the prototype's thread corresponds to having 750 rpm on the rotor shaft when the translator is moved with 0.25m/s.

Table 6.2: Parameters of 17kN MLS prototype [C].

Parameter	Value	Parameter	Value
Stall force	17 kN	Stroke	400 mm
Magnet diameter	8 mm	Rotor diameter	105 mm
Magnet thickness	5 mm	Rotor length	410 mm
Number of magnets	4340	Translator outer diameter	142 mm
Total magnet mass	8.5 kg	Translator length	1078 mm
Magnetic airgap	1.5 mm	Maximum angular velocity	125 rad/s
Lead	20 mm	Maximum linear velocity	0.4 m/s

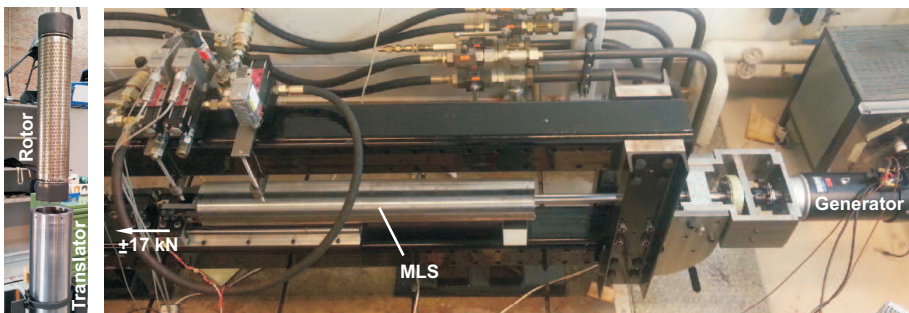


Figure 6.25: MLS prototype with $\pm 17 \text{ kN}$ and 0.40 m stroke designed at Aalborg University [C].

The full scale MLS design in Fig. 6.26 with a stall torque of 500kN was performed in [C]. The design shows that a MLS with an outer diameter of $\text{Ø}350 \text{ mm}$ is required. In

comparison, an asymmetric hydraulic cylinder may produce (-500kN,+ 840kN) with a rod of Ø110mm, inner diameter Ø175mm and outer diameter of Ø225mm.

To look at the force density and permanent magnet utilisation, a comparison is made in Tab. 6.3 with the 950kN Archimedes Wave Swing (AWS) generator. The generator consist of two parallel stacks [103]. Taking into account the 50% longer stroke of the AWS, about 6 times the magnet mass is required in linear generator design, along with a lot of copper, compared to the MLS. The amount of copper in the MLS-PTO will be determined by the high-speed generator, but will be much lower due to the increased speed.

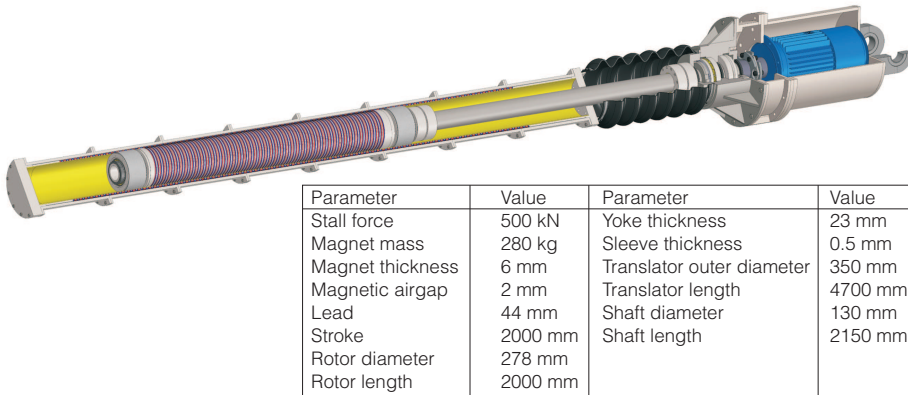


Figure 6.26: Full scale design given in [C] for the Wavestar C5.

Table 6.3: Comparison of MLS in [C] and linear generator for Archimedes-wave-swing in [103].

Parameter	MLS	AWS Linear generator
Stall force	500 kN	2x 425 kN
Magnet mass	280 kg	2x 2250 kg
Copper mass	N/A	2x 3600 kg
Stroke	2000 mm	3600 mm
Rotor/Stator length	2000 mm	3000 mm
Translator length	4700 mm	7600 mm

Having determined that the MLS is implementable , the next aspect is to treat the MLS's dynamic behaviour.

6.3.2 Dynamics of the MLS

For adequate power production, PTO force control is required. Accordingly, no ratchet mechanism is present, which means that the rotor of the MLS (and generator) will reverse direction every half wave period. This section investigates if the MLS have sufficient force to accelerated and de-accelerate the inertia, and how this will affect the power production.

By analysing the system in Fig. 6.27a, the moment of mass inertia of the rotor and generator may be mapped to an equivalent inertia about the arms pivot. The PTO torque τ_{PTO} is given as:

$$\tau_{PTO} = F_{MLS} d_A \quad [N] \quad (6.12)$$

where F_{MLS} is the force applied by the MLS to the float arm.

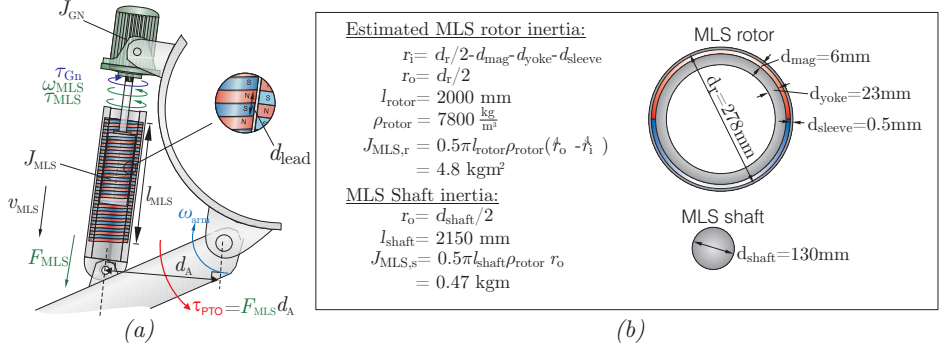


Figure 6.27: Modelling of MLS.

If the lead of the magnetic lead screw is denoted d_{lead} , see Fig. 6.27, the relation of the angular velocity of the rotor ω_{MLS} and the relative linear velocity of translator and rotor v_{MLS} may be found as:

$$v_{MLS} = \frac{d_{lead}}{2\pi} \omega_{MLS} = D_{\omega,MLS} \omega_{MLS} \quad \left[\frac{m}{s} \right] \quad (6.13)$$

where $D_{\omega,MLS}$ [m/rad] is the displacement of the translator per rotation of the rotor in radians.

The force and torque relations are as follows:

$$F_{MLS} = \frac{1}{D_{\omega,MLS}} \tau_{MLS} \quad [N] \quad (6.14)$$

$$F_{MLS} = \frac{1}{d_A \tau_{PTO}} \quad [N] \quad (6.15)$$

The gear ratio γ_g from ω_{arm} to ω_{MLS} is given as:

$$\left. \begin{array}{l} v_{MLS} = D_{\omega,MLS} \omega_{MLS} \\ v_{MLS} = d_A \omega_{arm} \end{array} \right\} \Rightarrow \frac{\omega_{MLS}}{\omega_{arm}} = \gamma_g = \frac{d_A}{D_{\omega,MLS}} = \frac{2\pi}{d_{lead}} d_{arm} \quad [-] \quad (6.16)$$

If no load τ_{Gn} is applied to the MLS, the load F_{MLS} will be determined by the mass-moment of inertia, which gives a torque load on the MLS of:

$$\tau_{MLS} = (J_{MLS} + J_{Gn}) \dot{\omega}_{MLS} = (J_{MLS} + J_{Gn}) \gamma_g \dot{\omega}_{arm} \quad [Nm] \quad (6.17)$$

Inserting into the absorber's equation of motion Eq. (2.31) gives:

$$\begin{aligned}\dot{\omega}_{\text{arm}}(J_{\text{mech}} + J_{\text{add}}) &= -k_{\text{res}}\theta_{\text{arm}} - \omega_{\text{arm}}B_{\text{hyd}} - \tau_{\text{MLS}}\gamma_{\text{g}} \\ &\quad \downarrow \\ \dot{\omega}_{\text{arm}}(J_{\text{mech}} + J_{\text{add}} + (J_{\text{MLS}} + J_{\text{Gn}})\gamma_{\text{g}}^2) &= -k_{\text{res}}\theta_{\text{arm}} - \omega_{\text{arm}}B_{\text{hyd}}\end{aligned}\quad (6.18)$$

Thus, seen from absorber and arm, the rotor and generator inertia is scaled with the square of the gear ratio γ_{g}^2 . The expression for the resulting natural frequency of the float and arm now becomes:

$$\omega_{\text{C5}} = \sqrt{\frac{k_{\text{res}}}{J_{\text{add}} + J_{\text{mech}} + (J_{\text{MLS}} + J_{\text{Gn}})\gamma_{\text{g}}^2}} \quad \left[\frac{\text{rad}}{\text{s}} \right] \quad (6.19)$$

In [C] lead sizes down to 10mm are explored (smaller lead \Rightarrow higher gearing). Assuming a lead of 20mm, which gives 1500rpm at 0.5m/s, gives a gearing ratio γ_{g} of:

$$\gamma_{\text{g}} = \frac{2\pi}{14 \cdot 10^{-3} \text{m}} \cdot 2.36 \text{m} = 741 \quad (6.20)$$

Hence, with this ratio the inertia of MLS and generator is amplified with approximately 0.55e6 when mapped to the float arm. Estimation the inertia J_{MLS} of the 500kN MLS is performed in Fig. 6.27, where an average density of yoke and magnets of 7800kg/m² has been assumed. This gives $J_{\text{MLS}} = 5.25 \text{kgm}^2$. Thus with a lead of 20mm, the reflected inertia becomes $J_{\text{MLS}} \cdot 741^2 = 2.9 \text{kgm}^2$, which is actual more than the mechanical inertia of the absorber, including the 15m³ of ballast water.

The absorber natural frequency without the magnetic lead screw is,

$$\omega_{\text{N}} = \sqrt{\frac{k_{\text{res}}}{J_{\text{add}} + J_{\text{mech}}}} = 1.8 \frac{\text{rad}}{\text{s}} \Rightarrow T_{\text{C5}} = 3.5 \text{s} \quad (6.21)$$

where the values of Tab.6.5 have been inserted. This corresponds to a natural oscillation period of 3.5s. The new resulting natural frequency of the float and arm with the magnetic lead screw rotor will be:

$$\omega_{\text{C5}} = \sqrt{\frac{k_{\text{res}}}{J_{\text{add}} + J_{\text{mech}} + (J_{\text{r}})\gamma_{\text{g}}^2}} = 1.38 \text{rad/s} \Rightarrow T_{\text{C5}} = 4.55 \text{s} \quad (6.22)$$

Hence, the absorbers natural period is slowed with one second due to the MLS inertia. Increasing the natural period to 4.55 s is an advantage, see Tab. 3, as the primary energy production happens in sea states with mean periods greater than 4.5s. The table is valid for Hanstholm. For sites more distant from the coast, the wave period will in general be longer. Hence, it can be concluded that the reflected inertia may actual be an advantage, also for points absorber's in general, as they often have a too high natural frequency compared to the wave climate.

Table 6.4: Indication of primary energy production. The table is for Hansthalm harbour.

H_{m0} [m]	Mean wave period T_{02} [s]						Sum [%]	Main region of annual production
	2-3	3-4	4-5	5-6	6-7	7-8		
0.0-0.5	2.65	8.18	1.84	0.38	0.14	0.04	13.2	Main region of annual production
0.5-1.0	1.22	19.2	11.4	2.21	0.18	0.08	34.4	
1.0-1.5	0.00	6.84	13.0	2.96	0.30	0.04	23.2	
1.5-2.0	0.00	0.33	9.58	3.05	0.29	0.04	3.3	
2.0-2.5	0.00	0.02	3.34	4.60	0.20	0.04	8.2	
2.5-3.0	0.00	0.01	0.22	3.89	0.21	0.02	4.4	
Sum[%]	3.87	34.6	39.5	18.6	2.72	0.68	100	

$J_{\text{add}}(0.2\text{ Hz})$	$2.0\text{e}6\text{ kgm}^2$	k_{res}	$14\text{e}6\text{ Nm}$
J_{mech}	$2.45\text{e}6\text{ kgm}^2$	d_{arm}	2.36 m

Table 6.5: C5 constants.

The next aspect is whether the MLS has sufficient force for handling the inertia load. The peak angular acceleration of the absorber arm $\dot{\omega}_{\text{arm,peak}}$ is around 0.5 rad/s^2 . For the lead of $d_{\text{lead}} = 20\text{ mm}$, this give an inertial load $\tau_{\text{MLS,J}}$:

$$\tau_{\text{MLS,J}} = J_{\text{MLS}}\dot{\omega}_{\text{MLS}} = J_{\text{MLS}}\gamma_g\dot{\omega}_{\text{arm,peak}} = 1945\text{ Nm} (\sim F_{\text{MLS}} = 611\text{ kN}) \quad (6.23)$$

The stall force of the MLS is 500 kN , which will be exceeded at an acceleration of 0.5 rad/s^2 . This results in the MLS thread skipping. Thread skipping may not be a problem, as it is only the magnetic fields being kipped (analogue to how the Snapper operates, repeatedly kipping the magnetic coupling), until the load is reduced below the stall force. However, due to the sinusoidal shaped kipping-force, high vibrational loads may be introduced. To avoid this, the lead is increased to 25 mm to lower the inertial load. This results in rotor speed of 1200 rpm at 0.5 m/s , and a gearing ratio $\gamma_g = 593$. Adding a generator inertia of $J_{\text{Gn}} = 0.25\text{ kgm}^2$, this gives the following set-up:

$$\begin{aligned} \text{Reflected inertia:} & \quad (J_{\text{MLS}} + J_{\text{Gn}})\gamma_g\dot{\omega}_{\text{arm}} = 1.94\text{e}6\text{ kgm}^2 \\ \text{Inertial load:} & \quad \tau_{\text{MLS,J}} = (J_{\text{MLS}} + J_{\text{Gn}})\gamma_g\dot{\omega}_{\text{arm,peak}} = 1611\text{ Nm} (\sim F_{\text{MLS}} = 409\text{ kN}) \\ \text{Natural frequency:} & \quad \omega_{\text{C5}} = \sqrt{\frac{k_{\text{res}}}{J_{\text{add}} + J_{\text{mech}} + (J_{\text{r}})\gamma_g^2}} = 1.48\text{ rad/s} \Rightarrow T_{\text{C5}} = 4.24\text{ s} \end{aligned}$$

Hence, the MLS is now able to handle the inertial load. The next aspect is whether the MLS is simultaneously able to handle the generator applied torque to extract energy. If the generator mainly provides a damping torque ($\propto \omega_{\text{arm}}$), this will be 90° out of phase with the inertial load ($\propto \dot{\omega}_{\text{arm}}$), hence when the acceleration is at highest, the applied generator torque will be zero. This would be true for the linear damping WPEA, and with the lowered natural frequency due to the inertia load, it may be possible, that the generator may be operated more as a linear damper, while maintaining adequate energy extraction.

6.3.3 Power Production with MLS

To evaluate power production with the MLS, linear damping and OCIR control have been evaluated. The OCIR control has a tendency to use a high torque load at zero velocity, which is undesired for electrical machines, as a high current is required while

producing no power. To avoid this for increasing generator performance, the control has been modified such that the generator may first load above 150rpm. The generator is furthermore controlled such that it may not load above the available kip-force of the MLS:

$$|\tau_{Gn}| \leq F_{\text{stall}} - \left| \omega_{\text{arm}} \gamma_g (J_{\text{MLS}} + J_{\text{Gn}}) \frac{1}{D_{\omega, \text{MLS}}} \right| \quad (6.24)$$

The power matrices are shown in Tab. 6.6 comparing linear damping and OCIR control for a PTO with and without the reflected inertia of the MLS. Due to the lowering of the natural frequency, the linear damping strategy performs very well for the MLS. If the OCIR WPEA is applied, the performance is further increased. However, the OCIR control without the MLS inertia actually performs better, even though this is a restive strategy. Thus, it may be concluded that with less inertia, the PTO may better manipulate the absorber response.

Table 6.6: Power matrices of average extracted power [kW] for MLS PTO.

Normal PTO with $t_{\text{PTO,max}}=1.2$ MNm					MLS PTO with $t_{\text{PTO,max}}=1.2$ MNm and added inertia						
Linear damping:		T_{02} [s]				Linear damping:		T_{02} [s]			
		3.5	4.5	5.5	6.5			3.5	4.5	5.5	6.5
H_{res} [m]	0.75	2.4	2.6	0.65	0.37	H_{res} [m]	0.75	2.8	4.1	3.6	1.2
	1.25	6.7	7.3	7.2	6.8		1.25	8.3	11.5	10.1	9.0
	1.75	13.0	14.3	14.1	13.3		1.75	16.5	22.4	19.8	17.1
	2.25	21.6	23.7	23.2	21.7		2.25	27.2	36.4	32.2	27.3
	2.75	32.2	35.2	34.0	31.7		2.75	40.9	52.7	46.9	39.3
OCIR:		T_{02} [s]				OCIR:		T_{02} [s]			
		3.5	4.5	5.5	6.5			3.5	4.5	5.5	6.5
H_{res} [m]	0.75	4.1	6.5	7.4	7.3	H_{res} [m]	0.75	3.3	4.7	4.5	3.7
	1.25	11.0	15.3	16.2	15.6		1.25	9.7	13.3	13.0	11.7
	1.75	20.5	25.9	26.2	23.3		1.75	18.6	23.7	23.6	21.1
	2.25	31.8	37.9	37.2	34.3		2.25	29.3	36.7	34.7	28.8
	2.75	44.6	51.2	49.1	44.3		2.75	41.3	52.7	47.2	41.0

To simulate the performance of the MLS PTO, a simplified dynamic model of the MLS PTO has been made. An overview of the model content is shown in Fig. 6.28. The k_{MLS} describes the force of the MLS given as the relative linear displacement of rotor and translator, and B_{MLS} is a small damping coefficient to stabilize the coupling. As the MLS will be processing a lot of reactive power due to the inertial load, this will generate a loss. To investigate this issue, the MLS has been given a friction, which is defined to always give a loss of $1 - \eta_{\text{MLS}}$ of the instantaneous power between the MLS and float arm.

To investigate the generator performance, an efficiency map has been found of a 150kW permanent-magnet motor/generator for hybrid auto-mobile Fig. 6.29a. The shown efficiency is in generator mode, including inverter. The motor is designed for a higher speed range, where the generator sought in this evaluation should be rated for about 1200rpm with top-speed of 2000rpm. To give a peak damping torque τ_{PTO} of 1MNm, the generator must produce 1600MNm, which at 1200rpm corresponds to a peak power

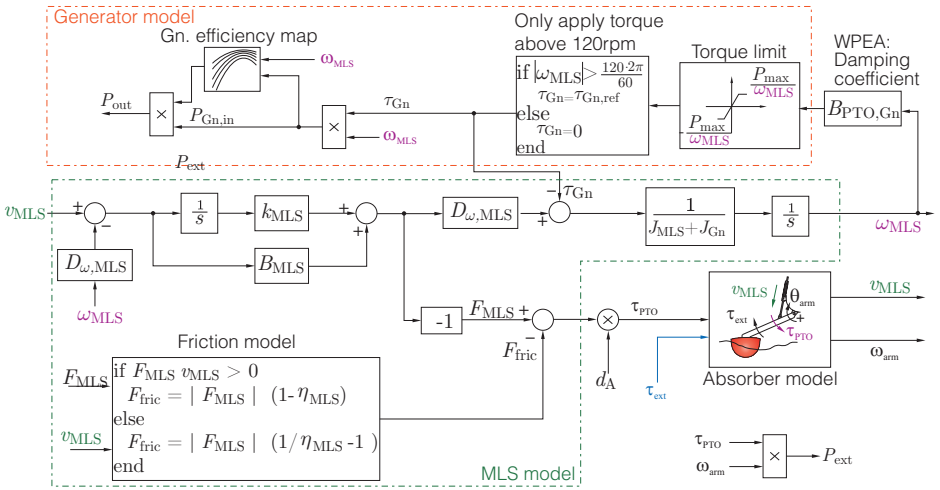


Figure 6.28: Model for evaluation of the MLS concept.

of 200kW. If 100% overload is allowed as in Fig. 6.29a and 1200rpm is the rated speed, the rated power is 100kW.

The efficiency map of Fig. 6.29a has been fitted in MATLAB to give the surface in Fig. 6.29b. The speed and power have been scaled to a rated speed of 1200rpm and 200kW peak power. Thus, a generator as in Fig. 6.29b is imagined available for the design.

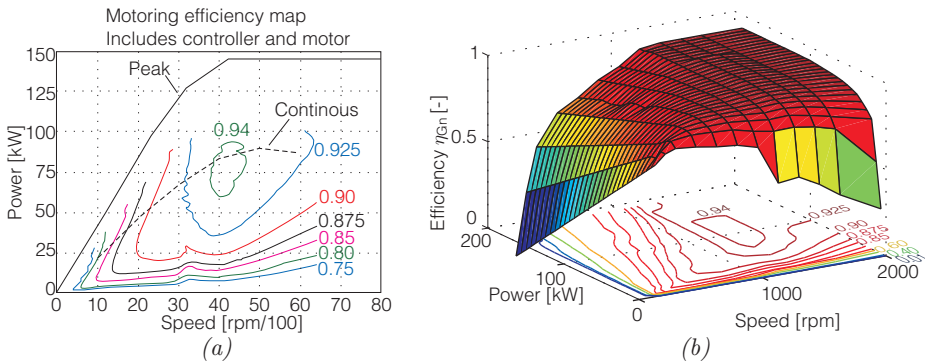


Figure 6.29: In (a) an efficiency map for PowerPhase145 by UQM [251]. In (b) the efficiency map used for generator evaluation.

Additional parameters for describing the MLS are listed in Tab. 6.7. The conversion efficiency from mechanical power input to shaft output of the MLS is assumed to be 0.95. Simulations for the sea states in Tab. 6.8 have been performed, with trajectories for the second sea state seen in Fig. 6.30. The MLS drives the generator up to 1500rpm

in the shown interval. Torque wise, it is interesting to see that despite the inertial load is using most of the available torque (1990Nm), there is plenty of room for loading with the generator due to the 90° phase-shift between inertial and damping load. The total torque load of the MLS τ_{MLS} is only about 10% higher compared to the peak values of inertial and damping loads.

The average efficiencies of the generator $\bar{\eta}_{\text{Gn}}$ and the MLS PTO as a whole $\bar{\eta}_{\text{tot}}$ are listed in Tab. 6.7. The total average efficiency is about 0.80 (excluding grid inverter) and the generator operates around 0.85. The efficiency will be a bit lower, as the used efficiency map of MLS and generator does not incorporate the aspect of possible idle losses of generator/inverter, and Coulomb like losses in the MLS, which may dominate the low power regime.

Overall, if the MLS may be designed with a efficiency of 0.90 from linear input to shaft output, and the a generator with the performance in Fig. 6.29b, the PTO is found to be a very good solution. One issue is that the solution thus not incorporates power smoothing, i.e. the output power looks like the bottom-graph of Fig. 6.30.

k_{MLS}	1.2e10 N/m	B_{MLS}	1.2e8 kg/s	η_{MLS}	0.95 Nm
------------------	------------	------------------	------------	---------------------	---------

Table 6.7: *MLS constants used.*

Table 6.8: *Simulation results of the MLS PTO.*

	$\bar{\eta}_{\text{Gn}}$	$\bar{\eta}_{\text{tot}}$	\bar{P}_{ext}	\bar{P}_{out}
Sea state: $H_{\text{m}0}=1.00\text{ m}$, $T_{0,2}=3.5\text{ s}$	0.839	0.785	5.13	4.027
Sea state: $H_{\text{m}0}=1.75\text{ m}$, $T_{0,2}=4.5\text{ s}$	0.881	0.831	22.83	18.97
Sea state: $H_{\text{m}0}=2.50\text{ m}$, $T_{0,2}=5.5\text{ s}$	0.852	0.80	39.91	32.06

6.4 Choice of PTO for Further Investigation

Overall, the DDC PTO is viewed as being the best suited PTO according to the feasibility study. The concept allows incorporating accumulators without extra components and allows operating 20 absorbers with only a few main generators. The DDC may be implemented at sufficient low loss with tested standard components, which gives potential of high reliability. Control-wise, the DDC is inheritable a four-quadrant system, where reactive power only travels between cylinder and accumulators. Thus, the DCC may implement reactive control, which is viewed as a strength, as this is an documented strategy at Wavestar. A concern of the DCC is the mechanically load induced by the discrete force control of DCC. Thus, to ensure compliance of the mechanical system, a detailed dynamical mapping of the mechanical system should be performed as a part of the DDC design to avoid exciting the structural Eigen-frequencies. This is left for future work. However, discrete force control is also being introduced in the mobile hydraulic sector (Back-hoe loaders, forestry forwarders, etc., [252]), thus mechanical compliance is achievable, as these DDC-units replace the current cylinders.

The MLS PTO is viewed as being a very unique PTO solution, especially for single

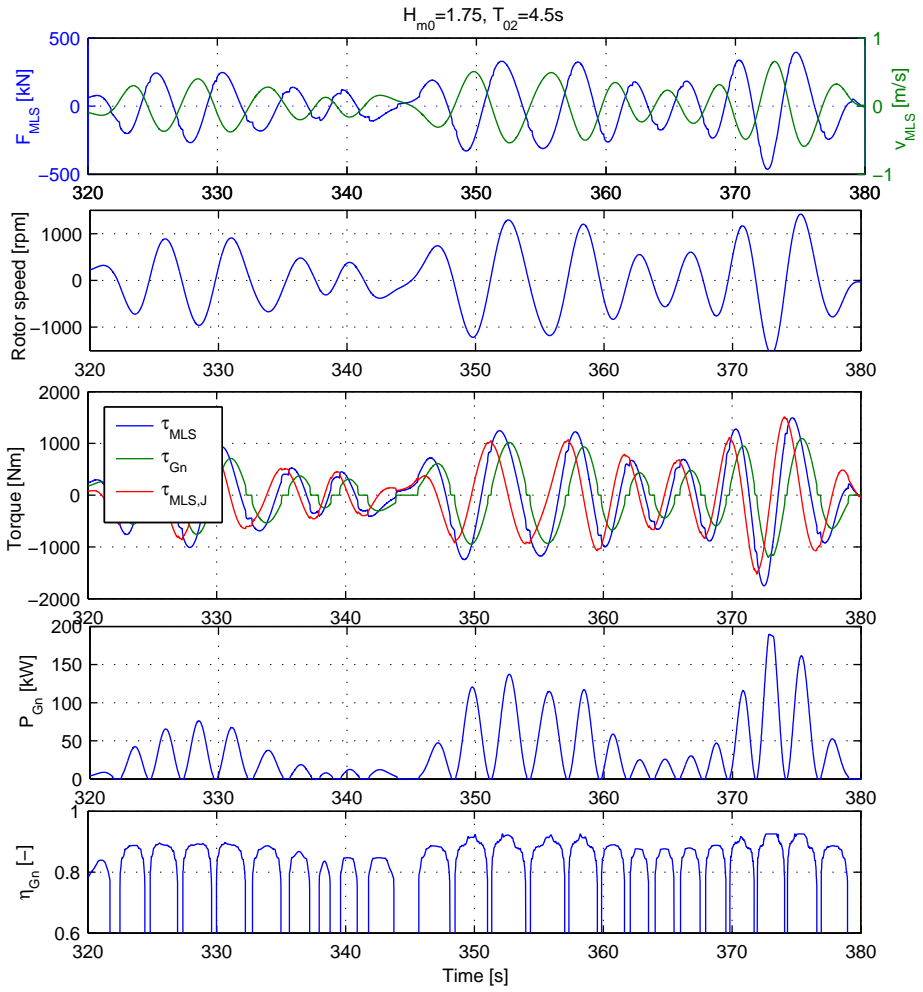


Figure 6.30: Simulation of the MLS PTO.

absorbers, as its outer appearance resembles a simple compact cylinder, having a three phase AC power output. Concept wise, the force density and magnetic layout has already been proven through the 17kN prototype. Future work is required on ensuring the lifetime of the mechanical design and improvements. A drawback of design is only allowing power smoothing through electrical means, e.g. super-capacitors. Control-wise, the inertia load of the MLS may be solved by integrating it into the control strategy.

The DDPM based solutions are also highly attractive and resemble known hydro-static transmission solutions, where the main difference is shifting to a DDPM pump/motor. To use accumulators, separate DDPM pump/motors are required. If the generator is designed for the average power of an absorber, e.g. 50kW, and the peak power is 200kW then the DDPM for the accumulator has to be rated for 150kW, while still requiring the cylinder connected DDPM to have a rating of 200kW. To reduce the DDPM overhead, four absorbers may be configured to operate separate DDPM slices on a common shaft with one generator. An issue with the DDPM solution is that the motor types are not commercially available yet.

Based on this evaluation, the DDC is chosen for full design and full simulation with 20 absorbers. A prototype for a single absorber is also implemented and tested in Chapter 8.

Design and Validation of DDC PTO System

Design and simulation of a complete DDC based PTO system for a 20 float Wavestar C5 is performed in paper [A]. The paper presents a complete PTO system for a 20 float Wavestar, which is rigorously modelled from incident waves to the electric output to grid. The paper employs the 20-float hydro-dynamic model of the C5 presented in Ch.2. The resulting model of +600 states is simulated in different irregular seas, showing that power conversion efficiencies from wave to grid above 70% is achievable for both small and large waves.

An overall description of the PTO layout is presented in this chapter, along with a modelling overview, PTO control design and simulation results. The chapter is based heavily on paper [A].

7.1 PTO Layout

The PTO concept is illustrated in Fig. 7.1 for a 20 float Wavestar with 5m diameter floats. As seen in Fig. 7.1a, each float arm is equipped with a Discrete Displacement Cylinder (DDC)-system, consisting of a multi-chambered cylinder with integrated shifting manifold, controlling the resulting force F_{PTO} . These cylinders provide independent force control of the floats. All cylinders supplies oil flow into common pressure line system, consisting of three pressure lines:

- Low pressure line p_L : 10 bar-30 bar
- Mid (intermediate) pressure line p_M : 70 bar-170 bar
- High pressure line p_H : 150 bar-320 bar

These pressure line runs through the length of the Wavestar WEC, thereby collecting all the extracted power into a common hydraulic energy storage. Hydraulic motors and generators convert the stored hydraulic energy to electricity. In this way the complicated wave power extraction process and the electricity generation becomes decoupled.

7.1.1 Hydraulic Motors and Generators

Four main pairs of hydraulic motors and generators are placed on the high pressure line for power generation. These generators are strategic distributed across the Wavestar

WEC (at float row 2, 5 and 8) to minimise pipe losses. Two parallel generators are placed at float row 5 for extra generator capacity in the centre of the system during high energetic sea states. Each motor and generator pair consist of a 160kW asynchronous generator driven by a $250\text{cm}^3/\text{rev}$ hydraulic bent-axis motor, operating the generator at a maximum torque of 1193Nm at the delta pressure of 300bar.

At each generator point a storage battery of gas loaded hydraulic accumulators is placed. These accumulators perform short terms energy storage for smoothing the extracted wave power. The size of the storage may be increased as desired to meet the required smoothing level.

As the pressures in the lines are only slowly varying due to the accumulators, the torque produced by the motors will also be slowly varying, thereby driving the generators with a very constant load. To adapt to the overall variation in power input from the waves during a sea state, the speed of the generators is controlled using a converter. Each set of generator has its own converter, allowing speed control of the generators while feeding 690V at 50Hz to the grid. During less energetic seas, different combinations of generators and converters may be closed down, such that only the required number of generators is operating.

7.1.2 Pressure Line System and Accumulators

Power generation is performed from the high pressure line, having the largest storage capacity. The hydraulic motors extract power from the high pressure line and delivers flow back to the low pressure line in a closed-circuit manor. The low pressure line is pressurised up to 20 bar to avoid cavitation in the cylinders during pressure shifting. The hydraulic motors are fixed displacement bent-axis motors, whose efficiency is up to 95%.

To filter the oil in the closed-circuit system and replenish flow leakage, a charging pump is installed, feeding flow into the low pressure line.

As earlier discovered, an intermediate pressure is introduced for increasing the efficiency of the DDCs.

For power smoothing and stabilising pressure lines, batteries of gas loaded hydraulic piston accumulators are placed on each line. To have a good utilisation of the accumulators, the pressure lines are varied with minimum a factor of two between minimum and maximum pressure. At these conditions a 50L piston accumulator is able to store about 23L oil. Thus, a battery of 12 may store 276L of high pressure oil, which may keep a $250\text{cm}^3/\text{rev}$ motor running at 1000RPM for more than one minute.

7.1.3 DDC-Module - Multi-chambered Cylinder with Manifold

The core technology for enabling the PTO concept with common pressure lines was the throttle-less force control of the cylinder. The cylinders in Fig. 7.1a are shown in Fig. 7.1b. The used cylinders have three active chambers, where each chamber may be connected to either low, mid or high pressure. As the piston areas of the chambers varies in size, $3^3 = 27$ different resulting forces F_{PTO} may be generated as illustrated in Fig. 7.1d.

DDC PTO for Wavestar 20 float C5-concept:

- DDC-modules on each floats
- 3 common pressures lines for all floats:
 - High pressure
 - Intermediate (Mid) pressure
 - Low pressure
- 4 generators ~ 4x160kW.
- 4 fixed displacement bent-axis hydraulic motors ~ 4x250cc ($\eta=95\%$)
- Accumulators may be added as required for power smoothing
- 27 discrete forces available in DDC for control.
- Up-to $\pm 500\text{kN}$ may generated at each DCC (300bar)
- Generator speed controlled using inverters to adapt to overall available wave power
- Generators and motors sets may be disengaged during low energy sea conditions
- All components are within machine main tube

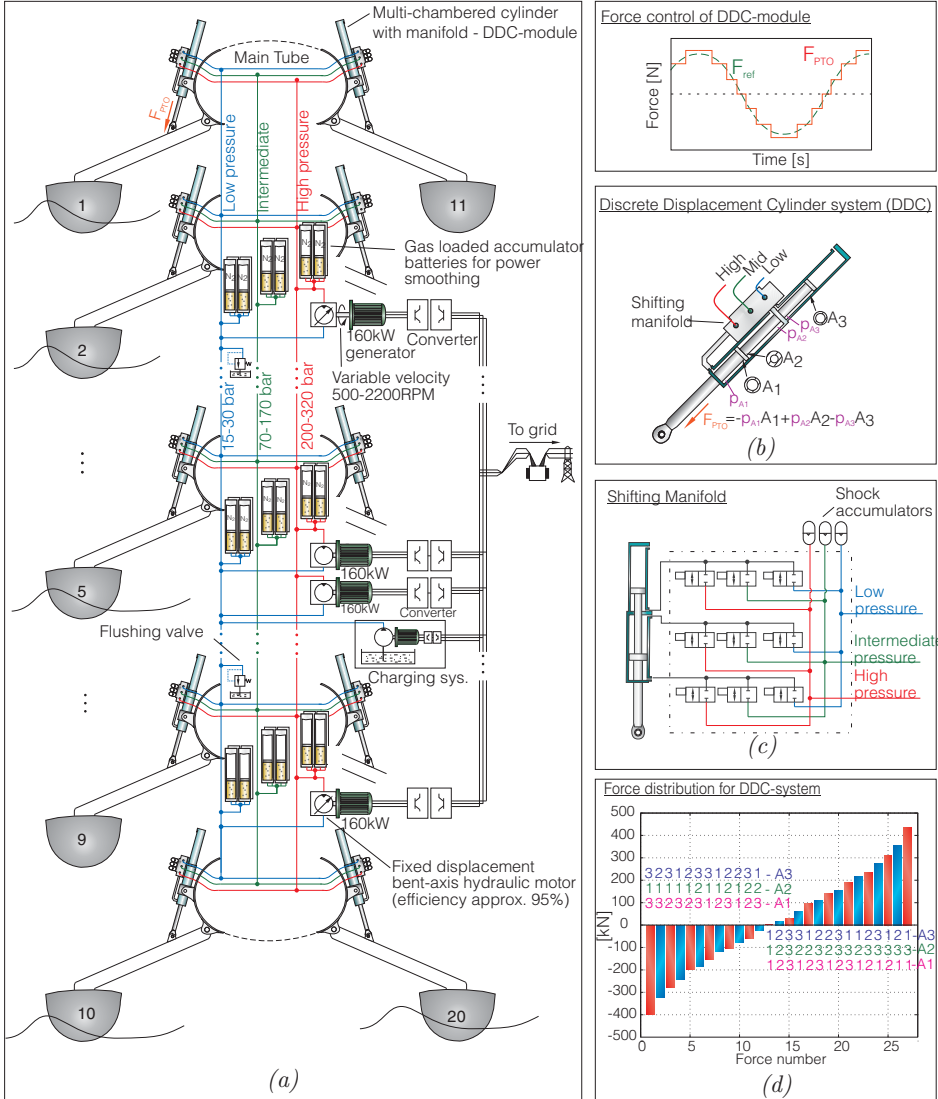


Figure 7.1: From [A]. In (a) an overview of the PTO concept for the Wavestar WEC. In (b) the DDC-system, consisting of a multi-chambered cylinder with integrated shifting manifold for discrete throttle-less force control. In (c) a sketch of the shifting manifold and in (d) the illustration of the 27 available forces.

The stroke of the cylinder is 3 m. To perform the shifting between pressures within the chambers, a shifting manifold as in Fig. 7.1c with nine fast on/off valves is used (15 ms response time.). The pressure drop across the valves is low, i.e. less than 3 bar at steady state flow.

The manifold is directly mounted on the cylinder to reduce volume (compression losses) and to reduce line transmission phenomena in the connections between manifold and chambers. The DDC-system shifts force approximately every 400 ms. To supply/consume the short flow pulses required for compression or decompression of the volumes, small accumulators are mounted directly on the DDC-manifold.

An important feature of the DDC-system is to be able to process extreme power levels with low losses, as the cylinder chambers are directly connected to the pressure lines when in a given force configuration. At low power levels, the flow losses are even relative lower. The compression losses are more or less constant, becoming more dominant at lower power levels. To this end, the pressure levels are reduced at low energy seas to maintain efficiency, as the high forces are not required under these conditions.

Another important feature of the PTO concept with the DDC-modules is to always be able to reduce the load force independent of the float velocity. In this way, the WEC may always reduce the power absorption of the floats if full load capacity is reached, similar to wind turbine pitching out of the wind.

Regarding control of the floating intermediate pressure line, it was shown in Sec. 6.2.1 that naturally, the net-flow into the intermediate pressure line close to zero. Thus, only a small amount of control is added to the DDC-system, guaranteeing that the net-flow into the mid pressure system is zero over time.

7.2 Modelling Overview

An overview of the modelled sub-systems is seen in Fig. 7.2. These are treated in the shown order. The derived equations are implemented in Matlab/Simulink[®] and solved with a Runge-Kutta solver, running at a fixed step time of 0.5 ms.

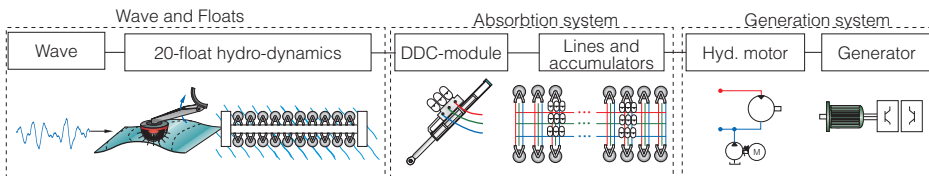


Figure 7.2: Modelled sub-systems of the Wavestar WEC and PTO system.

The wave model is implemented using the white noise method. The 20 absorber model is as described in Sec. 2.4, taking into account the dispersion and the diffracted wave field of the 20 absorbers. The cross radiation is however omitted as it considered to mainly influence the WPEA aspect, than validation of the PTO, which is the focus of the paper.

A complete hydraulic model is implemented, with flow continuities, valve dynamics, hose and fittings losses, accumulator thermal losses and hydraulic motor losses. Furthermore, transmission line models are included instead of modelling volume as purely capacitive. The line dynamics are included as these may be excited due to the fast shifting transients.

Models of bent-axis motor and a simplified generator model are also included. The inverter losses are describes as a power dependent efficiency map.

7.3 Control of a 20 Absorber PTO

The overall control structure is shown in Fig. 7.3. As WPEA the causal reactive control in Sec. 4.2.1 is utilised. The reactive control is utilised as the reactive power only travels between cylinder and accumulator, and have verified performance for the Wavestar WEC. Thus, given the sea state and PTO efficiency information ($H_{m,0}, T_p, \eta_{PTO}$) the force reference to the cylinder is calculated as,

$$F_{ref} = \gamma \left(B_{PTO}(H_{m,0}, T_p, \eta_{PTO}) \dot{\theta}_{arm} + K_{PTO}(H_{m,0}, T_p, \eta_{PTO}) \theta_{arm} \right) \frac{1}{d_A(\theta_{arm})} \quad (7.1)$$

where γ is a coefficient which the system control may use to reduce the power absorption if the pressure lines are saturated.

To make the DDC track the WPEA generated force reference, the force shift algorithm presented in Sec. 6.2.1 is applied, choosing the most efficient within an allowed band of the reference.

The shifting loss from shifting from force x to y is found summing the losses Eq. (6.3) for pressure changes in the individual volumes:

$$E_{shift}(x, y) = \frac{1}{2} (p_{A1,old} - p_{A1,new})^2 \frac{V_{A1}(x_c)}{\beta} + \frac{1}{2} (p_{A2,old} - p_{A2,new})^2 \frac{V_{A2}(x_c)}{\beta} + \frac{1}{2} (p_{A3,old} - p_{A3,new})^2 \frac{V_{A3}(x_c)}{\beta} \quad (7.2)$$

Note that the pressures $p_{Ax,old} = p_{Ax,new}$ may be equal, as the pressure is not necessarily shifted in all chambers.

When a force shift is initiated, the control sends out a matrix \mathbf{u}_c of control values for the nine on/off valves, corresponding to the desired pressure configuration. Regarding valve timing, it was found in [E] that a small amount of overlap between opening and closing of the valves for a single volume was desirable, thus a 3ms overlap is used. As the valves have 12ms opening and closing time, the signal to the opening valve is delayed 9ms. This is illustrated in Fig. 6.13c.

The purpose of the system control is to:

1. Avoid the high pressure accumulator storage from depletion or saturating.
2. Keep the intermediate line floating between high and low pressure.

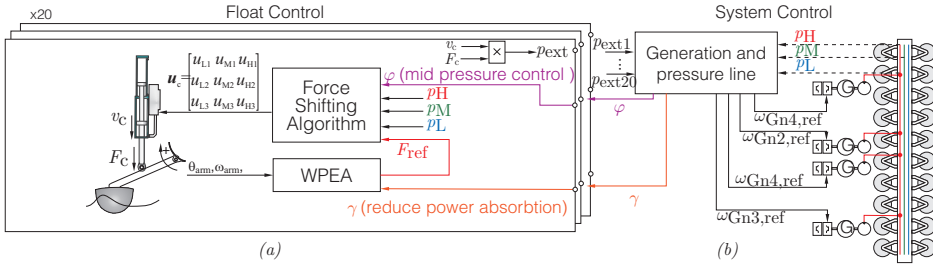


Figure 7.3: Control structure for PTO on C5.

3. Ensure a steady power production as possible while satisfying 1 and 2.
4. Choose the proper number of generators for a given sea state.
5. Reduce power absorption when full load capacity is reached.

To control the pressure in the intermediate pressure line, the force shifting control continuously identifies the force combinations that would currently supply or consume flow from the mid pressure line. For these configurations an “artificial” energy loss φ is added in Eq. (7.2) by the system control to either penalize supplying or consuming flow from the mid pressure line.

To maintain a stable power production, the generators are set to initially produce the expected average power $p_{avg,expected}$ in the current sea state. An initial guess is given based on the current sea state when starting production, where-after a moving average is used based on the absorbed power over a window of 5 minutes. The number of active generators k_{GN} is then chosen, such that generation capacity is roughly $p_{avg,expected}$ plus 30%. All active generators are operated at the same speed ω_{GN} .

To avoid the high pressure accumulator storage from depleting or saturating, the power generation is increased or decreased based on the pressure in the accumulators. This is performed through the coefficient ψ . The speed reference is then given as ω_{GN} ,

$$\omega_{GN,ref} = \frac{p_{avg,expected} \frac{1}{\eta_{to-Gn}} \psi}{p_H k_{GN} D_M} \quad (7.3)$$

where D_M is the total active motor displacement in $[m^3/rad]$. As $p_{avg,expected}$ is the absorber power, the efficiency from cylinder to power out of the generator η_{to-Gn} is required to calculate the average generator power. The maximum allowed speed is set according to 180kW per generator, which is 15% overload. The lowest speed is set to 400RPM.

The high pressure is set to be between 150 bar and 300 bar, thus the map in Fig. 7.4 for ψ is used. Finally, if pressure is still reaching 300 bar the value γ is manipulated, such that the float reduces power absorption, see Fig. 7.4. This is similar to turbines pitching out of the wind when rated production is reached.

The mid pressure is to be floating between high and low pressure for optimising the DDC efficiency. Hence the “reference” $p_{M,\text{ref}}$ for the mid-pressure line is,

$$p_{M,\text{ref}} = \frac{p_H + p_L}{2} \quad (7.4)$$

Based on this, the penalty value φ is set according to Fig. 7.4.

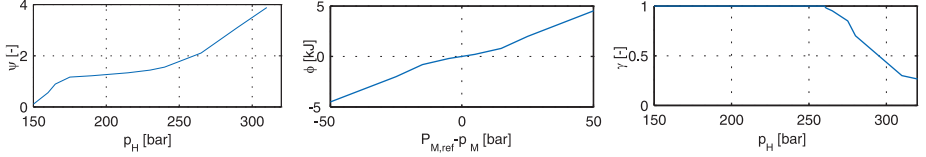


Figure 7.4: Maps for the different system control parameters ψ , φ and γ .

7.4 Simulation Results

The modelled PTO system is evaluated for the three sea states, corresponding to small, medium and high production cases respectively. The results are shown for an incoming wave angle of $\theta_w = 0^\circ$. The PTO performance is nearly independent of wave direction, as the accumulators handle the wave-to-wave power fluctuation.

First, the PTO is overall evaluated for the three sea states. Afterwards, the cylinder force tracking and control performance is inspected.

Simulation for a medium sea state is given in [A] and shown in Fig. 7.5. All four generators are active, varying speed according to overall power level. The PTO system is capable of smoothing out the varying power absorption using the accumulators, whereby the power output to grid is fairly stable. The storage capacity is almost fully used as the high pressure shows a variation between 160 bar and 300 bar. The system is capable of completely absorbing the 10 seconds long 2MW peak while maintaining a steady production around 400kW. This demonstrates one of the important properties of the PTO.

Inspecting the inter-mediate pressure level, the simulation validates that control is able to balance the intermediate pressure to have zero net-flow.

To evaluate how efficiently the PTO converts the absorbed power, the power input and output of the different sub systems have been integrated during the simulation to identify the sub-system losses.

$$P_{\text{in,avg}} = \frac{1}{t_{\text{end}}} \int_0^{t_{\text{end}}} P_{\text{in}}(t) dt, \quad P_{\text{out,avg}} = \frac{1}{t_{\text{end}}} \int_0^{t_{\text{end}}} P_{\text{out}}(t) dt, \quad \eta = \frac{P_{\text{out,avg}}}{P_{\text{in,avg}}} \quad (7.5)$$

The system is divided as shown in Fig. 7.6. To take into account the difference in stored energy before and after is then mapped into an equivalent average power input $P_{\Delta\text{init}}$ to the pressure line system.

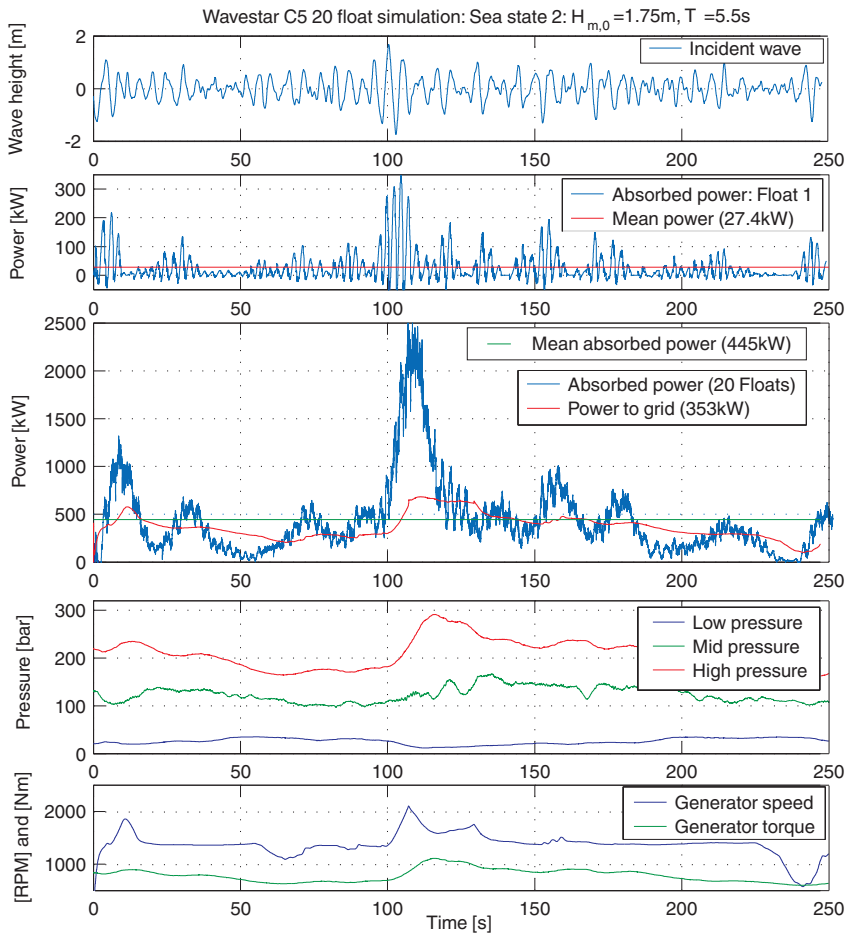


Figure 7.5: PTO simulation results for Wavestar C5 for sea state 2 from [A].

The results are summarised in Tab. 7.1 for the different sea state, showing the average power inputs and outputs. The total PTO efficiency η_{tot} is 70%, 73%, 71% for the three sea states respectively. Thus, despite the varying power levels and a factor 10 between mean and peak power the PTO system is able to maintain efficiency.

The motors and generator all operate around 94% and 95% as expected in the operating conditions. Most important in the results is that the DDC-system is able to maintain an overall efficiency of $\eta_{\text{DDC}} = 90\%$, which is the core technology for enabling the PTO concept. The actual power conversion efficiency is actually higher, as reactive control is being performed, making the average processed power larger than the average input power.

Sea state	DDC-System			Pressure Lines & Accumulators						Hyd. Motors			Generators			Inverters			Total		
	In	Out	Eff.	In			Out			In	Out	Eff.	In	Out	Eff.	In	Out	Eff.	Out	Eff.	
	P_{in}	P_{DDC}	η_{DDC}	P_{DDC}	P_{ch}	$P_{\Delta\text{init}}$	P_{fl}	P_{ac}	η_{ac}	P_{ac}	P_{M}	η_{M}	P_{M}	P_{Gn}	η_{Gn}	P_{Gn}	P_{che}	P_{inv}	η_{inv}	P_{grid}	η_{tot}
SS1	113.6	100.1	0.88	100.1	4.49	17.8	4.00	116.5	0.98	116.5	109.2	0.94	109.2	103.7	0.95	103.7	5.00	103.8	0.95	94.1	0.70
SS2	460.7	416.8	0.90	416.8	5.49	12.45	5.36	415.8	0.97	415.8	389.6	0.94	389.6	372.0	0.96	372.0	6.08	372.0	0.95	347.9	0.73
SS3	747.4	670.2	0.90	670.2	6.0	5.87	6.35	644.5	0.95	644.5	595.5	0.93	595.5	559.3	0.96	559.3	6.66	559.3	0.95	534.8	0.71

Table 7.1: Efficiencies of sub-systems in Fig. 7.6. SS1, SS2 and SS3 abbreviates the three tested sea states.

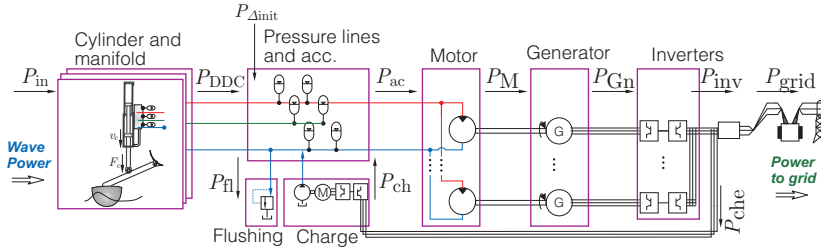


Figure 7.6: Power input and output of the different sub systems.

To inspect the control performance, the operation of the cylinder and manifold of float number 1 is shown in Fig. 7.7. The control tracks the force reference with the discrete steps adequately, and is excellent at not performing extra unnecessary shifts, when the variation in force reference is small, for example at time 160s and at time 166s.

Looking at the pressures within the three chambers, the shifting algorithm optimises efficiency by mostly shifting one pressure at a time and using the mid pressure as an intermediate level. The chamber A2 is the largest chamber, and thereby the most energy expensive to shift. This is seen in the control output, as A2 is the chamber which experiences the lowest number of pressure shifts, whereas the smallest chamber A3 experiences the most pressure shifts.

In the zoom in on the pressure, the shifting transients in pressure may be seen. The fast oscillatory behaviour in the transients are due to the fact that the flow may oscillate between cylinder chamber and manifold accumulator due to the pipe line between valve

and cylinder. These are most pronounced for the A1 chamber, as this chamber has the longest pipe connection, thereby increasing the effect of pipe “inductance”. The slower oscillation in pressures p_H and p_M are likewise caused by flow oscillating between the small manifold accumulators and the large storage accumulator batteries.

In Fig. 7.8 the system control performance is shown. The mid pressure reference $p_{M,ref}$ is set between low and high pressure, and the mid pressure is effectively kept floating around this reference by manipulating the force shifting algorithms. This was implemented by given a penalty for shifting to force configuration which will take the mid pressure father away from the reference. The penalising “energy” input φ to the force shifting algorithms is seen in the figure.

In Fig. 7.8 the temperature variation in one of the high pressure storage accumulator is seen. The process is not isothermal, as the temperature is highly varying, and the process is not purely adiabatic either, as the temperature and pressure do not always return to same initial conditions. Thus the inclusion of heat transfer between accumulator and environment in the model is justified.

Finally, Fig. 7.8 shows how the system control uses the γ input to downscale the aggressiveness of the float absorption, such that high pressure stays below 320 bar.

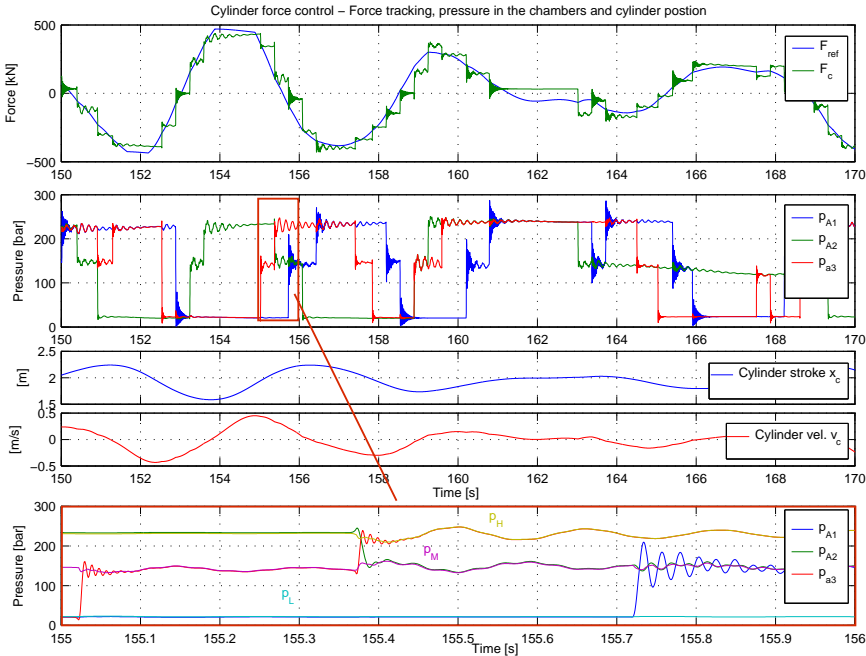


Figure 7.7: Force tracking of cylinder.

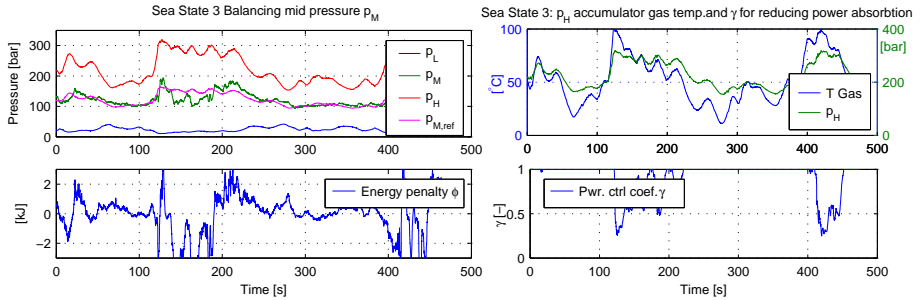


Figure 7.8: Controller performance and gas temperature of accumulators.

7.5 Summary

The design and simulation of the 20 absorber system demonstrates that the PTO-system is capable of solving the following challenges:

- Handle high peak power input while maintaining component efficiency - *the DDC maintains above 90% efficiency, and remaining components are all above 94% in efficiency.*
- Full controllability of applied PTO torque - *the DDC offers 27 force steps and four quadrant mode.*
- Incorporating a short term storage for supplying reactive power - *reactive power is only processed by DDCs and accumulators.*
- Incorporating an efficient energy storage for power smoothing - *the generators are operated independent of the wave absorption. Energy storage installed for operating generators at 1500 RPM for one minute.*
- Maintain PTO efficiency in small waves when operating at 15% of full load capacity - *total efficiency maintained above 70% in all sea states.*
- Be able to reduce power absorption when full load capacity is reached- *the DDCs reduce absorption when the WEC reaches full load.*
- Being scalable to future multi MW systems.

Based on modelling the system from wave-to-wire, the overall efficiency of the PTO was found to be beyond 70% in all sea conditions.

The utilised WPEA was based on causal reactive. The algorithm was tuned to take into account the efficiency of the PTO to maximise electrical power production.

The WPEA determined load force reference was applied using the DDCs mounted on each float. The DDC modules directly convert and store the absorbed wave power as high pressure energy in the accumulators with a loss less than 10%.

An extra intermediate pressure line was added for improved efficiency of the DCC. It was shown that by overall system control the net flow to the intermediate line could be kept at zero, hence extra pumps and motors for supporting this line is not required. The simulations verified that when reaching full load capacity, the system would reduce the power absorption using the DDCs such that full load is sustained, but no extra energy has to be dissipated internally in the system.

Regarding scalability, the DDC-modules are fully scalable to be increased to larger systems. Currently, commercial valves with the required transient opening and closing times (≤ 15 ms) are available with only 2% loss at 1.8 MW and with a peak power level of more than 4MW. This is more than required for e.g. a 6MW Wavestar system with 20 floats. Also, valves may be easily used in parallel, thereby also increasing redundancy. Regarding hydraulic motors, commercial 1000cc high speed motors are available, producing 750kW at 300 bar and 1500RPM. Within the wind turbine industry, hydraulic transmissions are also being investigated, leading to development of fast multi-MW motors with high efficiency, e.g. the DDPMS. These DDPMS may replace the bent-axis motors, leading to the option of operating at fixed generator speed of the 1500RPM, thereby potentially removing the power converters.

The size of the storage may be increased as desired. The storage size is a cost optimisation problem between power smoothness and accumulators cost. Increasing the storage does not reduce the overall efficiency, as the round-trip efficiency of accumulators is around 97%. Instead, increasing storage may increase efficiency and durability, as it narrows/stabilises the operating region of the remaining PTO components, thereby making them operate near their optimum point at a constant load.

Looking at potential improvements, the control of the DDC-modules do not take into account e.g. cylinder velocity and simultaneous shifting of multiple-chambers. The system control may also be improved to better use the energy storage capacity to stabilise and increase energy production. Also, further optimisation on the pressure line network may be performed, reducing pipe losses and improving transient behaviour. Improved hydraulic motor-efficiencies are also obtainable with commercial available components (96% efficiency) and DDPMS.

With the potential improvements, the PTO concept has been assessed to be able to reach about 80% efficiency from mechanical input to electrical output.

Full Scale Test-bench and PTO Prototype

The main technological innovation in the PTO concept is the DDC module. If this design may be tested and verified, the PTO concept as a whole is considered possible. To this end, a full scale DDC prototype has been designed and implemented. To test the 420kN DDC in real wave conditions, a full scale test-bench has been designed and implemented.

This chapter introduces the full-scale test-bench, the prototype PTO and early test-results of the prototype DDC.

8.1 The Prototype DDC

To implement a DDC requires a valve-manifold and a multi-chambered cylinder. An important aspect of the tests is to investigate required valve performance and control hereof. Thus, use of the intended on/off valves will be a hindrance for easy testing of different opening characteristics and response times. Therefore, the TDP32 fast 2/2-proportional valves shown in Fig. 6.22 have been chosen, having opening/closing time of 12ms. These valves may then basically be used to emulate an arbitrary on/off valve characteristic.

Three piston accumulators have been used as the shock absorbing accumulators. To test the primary side or DDC module, the interface of a secondary side is required, consisting of the three pressure lines. Testing the secondary side with generator and bent-axis motor would not make sense, as this first becomes realistic with multiple absorbers supplying the secondary side. Accordingly, a system for emulating the secondary side has been designed instead. The emulation must be able to create three controllable pressure lines, and be able to evaluate the amount of energy transferred between the primary and secondary side of the PTO.

The prototype PTO set-up is illustrated in Fig. 8.1. To handle the generated hydraulic power by the primary side, a closed-circuit variable displacement 250cc pump/motor is placed between high pressure line and low pressure line. The hydraulic motor powers a 90kW generator.

To control the pressure of the mid pressure line, two proportional valves are installed between the lines. To increase pressure in the mid pressure line, flow may be directed from high pressure to mid pressure. To decrease pressure, flow may be directed from mid pressure to low pressure.

To measure the amount of hydraulic power delivered to the secondary stage by the primary stage, flow sensors are equipped where flow exists the pressure lines, either via the hydraulic motor, or by the two proportional valves.

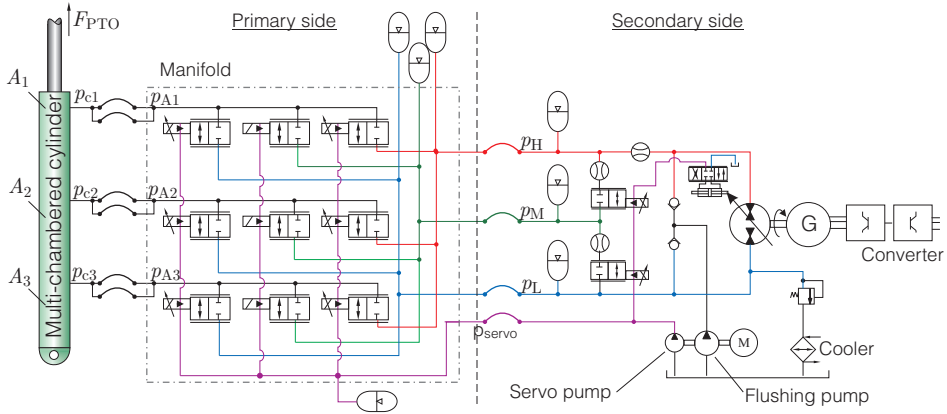


Figure 8.1: Simplified hydraulic diagram of the prototype PTO.

8.2 Full Scale PTO Test-Bench

To test the prototype, a full scale test-bench has been designed and realised (Fig. 8.2), which exerts the PTO cylinder by using another hydraulic cylinder (referred to as the wave cylinder). The test-bench is illustrated in Fig. 8.3.

The test-bench is divided into a wave side and a PTO side. The wave side consists of the hydraulic pump station, wave cylinder and a moving cart with force sensor, connecting the PTO and wave cylinder. The wave side is designed such that it is capable of emulating both wave forces and the float dynamics, achieving that the PTO cylinder will be experiencing the same load characteristics as on the real Wavestar C5 in irregular waves. The wave cylinder has a stroke of 3m and is able to exert a force of 840 kN on the PTO cylinder.

The test-bench is constructed as a steel tube for absorbing the loads of the two cylinders working up against each other. The wave cylinder is flanged mounted on the steel tube and the PTO cylinder is mounted internally in the steel tube. An overview of the different test-bench-components is given in Fig. 8.4.

The hydraulic pump station consists of two variable displacement axial piston pumps (250cc and 125cc). The pumps are driven at a fixed speed of 1500rpm and are controlled to maintain a fixed supply pressure up to 350bar. The wave cylinder is controlled using a high bandwidth 4/3-way valve, enabling control of the fluid into each chamber of the wave cylinder. Using the valve, the differential pressure (thereby the force) of the wave cylinder is controlled. The force reference to the wave cylinder is computed by performing on-line simulation of wave and float dynamics using feedback from cylinder

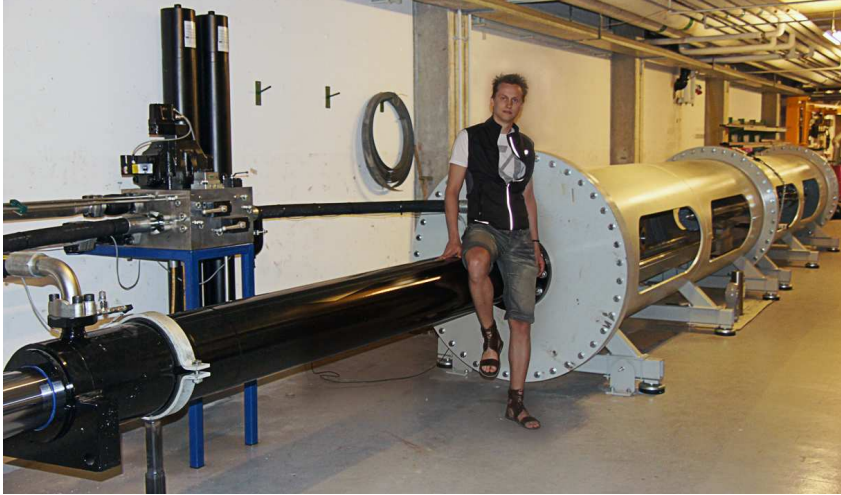


Figure 8.2: The PTO test-bench installed at the Department of Energy Technology, Aalborg University.

position, velocity and force.

For easy access the manifold of the DDC has been mounted external to the tube. This introduces hose connections of 2-4m length from manifold to cylinder, which may give challenges due to the increased line inductance.

8.3 Test-bench Simulation Model

A complete SIMULINK model of the test-bench with PTO has been developed, containing all components. To verify the model, a simple controller is implemented on the wave cylinder control valve (inverse orifice) and is given a sine-wave as reference. The PTO is given some “random” inputs to the on/off valves to load the wave cylinder. The simulation models is applied the same initial condition, the same basic controller and on/off valves input. Comparison of measurements and simulated results is performed in Fig. 8.5 and Fig. 8.6, showing very good agreement.

8.4 Test-Bench Control Design

The problem faced with the control of the test-bench is to get a hydraulic actuated system with only a few 1000kg of mass to emulate the dynamics of an absorber, having a mass moment inertia of $4e6\text{kgm}^2$. The problem would be trivial if the PTO did not excite the un-damped natural frequency of the wave cylinder (around 25Hz), however, the discrete nature of the tested PTO is going to excite these frequencies. As these do not exist in the real absorber, these have to be suppressed by the wave cylinder control.

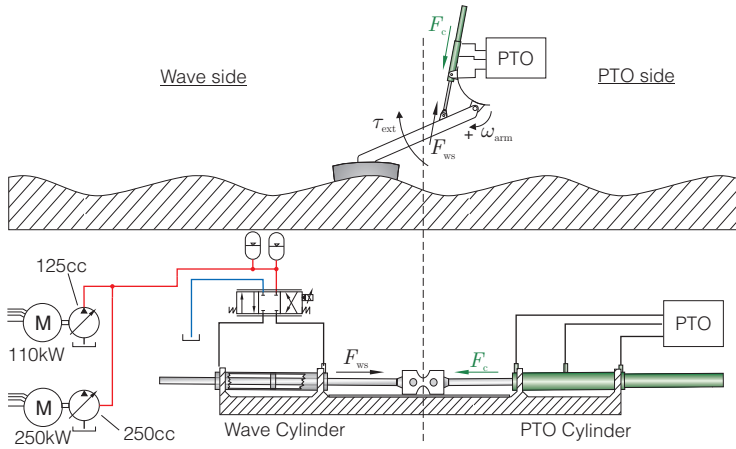


Figure 8.3: Illustration of test-bench.



Figure 8.4: Test-bench components.

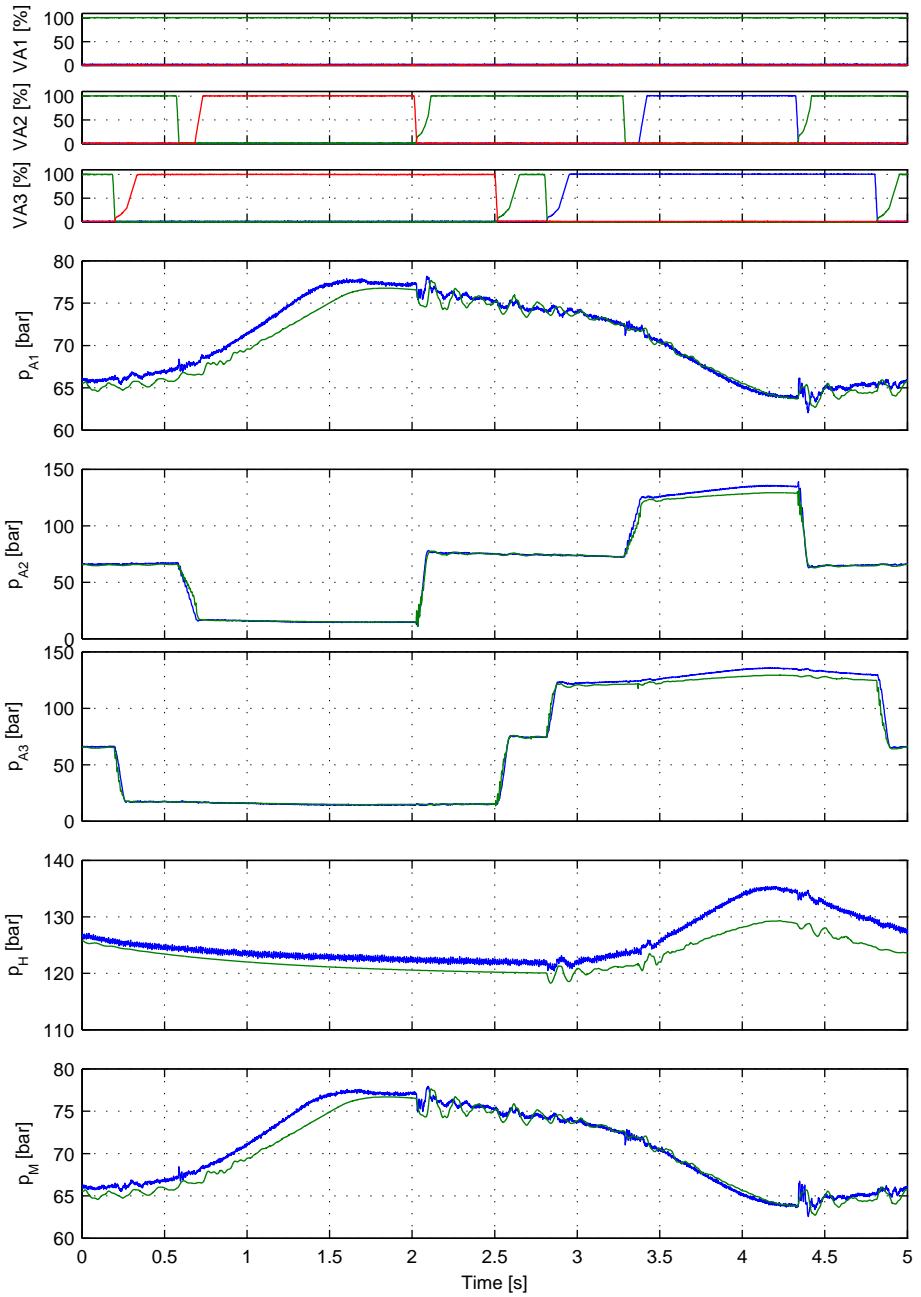


Figure 8.5: Comparison of test-bench measurements (blue) and model output (green) for same initial conditions and valve inputs (continued in Fig. 8.6).

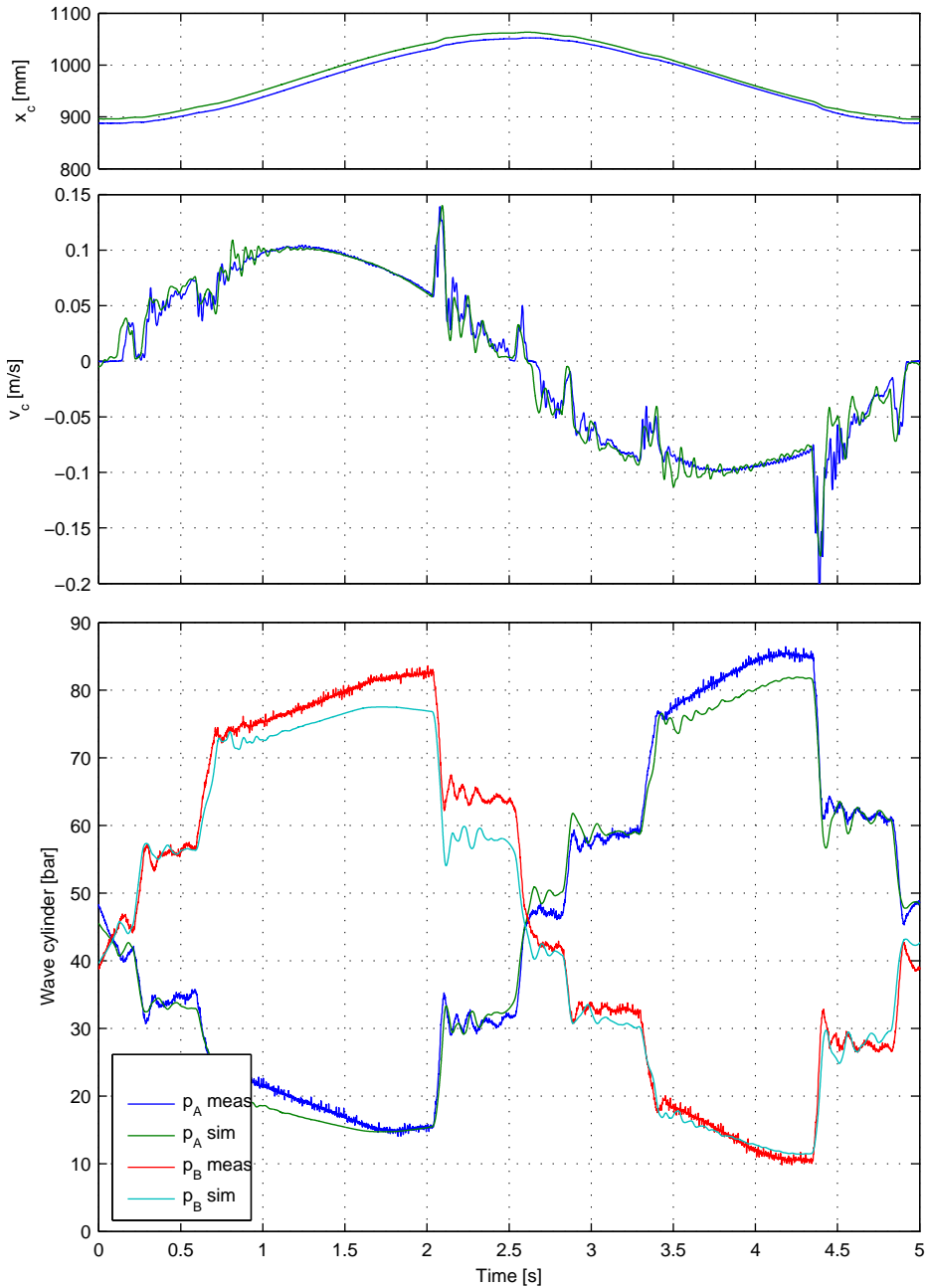


Figure 8.6: Comparison of test-bench measurements (blue) and model output (green) for same initial conditions and valve inputs.

The overall structure of the control is seen in Fig.8.7. An on-line simulation is performed of the absorber dynamics, where an arbitrary irregular wave may be given. The absorber model also reacts on the PTO load using the measured force. The model generates references $x_{c,ref}$ and $v_{c,ref}$, corresponding to correct PTO cylinder movement according to the model.

To control the wave cylinder, two parallel 4/3-way servo valves are used. One large valve P (Parker D111FP) for the main flow and a valve M (MOOG D664) for performing control around zero velocity. The P valve is with 10% overlap, and has a high sensitivity (1000L/min@5 bar). The M valve is used around zero velocity to compensate the dead-band of the P valve and to control at low velocities. Bandwidth wise the valves are similar as seen in the characteristics in Fig. 8.8.

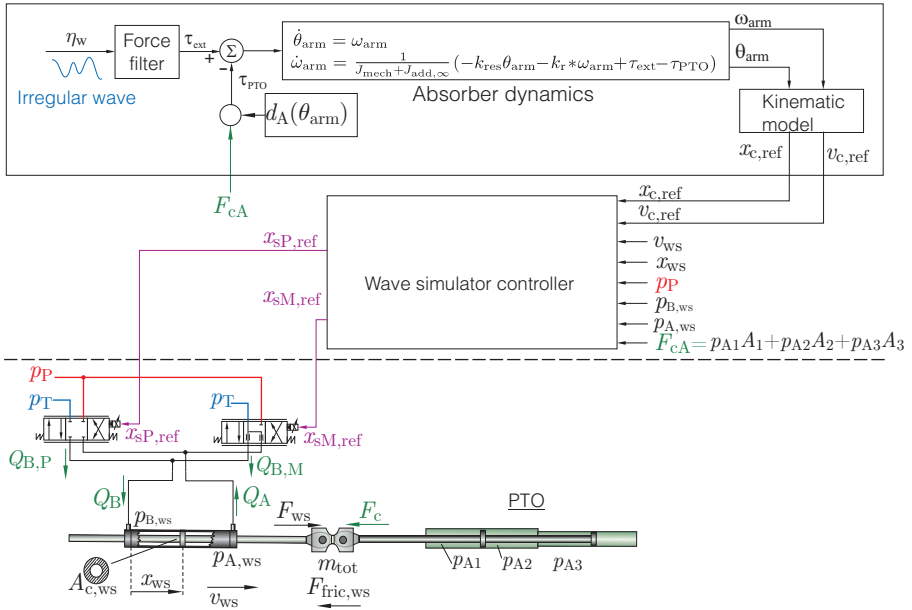


Figure 8.7: Control structure.

To linearise the valves gain, and inverse orifice equation is implemented, such that the controller gives a flow reference Q_{ref} , which based on the pressure difference across the spool Δp is mapped to the required valve area $A_{o,r}$,

$$A_{o,r} = \frac{Q_{ref}}{C_d \sqrt{\frac{2}{\rho_{fluid}} |\Delta p|}} \quad (8.1)$$

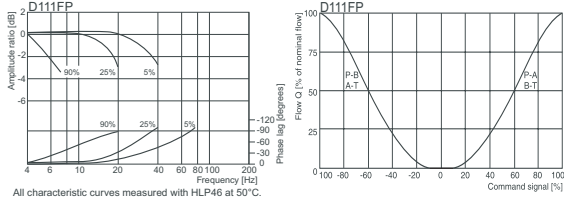
where Δp is the pressure difference $p_P - p_A$ or $p_P - p_B$ depending on the active metering edge.

The valves are operated in parallel, where the total requested valve opening area $A_{o,r}$ is

Parker valve

Catalogue HY11-3500/UK		D111FP
General		
Size		NG32 (CETOP 10)
Hydraulic		
Nominal flow at $\Delta p = 5$ bar per control edge	[l/min]	1000
Max. recommended Flow (Symmetric flow)	[l/min]	3000
Leakage at 100 bar		
Overlapped spool	[ml/min]	1000
Pilot	[ml/min]	< 1000
Pilot supply pressure	[bar]	20...350
Pilot flow, step response at 210 bar	[l/min]	40
Static / Dynamic		
Step response at 100% stroke τ_1	[ms]	45
Frequency response		
Amplitude $\pm 5\%$ at 210 bar	[Hz]	40
Phase $\pm 5\%$ at 210 bar	[Hz]	75

Parker Hannifin GmbH



Moog valve

Model		D364
Rated flow (35bar per land)	[l/min]	100
Max flow	[l/min]	185
Max pressure	[bar]	350
Response time:	[ms]	≤ 20

Figure 8.8: Valve characteristics of used proportional valves.

divided amongst the two valves as,

$$A_{o,M} = \begin{cases} A_{o,r} & ; A_{o,r} < 0.25 \cdot A_{o,M,\max} \\ 0.25 \cdot A_{o,M,\max} (2 - A_{o,M,\max}/A_{o,r}) & ; A_{o,r} \geq 0.25 \cdot A_{o,M,\max} \end{cases} \quad (8.2)$$

$$A_{o,P} = \begin{cases} 0 & ; A_{o,r} < 0.25 \cdot A_{o,M,\max} \\ A_{o,r} - A_{o,M} & ; A_{o,r} \geq 0.25 \cdot A_{o,M,\max} \end{cases} \quad (8.3)$$

where $A_{o,M,\max}$ and $A_{o,P,\max}$ are the maximum opening area of the valves. The above gives a seamless transition between using the M-valve to mainly using the P-valve.

The requested total area of the two valves is then mapped into spool references $x_{sP,\text{ref}}$ and $x_{sM,\text{ref}}$ using the opening characteristics that may be derived from Fig. 8.8.

To remove the dead-band of the P valve, a dead-band compensation $x_{sP,\text{db}}$ is added to the spool-reference, which is ramped up and down based on the sign of the cylinder velocity reference:

$$\dot{x}_{sP,\text{db}} \begin{cases} 20 & ; v_{ws,\text{ref}} > 0.01 \wedge x_{sP,\text{db}} < 9\% \\ -20 & ; v_{ws,\text{ref}} < -0.01 \wedge x_{sP,\text{db}} > -9\% \\ -20 \operatorname{sgn}(x_{sP,\text{db}}) & ; \text{else} \end{cases} \quad (8.4)$$

$$(8.5)$$

Using flow continuity and Newton's second law, the following non-linear state-spate

representation of the wave side is obtained:

$$\dot{x}_s = v_s \quad (8.6)$$

$$\dot{v}_s = -2\zeta_s\omega_{n,s}v_s - \omega_{n,s}^2x_s + \omega_{n,s}^2x_{s,\text{ref}} \quad (8.7)$$

$$\dot{p}_A = \frac{\beta_{\text{eff}}}{A_{c,ws}x_{c,ws} + V_{0A}}(-v_{c,ws}A_{c,ws} + Q_A) \quad (8.8)$$

$$\dot{p}_B = \frac{\beta_{\text{eff}}}{(x_{c,\text{max}} - x_{c,ws})A_{c,ws}x_{c,ws} + V_{0B}}(v_{c,ws}A_{c,ws} - Q_B) \quad (8.9)$$

$$\dot{x}_{c,ws} = v_{c,ws} \quad (8.10)$$

$$\dot{v}_{c,ws} = \frac{-F_{\text{fric},ws} - F_c + (p_A - p_B)A_{c,ws}}{m_{\text{tot}}} \quad (8.11)$$

where the system is modelled as having a single equivalent valve with spool position x_s . As the valves have similar band-width and both are going to be linearised, this is a fair assumption. The spool is modelled as second order dynamics with natural frequency $\omega_{n,s}$ and damping ζ_s . The flows Q_A and Q_B are given by the orifice equation and the opening areas $A_{o,M}$ and $A_{o,P}$.

For control design the above model state-space model is linearised. This is performed by defining the the load pressure $p_L = p_A - p_B$ and load flow $Q_L = Q_A + Q_B$:

$$\dot{x}_s = v_s \quad (8.12)$$

$$\dot{v}_s = -2\zeta_s\omega_{n,s}v_s - \omega_{n,s}^2x_s + \omega_{n,s}^2x_{s,\text{ref}} \quad (8.13)$$

$$\dot{p}_L = -2\frac{\beta_{\text{eff}}}{V_0}v_{c,ws}A_{c,ws} + 2\frac{\beta_{\text{eff}}}{V_0}Q_L \quad (8.14)$$

$$\dot{x}_{c,ws} = v_{c,ws} \quad (8.15)$$

$$\dot{v}_{c,ws} = \frac{-B_{ws}v_{c,ws} - F_c + p_L A_{c,ws}}{m_{\text{tot}}} \quad (8.16)$$

where the cylinder is linearised in centre position, i.e. $V_0 = \frac{1}{2}(V_{0A} + V_{0B}A_{c,ws}x_{c,\text{max}})$. This is also the actual operating point, as the wave cylinder is in centre position when the PTO cylinder is “resting” in calm water. The coefficient B_{ws} is the linearised viscous friction coefficient.

The load flow is given as,

$$Q_L = \begin{cases} x_s A_o C_d \left(\sqrt{\frac{2}{\rho}|p_P - p_A|} + \sqrt{\frac{2}{\rho}|p_B - p_T|} \right); & x_s \geq 0 \\ x_s A_o C_d \left(\sqrt{\frac{2}{\rho}|p_P - p_B|} + \sqrt{\frac{2}{\rho}|p_A - p_T|} \right); & x_s < 0 \end{cases} \quad (8.17)$$

however, due to the symmetry of cylinder and spool, $(p_P - p_B) = (p_A - p_T) = (p_P - p_T) - \frac{1}{2}p_L$ at steady-state, hence

$$Q_L = x_s A_o C_d 2\sqrt{\frac{2}{\rho}|(\bar{p}_P - \bar{p}_T) - \frac{1}{2}\bar{p}_L|} \quad (8.18)$$

where the bar above the symbols indicate operating point value.

To use the fact that the valve is linearised in Eq. (8.1), the control input to the system is redefined to be a flow reference Q_{ref} by letting:

$$x_{s,\text{ref}} = \frac{Q_{\text{ref}}}{A_o C_d 2 \sqrt{\frac{2}{\rho} |(\bar{p}_P - \bar{p}_T) - \frac{1}{2} \bar{p}_L|}} \quad (8.19)$$

The resulting linearised system matrices of $\dot{\mathbf{x}}_{\text{ws}} = \mathbf{A} \mathbf{x}_{\text{ws}} + \mathbf{B} u_{\text{ws}}$ is shown below,

$$\mathbf{A} = \begin{pmatrix} 0 & 1 & 0 & 0 & 0 \\ -\omega_{n,s}^2 & -2\omega_{n,s}\zeta_s & 0 & 0 & 0 \\ \frac{2\beta_{\text{eff}}}{V_o} A_o C_d \sqrt{\frac{2}{\rho} |(\bar{p}_P - \bar{p}_T) - \frac{1}{2} \bar{p}_L|} & 0 & 0 & 0 & -\frac{2A_c \beta_{\text{eff}}}{V_o} \\ 0 & 0 & 0 & 0 & 1 \\ 0 & 0 & \frac{A_c}{m_{\text{tot}}} & 0 & -\frac{B_{\text{ws}}}{m_{\text{tot}}} \end{pmatrix}$$

$$\mathbf{B} = \begin{pmatrix} 0 \\ \frac{\omega_{n,s}^2}{2A_o C_d \sqrt{\frac{2}{\rho} |(\bar{p}_P - \bar{p}_T) - \frac{1}{2} \bar{p}_L|}} \\ 0 \\ 0 \\ 0 \end{pmatrix}, \mathbf{C} = (0 \ 0 \ 0 \ 1 \ 0), \mathbf{D} = 0$$

where the state vector is $\mathbf{x}_{\text{tb}} = (x_s \ v_s \ p_L \ x_{\text{ws}} \ v_{\text{ws}})^T$ and the control input is $u_{\text{ws}} = Q_{\text{ref}}$, which is mapped to a spool position when implemented using Eq. (8.1).

The poles and zeros of the system is seen in Fig. 8.9, showing that the system has an un-damped natural frequency of 13Hz and damping of 0.07. The system should be able to track velocity and position, however the root-locus for applying position and velocity feedback is seen in Fig. 8.10, showing that these will only remove damping until the system becomes unstable.

A_{ws}	0.0236 m^2	V_o	0.04 m^3	p_T	$1\text{e}5 \text{ Pa}$	p_P	$180\text{e}50 \text{ Pa}$
β_{eff}	$6000\text{e}5 \text{ Pa}$	ρ_{fluid}	860 kg/m^3	$\omega_{n,s}$	440 rad/s	ζ_s	0.9
C_d	0.6	A_o	$64.3\text{e}-6 \text{ m}^2$	m_{tot}	2750 kg	B_{ws}	$30\text{e}3 \text{ kg/s}$

Table 8.1: Wave cylinder parameters.

To make the system overall track the reference without relying on feed-back, the cylinder velocity reference $v_{c,\text{ref}}$ may be mapped into a flow feed-forward for the cylinder $Q_{\text{ref}} = A_{c,\text{ws}} v_{c,\text{ref}}$ which gives the steady-state value of the control signal. A “light” position feed-back may then be added, removing the errors in the valve’s realisation of the flow. However, this method will not give any damping of the system’s natural modes, which will be excited by the PTO load.

A root-locus for pressure feed-back is also shown in Fig. 8.10, showing that up till a certain gain, this will improve the damping of the system. However, this feed-back will try to force the pressure difference to zero, which is undesired when applying a load disturbance (the PTO): The system will try to resist giving the required force to

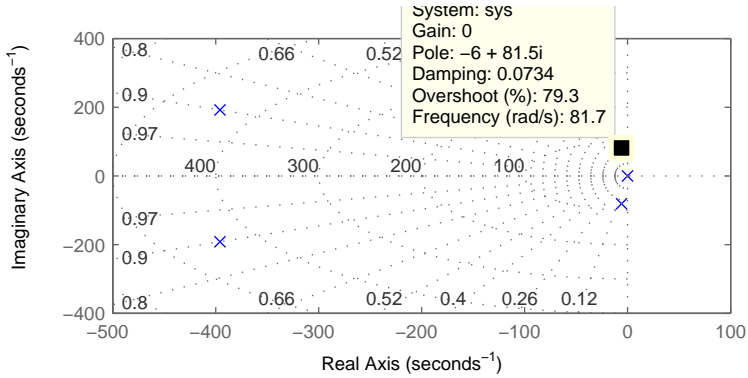


Figure 8.9: Pole-zero map of linearised wave cylinder system.

suppress the PTO load and instead give in to the load and move undesirable (but well damped).

To remove the incorrect steady-state contribution of the pressure feed-back, a high pass filter may be added such that the used feed-back is $p_{L,H}$:

$$p_{L,H} = \frac{s}{s + \omega_{HP}} p_L \quad (8.20)$$

Using this feed-back will still result in the system given into a sudden change in PTO load, as the required change in wave cylinder pressure is being suppressed.

Instead of using Eq.(8.20) it is realised, that the load disturbance is know from the PTO F_{pA} (from pressure measurements in the PTO cylinder), hence, the steady-state value of p_L is known and may be applied as a disturbance feed-forward, such that following should be controlled to zero:

$$\frac{s}{s + \omega_{HP}} \left(p_L - \frac{F_{PTO}}{A_{ws}} \right) \quad (8.21)$$

Accordingly, the control system will both try to dampen the response while controlling the force to match the PTO load, suppressing the PTO disturbance.

To solve the complex control problem, the controller is formulated as a full state-feedback, which is solved based on the Linear-quadratic Regulator design (LQR), which minimizes the following cost function,

$$J = \int \mathbf{x}^T \mathbf{Q} \mathbf{x} + \mathbf{u}^T \mathbf{R} \mathbf{u}^T dt \quad (8.22)$$

where the state-vector in this case is $\mathbf{x}_{tb} = (x_s, v_s, p_L, x_{ws}, v_{ws})$.

As R is a scalar in this case, the value may be set to one, thus the control is solemnly adjusted using the diagonal matrix Q . First only the error in the cylinder position in

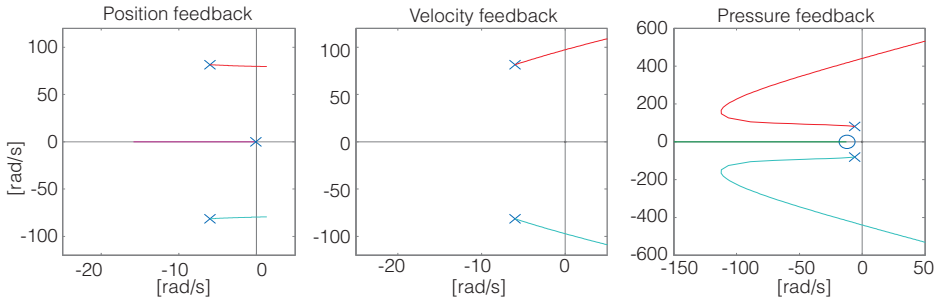


Figure 8.10: Different root-loci for the wave cylinder system.

penalised in the LQR's cost-function to obtain desired position control bandwidth. This is obtained at a weight of 0.08, which is solved in MATLAB ,

$$F = -lqr(A, B, \text{diag}([0 \ 0 \ 0 \ 0.08 \ 0]), 1) \quad (K = lqr(SYS, Q, R))$$

, where the resulting closed-loop poles are given as the eigen-values of $A + BF$. The control gives a bandwidth of 11.6rad/s of the dominating first order pole. The resulting closed-loop poles (green) are seen in Fig. 8.11, where the open-loop poles are blue. The position penalty gives nearly no-additional damping. Resultantly, a penalty on the velocity error is added. Increasing this penalty from 0 to 0.025 at increments of 0.005 is shown in Fig. 8.11, where finally a damping of 0.3 is obtained for the complex-pole pair,

$$F = -lqr(A, B, \text{diag}([0 \ 0 \ 0 \ 0.08 \ 0.025]), 1)$$

and the bandwidth of the position loop is 9.72rad/s, which is still a factor of 5 faster than frequency of the absorber dynamics, which it is going to track. A block diagram of the implemented controller is given in Fig. 8.12, which combines a flow feed-forward with a state-feedback, and where a disturbance feed-forward is used from the PTO side based on measured pressures. A simple observer is implemented to get the spool states.

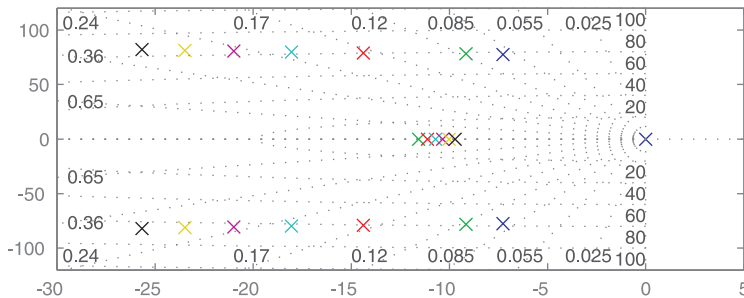


Figure 8.11: Pole location for different state feed-backs. The blue poles are the open-loop system.

Controller tests are shown Fig. 8.13, where a flow-feed forward with a position feed-back is first tested. The system tracks a sine wave while being subjected to discrete force steps

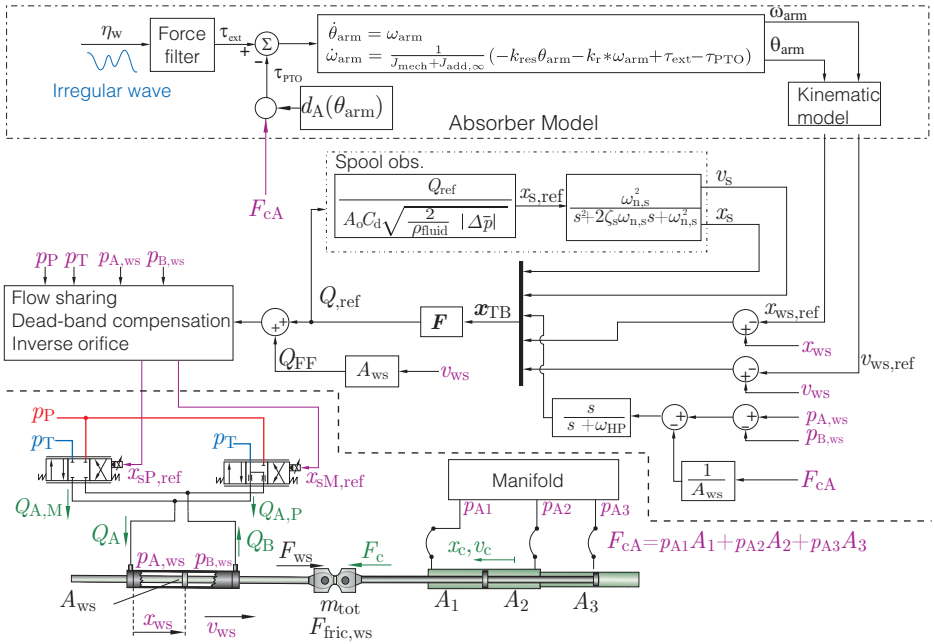


Figure 8.12: Block diagram of test-bench controller.

by the PTO. The simulated and measured response shows very good agreement. The state-feed with no disturbance feed-forward dampens the response, however, the control gives in to the disturbance, as it resists the required pressure change. By adding the disturbance feed-forward to the state-feedback, it retains the damping while suppressing the disturbance. The control has been tuned lightly to give increased robustness of the control during the test-bench commissioning and initial PTO tests. Increasing the disturbance-suppressing performance is left for future work.

8.5 Test-Bench Control Test

To test the emulation of the absorber dynamics, the PTO cylinder is given an initial position of 0.8m, corresponding to lifting the absorber approximately 0.75m out of the water, and then the test is started. The response is shown in the left plot of Fig. 8.14, showing that the cylinder tracks the calculated response of the absorber. A similar test is conducted for pushing the absorber into the water, and let it return to its equilibrium. When the cylinder velocity reference is low and the cylinder is within 15mm of the steady-state value, logic has been implemented to stop controlling the cylinder.

A step is given by the PTO in calm water to test how the wave cylinder reacts to the PTO force. The result is seen in Fig. 8.15, showing the test-bench correctly.

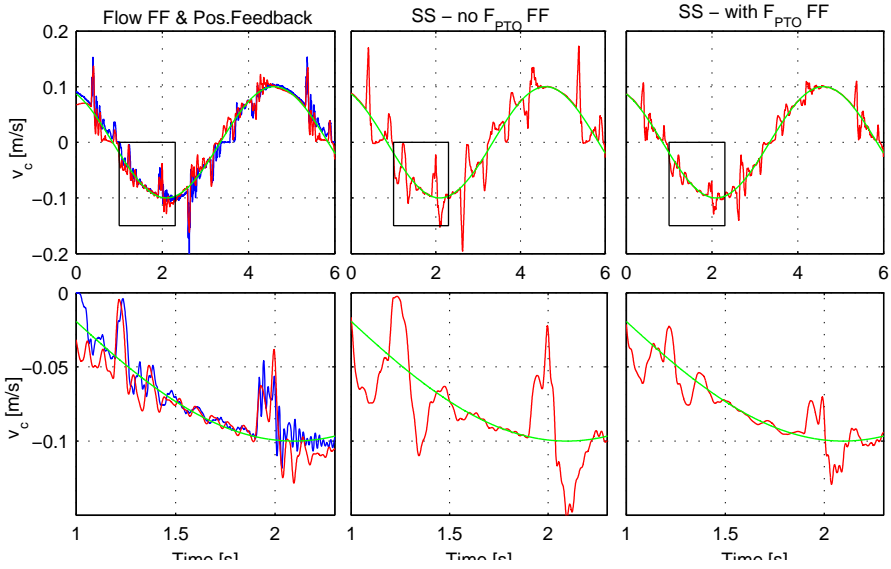


Figure 8.13: Controller tests. The blue curves are measured and red is simulated. The green curve is the velocity reference.

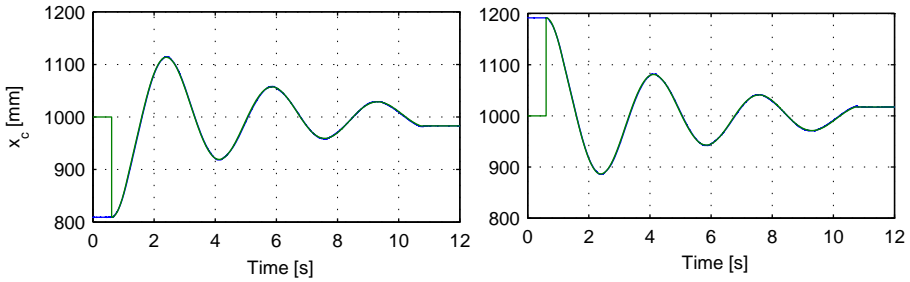


Figure 8.14: Test of test-bench absorber emulation. The green in the reference and blue is the actual cylinder position.

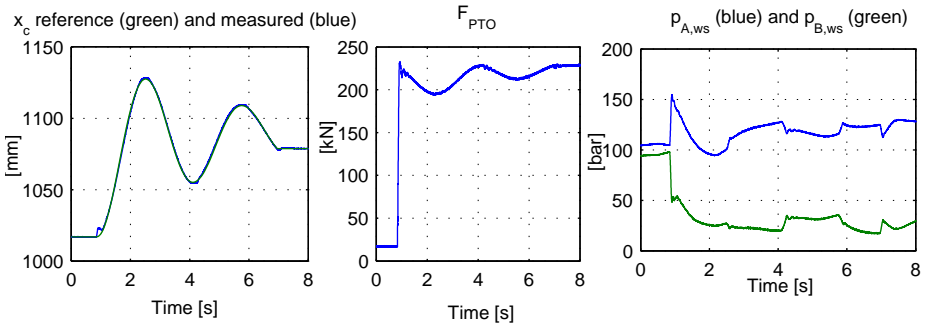


Figure 8.15: Test of test-bench reaction to PTO cylinder.

To get a visual feed-back of what the test-bench is doing during tests, an interface has been written in MATLAB as seen in Fig. 8.16, where measurements from the test-bench are send to a 3D-model in real-time. The interface visualises the cylinder movement and the equivalent movement of the C5 absorber. This is shown together with the emulated wave. Also, the internal states of the PTO may be seen.

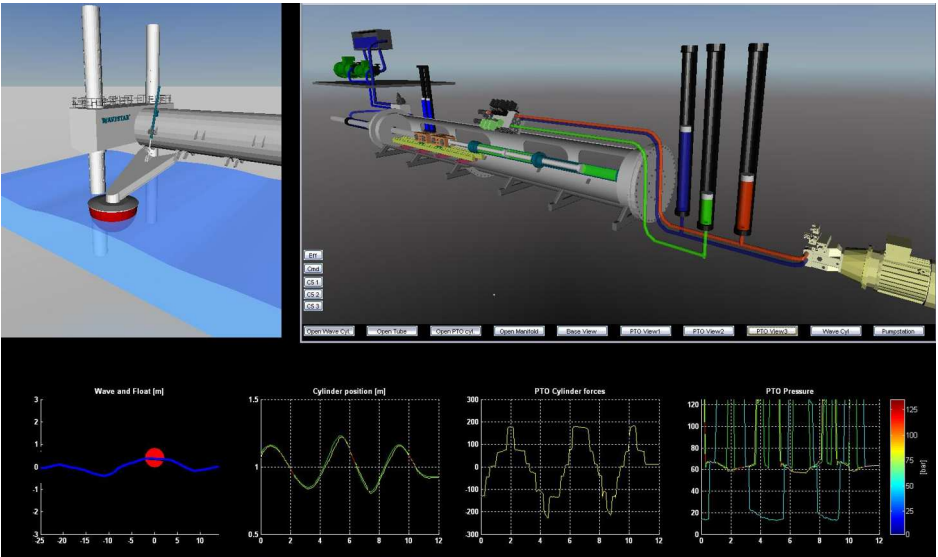


Figure 8.16: Test-bench realtime visualisation.

8.6 PTO Model

To validate simulation model used for PTO design, a dynamic model of the DDC prototype and the secondary side has been made to compare with measurements. The models

include valve dynamics, transmission line models and accumulator models.

The complete model is not going to be presented, however a sub-model is presented on how the three valves of the DDC is connected to a chamber through a transmission line. The transmission line model is similar to the one presented in paper [G] and [A].

To analyse pressure propagation in lines experiencing large pressure changes, the model in [253] may be applied. The approach is to discretise the transmission line into a number of mass elements as in Fig. 8.17, where the flow continuity and momentum equation are applied to each element, yielding a system of ordinary differential equations

$$\dot{p}_i(t) = (Q_{i-1}(t) - Q_i(t)) \frac{\beta_{\text{eff}}}{\Delta x A_H} \quad (8.23)$$

$$\dot{Q}_i(t) = (p_i(t) - p_{i+1}(t) - p_{H_i, \text{fric}}(Q_i)) A_H \frac{1}{\Delta x \rho_{\text{fluid}}}, \quad (8.24)$$

where $p_{H_i, \text{fric}}(Q_i)$ is a function describing the line's friction or flow resistance. The flow $Q_0 = Q_{\text{in}}$ is the input flow to the hose at the valve and $p_{n+1} = p_c$ is the pressure in the cylinder connected to the hose. The connection between manifold and volume consists of both pipe and hose, where two mass-elements are used for each as shown in Fig. 8.17.

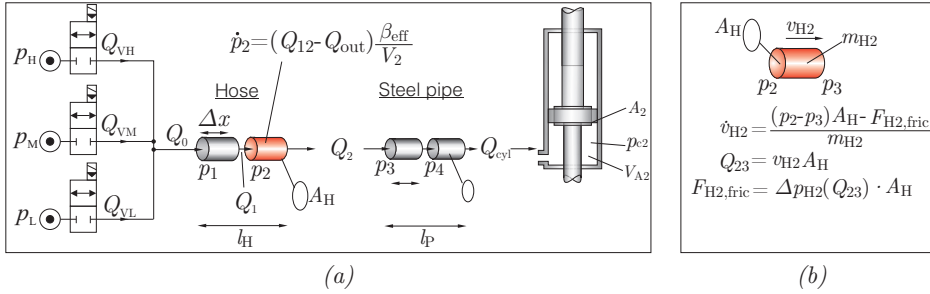


Figure 8.17: Model of volume and hose.

The friction term $p_{H_i, \text{fric}}(Q_i)$ is the total resistance (fittings, orifices, hose) of the line piece. Pressure drop in a straight pipe/hose p_λ may be described using Darcy's equation

$$p_\lambda = \underbrace{\frac{0.3164}{Re^{0.25}} \frac{\Delta x}{d_i} \rho \frac{1}{2} \left(\frac{Q_i}{\frac{1}{4} d_i^2 \pi} \right)^2}_{\text{turbulent}} \underbrace{\left(\frac{1}{2} + \frac{1}{2} \tanh \left(\frac{2300 - Re}{100} \right) \right)}_{\approx 0 \text{ for } Re < 2200} + \underbrace{\frac{128 \nu \rho \Delta x Q_i}{\pi d_i^4}}_{\text{laminar}} \underbrace{\left(\frac{1}{2} + \frac{1}{2} \tanh \left(\frac{-2300 + Re}{100} \right) \right)}_{\approx 0 \text{ for } Re > 2400} \quad (8.25)$$

where Δx is the line length, d_i is the lines inner diameter and ν is the kinematic viscosity of the fluid. Decision of flow regime is performed using Reynolds number Re :

$$Re = \frac{v_i d_i}{\nu} \quad (8.26)$$

The use of the hyperbolic-tangent expression in Eq. (8.25) is for creating a smooth transition between linear and turbulent pressure drop for increased robustness of the

simulation. $Re=2300$ is used as the transition number. The pressure drops p_ξ of fitting are described as,

$$p_\xi = \xi \frac{\rho}{2} Q_i^2 \left(\frac{1}{\frac{1}{4} d_i^2 \pi} \right)^2 \quad (8.27)$$

where ξ if a friction coefficient for a given fitting type. Thus, for a line with n fittings and a line piece, the pressure drop $p_{H_i, \text{fric}}(Q_i)$ due to the total line resistance may be written as:

$$p_{H_i, \text{fric}}(Q_i) = p_{\lambda, i}(Q_i) + p_{\xi, 1}(Q_i) + \dots + p_{\xi, n}(Q_i) \quad (8.28)$$

The total pressure resistance is seen in Fig. 8.18a for a 1 1/4 inch hose with a 45°-fitting and a T-piece fitting for modelling the manifold losses. Based on measurements on test-bench, it is has been experienced that adding a Coulomb like friction is required to make the model agree. This is shown in Fig. 8.18b. For 1 1/4" hoses, the Coulomb friction is set to 2000 Pa/m, e.g. 1000 Pa for 0.5m hose. The implemented line model in SIMULINK is seen in Fig. 8.19. A list of the hose and pipe lengths is given in Tab. 8.2. An overview of the complete PTO model in SIMULINK is shown in Fig. 8.20.

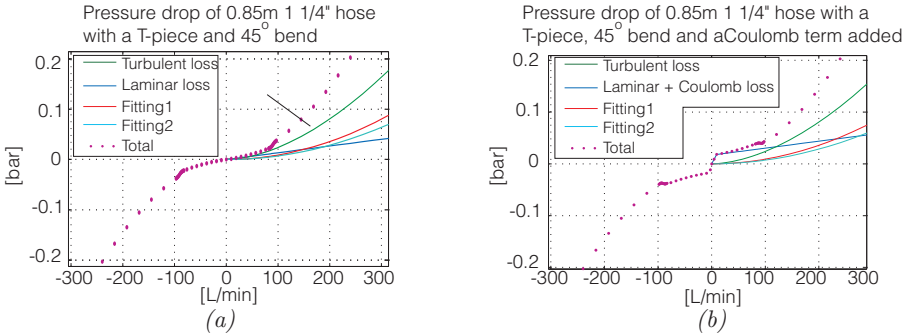


Figure 8.18: Hose frictions.

$l_{HA1} = 4.35$ m	: Length of parallel 1 1/2" hoses from manifold to chamber A1
$l_{HA2} = 1.35$ m	: Length of parallel 1 1/4" hoses from manifold to pipes to A2
$l_{PA2} = 1.2$ m	: Length of parallel pipes ($\varnothing 38$ mm) to chamber A2
$l_{HA3} = 1.7$ m	: Length of parallel 1 1/4" hoses from manifold to pipes to A3
$l_{PA3} = 1.5$ m	: Length of parallel pipes ($\varnothing 38$ mm) to chamber A3

Table 8.2: PTO cylinder connections. Note that the given lengths are for one of the parallel lines.

8.7 Initial DDC-Module Tests

In these initial tests, the purpose is to explore the effect of valve switching by gradually reducing from 150ms to 15ms shifting times. The test should show to what degree the line dynamics are being excited, and validate transmission line models.

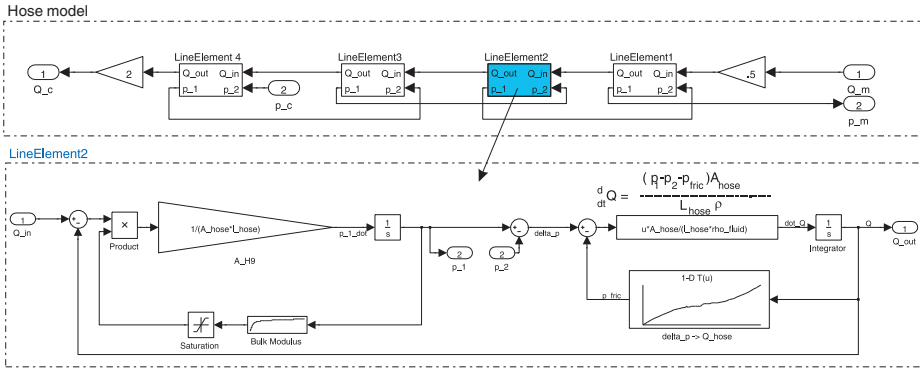


Figure 8.19: Implemented line model.

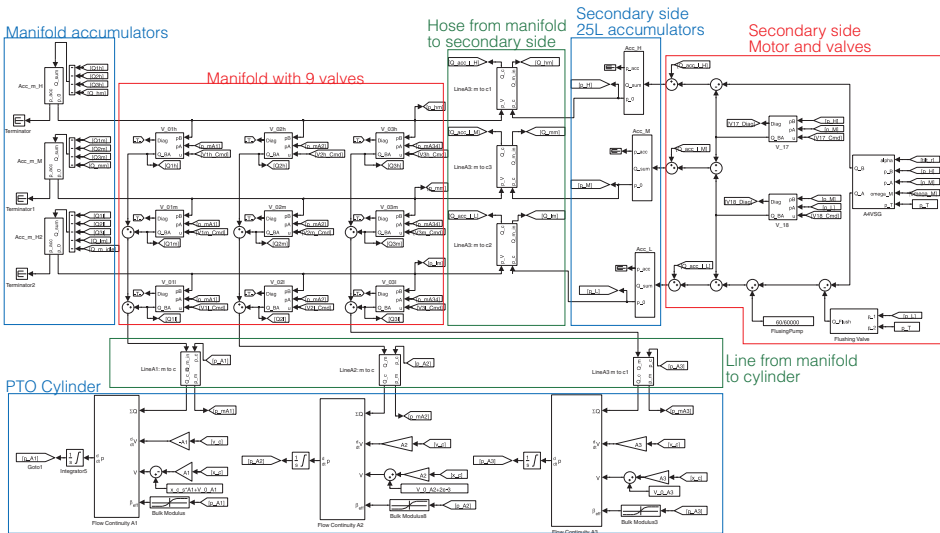


Figure 8.20: Simulink model of PTO system.

In the first test the PTO cylinder is fixed in position by the wave cylinder. The smallest PTO chamber (A3) is used in the test. The chamber is shifted between 16 and 110 bar, which corresponds to a shift between low and intermediate pressure in a final design. The measured and simulated responses are seen in Fig. 8.21. The valves switching times tested are 150 ms, 70 ms, 35 ms and 15 ms. The p_{c3} is the pressure in the cylinder chamber and p_{A3} is just down-stream of the valves at the manifold.

The test shows, that as the switch time is reduced, the line dynamics are being increasingly excited. The pressure at the line beginning p_{A3} at the manifold is relative calm, however this is certainly not the case in the cylinder chamber. Operating the valves at a 15 ms ramp, a pressure overshoot to the levels of 151 bar is experienced before settling on the 110 bar, i.e. 37% overshoot. The response is also very under-damped.

To validate the model, the model has been given the same initial conditions and the valve references as input. The figure shows both measured and simulated spool position, which are in very good agreement.

Comparing the pressure response with the model, the model shows very good agreement for all measured responses, capturing over-shoot and oscillation frequency. However, the model has a tendency to be slightly less damped compared to the measurements, despite adding the mentioned Coulomb term to the line resistance. The structure of line-models is assessed to be adequate.

The shown degree of the oscillatory behaviour and overshoot will yield severe mechanical stress on the system and may give cavitation in the cylinder. Test of shifting down in pressure from 110 bar to 16 bar is shown for chamber 2 and 3 in Fig. 8.22, clearly indicating that the chambers cavitate. Similar responses are obtained by simulation in Fig. 8.22, adding to the confidence of applied models.

The large peaks are caused by the long transmission lines in the test-bench setup, where the lines are 3-4 m each. This is very long compared to the initial idea of directly mounting the manifold on the cylinder. Using the validated models, simulation has been performed where the lines are reduced to 1/5 of the current length. The result is shown in Fig. 8.23 for all three chambers, and for both 100 bar and 220 bar step. The over-shoot is reduced to about 8%. The slower oscillation seen for e.g. chamber 1 is caused by a low frequent oscillation between manifold accumulators and secondary side accumulators. Thus, if the manifold could be mounted directly on the cylinder, problems with line dynamics will be minimised, but should still be checked.

8.8 DDC-Module Test with Moving Cylinder

In paper [E] it was identified that 15 ms valve opening/closing time was required to avoid cavitation or pressure spikes during pressure shifting with a moving cylinder. Accordingly, a series of test has been performed, where a chamber is systematic shifted between 20 bar and 120 bar for a range of cylinder velocities and valve response time. Four combinations of pressure shift and velocity were defined in Fig. 6.19 on page 185. The worst shifts were shown to be the cases, where the pressure gradient caused by

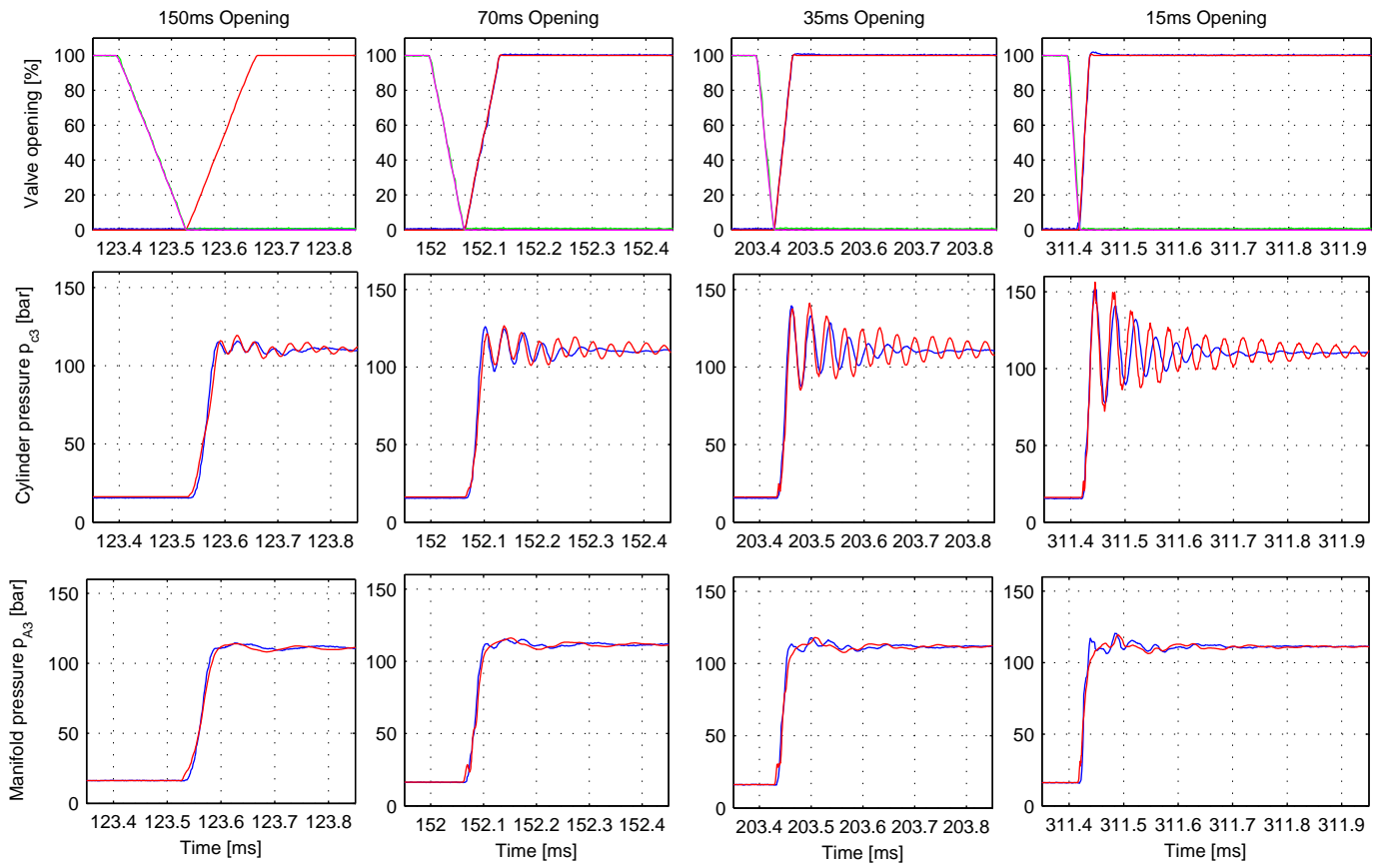


Figure 8.21: Responses from shifting on the A^3 chamber. Blue lines are measurements and red are simulated responses.

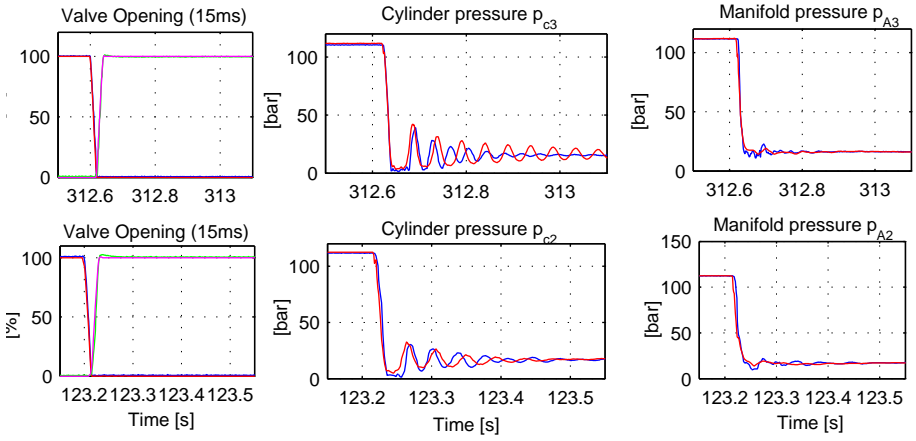


Figure 8.22: Responses from shifting on chamber 2 and 3. Blue lines are measurements and red are simulated responses.

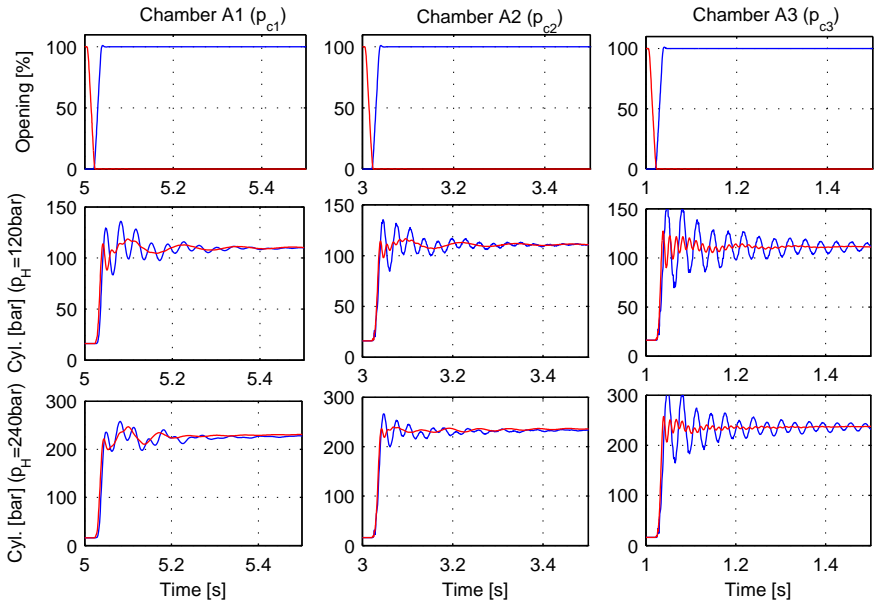


Figure 8.23: Blue curves are simulated responses with original line length. The red are simulated responses with 1/5 line lengths.

the displacement was in disagreement with desired pressure change. This corresponds to case 1 and 2 in Fig. 6.19. Resultantly, these are used for verifying required valve response time.

In Fig. 8.24 shifts have been tested with the cylinder moving at 0.3m/s where valve switching times of 50ms, 35ms, 25ms, 20ms and 15ms are tested. Each cylinder chamber has a relief valve set to 145bar in the tests. The results show that a switching time of 20ms is required to avoid hitting the relief valve pressure. Moreover, 15ms is required to not exceed the 10bar overshoot when no overlapping of valve opening is used.

There is a risk of cavitation when shifting up in pressure with the chamber expanding. Accordingly, each chamber also has an anti-cavitation valve in the manifold parallel to the on/off valves. The tests show that to affect the pressure dynamics in this case, 15ms is also required, otherwise the system relies on the check-valves.

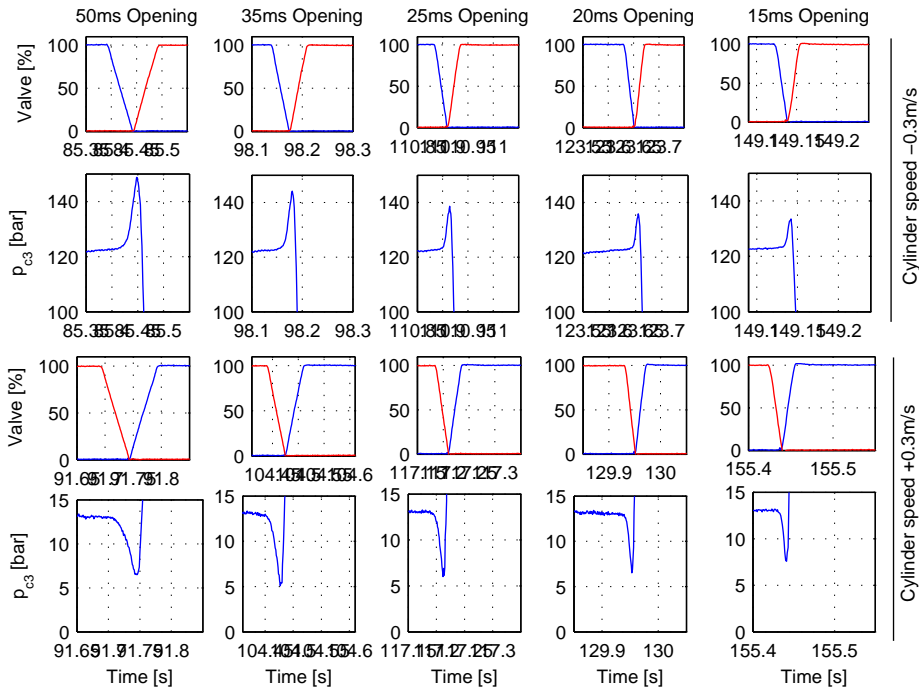


Figure 8.24: Test of required response time on the A3-chamber.

Verifying the expected valve requirements is a good thing, however, the 15ms fast shifts will induce the heavy and devastating oscillations in the lines. To this end, the verified simulation model has been applied to try and find an opening characteristic minimising the oscillations while preventing cavitation and pressure peaks.

8.9 Improved Control of DDC-Module

When shifting, it will always be advantageous to start by closing the valve as fast as possible as this does not excite line dynamics. Thus the 15ms is maintained here. By optimising the opening characteristic using the simulation model, the opening characteristic in Fig. 8.25 has been obtained, which gives a controlled pressure change without exciting the line dynamics (improved shift plots), which occurs for the “normal shift”. The shifts are performed for a piston speed of 0.2m/s for shift case 1 and 2. The improved shift immediately opens the valve a small amount in 5ms, and then opens to achieve a controlled pressure change. The method has the same performance regarding avoiding peaks or cavitation as the normal shift procedure.

The blue pressure curves in Fig. 8.25 are from experimental testing, where the green curves are simulation, verifying the performance found in simulations.

The improved opening characteristic is experimentally tested for different cylinder velocities in Fig. 8.26, showing that with a fixed opening characteristic a fair dynamic performance is achieved in all cases.

Looking at the 0.3m/s, the pressure peak when shifting down is longer and higher than for the normal shifts. The reason is that the small initial opening is too small for both consuming the de-compression flow and the displacement flow. Hence, the pressure first begins to decrease when the valve is further opened. Further optimisation is required to see if a better opening characteristic may be found, providing sufficient performance for all cases. Adjusting the amount of overlap may also be used to compensate for this behaviour. This study is being performed in near future. However, the proposed improved shift method is used in the following to get an initial validation that both test-bench and DDC may operate in irregular waves.

8.10 Test of DDC in Irregular Wave

At the time of writing this dissertation, the PTO Prototype is still in its commissioning phase, where systematic tests are focused to confidently work towards full load capacity with a well documented process. Resultantly, the PTO is currently operating at 120bar on the high pressure level, which “only” gives ± 200 kN. This is adequate for small waves of about 0.75m significant wave height. Resultantly, a test is carried out with this wave, where the PTO control (WPEA) is implemented as a simple linear damping strategy to avoid congesting the initial PTO results with complicated WPEAs.

The measured results are seen in Fig. 8.27. The DDC varies the force F_{PTO} as desired to apply a damping force, and when inspecting the used valves, the force shift algorithm (Fig. 6.13) most often uses the A3 volume for shifting. This is as expected as this is most energy efficient.

Inspecting the cylinder chamber pressures p_{C2} and p_{C3} , a well-damped behaviour is witnessed with no pressure spikes and cavitation due to the use of the improved shift strategy. The cylinder pressures at the manifold p_{A1} , p_{A2} and p_{A3} also show a steady

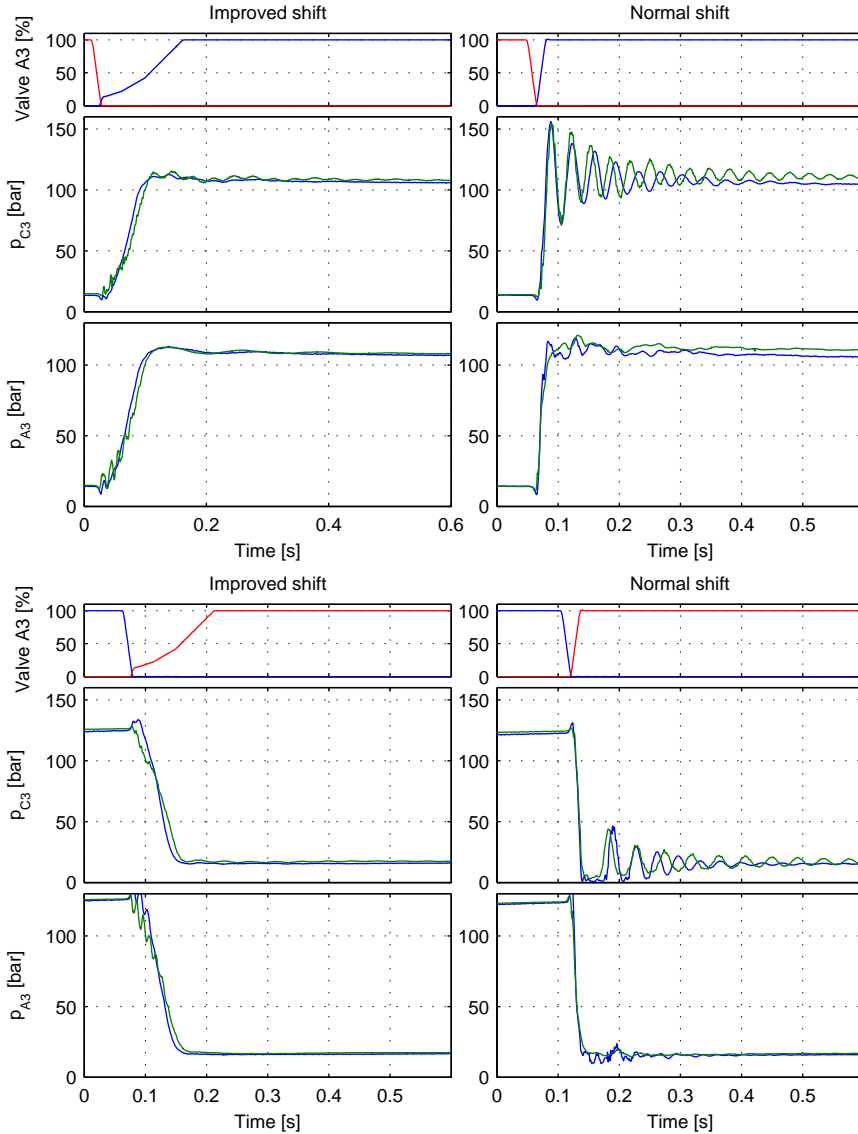


Figure 8.25: Blue curves are measured results and green are simulated.

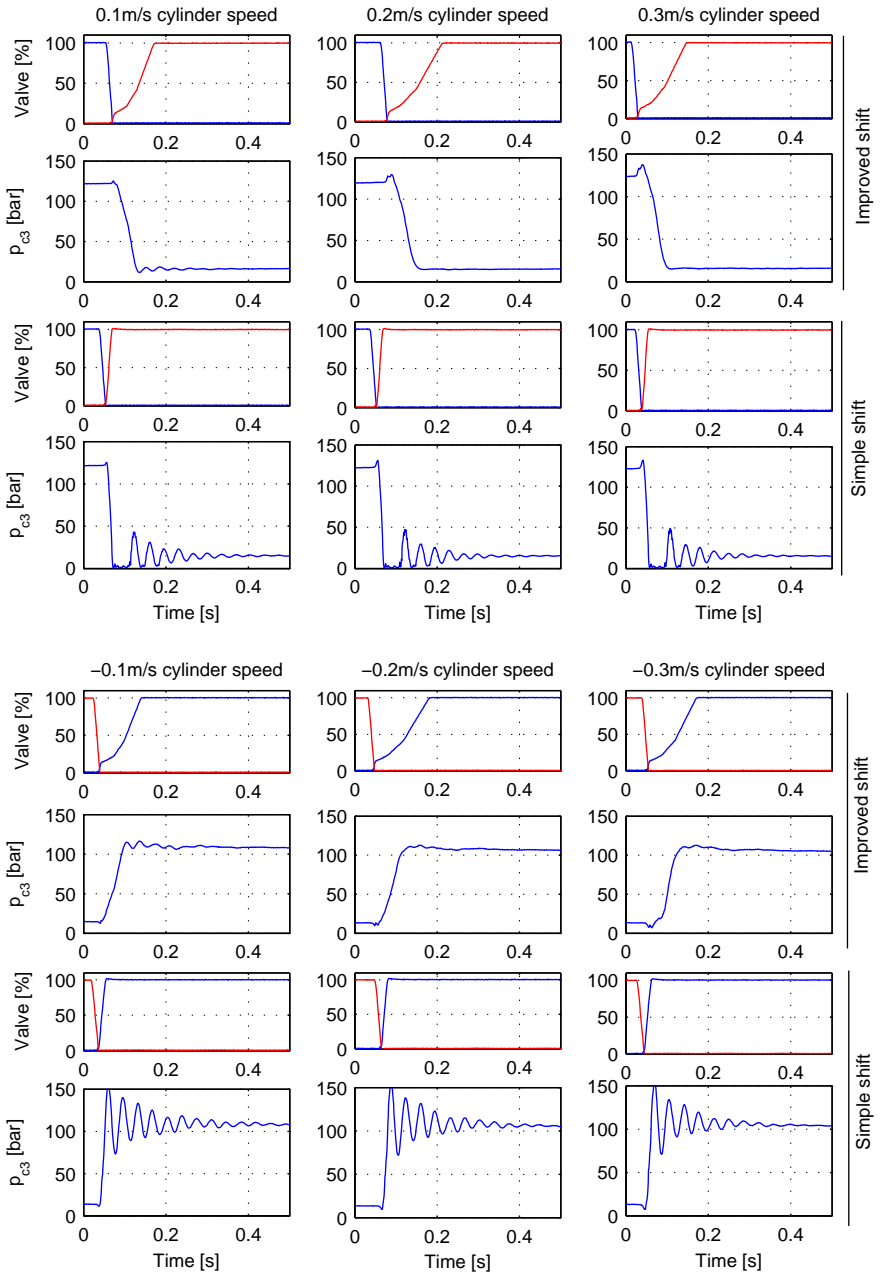


Figure 8.26: Improved shifts and normal shift measurements for chamber A3.

behaviour.

Tracking wise, the wave cylinder tracks the position reference $x_{c,\text{ref}}$ accurately. The used wave input is shown along with the equivalent float position realised by the test-bench. The pressure lines are controlled to have a steady level in the tests, thus the output power of the pressure lines is not attempted smoothed as in the real secondary side of the PTO.

An average power of only 7.6kW is measured as the extracted power in these small waves. The low power level is also due to testing with linear damping instead of employing reactive control or the OCIR-control. The hydraulic power delivered to the hydraulic motor and mid-pressure line is measured using the flow sensors and pressure sensors. An output of 6.2kW is measured, thus the efficiency of the DDC is about 81%, where 90% was the initial target. The estimated results should be seen in the light that the average input power level is only 7.6kW, where the peak power level of the tested DDC is 210kW (420kN@0.5m/s). The output power is also an early estimate as the calibration of all sensor signals for energy measurement is not verified yet.

The DDC is characterised in having a constant loss from shifting. Hence, increasing the power level through better control will automatically improve performance. Moving to higher waves than the 0.75m will also provide a more realistic performance view as the power levels reach the appropriate levels.

8.11 Summary

To test the DDC prototype, a full-scale PTO test-bench was commissioned, which comprised a 840kN hydraulic cylinder supplied by a 350kW pump station. The “wave” cylinder is used to load the PTO cylinder. The problem faced with the control is to get a hydraulic actuated system to emulate the dynamics of an absorber in waves, having a mass moment inertia of 4000,000kgm². The difficult part was to suppress the un-damped natural frequency of the wave cylinder, which is repeatable excited by the discrete nature of the tested PTO. To perform the control, a state-feedback based control was developed based on a verified model. The state-feedback used a disturbance feed-forward from the PTO, giving the wave cylinder the ability to emulate the absorber dynamics while suppressing its natural modes. This was verified through tests.

The implemented prototype DDC comprised a prototype valve manifold and a multi-chambered cylinder, which were connected using hoses and pipes. An important aspect of the tests was to investigate required valve performance. Accordingly, fast proportional valves were used, which allowed emulating different types of on/off valves. A secondary side of the PTO was designed to implement the three pressure lines.

When testing the PTO, the line (hose and pipe) dynamics showed to highly influence the response. Operating the valves at a 15ms made the pressure overshoot to the level of 150bar before finally settling on 110bar. When shifting down the pressure the line dynamics caused cavitation in the cylinder chamber. The experienced phenomena in the lines may be viewed as a water-hammer effect, where the sudden braking of

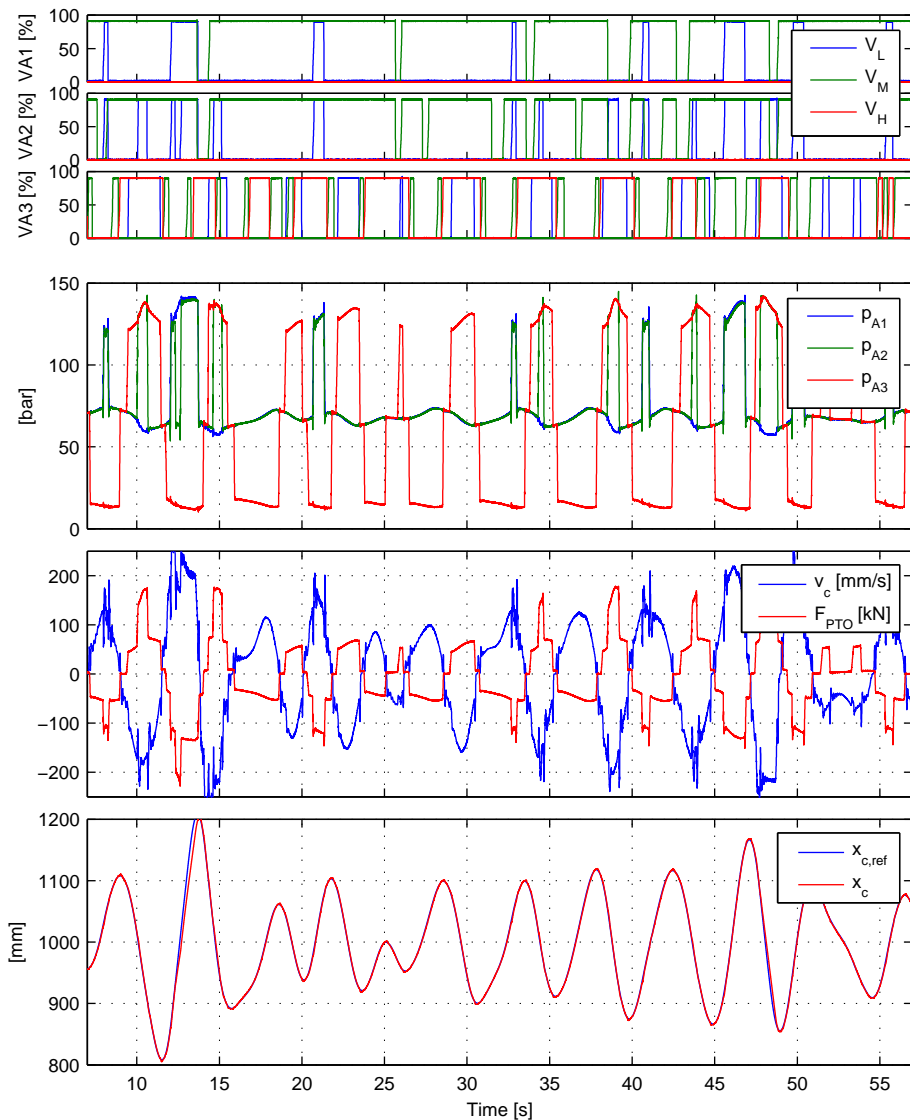


Figure 8.27: Test of DCC in small irregular waves.

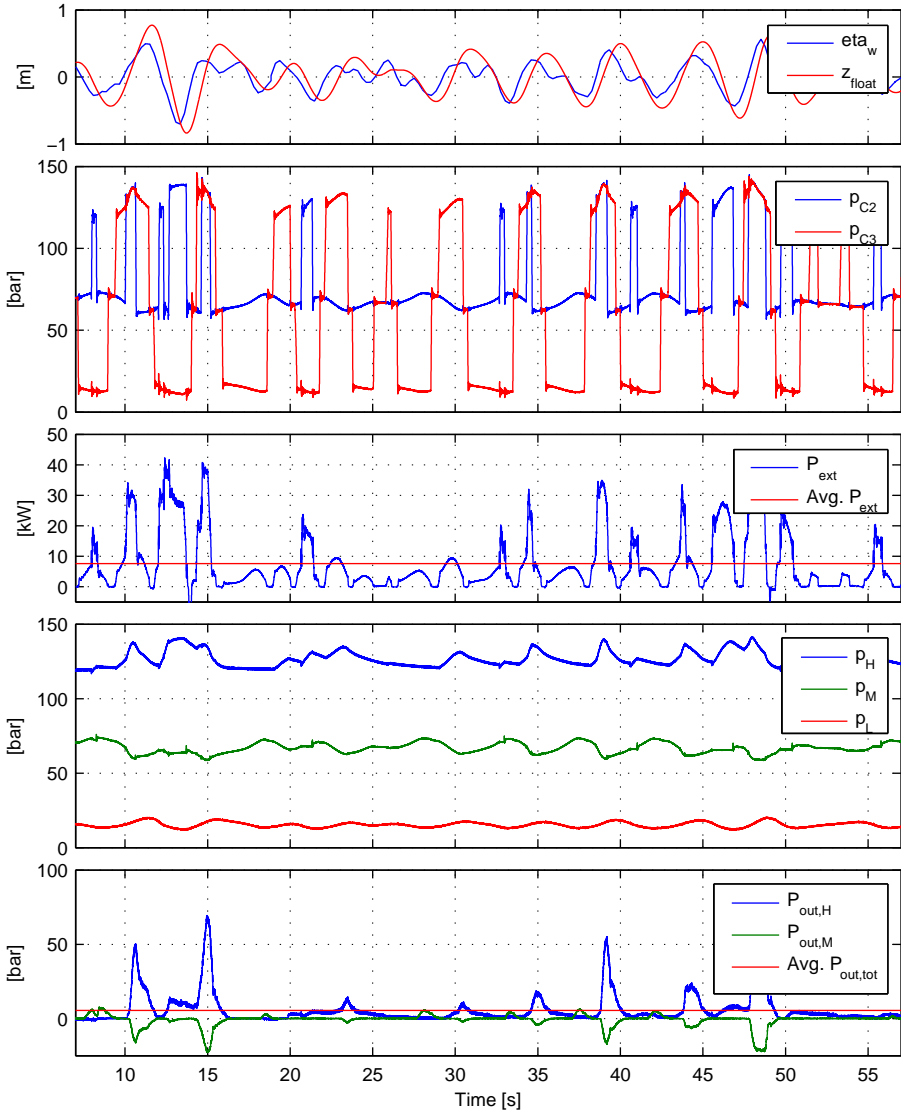


Figure 8.28: Fig. 8.27 continued.

the accelerated fluid in the lines causes an impact pressure. The lines dynamics were modelled by discretising it into four mass elements. The models were verified to be fairly accurate.

Tests revealed that the earlier determined requirement of 15 ms valve closing and opening time was required to avoid pressure peaks in the cylinder chamber. A modified opening characteristic was presented to achieve the 15ms and still have a dampened response with the long lines.

The improved shift was implemented and an irregular wave test was conducted with the DDC in production mode. The DDC was shown to track the force reference and behave as expected. Due to still being in the commissioning phase of the PTO, it was only tested at a low part load. At an input of 7.6kW, the output to the pressure lines was estimated to be 6.2kW, i.e. the DDC performing at an efficiency of 81%. The estimated result should be seen in the light, that the peak power level of the tested DDC is 210kW

Future work comprise of fully commissioning the DDC and test-bench and reaching 90% efficiency of the DDC in irregular waves. Future work also consists of mapping the found improved open-characteristic to an on/off valve implementation.

Conclusion, Summary and Future Work

With the overall purpose of developing a PTO for multi-absorber systems, this dissertation has identified and set forth three solutions with the proper qualities of force density, controllability and efficiency:

- A hydraulic PTO, implementing a *Discrete Displacement Cylinder* (DDC), allowing high-efficient force control while converting the power of a linear motion into energy in a high pressure accumulator storage. The concept allows the DDCs of multiple absorbers to supply the same energy storage, while a hydraulic motor steadily drives a generator.
- A magnetic gear PTO using a *Magnetic Lead Screw* to directly convert linear motion into high speed rotational motion for driving a conventional permanent magnet generator.
- A hydraulic PTO using a normal cylinder and a *Digital Displacement Pump/Motor* (DDPM) to form a high-efficient hydro-static transmission, where four absorbers power one generator by having the DDPMs on a common shaft. Storage is implemented by having additional DDPMs on the shaft, which in turns stores and retrieves energy from an accumulator storage.

The DDC-concept was fully designed, leading to the documented design and test of a working full-scale 420kN prototype. The magnetic lead screw concept was also discussed, and was designed and tested in an intermediate scale of 17kN made possible by master students.

The foundation for setting forth these recommended PTO designs is a refined analysis of PTO, waves, absorber and control, providing the required insight into their complex interplay. The established insight allows both evaluating known PTO solutions, but also to be used actively to properly establish the qualitative and quantitative requirements of new PTOs.

Summary

The elements and findings required to establish the insight and framework for PTO design are summarised:

A Mechatronic Design Problem: Acknowledging that the PTO design is a mechatronic problem defined the main approach of this dissertation. Finding optimum solutions and performing cost-efficient development require model based approaches. This was demonstrated with the mutual optimisation of PTO size and control design.

The Essential Models: Both a single absorber model and a 20 absorber model were developed based on applying linear wave theory. For a sufficient realistic wave generation, a white noise approach was applied. Model verification was accomplished using a 1:20 scale absorber in a wave tank. Near perfect agreement was found between the model and measurements regarding movement, power and forces. The verified model gave a sound foundation for the heavy use of model based approaches.

Reactive Control in Practise: The idea of reactive control for increasing power absorption dates back to the 1970's, but still its feasibility for real PTO systems with losses was questionable. An analytical result was provided in the dissertation to both analyse and design the reactive control with inclusion of PTO efficiency. The result proved that reactive control is highly beneficial at even "low" PTO efficiencies as 60%.

Understanding Optimal Control: The uncompromising idea of optimal reactive control condensed in the non-causal complex-conjugated control formulation is a fundamental result in wave energy. Accordingly, a chapter was used to reach a robust appliance of the control. The chapter showed the relation of different causal implementation of the control in the frequency domain, and suggested a new family of causal approaches. The new family is based on partially cancelling absorber dynamics, while moving the peak of the flatten frequency response to the energy content of the wave. The simplest version in the family was used, namely the spring based reactive control. It was chosen as a good robust solution as it allows tuning the resonance frequency and widens the frequency response.

Validating Models for Control: Wave tank tests were performed to prove the reactive control. Near perfect agreement was found between the measured and simulated trajectories of movement and power. The tests validated the use of the developed models for control design and simulations.

Comparison of Classic WPEAs as a Function of PTO Characteristics: 40 years of wave energy have lead to a range of different Wave Power Extraction Algorithms (WPEA), however with limited focus on the interplay with PTO, and how the performance of different WPEAs compare. A novel approach was presented where all "classic" point absorber WPEAs are optimised according to a generic PTO formulation. The formulation included efficiency, force limitations and finite control bandwidth. The optimisation was solved by performed using numerical optimisation in irregular waves. The developed framework allowed comparing the performance (annual production to grid) of all the WPEAs as a function of PTO properties, yielding the following conclusions:

- For a resistive PTO with continuous control, the developed non-linear OCIR control is the best choice.
- The tested reactive control is only better than the OCIR control if the conversion efficiency of the PTO (the reactive part) is above 90%.
- The four-quadrant property of a PTO should only be actively strived for if the conversion efficiency of the part where the reactive power travels is above 90%.
- Latching control requires adding a latching mechanism with three times higher torque capacity to be competitive with the OCIR, while having the same PTO for applying continuous damping control during movement.
- If a PTO only allows applying a constant force damping, de-clutching control is the best choice - latching control with Coulomb damping requires three times higher torque to be competitive.
- Linear damping should never be used as it is a waste of controllability - apply a non-linear resistive strategy as the OCIR instead.
- Ratchet based PTOs or Coulomb damping PTOs should be avoided unless the PTO and WEC can be made extremely cheap.

The OCIR Control: The OCIR control suggested in this work is a causal non-linear control, achieving similar manipulation of the absorber response as reactive control. The manipulation is achieved using non-linear damping, i.e. the Oscillation Control is Implemented Resistively (OCIR). The control was shown to be a superior resistive control technique with good utilisation of available force, performing similar to reactive control for a 90% efficient PTO.

The developed framework on the interplay between PTO and control was applied to evaluate State-of-the art in PTO systems. A comprehensive review was conducted, where all known PTOs and relevant technologies were more or less reviewed and assessed according to expected force density, controllability (available WPEAs), expected annual production (based on WPEA and part load performance) and power smoothing capability. A scoring system was made to keep track of all the different PTOs, and though the given scores may always be debated, the scoring system gave a nice initial sorting of the 19 assessed PTOs. The conclusions from the review were:

- Direct driven electrical machines are infeasible due to a very low force density. Between 11,000kg and 20,000kg of active magnetic material (magnets, coils, iron) is required for a 420kN generator to produce an average of up to 55kW. The diameter of the machine is more than 1m.
- The magnetic lead screw is viewed as a possible solution as two parallel screws with a diameter of 0.25m may provide 630kN. No studies or prototype exist prior this work. The screw may directly drive a conventional generator at high speed.
- Magnetic gear implementation, based on repeatedly snapping a magnetic coupling to obtain pulses of high speed movement, gives a poor production as a Coulomb like damping is provided.

- Mechanical solution as for example ball screws may show the required force density and efficiencies, but are viewed as not having the durability.
- Ratchet mechanisms lead to very poor power extraction and should be avoided. Double ratchets do not improve the performance.
- A hydraulic cylinder around $\varnothing 25$ cm and 1600 kg may give 420 kN. The problem is to control the force of the cylinder while efficiently converting the produced flow into electricity.
- Suggested hydro-static transmission combining a cylinder and a DDPM is viewed as good solutions, but the DDPMs are still in a pre-commercialisation phase.
- Hydraulic accumulators are viewed as best suited storage technology for wave energy. It may cover both wave-to-wave and wavegroup-to-wavegroup power smoothing. It has a high power density and low cost, combined with a round trip efficiency of about 94%.
- Discrete control of a hydraulic cylinder by pressure shifting seems to give the required efficiency while providing force control.
- Efficient and durable hydraulic PTOs with constant force control exist, but have a poor extraction.

Based on state-of-the-art, the three potential PTO solutions listed at the beginning of this chapter were suggested for the 20 absorber system.

The DDPM Hydro-Static Transmission: The DDPM based PTO was more or less as state-of-art, just expanding the layout to multi-absorber system. The layout connected four absorbers to one generator.

Magnetic Lead Screw PTO: The disclosed Magnetic Lead Screw (MLS) based PTO is a novel design. Magnets are placed on both rotor and translator, and the MLS is used to directly drive a generator (without a ratchet mechanism). The scaled prototype demonstrated the expected force density, and verified a mechanical design of the MLS. An analysis was made on how the repeated acceleration and de-acceleration of MLS and generator affected the control. First it was calculated, that the MLS had sufficient force to handle the inertial load at a gearing ratio, providing a generator speed above 1000 rpm. Hereafter, it was shown that the inertial load may actually be incorporated into the control as a “free” and desired lowering of the natural frequency of the absorber. Also, the required generator efficiency and MLS efficiency for feasibility was determined and may be found in the dissertation.

DDC PTO: An optimised version of DCC-PTO was developed using a refined analysis method, which accurately predicted the DDC performance without performing time consuming hydraulic simulations. The analysis showed that if on/off valves with 15 ms response time are used, the DDC can maintain a 90% efficiency from linear motion to hydraulic energy in the accumulator storage. The concept allows

incorporating accumulators and operating 20 absorbers with a few central generators. The DDC may be implemented at sufficient low loss with tested standard components, which gives a potential of high reliability. Control-wise, the DDC is inherently a four-quadrant system, where reactive power only travels between cylinder and accumulators. Thus, the DDC may implement reactive control, which is viewed as a strength, as this is a documented strategy at Wavestar.

Accordingly, the DDC was chosen for full design. Based on modelling the system from wave-to-wire and performing irregular wave simulations, the overall efficiency of the PTO was found to be beyond 70% in all sea conditions.

To verify and test the DDC, a full-scale prototype was designed and tested for one absorber. To test the DCC, a full-scale PTO test-bench was commissioned. It comprised a 840kN hydraulic cylinder supplied by a 350kW pump station, which emulated the absorber load on the DDC.

Full Scale Test-Bench: The problem faced with the control was to get a hydraulic actuated system to emulate the dynamics of an absorber in water. A state-feedback based control was developed, tracking an on-line simulation model of the absorber dynamics. This gave the wave cylinder the ability to emulate the absorber dynamics while suppressing its natural modes. The absorber was shown to emulate the absorber dynamics and responded correctly to PTO loads.

DDC Prototype: The implemented DDC prototype comprised a valve-manifold and a multi-chambered cylinder, which were connected using hoses and pipes. Tests revealed that the earlier determined requirement of 15ms valve closing and opening times was required to avoid pressure peaks during shifting. When testing the PTO, the hose dynamics showed to highly influence the response, giving an impact pressure 37% higher than steady-state pressure. The line dynamics were modelled and agreed with measurements. An improved shift was developed removing the impact pressure. The DDC was shown to track the force reference and behave as expected. Due to still being in the commissioning phase of the PTO, it was only tested at a low part load. At an input 7.6kW, the output to the pressure lines was estimated to 6.2kW, i.e. the DDC performing at an efficiency of 81%. The estimated results should be seen in the light, that the peak power level of the tested DDC is 210kW.

Future Work

Causal Reactive Control: The Ψ_α WPEA suggested in Ch. 3 with partial cancellation of absorber dynamics should be further evaluated. This includes showing ideal performance in irregular waves by simulations. The design should also be designed according to PTO efficiency and then compared to e.g. the spring-based reactive control. Further analysis of the stability and sensitivity should be performed. Adding non-linear hydro-statics to the design should also be investigated.

Analytical Solution to Reactive Control with Losses: By doing e.g. a good approximation of the $\tanh^{-1}()$ term in Eq. (3.53), a direct solution to finding X_c and R_c may be possible.

Improved Spring Control: In the used spring based reactive control, a simple damping coefficient is applied. In the $\Psi_\alpha|_{\alpha_1=0}$ in Ch.3, the radiation term is cancelled. The performance of this version of the reactive control should be investigated.

OCIR Control: The non-linear OCIR control should be tested in wave-tank to further verify performance. Also, as a non-linear damping law may perform similar to a linear reactive control law, it would be likely that an even better non-linear reactive control law exists. A non-linear law is being investigated, where the active period is not set to zero as in the OCIR, but scaled non-linearly compared to the resistive parts. An investigation should be performed with the OCIR, where the radiation term is cancelled too. It could also be interesting to base an OCIR on the inverse control.

20 Absorber Model: The used 20 absorber model omitted the cross radiation terms. Hence, inclusion of cross radiation terms should be performed, followed by an exploration on how this affects the control and performance. This could include investigating coordinated control to exploit the radiation interference.

Getting Mechanical Design into the Loop: Analysis of structural loads has not been a part of this dissertation. To optimise the total cost of energy instead of annual production, this aspect should be included. Hence, when optimising the annual production, the structural design should be evaluated, probably leading to a resizing of the PTO. The different PTOs and WPEAs also induce different structural loads.

DDC Prototype: The work on the prototype DDC continuous. The design is following the scheduled series of tests, and should soon be operating at full capacity. A new on/off valve combination to mimic the improved shift is being investigated. A large list of control and algorithm improvements is going to be tested in near future.

DDC PTO: Further investigation to optimise PTO layout. Especially the number of accumulator batteries and the interaction with the interconnecting pipe-lines are areas of further studies.

Test-bench: Further optimisation of control using the state-feedback control is being performed, as the analysis showed that harder tuning is possible.

Conclusion

By a refined treatment of the interplay between PTO and wave power extraction methods, the dissertation has achieved an applicable two-way design framework, allowing both specification and evaluation of PTO systems. The centre of this framework is an analysis of all classic extraction algorithms as a function of PTO requirements. The methodology and obtained performance curves of the extraction algorithms are easy comprehensible, and may hopefully be applied as a design procedure for control of PTOs.

A new non-linear damping approach is developed, boosting new-life to PTOs previously relying on linear damping control. The control gives a power increase from 50% to 100% compared to linear damping, possibly exceeding performance of some latching controlled and reactively controlled PTOs.

By demonstrating design and implementation of two new PTOs, the dissertation hopefully leaves both new ideas and an applicable framework on PTO design and extraction control, which may aid in future development of wave energy.

Bibliography

- [1] João Cruz, editor. *Ocean Wave Energy - Current Status and Future Perspectives*. Springer Verlag, 2008.
- [2] D. L. P. Strange, T. Tung, G. C. Baker, G. Hagerman, L. F. Lewis, and R. H. Clark. Renewable energy resources: opportunities and constraints 1990-2020. *World Energy Council*, pages 321–358, 1993.
- [3] Kester Gunn and Clym Stock-Williams. Quantifying the global wave power resource. *Renewable Energy*, 44(0):296 – 304, 2012.
- [4] IEA. Key world energy statistics, 2012.
- [5] Ana Brito e Melo. Annex a ocean energy state of the art, 2009.
- [6] Wave Star A/S. <http://wavestarenergy.com/>.
- [7] Pelamis Wave Power Ltd. <http://www.pelamiswave.com/>.
- [8] Aquamarine Power Ltd. <http://http://www.aquamarinepower.com/>.
- [9] AW-Energy Oy. <http://aw-energy.com/>.
- [10] Matti Vuorinen and Erkki Kasanen. Wave energy recovery system. Patent US20130047601A1, 2023.
- [11] Ocean Power Technologies. <http://www.oceanpowertechnologies.com/>.
- [12] Seabased AB. <http://www.seabased.com/>.
- [13] EU-OEA. Oceans of energy, 2010.
- [14] EREC. Mapping renewable energy pathways towards 2020, 2011.

- [15] Offshore WIND staff. Belgium: Thv mermaid to construct final north sea offshore wind farm. *offshoreWIND.biz*, 6 2012. <http://www.offshorewind.biz/2012/06/29/belgium-thv-mermaid-awarded-concession-to-construct-final-north-sea-offshore-wind-farm/> (Accessed 21-10-2013).
- [16] EUROPEAN COMMISSION. The ocean of tomorrow projects (2010-2012). joining research forces to meet challenges in ocean management. ISBN 978-92-79-26745-1, 2013.
- [17] Jens P. Kofoed. Ressourceopgørelse for bølgekraft i danmark, 2009. WE1.2.
- [18] Carbon Trust. Uk wave energy resource, 2012.
- [19] Tom Thorpe. Chapter 15 - wave energy. In Judy Trinnaman and Alan Clarke, editors, *2004 Survey of Energy Resources (Twentieth Edition)*, pages 401 – 417. Elsevier Science, Oxford, twentieth edition edition, 2004.
- [20] WaveNet. Results from the work of the european thematic network on wave energy, 2003.
- [21] S. H. Salter. Wave power. *Nature*, 249:720 – 724, 1974).
- [22] Jamie Taylor. Power for change - 2 (of 13) the duck wave energy device, 2000. <http://www.mech.ed.ac.uk/research/wavepower/Videos.htm>.
- [23] Gary Nolan and John Ringwood. Control of a heaving buoy wave energy converter for potable water production. In *In proc. Irish Signal and Systems Conference, Dublin*, 2006.
- [24] J. Cruz and S. Salter. Numerical and experimental modelling of a modified version of the edinburgh duck wave energy device. *IMechE Part M.*, 220:129–147, 2006.
- [25] D.C. Hicks, C.M. Pleass, and G.R. Mitcheson. Delbuoy: wave-powered seawater desalination system. In *OCEANS '88. A Partnership of Marine Interests. Proceedings*, pages 1049–1054 vol.3, 1988.
- [26] Harold H. Hopfe. Wave energy desalination. Patent US4335576 A, 1980.
- [27] S. H. Salter, J. R. M. Taylor, and N. J. Caldwell. Power conversion mechanisms for wave energy. In *Proceedings of the Institution of Mechanical Engineers, Part M: Journal of Engineering for the Maritime Environment*, 2002.
- [28] J. Falnes. Optimum control of oscillation of wave-energy converters. *International Journal of Offshore and Polar Engineering*, 12(2):147–155, 2002.
- [29] Stephen Salter. *Power conversion systems for ducks*, pages 100–108. Institution of Electrical Engineers, 1971.
- [30] Morten Kramer, Laurent Marquis, and Peter Frigaard. Performance evaluation of the wavestar prototype. In AbuBakr S. Bahaj, editor, *9th EWTEC 2011*. University of Southampton, 2011.
-

-
- [31] IAHR. List of sea state parameters. *Journal of Waterway, Port, Coastal, and Ocean Engineering*, 115(6):793–808, 1989.
- [32] J. Falnes. *Ocean Waves and Oscillating Systems*. Cambridge University Press, 2002.
- [33] Thomas Lykke Andersen and Peter Frigaard. Lecture notes for the course in water wave mechanics. ISSN 1901-7286, DCE Lecture Notes No. 24.
- [34] K. Hasselman, T. P. Barnett, E. Bouws, D. E. Carlson, and P. Hasselmann. Measurements of wind-wave growth and swell decay during the Joint North Sea Wave Project (JONSWAP). *Deutsche Hydrographische Zeitschrift*, 8(12), 1973.
- [35] DNV. Recommended practice dnv-rp-c205 - environmental conditions and environmental loads, 2010.
- [36] Charalambos C. Baniotopoulos, Claudio Borri, and Theodore Stathopoulos, editors. *Environmental Wind Engineering and Design of Wind Energy Structures*. Springer, 2011.
- [37] J.-B. Saulnier, P. Ricci, and A. H. Clément and. Mean power output estimation of wecs in simulated sea. In *Proceedings of the 8th EWTEC, Uppsala, Sweden*, 2009.
- [38] M.J. Tucker, P.G. Challenor, and D.J.T. Carter. Numerical simulation of a random sea: a common error and its effect upon wave group statistics. *Applied Ocean Research*, 6(2):118 – 122, 1984.
- [39] M.J. Ketabdari and A. Ranginkaman. Simulation of random irregular sea waves for numerical and physical models using digital filters. *Transaction B: Mechanical Engineering*, 16(3):240–247, 2009.
- [40] wamit. Wamit. www.wamit.com, 2011.
- [41] J. Falnes. On non-causal impulse response functions related to propagating water waves. *Applied Ocean Research*, 17(6):379 – 389, 1995.
- [42] Griet De Backer. *Hydrodynamic Design Optimization of Wave Energy Converters Consisting of Heaving Point Absorbers*. PhD thesis, Coastal Engineering Division & Maritime Technology Division Department of Civil Engineering Faculty of Engineering Ghent University, 2009. WE0, WE2, WE3.3, WE5.0.
- [43] Hans F. Burcharth, Søren R.K. Nielsen, and Kjeld Schaarup-Jensen. A three dimensional sea facility for deep and shallow water waves. In *Proceedings of the Fifth International Symposium on Offshore Mechanics and Arctic Engineering*, volume 1. American Society of Mechanical Engineers, 1986.
- [44] M. Kramer, J.E. Pedersen, and M. Pedersen. *Bevægelser af bølgepåvirket Tension Leg Platform og hjælpefartøj*. Aalborg Universitet, 2001.
-

-
- [45] Morten Kramer, Francesco Ferri, Andrew Zurkinden, Enrique Vidal, and Jens P. Kofoed. Experimental validation of numerical models for wave energy absorber. *2nd SDWED symposium, Advances in Modelling of Wave Energy Devices*, Thursday April 26, 2012, 2012.
- [46] Johannes Falnes. Radiation impedance matrix and optimum power absorption for interacting oscillators in surface waves. *Applied Ocean Research*, 2(2):75 – 80, 1980.
- [47] D. Valerio, P. Beirao, M.J.G. Mendes, and J. Sa da Costa. Comparison of control strategies performance for a wave energy converter. In *Control and Automation, 2008 16th Mediterranean Conference on*, pages 773 –778, june 2008.
- [48] E. Tedeschi, M. Carraro, M. Molinas, and P. Mattavelli. Effect of control strategies and power take-off efficiency on the power capture from sea waves. *Energy Conversion, IEEE Transactions on*, 26(4):1088 –1098, dec. 2011.
- [49] E. Tedeschi and M. Molinas. Impact of control strategies on the rating of electric power take off for wave energy conversion. In *Industrial Electronics (ISIE), 2010 IEEE International Symposium on*, pages 2406 –2411, july 2010.
- [50] Rico H. Hansen and Morten M. Kramer. Modelling and control of the waves-tar prototype. In *In proc. of 9th European Wave and Tidal Energy Conference, EWTEC*, 2011. WE2.1, WE5, WE6.1.
- [51] Guang Li, George Weiss, Markus Mueller, Stuart Townley, and Mike R. Belmont. Wave energy converter control by wave prediction and dynamic programming. *Renewable Energy*, 48(0):392 – 403, 2012.
- [52] J.C. Lagarias, J. A. Reeds, M. H. Wright, and P. E. Wright. Convergence properties of the nelder-mead simplex method in low dimensions. *IAM Journal of Optimization*, 9(1), 1998.
- [53] Johannes Falnes. Optimum control of oscillation of wave-energy converters, June 1993.
- [54] A. Babarit, G. Duclos, and A.H. Clément. Comparison of latching control strategies for a heaving wave energy device in random sea. *Applied Ocean Research*, 26(5):227 – 238, 2004.
- [55] António F. de O. Falcão. Phase control through load control of oscillating-body wave energy converters with hydraulic pto system. *Ocean Engineering*, 35(3-4):358 – 366, 2007.
- [56] António F. de O. Falcão. Modelling and control of oscillating-body wave energy converters with hydraulic power take-off and gas accumulator. *Ocean Engineering*, 34:2021–2032, 2007. WE2.3, WE3.1.2.
- [57] A. Babarit and A.H. Clément. Optimal latching control of a wave energy device in regular and irregular waves. *Applied Ocean Research*, 28(2):77 – 91, 2006.
-

- [58] Aurélien Babarit, Michel Guglielmi, and Alain H. Clément. Declutching control of a wave energy converter. *Ocean Engineering*, 36(12-13):1015 – 1024, 2009.
- [59] S. M. Muyeen, editor. *Wind Energy Conversion Systems*. Springer, 2012.
- [60] Rico Hjern Hansen, Torben Ole Andersen, and Henrik C. Pedersen. *Determining required valve performance for discrete control of PTO cylinders for wave energy*, pages 565–578. American Society of Mechanical Engineers, 2012.
- [61] Rajeswari Chandrasekaran. *Modeling of electrochemical energy storage and energy conversion devices*. PhD thesis, Georgia Institute of Technology, 2010.
- [62] Jefferson W. Tester, Elisabeth M. Drake, Michael J. Driscoll, Michael W. Golay, and William A. Peters. *Sustainable Energy - Choosing Among Options*. MIT Press, 2005.
- [63] Jan-Ove Palmberg. Vad har ett 60 aar gammalt flygplan och framtidens hjullasttare geensamt?, 2013. Tunga fordon; Tema hybriddrivsystem, 10 april, 2012. Seminarium om drivsystem för drivsystem för energieffektiva tunga fordon. www.ifsfluid.se/Seminarium%20Hybriddrifter/Presentation%201%20-%20Jan-Ove%20Palmberg.ppt. Accessed 29-09-2013.
- [64] Petter Krus. Hydraulmekaniska hybridsystem., 2012. Tunga fordon; Tema hybriddrivsystem, 10 april, 2012. Seminarium om drivsystem för drivsystem för energieffektiva tunga fordon. <http://www.ifsfluid.se/Seminarium%20Hybriddrifter/Hybriddrifter-seminarium.htm>.
- [65] Konrad Reif, Karl-Ernst Noreikat, and Kai Borgeest, editors. *Kraftfahrzeug-Hybridantriebe*. Springer Vieweg, 2012. ISBN: 978-3-8348-0722-9.
- [66] Keith Collantine. Kers explained: how a mechanical kinetic energy recovery system works. *F1 Fanatic*, 2009.
- [67] Flybrid Automotive Limited 2013. Original f1 system. <http://www.flybridsystems.com/F1System.html>. Accessed 23-09-2013., 2013.
- [68] Albert Boretti. F1 2014: Turbocharged and downsized ice and kers boost. *World Journal of Modelling and Simulation*, ISSN 1 746-7233, England, UK, 9(2):150–160, 2013.
- [69] Win Rampen. *The Development of Digital Displacement Technology*, chapter Keynote address, pages 12–17. Fluid Power and Motion Control (FPMC), 2010.
- [70] H. Douglas and P. Pillay. Sizing ultracapacitors for hybrid electric vehicles. In *Industrial Electronics Society, 2005. IECON 2005. 31st Annual Conference of IEEE*, pages 6 pp.–, 2005.
- [71] Andrew Burke. Ultracapacitors: why, how, and where is the technology. *Journal of Power Sources*, 91(1):37 – 50, 2000.
-

- [72] D.B. Murray, M.G. Egan, J.G. Hayes, and D.O. Sullivan. Applications of super-capacitor energy storage for a wave energy converter system. In *European Wave and Tidal Energy Conference*, September 2009.
- [73] Poncar Silesia. Bladder accumulators type as and asp - e 01-12, 2013.
- [74] Poncar Silesia. Piston accumulators e 04-11, 2013.
- [75] Hydroll. Piston accumulator - installation and operation manual. rev. 2013-02, 2013.
- [76] L. Helle and S. Munk-Nielsen. Comparison of converter efficiency in large variable speed wind turbines. In *Applied Power Electronics Conference and Exposition, 2001. APEC 2001. Sixteenth Annual IEEE*, volume 1, pages 628–634 vol.1, 2001.
- [77] A. Grauers. Efficiency of three wind energy generator systems. *Energy Conversion, IEEE Transactions on*, 11(3):650–657, 1996.
- [78] Danfoss. Fc 300 design guide - mg.33.bc.02.
- [79] N. Iwabuchi, A. Kawahara, T. Kume, T. Kabashima, and N. Nagasaka. A novel high-torque reluctance motor with rare-earth magnet. *Industry Applications, IEEE Transactions on*, 30(3):609–614, 1994.
- [80] H. Polinder, M.E.C. Damen, and F. Gardner. Linear pm generator system for wave energy conversion in the aws. *Energy Conversion, IEEE Transactions on*, 19(3):583–589, 2004.
- [81] Lei Huang, Haitao Yu, Minqiang Hu, Jing Zhao, and Zhiguang Cheng. A novel flux-switching permanent-magnet linear generator for wave energy extraction application. *Magnetics, IEEE Transactions on*, 47(5):1034–1037, 2011.
- [82] M. A. Mueller. Electrical generators for direct drive wave energy converters. *Generation, Transmission and Distribution, IEE Proceedings-*, 149(4):446–456, 2002.
- [83] Oskar Danielsson. Design of a linear generator for wave energy plant. Master’s thesis, Uppsala University School of Engineering, 2003.
- [84] O. Danielsson, M. Eriksson, and M. Leijon. Study of a longitudinal flux permanent magnet linear generator for wave energy converters. *International Journal of Energy Research*, 30:1130–1145, 2006.
- [85] Jiabin Wang, G.W. Jewell, and D. Howe. A general framework for the analysis and design of tubular linear permanent magnet machines. *Magnetics, IEEE Transactions on*, 35(3):1986–2000, 1999.
- [86] N. Bianchi, S. Bolognani, D.D. Corte, and F. Tonel. Tubular linear permanent magnet motors: an overall comparison. In *Industry Applications Conference, 2002. 37th IAS Annual Meeting. Conference Record of the*, volume 2, pages 1266–1273 vol.2, 2002.
-

- [87] J. Prudell, M. Stoddard, E. Amon, T. K A Brekken, and A. Von Jouanne. A permanent-magnet tubular linear generator for ocean wave energy conversion. *Industry Applications, IEEE Transactions on*, 46(6):2392–2400, 2010.
- [88] J. Wang, G.W. Jewell, and D. Howe. Design optimisation and comparison of tubular permanent magnet machine topologies. *Electric Power Applications, IEE Proceedings -*, 148(5):456–464, 2001.
- [89] Jon Nicholas Baker. *Linear generators for direct drive marine renewable energy converters*. PhD thesis, Durham University., 2003.
- [90] H. Polinder, M.A. Mueller, M. Scuotto, and M. Goden de Sousa Prado. Linear generator systems for wave energy conversion. In *The 7th European Wave and Tidal Energy Conference*, 2007.
- [91] M. A. Mueller, H. Polinder, and N. Baker. Current and novel electrical generator technology for wave energy converters. In *IEEE International Electric Machines & Drives Conference 2007, IEMDC '07*, volume 2, pages 1401–1406, May 2007. WE3.2.
- [92] Erik Dore, Rafael Waters, and Fredrik Axelsson. A linear generator for submerged use and a method of producing electric energy. Patent WO2011149399 (A1), 2010.
- [93] Mats Leijon, Cecilia Boström, Oskar Danielsson, Stefan Gustafsson, Kalle Haikonen, Olivia Langhamer, Erland Strömstedt, Magnus Stålberg, Jan Sundberg, Olle Svensson, Simon Tyrberg, and Rafael Waters. Wave energy from the north sea : Experiences from the lysekil research site. *Surveys in geophysics*, 29(3):221–240, 2008.
- [94] N. Hodgins, Ozan Keysan, A. McDonald, and M. Mueller. Linear generator for direct drive wave energy applications. In *Electrical Machines (ICEM), 2010 XIX International Conference on*, pages 1–6, 2010.
- [95] Francisco Garcia, Marcos Lafoz, Marcos Blanco, and Luis Garcia-Tabares. Efficiency calculation of a direct-drive power take-off. In *9th European Wave and Tidal Energy Conference, EWTEC 2011*, 2011.
- [96] J.H. Prudell, A. Schacher, and K. Rhinefrank. Direct drive ocean wave energy electric plant design methodology. In *Oceans, 2012*, pages 1–7, 2012.
- [97] T.K.A. Brekken, K. Rhinefrank, A. von Jouanne, A. Schacher, J. Prudell, and E. Hammagren. Scaled development of a novel wave energy converter including numerical analysis and high-resolution tank testing. *Proceedings of the IEEE*, 101(4):866–875, 2013.
- [98] K. Rhinefrank, J. Prudell, and A. Schacher. Development and characterization of a novel direct drive rotary wave energy point absorber mts-ieee oceans conference proceedings. In *OCEANS 2009, MTS/IEEE Biloxi - Marine Technology for Our Future: Global and Local Challenges*, pages 1–5, 2009.
-

- [99] K. Rhinefrank, A. Schacher, J. Prudell, T.K.A. Brekken, C. Stillinger, J.Z. Yen, S.G. Ernst, A. Von Jouanne, E. Amon, R. Paasch, A. Brown, and A. Yokochi. Comparison of direct-drive power takeoff systems for ocean wave energy applications. *Oceanic Engineering, IEEE Journal of*, 37(1):35–44, 2012.
- [100] Kenneth Edward Rhinefrank, Bradford Storrs Lamb, Joseph Horan Prudell, and Alphonse Aloysius Schacher. Direct drive rotary wave energy conversion. Patent US20130043682 A1, 2013.
- [101] A.S. McDonald, M.A. Mueller, and H. Polinder. Structural mass in direct-drive permanent magnet electrical generators. *Renewable Power Generation, IET*, 2(1):3–15, 2008.
- [102] E. Spooner and J. Grimwade. Snappertm : an efficient and compact direct electric power take-off device for wave energy converters,. In *World Maritime Technology Conference - IMarEST 4th MAREC Conf*, March 2006. WE3.2.
- [103] N. Hodgins, Ozan Keysan, A.S. McDonald, and M.A. Mueller. Design and testing of a linear generator for wave-energy applications. *Industrial Electronics, IEEE Transactions on*, 59(5):2094–2103, 2012.
- [104] N. Hodgins, A. McDonald, J. Shek, O. Keysan, and M. Mueller. Current and future developments of the c-gen lightweight direct drive generator for wave & tidal energy. In *The 8th European Wave and Tidal Energy Conference*, 2009.
- [105] P. C J Clifton, R.A. McMAHON, and H. P Kelly. Design and commissioning of a 30 kw direct drive wave generator. In *Power Electronics, Machines and Drives (PEMD 2010), 5th IET International Conference on*, pages 1–6, 2010.
- [106] Kelly Hugh-Peter Granville. Low cost linear generator wave energy converters. Patent WO2010061199, November 2008.
- [107] M. A. Mueller and A. S. McDonald. A lightweight low speed permanent magnet electrical generator for direct-drive wind turbines. In *In proc. of EWEC*, 2008.
- [108] D. Bang, H. Polinder, G. Shrestha, and J.A. Ferreira. Review of generator systems for direct-drive wind turbines. In *In proc. of EWEC*, 2008.
- [109] H. Polinder, D. Bang, R. P J O M Van Rooij, A.S. McDonald, and M.A. Mueller. 10 mw wind turbine direct-drive generator design with pitch or active speed stall control. In *Electric Machines Drives Conference, 2007. IEMDC '07. IEEE International*, volume 2, pages 1390–1395, 2007.
- [110] M.A Mueller and N.J Baker. Direct drive wave energy converters. *I Mech E Journal of Power and Energy*, 219:223–234, 2005.
- [111] M. Blanco, M. Lafoz, and L.G. Tabares. Laboratory tests of linear electric machines for wave energy applications with emulation of wave energy converters and sea waves. In *Power Electronics and Applications (EPE 2011), Proceedings of the 2011-14th European Conference on*, pages 1–10, 2011.
-

- [112] M. Blanco, G. Navarro, and M. Lafoz. Control of power electronics driving a switched reluctance linear generator in wave energy applications. In *Power Electronics and Applications, 2009. EPE '09. 13th European Conference on*, pages 1–9, 2009.
- [113] Garret Brady, Cathal O’Loughlin, John Massey, David Griffiths, and Carlos Villegas. Design and test of a linear switched reluctance generator for use in wave-energy applications. In *4th International Conference on Ocean Energy, ICOE*, 2012.
- [114] M. Santos, M. Lafoz, M. Blanco, L. García-Tabares, F. Garcia, A. Echeandia, and L. Gavela. Testing of a full-scale pto based on a switched reluctance linear generator for wave energy conversion. In *4th International Conference on Ocean Energy, ICOE*, 2012.
- [115] William Dick and Carlos Villegas. Wave energy conversion system. Patent US20120139261 A1, 2009.
- [116] A. Serena, M. Molinas, and I. Cobo. Design of a direct drive wave energy conversion system for the seaquest concept. In *In proc. of the 4th Int. Conference on Ocean Energy*, 2012.
- [117] P.O. Rasmussen, T. O. Andersen, F. T. Joergensen, and O. Nielsen. Development of a high performance magnetic gear. In *Industry Applications Conference, 2003. 38th IAS Annual Meeting. Conference Record of the*, volume 3, pages 1696–1702 vol.3, 2003.
- [118] H. Bailey, R. C. Crozier, A. McDonald, M. A. Mueller, E. Spooner, and P. McKeever. Hydrodynamic and electromechanical simulation of a snapper based wave energy converter. In *IECON 2010 - 36th Annual Conference on IEEE Industrial Electronics Society*, pages 3085–3090, 2010.
- [119] E. Spooner, J.R. Bumby, R. Morgan, and J. Grimwade. A high force density generator using a slipping magnetic coupling. In *PEMD, UK*, 2006. WE3.2.
- [120] Edward Spooner. Magnetic force transmission. Patent EP1589643 (A2), 02 2004.
- [121] Richard Crozier, Helen Bailey, Markus Mueller, Ed. Spooner, Paul McKeever, and Alasdair McDonald. Hydrodynamics and electromechanical simulation of a wave energy converter with a novel non-linear pto. In *In proc. of 9th European Wave and Tidal Energy Conference, UK*, 2011.
- [122] P. McKeever, C. Ng, M. C. Taylor, E. Spooner, M. A. Mueller, and R. C. Crozier. Snapper wave energy capture - the mechanical challenge. *Magneus - The International Publication of the UK Magnetism Society*, page 28, 2011.
- [123] Darius Snieckus. A magnetic concept - recharge new article. www.rechargenews.com, November 2010.
- [124] Paul McKeever, Chong Ng, Brian Caffrey, Richard Crozier, and Ed Spooner. Snapper wave device development - the grid interface system. In *In proc. of the 9th European Wave and Tidal Energy Conference, UK*, 2011.
-

-
- [125] R. Crozier, H. Bailey, E. Spooner, P. McKeever, and M.A. Mueller. Analysis, design and testing of a novel direct-drive wave energy converter system. In *Renewable Power Generation (RPG 2011), IET Conference on*, pages 1–6, 2011.
- [126] Kenneth Rhinefrank, Alexandre RT. Yokochi, Annette von Jouanne, Manfred Dittrich, and Emmanuel Agamloh. Magnetic helical screw drive. Patent US2009251258 (A1), April 2009.
- [127] Emmanuel Agamloh, Ken Rhinefrank, Alan Wallace, Manfred Dittrich, and Annette Von Jouanne. Methods and apparatus for power generation. Patent GB 2443101B, 06 2010.
- [128] H.T. Faus. Magnetic transmission. Patent US2371511A, March 1945.
- [129] Nicholas Gerard Vitale. Rotary torque to axial force energy conversion apparatus. Patent US005984960A, July 1997.
- [130] Peter Schuster. Magnetic helix non-contacting linear drive. Patent US5079458A, Jan 1992.
- [131] J. Bakker. Mechanical vibrating system. Patent US3483412A, Dec 1969.
- [132] Lönne. Low voltage three phase squirrel cage asynchronous motors 11 - 315 kw. Technical information K 11?0305 E.
- [133] K. Atallah and D. Howe. A novel high-performance magnetic gear. *Magnetics, IEEE Transactions on*, 37(4):2844–2846, 2001.
- [134] X. Li, K.-T. Chau, M. Cheng, and W. Hua. Comparison of magnetic-gear permanent-magnet machines. *Progress In Electromagnetics Research*, 133:177–198, 2013.
- [135] Christopher G. Bright. Magnetic gear arrangement. Patent US20110156518 A1, 2011.
- [136] Yi Du, K.T. Chau, Ming Cheng, and Yubin Wang. A linear magnetic-gear permanent magnet machine for wave energy generation. In *Electrical Machines and Systems (ICEMS), 2010 International Conference on*, pages 1538–1541, 2010.
- [137] Tommy Larsen. A device for converting wave energy into mechanical energy. Patent EP2245300A2, 2010.
- [138] Arthur Pecher, Jens Peter Kofoed, Tommy Larsen, and Tanguy Marchalot. Experimental study of the weptos wave energy converter. In *International Conference on Ocean, Offshore and Arctic Engineering, OMAE2012*, 2012.
- [139] Arthur Pecher, Jens Peter Kofoed, and Tommy Larsen. Design specifications for the hanstholm weptos wave energy converter. *Energies*, 5(4):1001–1017, 2012.
- [140] Niels Arpe Hansen and Keld Hansen. Wavepowermachine. Patent EP1282746 B1, 2006.
-

-
- [141] WEPTOS. <http://www.weptos.com/technology/>.
- [142] Wei Tong, editor. *Wind Power Generation and Wind Turbine Design*. WIT Press, 2010.
- [143] WindStats. Wind turbine data summary tables, 2008.
- [144] George Corey. Rack and pinion wave motor power plant. Patent US 4108578 A, 1978.
- [145] James E. Eder and David B. Stewart. Wave energy converter and power take off system. Patent US20110084488 A1, 2011.
- [146] Medina Alvaro Jose Atilano and Trinkl Rafael Uzcategui. Wave-power system and method for generating energy at constant rotational speed at variable significant wave heights and periods. Patent WO2007146542, June 2006.
- [147] Emerson Industrial Automation. Gears and gear drives, 2001.
- [148] Miriam Metcalfe. Gearing up for efficiency. *Gear Solutions*, Jan:50–55, 2012.
- [149] Wei-Ming CHI and Philip R. Hart. Wec with improved power take off apparatus. Patent WO2010117414A2, March 2009.
- [150] Karl Merk. Device for generating energy using water waves. Patent WO9951877 (A1), 4 1998.
- [151] David B. Stewart and James Gerber. Wave energy converter utilizing internal reaction mass and spring. Patent WO2007064827, 2007.
- [152] Emmanuel B. Agamloh, Alan K. Wallace, and Annette von Jouanne. A novel direct-drive ocean wave energy extraction concept with contact-less force transmission system. *Renewable Energy*, 33(3):520 – 529, 2008.
- [153] Liu Ze, Wang Chuansheng, and Yang Weimin. Buoy and ball screw combined sea wave generator. Patent CN201517465 (U), 06 2010.
- [154] SKF. 4351 en - 2008-01 - roller screws, 2008.
- [155] SKF. Skf solution for plastic injection moulding. <http://www.skf.com/skf/campaign/mechatronicsin/injectionmoulding.html>.
- [156] Jochen Forstmann. *Kugelgewindetriebe im Einsatz an KunststoffspritzgieSSmaschinen - Lebensdauerprognose und Optimierung*. PhD thesis, University of Duisburg-Essen, 2010.
- [157] David. Pitch driven wave energy converter devices and systems. Patent US20120248774A1, 2012.
- [158] Thomson. *Datasheet on Precision Ball Screws*, 2010.
- [159] Sandor Bisztray Balku. Design development and tribology of reciprocating hydraulic seals. *Periodica Polytechnica Ser. Mech. Eng.*, 47(1):163–178, 2004.
-

-
- [160] Peter Windfeld Rasmussen, editor. *Hydrauli Staanbi*. Nyt Teknisk Forlag, 1996.
- [161] Ross Henderson. Design, simulation, and testing of a novel hydraulic power take-off system for the pelamis wave energy converter. *Renewable Energy*, 31(2):271 – 283, 2006.
- [162] Nik Scharmann, Christian Langenstein, and Dieter Wiltsch. Hydraulic converter. Patent WO2009132763, 2008.
- [163] Nik Scharmann, Franz Wirzberger, Andreas Vath, and Stefan Zimmermann. Converter and method for converting mechanical energy into electric energy. Patent WO2009132762A2, 2008.
- [164] Nik Scharmann, Stefan Zimmermann, Christian Langenstein, and Louis Verdegem. Converter and method for converting mechanical energy into electrical energy. Patent WO2009003598, November 2007.
- [165] Peter Antoszkiewicz. Hydraulic-electric transducer. Patent WO2008128830, 2007.
- [166] Eric Wood. Power generation systems in buoyant structures. Patent US4158780, 1975.
- [167] James S Gerber and David Stewart. Active impedance matching systems and methods for wave energy converter. Patent WO2005069824, January 2004.
- [168] Philip Wesby and Roy Targonski. System and method for hydraulic power transfer. Patent WO 2010032012, 2008.
- [169] Sauer-Danfoss. H1 bent axis variable displacement motors (11037153), 2012.
- [170] Rico Hjerm Hansen. Advanced power management of a telehandler using electronic load sensing. In *10th International Workshop on Research and Education in Mechatronics, Glasgow, UK*, September 10th-11st 2009.
- [171] Rico H. Hansen, Torben O. Andersen, and Henrik C. Pedersen. Development and implementation of an advanced power management algorithm for electronic load sensing on a telehandler. In *Fluid Power and Motion Control, Bath, UK*, 2010.
- [172] Michael Rygaard Hansen, Torben Ole Andersen, Henrik Clemmensen Pedersen, and Finn Conrad. Feasibility study of electronic load sensing concept for hydraulic variable displacement pump. In *In proc. of the 7th International Conference in Education and Mechatronics*. <Forlag uden navn>, 2006.
- [173] Henrik Clemmensen Pedersen, Torben Ole Andersen, and Michael Rygaard Hansen. Designing an electro-hydraulic control module for an open-circuit variable displacement pump. In *In proc. of the 9th Scandinavian International Conference on Fluid Power, SICFP'05*, 2005.
- [174] Ronan costello, John V. Ringwood, and Jochem Weber. Comparison of two alternative hydraulic pto concepts for wave energy conversion. In *9th European Wave and Tidal Energy Conference (EWTEC)*, 2011.
-

-
- [175] Enrique Vidal, Rico Hjerm Hansen, and Morten Mejlhede Kramer. Early performance assessment of the electrical output of wavestar's prototype. In *In proc. of the 4th International Conference on Ocean Energy, 17 October, Dublin, 2012*.
- [176] Kristof Schlemmer, Franz Fuchshumer, Norbert Boehmer, Ronan Costello, and Carlos Villega. Design and control of a hydraulic power take-off for an axisymmetric heaving point absorber. In *In proc. of the 9th European Wave and Tidal Energy Conference, EWTEC, 2011*.
- [177] Rico Hjerm Hansen, Torben Ole Andersen, and Henrik C. Pedersen. Model based design of efficient power take-off systems for wave energy converters. In *Proc. of the 12th Scandinavian International Conference on Fluid Power, SICFP 2011*, pages 35–49. Tampere University of Technology, Finland, 2011.
- [178] William H S Rampen, Niall Caldwell, and Uwe Stein. Annular valve. Patent US 7077378, 07 2002.
- [179] William Hugh Salvin Rampen, Uwe Stein, Fergus Robert McIntyre, Gordon Paul Voller, and Colin Francis Souza. Electronically controlled valves. Patent WO 2010/106361 A1, 2010.
- [180] Stephen Salter and William Rampen. Improved fluid-working machine. Patent EP 0494236 B1, 12 1990.
- [181] Stephen Salter and William Rampen. Pump control method and poppet valve therefor. Patent EP 0361927 B1, 1989.
- [182] William Rampen, Niall Caldwell, and Uwe Stein. Valve actuator. Patent WO 2010/048954 A1, 2009.
- [183] Onno Kuttler and Uwe Stein. Fluid working machine. Patent WO 2009/056138 A1, 2008.
- [184] Stephen Salter and Matthew Rea. Hydraulics for wind. In *In proc. of the European Wind Energy Conference in Hamburg in October, 1984*.
- [185] Kazuhisa Tsutsumi, Atsushi Maekawa, Masayuki Shimizu, Stephen Salter, Uwe Stein, William Rampen, Robert Fox, and Hauke Karstens. Wind turbine generator and tidal current generator with a hydraulic transmission. Patent US8358024 B2, 2013.
- [186] S. H. Salter. Digital hydraulics for renewable energy. In *World Renewable Energy Conference Aberdeen, 2005*.
- [187] Md. Ehsan, W.H.S. Rampen, and J.R.M Taylor. Simulation and dynamic response of computer controlled digital hydraulic pump/motor system used in wave energy power conversion. In *In proc. 2nd European Wave Power Conference, Lisbon.,* pages 305–311, November 1995.
- [188] S.H. Salter and W.H.S Rampen. The wedding cake multi-eccentric radial piston hydraulic machine with direct computer control of displacement. In *Proc. 10th International Conference on Fluid Power*, pages 47–64, 1993.
-

- [189] John Fitzgerald. Wave energy converter. Patent WO2008149084, 2007.
- [190] Niall James Caldwell. Electromagnetic actuator. Patent US 2009/0302251 A1, 12 2007.
- [191] Win Rampen. Gearless transmissions for large wind turbines - the history and future of hydraulic drives. In *A paper presented at DEWEK Bremen in 2006 by Dr. Win Rampen*, <http://www.artemisip.com/news-media/papers>, 2006.
- [192] Jan Erich Hemmelmann and Jacob Johannes Nies. Wind energy system with fluid-working machine with non-symmetric actuation. Patent US8074450 B2, 2011.
- [193] Uwe Stein. Hydraulische kraftuebertragung in windenergieanlagen. In *Paper by Artemis*, <http://www.artemisip.com/news-media/papers>, 2006.
- [194] G. S. Payne, A. Kiprakis, M. Ehsan, W. H. S. Rampen, J. P. Chick, and R. Wallace. Efficiency and dynamic performance of digital displacement hydraulic transmission in tidal current energy converters. In *Journal of Power and Energy, Part A : In Proceedings of IMechE.*, volume 221, pages 207–217, May 2007.
- [195] Lopez Fernando Gracia. Dynamic fluid energy conversion system and method of use. Patent WO 2008132550, October 2007.
- [196] Grégory S. Payne, Uwe B.P. Stein, Mohammad Ehsan, Niall J. Caldwell, and W H.S. Rampen. Potential of digital displacement hydraulics for wave energy conversion. In *In proc. of the 6th European Wave and Tidal Energy Conference, Glasgow, UK*, August 29th - September 2nd 2005.
- [197] Luke Wadsley. Optimal system solutions enabled by digital pumps. In *International Exposition for Power Transmission (IFPE)in Las Vegas*, 2011.
- [198] W.H.S. Rampen and S.H Salter. Measuring and predicting the frequency response of the digital hydraulic pump. In *5th Bath Int. Fluid Power Workshop, Component and Systems Design, Bath*, pages 155–166, 1992.
- [199] M. Ehsan, W.H.S Rampen, and S.H Salter. Computer simulation of the performance of digital-displacement pump-motors. *ASME International Mechanical Engineering Congress and Exposition*, 3:19–24, 1996.
- [200] Md. Ehsan, W. H. S. Rampen, and S. H. Salter. Modeling of digital-displacement pump/motors and their application as hydraulic drives for nonuniform loads. *Project B3 - Power Take-off Systems*, 122(1):210–215, 2000.
- [201] Ltd Mitsubishi Heavy Industries. Mhi begins test operation of large-scale wind power generation system adopting a hydraulic drive train - a world's first, at yokohama dockyard & machinery works - <http://www.mhi.co.jp/en/news/story/1301241616.html>. press information january 24, 2013 no.1616.
- [202] Niall Skinner. Wave energy converter device. Patent EP2284386A2, 2009.
-

-
- [203] A.R. Plummer and M. Schlotter. Investigating the performance of a hydraulic power take-off. In *In proc. of the 8th European Wave and Tidal Energy Conference*, 2009.
- [204] Peter Achten, Titus van den Brink, Jeroen Potma, Marc Schellekens, and Georges Vael. A four-quadrant hydraulic transformer for hybrid vehicles. In *In proc. of the 11th Scandinavian International Conference on Fluid Power, SICFP'09, June 2-4, Linköping, Sweden*, 2009.
- [205] P. A. J. Achten. Changing the paradigm. In *In proc. of the 10th Scandinavian International Conference on Fluid Power, SIFCP, Tampere, Finland*, 2009.
- [206] Peter A.J. Achten, Zhao Fu, and Georges E.M. Vael. Transforming future hydraulics: a new design of a hydraulic transformer. In *In proc. of the the 5th SICFP*, 1997.
- [207] Peter Achten, Georges Vael, Titus van den Brink, Jeroen Potma, and Marc Schellekens. Efficiency measurements of the hybrid motor-pump. In *In proc of yhe Twelfth Scandinavian International Conference on Fluid Power, SICFP'11,, 2011*.
- [208] Georges Vael, Peter Achten, and Jeroen Potma. Cylinder control with the floating cup hydraulic transformer. In *In proc. of the Eighth Scandinavian International Conference on Fluid Power, SICFP'03, May 7-9, Tampere, Finland*, 2003.
- [209] G. Vael, P. Achten, and Z. Fu. The innas hydraulic transformer - the key to the hydrostatic common pressure rail. In *SAE paper 2000-01-2561*, 2000.
- [210] Peter Achten. Pressure transformer. Patent US6116138, 2000.
- [211] R. Werndin and P. Achten. Efficiency performance and control aspects of a hydraulic transformer. In *In proc of the Sixth Scandinavian Int. Conference of Fluid Power, Tampere, Finland*, 1999.
- [212] P. Achten and C. Vael. Energy efficeincy of the hybrid. In *In prof of the th Int. Fluid Power Conference, Dresden, Germany*, 2008.
- [213] Vladimir Kalinin. Control for hydraulic system of wave energy device. Patent GB2459112, 2008.
- [214] Yukio Kamizuru, Matthias Liermann, and Hubertus Murrenhoff. Simulation of an ocean wave energy converter using hydraulic transmission. In *7th International Fluid Power Conference*, 2010.
- [215] Michael Livingstone and Andrew Plummer. The design simulation and control of a wave energy converter power take off. In *7th International Fluid Power Conference*, 2010.
- [216] Andrew Roberts, Michael Schlotter, Andrew Plummer, and Derek Tilley. Cfx / simulink co-simulation of awave energy converter. In *Fluid Power and Motion Control, Bath, UK*, 2010.
-

- [217] Andrew Hillis Chris Cargo, Andrew Plummer and Michael Schlotter. Optimal design of a realistic hydraulic power take-off in irregular waves. In *9th European Wave and Tidal Energy Conference, EWTEC 2011*, 2011.
- [218] C.J. Cargo, A.R. Plummer, A. J. Hillis, and M. Schlotter. Determination of optimal parameters for a hydraulic power take-off unit of a wave energy converter in regular waves. *Proceedings of the Institution of Mechanical Engineers, Part A: Journal of Power and Energy February*, 226, no. 1:98–111, 2012.
- [219] L. M. Yang, J. Hals, and T. Moan. A wear model for assessing the reliability of wave energy converter in heave with hydraulic power take-off. In *In proc. of the 8th European Wave and Tidal Energy Conference*, 2009.
- [220] C.J. Taylor, M.A. Stables, P. Cross, K. Gunn, and G.A. Aggidis. Linear and nonlinear modeling and control of a power take-off simulation for wave energy conversion. In *In proc. of 8th European Wave and Tidal Energy Conference*, 2009.
- [221] Adi Kurniawan, Eilif Pedersen, and Torgeir Moan. Bond graph modelling of a wave energy conversion system with hydraulic power take-off. *Renewable Energy*, 38(1):234 – 244, 2012.
- [222] Giorgio Bacelli, Jean Christophe Gilloteaux, and John Ringwood. State space model of a hydraulic power take off unit for wave energy conversion employing bondgraphs. In *In proc. of the World Renewable Energy Conferencem Glasgow*, 2008.
- [223] H. Eidsmoen. Simulation of a tight-moored amplitude-limited heaving-buoy wave-energy converter with phase control, 1996. The paper represents an extension and enlargement of the following published work: Eidsmoen, H.: "Simulation of a heaving-buoy wave energy converter with phase control". In proc. of the 2nd EWTEC. http://folk.ntnu.no/falnes/w_e/index-e.html.
- [224] H. Eidsmoen. Tight-moored amplitude-limited heaving-buoy wave-energy converter with phase control. *Applied Ocean Research*, 20(3):157 – 161, 1998.
- [225] H. Eidsmoen. Simulation of a slack-moored heaving-buoy wave energy converter with phase control, 1996. http://folk.ntnu.no/falnes/w_e/index-e.html.
- [226] H. Eidsmoen. Simulation of a heaving-buoy wave energy converter with phase control. In *In proc. of the Second European Wave Power Conference, Lisbon, Portugal, 8-10 November, 1995, ISBN 92-827-7492-9*, 1995.
- [227] Per Resen Steenstrup. An installation comprising a wave power apparatus and a support structure therefor. Patent WO2006108421, 2005.
- [228] P. Ricci, J. Lopez, M. Santos, J.L. Villate, P. Ruiz-Minguela, F. Salcedo, and A.F.deO. Falcao. Control strategies for a simple point-absorber connected to a hydraulic power take-off. In *In proc. of the 8th European Wave and TidalEnergy Conference, 7-10 September , Uppsala Sweden*, 2009.
-

- [229] P. Ricci, J. Lopez, M. Santos, P. Ruiz-Minguela, J.L. Villate, F. Salcedo, and A.F. de O Falca?o. Control strategies for a wave energy converter connected to a hydraulic power take-off. *Renewable Power Generation, IET*, 5(3):234–244, 2011.
- [230] Vladimir Kalinin. A wave energy conversion system. Patent WO2009153329, 2008.
- [231] Richard Yemm. Wave power apparatus. Patent WO2004088129, 2003.
- [232] Richard Yemm, David Pizer, and Chris Retzler. Floating apparatus and method for extracting power from sea waves. Patent WO0017519, 1998.
- [233] R. Yemm, D. Pizer, C. Retzler, and R. Henderson. Pelamis: experience from concept to connection. *Philos Transact A Math Phys Eng Sci*, 370(1959):365–80, 2012.
- [234] R. Yemm. Pelamis wec- intermediate scale demonstration v/06/00188/00/00/rep, 2003.
- [235] Richard Yemm. Pelamis wec - full-scale joint system test.pdf, 2003. WE6.2, WE3.1.3.1.
- [236] Lasa Aguirrebengoa Joseba [and Antolin Urbaneja Juan Carlos and Estensoro Astigarraga Francisco Jose. Power take-off device for wave energy transformation. Patent EP2466118(A1), 2012.
- [237] Joseba Lasa, Juan Carlos Antolin, Carlos Angulo, Patxi Estensoro, Maider Santos, and Pierpaolo Ricci. Design, construction and testing of a hydraulic power take-off for wave energy converters. *Energies*, 5(6):2030–2052, 2012.
- [238] Joseba Lasa, Juan Carlos Antolin, Patxi Estensoro, Carlos Angulo, Pierpaolo Ricci, and Maider Santos. Construction of a universal hydraulic power take-off for wave energy converters. mathematical modelling and validation. In *In proc. of the 9th European Wave and Tidal Energy Conference*, 2011.
- [239] M. Linjama, H-P. Vihtanen, A. Sipola, and M. Vilenius*. Secondary controlled multi-chamber hydraulic cylinder. In *The 11th Scandinavian International Conference on Fluid Power, SICFP'09, June 2-4, 2009, Linköping, Sweden*, 2009.
- [240] Ari Sipola, Hannu pekka Vihtanen, Matti Linjama, and Arto Laamanen. Digital hydraulic system. Patent WO2010040890, 2008.
- [241] Stefan Zimmermann and Nik Scharmann. Power plant for converting mechanical primary energy into another form of energy and method for converting mechanical primary energy in a power plant. Patent WO2010078890 (A2), 2009.
- [242] Helmut Kogler, Rudolf Scheidl, Michael Ehrentraut, Emanuele Guglielmino, Claudio Semini, and Darwin G. Caldwell. A compact hydraulic switching converter for robotic applications. In *In proc. of Bath/ ASME Symposium on Fluid Power and Motion Control*, 2010.
-

- [243] H Kogler and R Scheidl. Two basic concepts of hydraulic switching converters. In *In proc. of the First Workshop on Digital Fluid Power, DFP08, Tampere, Finland, 2009*.
- [244] B. Winkler and R. Scheidl. Development of a fast seat type switching valve for big flow rates. In *The Tenth Scandinavian International Conference on Fluid Power*, volume 10, pages 137–146, 2007.
- [245] Bernd Winkler, Andreas Ploeckinger, and Rudolf Scheidl. A novel piloted fast switching multi poppet valve. *International Journal of Fluid Power*, 11:7–14, 2010.
- [246] R. Scheidl, B. Manhartgrubel, H. Kogler, and M. Mairhofer. Hydraulic buck converter - concept and experimental results. In *In proc. of the 6th Int. Fluid Power Conference, Dresden, Germany, 2008*.
- [247] Kyle Merrill, Michael Holland, Mark Batdorff, and John Lumkes Jr. Comparative study of digital hydraulics and digital electronics. *International Journal of Fluid Power*, 11:45–51, 2010.
- [248] Gier Gertrudis and Maria Gerardus. Hydraulic cylinder for use in a hydraulic tool. Patent EP 1580437 B1, 2004.
- [249] S. Kim and H. Murrenhoff. Measurement of effective bulk modulus for hydraulic oil at low pressure. *Journal of Fluids Engineering, Transactions of the ASME*, 134(2), 2012.
- [250] Parker. Tdp valve - catalogue hy11-3500/uk, 2012.
- [251] UQM. Spm218-143-3 motor/generator, 2009.
- [252] NorrHydro. Norrdigi system solution. <http://www.norrhydro.com/en/norrdigi/norrdigi-system-solution.html>, 2013.
- [253] J.E. Funk and T.R. Robe. Transients in pneumatic transmission lines subjected to large pressure changes. *International Journal of Mechanical Sciences*, 12(3):245–257, 1970.
-

